UNIVERSITY OF Southampton

Faculty of Engineering and the Environment

The Effect of Fibre Reinforcements on the Mechanical Behaviour of Railway Ballast

by

Olufemi O. Ajayi

Thesis for the degree of Doctor of Philosophy

June 2014

University of Southampton

Faculty of Engineering and the Environment

Thesis for the degree of Doctor of Philosophy

ABSTRACT

The Effect of Fibre Reinforcements on the Mechanical Behaviour of Railway Ballast

by Olufemi Olayinka Ajayi

Ballast is a primary component of the railway track and it has several functions including the ability to resist vertical, lateral and longitudinal forces applied to the sleepers from the train wheels. In response to the stresses induced during a train passage, ballast typically experiences plastic settlement which can reach unacceptable magnitudes. Thus, ballast is the focus of the majority of maintenance and renewal activities. In response to the growing need for resilient track materials (including ballast) to cope with increasing train speed, load and frequency, means of optimizing its performance and minimizing maintenance requirements are required.

Ballast improvement techniques, such as the use of geogrids, have attracted a great deal of attention in terms of research, but huge potential for reducing costs through ballast improvement still exist. It has been shown from previous research that the use of randomly oriented fibres in sands can significantly improve their strength. This technique might be used to improve ballast strength and reduce track geometry deterioration. In addition, fibre reinforcements in ballast can potentially provide a new method of reinforcing ballast whilst maintaining the capability of withstanding typical tamping operations which are incompatible with geogrids. However, there is a lack of rigorous scientific understanding of the effects of fibre reinforcements on relatively large aggregates such as railway ballast.

This research examines the effect of random fibre inclusions on the packing structure of granular materials (coarse sand and scaled ballast) and describes the physical implications associated with the observed changes. The mechanical properties of fibre reinforced granular materials across different particle sizes and a hypothesis of fibre/particle reinforcement suitable for relatively large particles are presented. An image-based deformation measurement technique has also been used to investigate the effects of fibre reinforcements on the local deformation of triaxial specimens to corroborate the observed mechanical behaviour of the reinforced specimens. Finally, the mechanical behaviour of a fibre reinforced ballast layer below a cyclically loaded railway sleeper was investigated using a full scale laboratory tests.

Contents

ABSTRACT ..... **i**

Contents ..... **iii**

List of Tables ..... **vii**

List of Figures ..... **ix**

Declaration of Authorship ..... **xvii**

Acknowledgements ..... **xix**

Abbreviations ..... **xxi**

Symbols ..... **xxiii**

1 Introduction **1**

1.1 Background 1

1.2 Research Objectives 2

1.3 Organisation of this report 2

2 Literature Review **5**

2.1 Overview 5

2.2 Rail track 5

2.3 Ballast 6

2.3.1 Particle Characteristics 8

2.3.2 Bulk Characteristics 8

2.3.3 Loading Characteristics 9

2.4 Effects of Dynamic Loads on Railway Track 11

2.5 Use of Geosynthetics in Railway Ballast 12

2.6 Fibre Reinforcement of Sand 16

2.6.1 Fibre Properties 16

2.6.2 Bulk Properties of Reinforced Soil 18

2.6.3 Mechanical Behaviour of Fibre-Reinforced Sands 21

2.6.4 Stress Distribution in Fibres 25

2.6.5 Micromechanics of Fibre Reinforced Sands 28

2.7 Conclusions 31

3 Structure of Fibre Reinforced Granular Materials **33**

3.1 Introduction 33
3.2 Materials 34
3.2.1 Leighton Buzzard Sand (Fraction A) 34
3.2.2 Scaled Ballast 34
3.2.3 Fibres 36
3.3 Sample Preparation 37
3.3.1 Maximum dry density tests 38
3.3.2 Minimum dry density tests 38
3.4 Description of Parameters 39
3.5 Dry Density Test Results 41
3.6 Principles of fibre/particle interaction 43
3.7 Discussion 52
3.8 Conclusions 52
4 Monotonic Triaxial Tests on Granular Materials: Apparatus and Methods 55
4.1 Introduction 55
4.2 Monotonic Triaxial Test on reinforced LB sand 58
4.2.1 Test Apparatus 58
4.2.2 Calibration and Data Logging 59
4.2.3 Test Procedure 59
4.2.4 Description of Parameters 60
4.2.5 Typical Test Results 62
4.3 Monotonic Triaxial Tests on Scaled Ballast 64
4.3.1 Test Apparatus 64
4.3.2 Calibration and Data Logging 64
4.3.3 Test procedure 64
4.3.4 Typical Test Results 68
4.4 Conclusions 72
5 Monotonic Triaxial Tests on Granular Materials: Results and Analysis 73
5.1 Introduction 73
5.2 Leighton Buzzard Sand 73
5.3 Scaled Ballast 79
5.4 Behaviour of fibre reinforced granular materials at different scales 95
5.5 Fibre Reinforcement Mechanism in Granular Materials 103

5.5.1 Fibre/particle Interaction Mechanism Development 103
5.5.2 Tensile Force Mobilisation 104
5.6 Potential Applications in Railway Ballast 105
5.7 Conclusions 106
6 Image-Based Deformation Study of Reinforced Scaled Ballast Triaxial Specimens 109
6.1 Introduction 109
6.2 Experimental Set-Up 110
6.3 Brief description of technique 110
6.3.1 Pre-processing 111
6.3.2 Processing 111
6.3.3 Post-processing 115
6.3.4 Resolution, Precision and Accuracy 115
6.4 Typical results 116
6.5 Deformation characteristics of 1/5 SB triaxial specimens 119
6.5.1 Pre-peak Deformation 119
6.5.2 Post-peak Deformation 128
6.6 Discussion 136
6.7 Conclusions 137
7 Full-Scale Laboratory Tests on Fibre Reinforced Railway Ballast 139
7.1 Introduction 139
7.2 Southampton Railway Test Facility 140
7.3 Test Procedure 146
7.3.1 Test materials 146
7.3.2 Test setup 146
7.4 Results 149
7.4.1 Typical ballast layer settlement 149
7.4.2 Plastic Settlement 152
7.4.3 Stiffness 154
7.4.4 Longitudinal pressure 159
7.5 Discussion 162
7.6 Conclusions 162
8 Conclusions and Further Research 165
8.1 Conclusions 165

8.1.1 Packing structure of fibre reinforced granular materials 165
8.1.2 Mechanical properties of fibre reinforced LB sand, 1/5 and 1/3 scaled ballast 166
8.2 Implications of this research for future applications in railway ballast..... 167
8.3 Further research 168
Appendices..... 169
Appendix A 171
Appendix B 174
References..... 177

List of Tables

Table 3.1: Full size ballast specification, 1/3rd and 1/5th scale equivalent 35

Table 3.2: Coefficient of uniformity, C_u for the test materials 36

Table 3.3: Typical values of the basic properties of polypropylene and polyethylene fibres 37

Table 3.4: Materials used with the corresponding fibre properties 39

Table 3.5: Maximum standard deviation of the void ratios obtained from each test 41

Table 4.1: Fibre properties used for triaxial test 59

Table 5.1: Fibre content and fibre lengths used in the triaxial tests on LB sand 74

Table 5.2: Effect of varying V_{fr} and L_f on the stress ratio at $d = 0$, M and the mobilised friction angle at the onset of dilation, φ'_{dil} 78

Table 5.3: Triaxial test conditions, normalised dimensions of the fibres and grains used and fibre/particle numbers for triaxial test on 1/5 and 1/3 SB specimens 81

Table 5.4: Effect of V_{fr} on the rate of increase of mobilised strength with rate of dilation, β and stress ratio at $d = 0$, M when $L_N = 7.1$ and $W_N = 2.5$ 88

Table 5.5: Effect of L_N on the rate of increase of mobilised strength with rate of dilation, β and stress ratio at $d = 0$, M when $V_{fr} = 1.6\%$ and $W_N = 2.5$ 89

Table 5.6: Effect of W_N on the rate of increase of mobilised strength with rate of dilation, β and stress ratio at $d = 0$, M when $V_{fr} = 1.6\%$ and $L_N = 7.1$ 89

Table 5.7: Relative fibre/particle numbers for triaxial test on 1/5 and 1/3 SB specimens 97

Table 7.1: Fibres used for the full scale test 147

Table 7.2: Density of the test materials 147

List of Figures

Figure 2.1: Types of geosynthetics used as reinforcements in soil and aggregates, (a) geotextile, (b) geogrid, (c) geocell, (d) geomesh, (Ingold, 1994) (e) geocomposite (Indraratna et al., 2011) 6

Figure 2.2: Principle of track structure (a) cross-section (b) longitudinal section (after, Esveld, 2001) 7

Figure 2.3: Settlement response of fresh reinforced and unreinforced ballast plotted in (a) linear scale, (b) semi-logarithmic scale (after Indraratna et al., 2011) 10

Figure 2.4: Stresses on pavement elements: (a) principal stresses and planes (b) shear and normal stresses on horizontal and vertical planes (after Brown, 1996) 11

Figure 2.5: Permanent deformation of Materials A, B, C, and D as a result of cyclic loading with and without principal stress rotation (Gräbe and Clayton, 2009) 12

Figure 2.6: (a) Deformed triaxial sample with three geogrid layers, and (b) Contact force distribution and geogrid after partial horizontal and vertical loading (after McDowell et al., 2006) 14

Figure 2.7: Field assessment of the effect of a geocomposite layer on the average lateral strain of ballast (after Indraratna et al., 2010) 15

Figure 2.8: Displacement vectors of ballast particles at maximum load during the ninth load cycle, (a) Unreinforced sample (maximum magnitude of displacement vectors = 13mm); (b) reinforced sample (maximum magnitude of displacement vectors = 8.4mm) 15

Figure 2.9: Influence of aperture size on settlement of geogrid reinforced ballast (after Brown et al., 2007) 16

Figure 2.10: Improvement in shear strength of fibre-reinforced sand (after Sadek et al., 2010) 17

Figure 2.11: Possible sand-fibre interaction (a) Short random oriented fibre reinforced soil, and (b) Continuous thin filament reinforced soil (after Michalowski, 1997) 20

Figure 2.12: Coarse sand reinforced with polyamide fibres at different orientations (after Michalowski and Cermak, 2002) 21

Figure 2.13: Principal Stress Envelopes from Triaxial Compression tests on reinforced sand (after Maher and Gray, 1990) 22

Figure 2.14: Shear stress-horizontal displacement response for unreinforced and reinforced sand with fibre content (by weight) = 0.50% (after Yetimoglu and Salbas, 2003) 23

Figure 2.15: Stress-strain and volumetric response of fibre reinforced and unreinforced Osorio sand at a confining pressure of 200 kPa (after Heineck et al., 2005) 23

Figure 2.16: Fibre reinforced (continuous fibres) composite material (after Vinson and Chou, 1975) 27

Figure 2.17: Stress distribution of a fibre parallel to the applied tensile stress (a) Actual stress distribution, and (b) simplified stress distributions for $l > l_c$ and $l < l_c$ (after Fukuda and Chou, 1982) 27

Figure 2.18: Filament wrapped around clusters of grains (after Michalowski, 1997) 28

Figure 2.19: (a) Change in the configuration of fibre during isotropic compression, and (b) averaged tensile stress in fibres developed with macro deformation under isotropic compression (after Maeda and Ibraim, 2008) 29

Figure 2.20: Averaged tensile stress in fibres developed with macro deformation under shearing (after Maeda and Ibraim, 2008) 30

Figure 2.21: Contact fabric for granular matrix phase; (a) and (b) shows fabric in the direction of major and minor principal stress respectively (after Maeda and Ibraim, 2008) 30

Figure 3.1: Particle size distribution of Leighton Buzzard sand (fraction A), 1/5 and 1/3 scaled, and Network Rail standard ballast 35

Figure 3.2: Example particles in sieve intervals in millimetres: (a) 9.5 - 11.2; (b) 11.2 - 13.2; (c) 13.2 - 16.0; (d) 16.0 - 22.4; (e) 22.4 - 31.5; (f) 31.5 - 40.0; (g) 40.0 - 50.0; (h) 50.0 - 62.5 (after, Le Pen et al., 2014) 36

Figure 3.3: Fibres used in the laboratory tests (a) polypropylene and, (b) polyethylene 37

Figure 3.4: Cylindrical compaction mould used for the determination of the dry density of scaled ballast 39

Figure 3.5: Volumes of phases in a fibre reinforced granular material 41

Figure 3.6: Effect of increasing V_{fr} on the void ratio of (a) fibre reinforced LB sand, and (b) fibre reinforced 1/3rd scaled ballast 42

Figure 3.7: Void ratio e against volumetric fibre ratio V_{fr} plot for three scenarios of fibre-particle interaction compared with data for e_{min} for Leighton Buzzard sand 44

Figure 3.8: Variation of the local slope of the e/V_{fr}, α with V_{fr} for (a) LB sand and (b) Scaled ballast 46

Figure 3.9: Illustration of the effect of adding volume of fibres, V_f (a) Unreinforced granular material i.e. V_{T0}, V_{V0} and V_S; (b) Fibre reinforced granular material at constant V_{T0}, (V_S + ΔV_S) and (V_{V0} + ΔV_V); (c) Fibre reinforced granular material at constant V_S, (V_{T0} + ΔV_T) and (V_{V0} + ΔV_V) 47

Figure 3.10: Experimental results showing the relative rates of substitution (a) dV_s/dV_f, and (b) dV_v/dV_f at constant V_T for LB sand 50

Figure 3.11: Experimental results showing the relative rates of substitution (a) dV_s/dV_f, and (b) dV_v/dV_f at constant V_T for 1/3 scaled ballast 51

Figure 3.12: Phase relations diagram of (a) unreinforced (b) fibre reinforced granular material at constant V_T and compactive effort 52

Figure 4.1: Form indicators 56

Figure 4.2: Zingg plot to characterize particle form (redrawn from Zingg (1935), alternative descriptors in brackets selected from Blott and Pye (2008)) (after Le Pen et al., 2013) 56

Figure 4.3: Zingg plots of all scalene ellipsoid equivalent sphericity (SEES) data for (a) individual particles (b) averages 57

Figure 4.4: Cumulative distribution curves for S/L, the legend shows the catching sieves in mm57

Figure 4.5: (a) Triaxial set up showing the Mini-dyn apparatus without sample (b) Deformed triaxial sample at the end of the test 58

Figure 4.6: Typical plots of deviator stress and volumetric strain plotted against axial strain for unreinforced sand and reinforced sand specimens, tested dry at a cell pressure of 20 kPa... 63

Figure 4.7: (a) Triaxial test setup before placement of cell showing scaled ballast sample under suction, computer and pressure controllers (b) schematic of triaxial test setup 66

Figure 4.8: Specimen showing top cap arrangement 67

Figure 4.9: Fibre reinforced specimen preparation (a) Fibre and scaled ballast mixing (b) compaction (c) split mould containing fibre scaled ballast mixture placed on triaxial pedestal (d) scaled ballast triaxial specimen held under suction 67

Figure 4.10: Comparison of triaxial test on dry and saturated 1/3 SB samples at an effective stress of 30 kPa 69

Figure 4.11: Typical plots of (a) deviator stress and (b) volumetric strain against axial strain for unreinforced and reinforced 1/3 scaled ballast specimens with V_{fr} = 1.6% showing the effects of the additional of fibres and repeatability of the triaxial tests on reinforced specimens. Cell pressure = 30 kPa 70

Figure 4.12: Comparison of triaxial tests on 1/5 and 1/3 SB samples (a) stress ratio, q/p' (b) volumetric strain. Cell pressure = 30 kPa 71

Figure 5.1: Effect of varying V_{fr} on the stress ratio, q/p', mobilised angle of friction, φ'_{mob} and volumetric strain of reinforced LB sand at cell pressure = 20 kPa 75

Figure 5.2: Effect of varying L_f on the stress ratio, q/p', mobilised angle of friction, φ'_{mob} and volumetric strain of reinforced LB sand at cell pressure = 20 kPa 76

Figure 5.3: Effects of V_{fr} with constant L_f on the stress-dilation relationship of reinforced and unreinforced sand specimens 77

Figure 5.4: Effects of varying V_{fr} and L_f on the stress-dilation relationship of reinforced and unreinforced sand specimens 78

Figure 5.5: Effect of fibre reinforcement on the radial strain of reinforced and unreinforced sand specimens 79

Figure 5.6: Effect of increasing V_{fr} when L_N = 7.1 and W_N = 2.5 on (a) the effective friction angle (b) volumetric strain for reinforced 1/3 SB at a cell pressure of 30 kPa..... 82

Figure 5.7: Effect of increasing V_{fr} when L_N = 7.1 and W_N = 2.5 on (a) the effective friction angle (b) volumetric strain for reinforced 1/5 SB at a cell pressure of 30 kPa..... 83

Figure 5.8: Effect of increasing W_N when V_{fr} = 1.6% and L_N = 7.1 on (a) the effective friction angle (b) volumetric strain for reinforced 1/3 SB at a cell pressure of 30 kPa 84

Figure 5.9: Effect of increasing W_N when V_{fr} = 1.6% and L_N = 7.1 on (a) the effective friction angle (b) volumetric strain for reinforced 1/5 SB at a cell pressure of 30 kPa 85

Figure 5.10: Effect of increasing L_N when V_{fr} = 1.6% and W_N = 2.5 on (a) the effective friction angle (b) volumetric strain for reinforced 1/3 SB at a cell pressure of 30 kPa 86

Figure 5.11: Effects of varying L_N on the $T\varphi'_{mob}$ of reinforced 1/3 SB specimens with W_N = 2.5 and V_{fr} = 1.6% at different shear strains..... 87

Figure 5.12: Effects of varying W_N on the $T\varphi'_{mob}$ of reinforced 1/3 SB specimens with L_N = 7.1 and V_{fr} = 1.6% at different shear strains..... 87

Figure 5.13: Data smoothening for Dense 1/3 SB sample 89

Figure 5.14: Effects of V_{fr} on the rate of dilation, d, of 1/3 SB specimens while L_N = 7.1 and W_N = 2.5 (a) whole test, (b) when $d \geq 0$ 90

Figure 5.15: Effects of L_N on the rate of dilation, d of 1/3 SB specimens while V_{fr} = 1.6% and W_N = 2.5 (a) whole test, (b) when $d \geq 0$ 91

Figure 5.16: Effects of W_N on the rate of dilation, d of 1/3 SB specimens while L_N = 7.1 and V_{fr} = 1.6% (a) whole test, (b) when $d \geq 0$..... 92

Figure 5.17: Effect of L_N on Secant Modulus, E_s of fibre reinforced 1/3 SB with V_{fr} = 1.6% and W_N = 2.5..... 94

Figure 5.18: Effect of W_N on Secant Modulus, E_s of fibre reinforced 1/3 SB with V_{fr} = 1.6% and L_N = 7.1 94

Figure 5.19: Effect of V_{fr} on Secant Modulus, E_s of fibre reinforced 1/3 SB with W_N = 2.5 and L_N = 7.1..... 95

Figure 5.20: Fibre/particle number effects on mobilised friction angle and volumetric strain of reinforced 1/5 and 1/3 SB when L_N = 7.1 and W_N = 2.5 for V_{fr} = 1.6%..... 98

Figure 5.21: Fibre/particle number effects on mobilised friction angle and volumetric strain of reinforced 1/5 and 1/3 SB when L_N = 7.1 and W_N = 2.5 for V_{fr} = 3.2%..... 99

Figure 5.22: Effects of fibre/particle number, N_{fp} on $N\varphi'_{mob}$ for 1/5 and 1/3 SB specimens having similar L_N and W_N when, (a) V_{fr} = 1.6%, and; (b) V_{fr} = 3.2%..... 100

Figure 5.23: Mobilised friction angle and volumetric strain of reinforced 1/5 and 1/3 SB specimens at constant N_{fp}, L_N = 7.1 and W_N = 2.5..... 101

Figure 5.24: Normalised friction angle of reinforced 1/5 and 1/3 SB specimens at constant L_N = 7.1 and W_N = 2.5 (a) $N_{fp} \approx 1.3$, and; (b) $N_{fp} \approx 3$ 102

Figure 5.25: Potential fibre-pinch contact points in a fibre reinforced granular matrix with relatively (a) short fibre and (b) long fibre 105

Figure 6.1: The triaxial setup for image-based deformation study showing the transparent cell, cameras, uniform light source and light reflecting curtain 112

Figure 6.2: Coordinate axes, specimen, and the image plane in front of the triaxial cell, after Bhandari et al. (2012) 112

Figure 6.3: Schematic representation of the ray tracing technique for an individual ray: (a) 3D view and (b) plan view, after Bhandari et al. (2012) 113

Figure 6.4: Flow chart and structure of the image-based measurement technique (Bhandari et al., 2012) 114

Figure 6.5: Principle of digital image correlation (DIC) (after, Bhandari, 2009) 115

Figure 6.6: Typical captured image of a triaxial specimen during shear deformation showing measurement grids used for image-based deformation measurement 117

Figure 6.7: Stress ratio, q/p' and volumetric strain plotted against axial strain for unreinforced Dense 1/5 SB at cell pressure = 30 kPa showing deformation steps 117

Figure 6.8: Unreinforced 1/5 SB specimen typical fields for deformation stages 1-2% axial strain: (a) displacement vectors, (b) vertical displacement contours, (c) horizontal displacement contours, (d) maximum shear strain, and (e) volumetric strain 118

Figure 6.9: Photographs of triaxial specimens at the start and end of shear deformation carried out at 30 kPa cell pressure 120

Figure 6.10: Stress ratio, q/p', and volumetric strain plotted against axial strain for Dense and Loose unreinforced 1/5 SB specimens during pre-peak deformation 121

Figure 6.11: Stress ratio, q/p', and volumetric strain plotted against axial strain for reinforced 1/5 SB specimens during pre-peak deformation 121

Figure 6.12: Pre-peak displacement vectors for unreinforced 1/5 SB specimens (a) Dense (b) Loose 122

Figure 6.13: Pre-peak shear strain fields for unreinforced specimens (a) Dense 1/5 SB (b) Loose 1/5 SB 123

Figure 6.14: Pre-peak volumetric strain fields for unreinforced specimens (a) Dense 1/5 SB (b) Loose 1/5 SB 124

Figure 6.15: Pre-peak displacement vectors for fibre reinforced 1/5 SB specimens (a) N_{fp} = 0.76 (b) N_{fp} = 2.9 125

Figure 6.16: Pre-peak shear strain fields for fibre reinforced 1/5 SB specimens (a) N_{fp} = 0.76 (b) N_{fp} = 2.9 126

Figure 6.17: Pre-peak volumetric strain fields for fibre reinforced 1/5 SB specimens (a) N_{fp} = 0.76 (b) N_{fp} = 2.9 127

Figure 6.18: Stress ratio, q/p', and volumetric strain plotted against axial strain for unreinforced 1/5 SB specimens (post-peak deformation) 128

Figure 6.19: Stress ratio, q/p', and volumetric strain plotted against axial strain for fibre reinforced 1/5 SB specimens (post-peak deformation) 129

Figure 6.20: Post-peak displacement vectors for unreinforced 1/5 SB specimens (a) Dense (b) Loose 130

Figure 6.21: Post-peak shear strain fields for unreinforced 1/5 SB specimens (a) Dense (b) Loose 131

Figure 6.22: Post-peak volumetric strain fields for unreinforced 1/5 SB specimens (a) Dense (b) Loose 132

Figure 6.23: Post-peak displacement vectors for fibre reinforced 1/5 SB specimens (a) N_{fp} = 0.76 (b) N_{fp} = 2.9 133

Figure 6.24: Post-peak shear strain fields for fibre reinforced 1/5 SB specimens (a) N_{fp} = 0.76 (b) N_{fp} = 2.9 134

Figure 6.25: Post-peak volumetric strain fields for fibre reinforced 1/5 SB specimens (a) N_{fp} = 0.76 (b) N_{fp} = 2.9 135

Figure 7.1: Different views of SRTF during testing 141

Figure 7.2: Southampton Railway Test Facility (a) plan view (b) cross-section view (C-C) (c) Side view (A-A) (after Le Pen, 2008) 142

Figure 7.3: LVDT locations in the test rig (a) schematic of sleeper showing six LVDT locations (b) LVDT arrangement on sleeper during test setup (c) typical LVDT attachment showing connecting bracket (courtesy of Taufan Abadi) 143

Figure 7.4: Vertical load arrangement system (a) loading beam in contact with the 'Vee' loading socket (b) schematic diagram of the loading beam and loading socket (c) overhead reaction frame of the loading system (courtesy of Taufan Abadi) 144

Figure 7.5: Pressure plate instrumentation (a) instrumented wall panels showing the location of pressure plates (b) schematic diagram of a typical pressure plate attached to the wall of the rig showing its dimensions relative to the wall (c) image of a typical pressure plate showing four load cells glued to its corners (courtesy of Taufan Abadi) 145

Figure 7.6: Sleeper placed on top of compacted unreinforced ballast layer (courtesy of Taufan Abadi) 148

Figure 7.7: Fibre reinforced ballast layer in the test rig before compaction 148

Figure 7.8: Typical vertical deformation of the LVDTs during cyclic loading of unreinforced ballast (a) LVDT 1 and 2 (RHS of sleeper in Figure 7.3(a)), (b) LVDT 3 and 4(LHS of sleeper in Figure 7.3(a)) 150

Figure 7.9: Typical plastic vertical settlement of unreinforced ballast during cyclic loading after re-zeroing plastic deformation at 10 cycles (a) linear scale, (b) semi-log scale 151

Figure 7.10: Static load application to maximum cyclic load (98.1 kN) on unreinforced and fibre reinforced ballast layer 152

Figure 7.11: Average plastic deformation of reinforced and unreinforced ballast layer with increasing number of load cycles plotted (a) linear scale (b) semi-log scale 153

Figure 7.12: Plastic vertical strain plotted against the number of load cycles of reinforced and unreinforced ballast layer highlighting the potential benefit of fibre reinforcements 154

Figure 7.13: Sleeper support stiffness variation with increasing number of load cycles for unreinforced and reinforced ballast plotted in (a) linear scale (b) semi-log scale 156

Figure 7.14: Track stiffness of reinforced and unreinforced ballast calculated using deflections at the middle and corners of the sleeper plotted in (a) linear scale (b) semi-log scale.....157

Figure 7.15: Track/sleeper stiffness ratio, K_{TS} for reinforced and unreinforced ballast plotted in (a) linear scale (b) semi-log scale.....158

Figure 7.16: Schematic diagram of the cross-section of the test rig showing the locations of the pressure plates relative to the sleeper.....159

Figure 7.17: Variation of minimum longitudinal pressure, P_{min} with the number of cycles for (a) unreinforced ballast (b) fibre reinforced ballast.....160

Figure 7.18: Variation of maximum longitudinal pressure, P_{max} with the number of cycles for (a) unreinforced ballast (b) fibre reinforced ballast.....161

Declaration of Authorship

I, OLUFEMI OLAYINKA AJAYI, declare that the thesis entitled, 'The Effects of Random Fibre Reinforcement on the Mechanical Properties of Railway Ballast' and the work presented in the thesis are both my own, and have been generated by me as the result of my own original research. I confirm that:

- This work was done wholly or mainly while in candidature for a research degree at this University;
- Where any part of this thesis has previously been submitted for a degree or any other qualification at this University or any other institution, this has been clearly stated;
- Where I have consulted the published work of others, this is always clearly attributed;
- Where I have quoted from the work of others, the source is always given. With the exception of such quotations, this thesis is entirely my own work;
- I have acknowledged all main sources of help;
- Where the thesis is based on work done by myself jointly with others, I have made clear exactly what was done by others and what I have contributed myself;
- Parts of this work have been published as:

  Ajayi, O., Le Pen, L.M., Zervos, A. & Powrie, W. (2014). Effects of Random Fibre Reinforcement on the Density of Granular Materials. *In:* SOGA, K., KUMAR, K., BISCONTIN, G. & KUO, M. (eds.) *Geomechanics from Micro to Macro.* University of Cambridge, Cambridge UK: CRC Press/Balkema.

  Ajayi, O., Le Pen, L.M., Zervos, A. & Powrie, W. (2014). Feasibility Study of Random Fibre Reinforced Railway Ballast. *In:* ARROYO, M. & GENS, A. (eds.) *23rd European Young Geotechnical Engineers Conference.* Universitat Politecnica de Catalunya, Barcelona.

  Ajayi, O., Priest, J., Le Pen, L., Zervos, A. and Powrie, W. (2014). The Effect of Fibre Reinforcements on the structure of Granular Materials. *ASCE Geotechnical Special Publication* (In press).

Signed: ……

Date: ……

Acknowledgements

I would like to express my special appreciation and thanks to my PhD supervisory team consisting of Prof. William Powrie, Dr. Antonis Zervos, Dr. Louis Le Pen and Dr. Jeffrey Priest (formerly at the University of Southampton) who was a member of the supervisory team for the first two years into my PhD research. I would like to thank you all for encouraging my research and for allowing me to grow as a researcher. Your advice on both research as well as on my career have been invaluable. I would especially like to thank Dr. Athma Bhandari for the direction and guidance he showed me in utilising the image-based deformation measurement technique for triaxial samples.

I would also express my gratitude to the UK Engineering and Physical Sciences Research Council (EPSRC) through the TRACK21 Programme Grant (EP/H044949) and the University of Southampton for sponsoring this research.

A warm thanks to Letisha Rourke, Sinthuja Aigaran, Taufan Abadi and Sharif Ahmed who were my PhD student colleagues in the Rail research group. Your advice on laboratory experiment techniques and thought provoking discussions on various aspects of geomechanics have proved to be very stimulating and enlightening. A very special thanks to my colleague Taufan Abadi with whom the full scale tests on ballast were carried out and also assisting me in analysing and reporting the experiment correctly. I would also like to say thanks to Harvey Skinner and Karl Scammell for the technical support they gave me during the laboratory test campaign. I found their support to be innovative, robust and timely.

A special thanks to my family. Words cannot express how grateful I am to my mother (Abiola O. Ajayi) and father (Samuel O. Ajayi) for all of the sacrifices that you have made for my education. You have taught and shown me the way to excellence and I am very grateful for this. Your prayer for me was what sustained me thus far. I would also like to express my appreciation to my beloved wife, Malikana Mwenda Ajayi who consistently and fervently supported me both spiritually and emotionally in diverse ways during the course of my PhD research. Most importantly, all glory, praise and honour be to God who is the all-powerful, all knowing and whose love endures forever.

Abbreviations

CT	Computerised Tomography
DEM	Discrete Element Modelling
DIC	Digital Image Correlation
DSSS	Dynamic Sleeper Support Stiffness
FRB	Fibre Reinforced Ballast
JPEG	Joint Photographic Experts Group
LB	Leighton Buzzard
LVDT	Linear Variable Differential Transformer
NR	Network Rail
PE	Polyethylene
PP	Polypropylene
SB	Scaled Ballast
SRTF	Southampton Railway Test Facility

Symbols

A_{eff}	Effective cross-sectional area of sample
d	Rate of dilation
D_{50}	Average particle size
D_{f}	Fibre diameter
e	Void ratio
E_f	Fibre Young's Modulus
E_m	Young's modulus of membrane
E_{secant}	Secant modulus
H_0	Initial height
I_D	Density index
K	Sleeper support stiffness
K_{TS}	Sleeper-span stiffness ratio
l_c	Fibre critical length
L_f	Fibre length
L_N	Normalised length
N_{f}	Number of fibres
N_{fp}	Fibre/particle number
N_{p}	Number of particles
$N\varphi'_{mob}$	Normalised mobilised friction angle at onset of dilation
P	Longitudinal pressure
p'	Mean effective stress
Q	Ram load
q	Deviator stress
$T\varphi'_{mob}$	Normalised mobilised friction angle
V_{fr}	Volumetric fibre ratio
V_s	Volume of solids
V_T	Total volume

V_v	Volume of voids
W_N	Normalised width
α	Rate of increase of stress ratio with rate of dilation
ε_a	Axial strain
ε_r	Radial strain
ε_{vol}	Volumetric strain
v	Specific volume
σ_c	Cell pressure
σ_{fu}	Fibre ultimate strength
φ'_{mob}	Mobilised angle of friction
M	Stress ratio at $d = 0$

Chapter 1

Introduction

1.1 Background

Track costs constitute a major operational expense for railways. In 2012/13, Network Rail spent £3.7 bn on maintenance and renewals out of a total expenditure of £9 bn (NetworkRail, 2013). Ballast is a primary component of the railway track and it has several functions which include the ability to resist vertical, lateral and longitudinal forces applied to the sleepers from the train wheels. In response to the stresses induced during a train passage, ballast typically degrades and experiences plastic settlement. The effect of plastic settlement, in particular differential settlement can result in the imposition of speed restrictions and/or emergency remediation. Ultimately, all ballasted track requires periodic maintenance to restore line and level, typically this is by tamping. Over a lifecycle, ballast may undergo about 10 tamps over a 30 year period before renewal. Thus, ballast is the focus of the majority of maintenance and renewal activities. Despite recent research into the mechanical behaviour of ballast, a holistic understanding of the material and its response to typical loading and environmental conditions remains incomplete. In response to the growing demands placed on railway systems in terms of faster, heavier and more frequent trains, increased resilience, enhanced environmental performance and reduced cost, there is a need to develop cost effective ways of improving the performance and reducing the maintenance needs of railway ballast.

Ballast improvement techniques, such as the use of geogrids, have attracted a great deal of attention in terms of research, but huge potential for reducing costs through ballast improvement still exists. Research into the behaviour of sands has shown that the use of randomly oriented fibres can significantly improve the strength of sand. The technique may also be used to improve ballast strength and thereby reduce rates of track geometry deterioration. However, current scientific understanding of the factors influencing this

improvement in sand behaviour is incomplete, and therefore the potential benefit for ballast is unknown.

The aim of this research is to assess the potential for improving the mechanical properties of ballast by the addition of fibres. The development of this understanding will contribute to one of the key objectives of the UK Rail Technical Strategy, which is to increase track resilience by developing alternative materials to provide greater reliability, reduce whole-life costs, reduce tamping and improve longevity.

1.2 Research Objectives

The aim of this research will be achieved through the following objectives:

1. Develop a specimen preparation procedure for fibre reinforced ballast specimens meeting even and random orientation distribution requirements.
2. Investigate the effect of the addition of fibres to scaled ballast on its void ratio/density.
3. Determine the influence of fibre properties (e.g. fibre length, width, fibre content) on the stress-strain response of reinforced sand and scaled ballast samples through monotonic triaxial testing.
4. Develop scaling parameters for the fibre reinforcements for future use in full scale ballast aggregates.
5. Perform full scale laboratory tests on fibre reinforced ballast to establish the viability of the proposed reinforcement technique.

1.3 Organisation of this report

This report consists of seven chapters, as follows:

1. Chapter 2 presents a review of the relevant literature.
2. Chapter 3 presents the materials used in the research and also describes the sample preparation techniques. The parameters of a reinforced granular material are described and the effects of the addition of fibres on the packing structure of granular materials are explained.
3. Chapter 4 describes the methods used in carrying out monotonic triaxial tests on fibre reinforced Leighton Buzzard (LB) sand (Fraction A), 1/5 and 1/3 scaled ballast (SB). It also discusses the repeatability of triaxial tests on fibre reinforced specimens, and compares triaxial tests on dry and saturated 1/3 SB tests and 1/5 and 1/3 SB samples.

4. Chapter 5 examines the mechanical behaviour of fibre reinforced granular materials (i.e. LB sand, 1/3 and 1/5 scaled ballast) in monotonic triaxial tests. Data on the influence of fibre content, fibre length and width on the strength and deformation of reinforced specimens is presented. New insights regarding the interaction mechanisms of fibres and particles are presented and the potential application to full scale ballast discussed.
5. In chapter 6, an image-based deformation measurement method is used to study the local deformation of fibre reinforced triaxial specimens.
6. Chapter 7 presents the mechanical behaviour (e.g. plastic settlement, stiffness, stress distribution) of a fibre reinforced ballast (FRB) layer determined using the Southampton Railway Test Facility (SRTF).
7. Chapter 8 presents the conclusions and recommendations for future work.

Chapter 2

Literature Review

2.1 Overview

Research has been carried out to investigate the performance of ballast both in the laboratory and in the field. Studies have addressed several issues including the particle characteristics, its mechanical behaviour under static and cyclic loading, and particle crushing. Several laboratory-based railway ballast related studies have been carried out including those by Raymond and Davies (1978); Indraratna et al. (1998); Suiker et al. (2005); Anderson and Fair (2008); Aursudkij et al. (2009); Sevi and Ge (2012). The reinforcement of ballast by placing geosynthetic layers to improve its mechanical properties has been investigated by many researchers (e.g. Raymond and Ismail, 2003; Brown et al., 2007; Indraratna et al., 2010).

The concept of enhancing soil properties (e.g. shear strength, filtration, separation, drainage) with geosynthetics has been in existence for a long time (Ingold, 1994). Geosynthetics that have a primary function of reinforcing soil or aggregates include geotextiles, geogrids, geocells, geomeshes and geocomposites (a combination of the aforementioned types of geosynthetics) (Figure 2.1). The concept of the reinforcement mechanism is based on utilising the tensile strength of the reinforcing element to improve the strength and deformation characteristics of the soil. The use of random oriented fibres in soils is believed to produce a better distribution of stress within the soil, and inhibits the development of potential weak planes.

2.2 Rail track

Modern rail track (Figure 2.2) components may be classified into two main categories. The ballast component in the substructure category is of particular interest in this research.

a) Superstructure – this consists of rails, fastening systems and sleepers, and;

b) Substructure – this comprises ballast, sub ballast, and subgrade.

The substructure components provide a means through which wheel loads on the sleepers are transmitted to the subgrade without causing failure of the soil.

Vertical and lateral forces are applied to each sleeper. The vertical force may be defined as the sum of the quasi-static and dynamic forces (Esveld, 2001) while the lateral force component is mainly due to the lateral wheel force (Selig and Waters, 1994).

2.3 Ballast

The ballast layer is required to perform many functions such as retaining track alignment, reducing the sleeper bearing pressure transmitted to the underlying materials and providing drainage to the track.

The mechanical response of ballast is generally governed by the characteristics of the particles, bulk properties of the granular assembly, loading characteristics, and particle degradation (Indraratna et al., 2011). The governing characteristics discussed in the following sections are not exhaustive but are those most relevant to the proposed reinforcement technique.

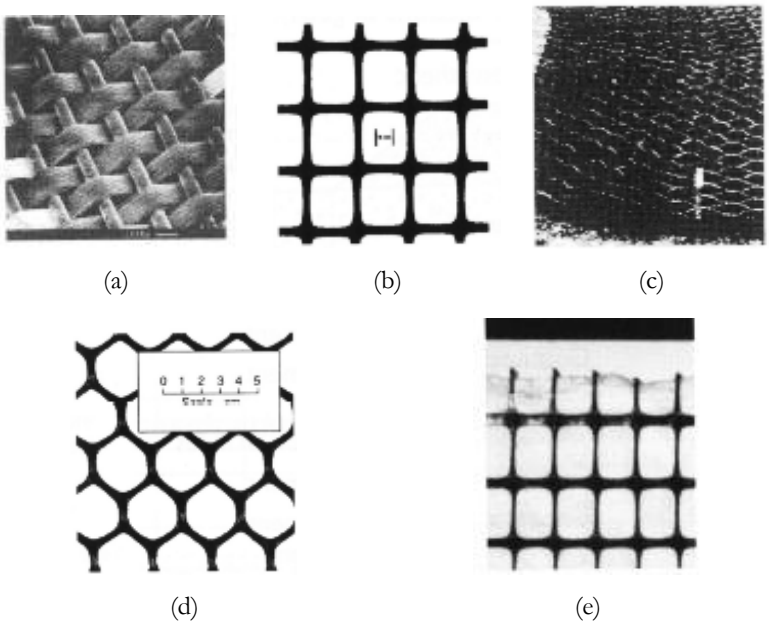

Figure 2.1: Types of geosynthetics used as reinforcements in soil and aggregates, (a) geotextile, (b) geogrid, (c) geocell, (d) geomesh, (Ingold, 1994) (e) geocomposite (Indraratna et al., 2011)

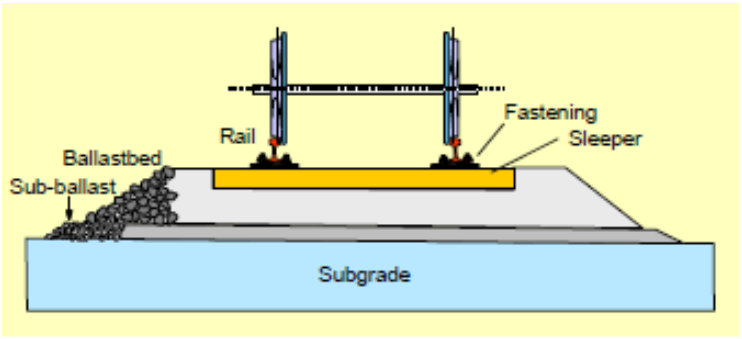

(a)

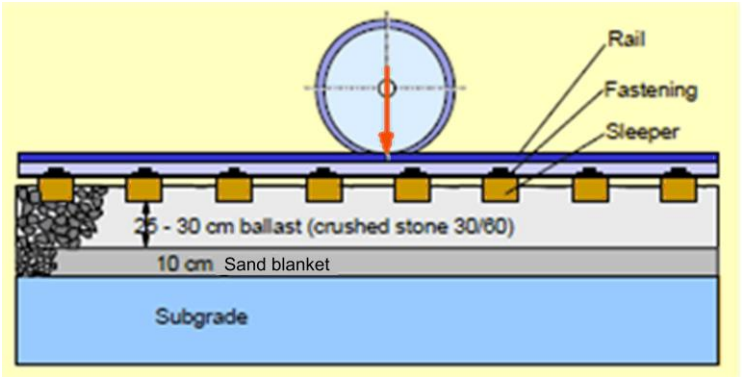

(b)

Figure 2.2: Principle of track structure (a) cross-section (b) longitudinal section (after, Esveld, 2001)

2.3.1 Particle Characteristics

Particle size distribution

The influence of particle size on the mechanical behaviour of ballast has been studied by several researchers. Key findings include the effect of particle size on the angle of shearing resistance, permanent deformation and resilient modulus of ballast. Ballast particle size typically ranges between 20 mm and 63.5 mm. The effect of ballast particle size on the angle of shearing resistance has been shown to be small. Indraratna et al., (1998) concluded that the peak friction angle of more broadly graded ballast is higher than that of a more uniformly graded ballast sample while Anderson and Fair (2008) showed that a decrease in the mean grain size did not produce a significant reduction in peak friction angle.

In terms of permanent deformation under cyclic loads, Raymond and Diyaljee (1979) demonstrated that well-graded ballast showed greater resistance to cyclic loads in terms of a lower plastic settlement than large sized ballast particles with uniform gradation. Janardhanam and Desai (1983) showed that the particle size did not appear to significantly influence ballast strains at various stress levels and volumetric strains. Anderson and Fair (2008) showed that the smaller ballast particles (between 10 - 20 mm) are more prone to cyclic deformation than larger ballast particles.

Janardhanam and Desai (1983) concluded that the particle size influences the resilient modulus of ballast with the modulus increasing with mean grain size. Anderson and Fair (2008) however reported a larger resilient modulus with smaller ballast sizes. The differences in the mechanical behaviour of ballast particle sizes as demonstrated in previous research is unclear.

Other particle characteristics

The frictional resistance of a loaded surface is due to the surface roughness of the bodies in contact. Cavarretta et al. (2011) demonstrated that the inter-particle coefficient of friction of glass ballotini increased significantly as the surface roughness increased. It is generally understood that the surface roughness of particles influences the macroscopic behaviour (e.g. shear strength) of granular materials. In railway ballast, Thom and Brown (1989) demonstrated that an increase in the apparent surface roughness of ballast offers higher resistance to plastic strain and increased resilient modulus.

2.3.2 Bulk Characteristics

The behaviour of ballast is linked to the overall aggregate characteristics which include aggregate particle size distribution and void ratio/density. It is generally understood that

particle size distribution plays a key role in the deformation behaviour of granular materials. Indraratna et al. (1998) showed that the mobilised strength of ballast increases when the material is more broadly graded. The particle size distribution of ballast is closely linked to the void ratio/density it can achieve when compacted. Uniformly graded ballast exhibits generally lower densities than well-graded ballast. Selig and Waters (1994) demonstrated that well graded ballast is stiffer due to its smaller void ratio. In terms of track stability, Indraratna et al. (1998) showed that the most critical stage in ballast life is immediately after construction when it is at its loosest state.

2.3.3 Loading Characteristics

Confining Pressure

The effect of confining pressure on the strength and deformation characteristics of soils and granular materials is well known. The effect of confining pressure has been particularly reported on the non-linear failure envelope of large aggregates at low mean normal stresses (e.g. Charles and Watts, 1980; Indraratna et al., 1994). At higher confining stress levels (e.g. > 100 kPa), particle breakage and slippage is considered to be the mechanism by which shear deformation occurs rather than the dominant dilatancy effects at low confining stress levels.

Number of load cycles

It is generally accepted that the permanent settlement and lateral deformation of ballast increases as the number of load cycles increases. The rate of deformation however decreases with increasing number of load cycles. In ballast, the permanent axial strain per cycle typically decreases significantly after the first few cycles and the rate of decrease reduces gradually as the number of cycles increases (e.g. Anderson and Fair, 2008; Aursudkij et al., 2009; Indraratna et al., 2010). The non-linear variation of ballast settlement with increasing number of load cycles (Figure 2.3(a)) becomes linear when the settlement data is presented in a semi-logarithmic scale (Figure 2.3(b)). Ballast settlement under cyclic loading can typically be represented by (e.g. Indraratna et al., 2011):

$$S = a + b \cdot \ln N \tag{2.1}$$

where, S is the ballast settlement, N is the number of load cycles, and a and b are two empirical constants depending on the type of ballast, geosynthetics used, initial density and the degree of saturation.

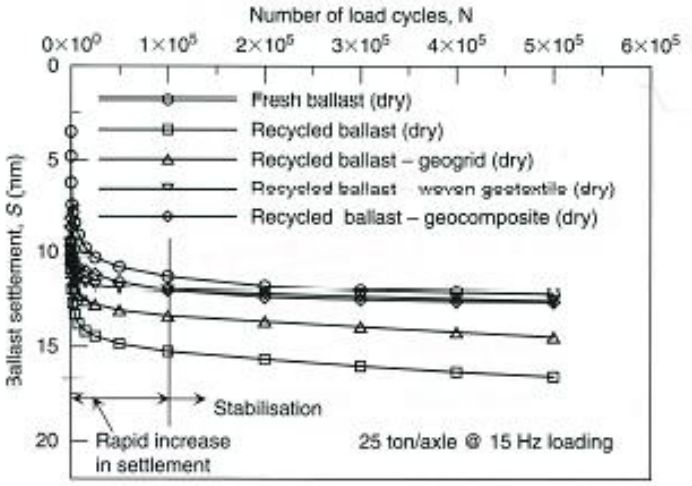

(a)

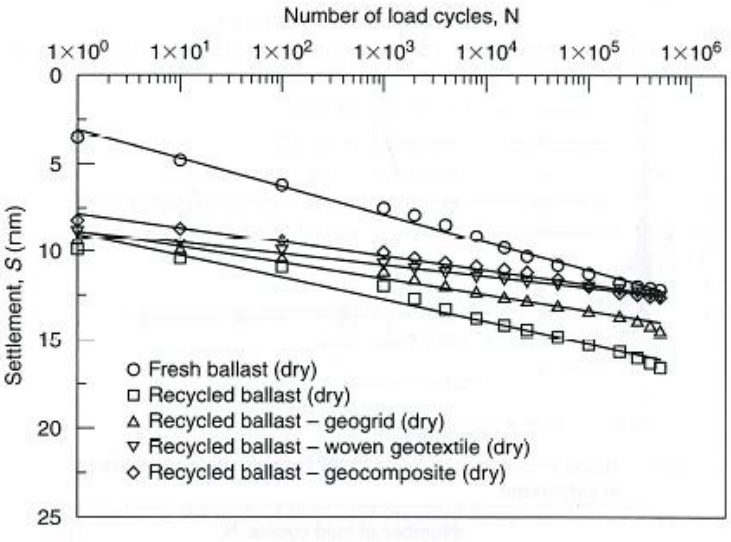

(b)

Figure 2.3: Settlement response of fresh reinforced and unreinforced ballast in a laboratory test plotted in (a) linear scale, (b) semi-logarithmic scale (after Indraratna et al., 2011)

2.4 Effects of Dynamic Loads on Railway Track

The typical applied wheel load on railway ballast is transient (i.e. moving wheel load) like those experienced in road pavements. As a train passes, the changes in stress within an element of soil below a railway track are complex and involve a rotation of the principal stress directions (Figure 2.4) (Brown, 1996). Gräbe and Clayton (2009) reported very large increases in permanent strains than those observed in cyclic triaxial tests when principal stress rotations (PSR) were applied to a railway subgrade material (Figure 2.5). Similarly, Ishikawa et al. (2011) also reported larger permanent vertical displacement when a moving-wheel load is applied on a $1/5^{th}$ scale model railway track as compared to a single-point loading mode. In terms of the effect of PSR on resilient modulus, (Gräbe and Clayton, 2014) demonstrated that magnitude of the reduction in the resilient modulus of subgrade materials due to PSR depends on the stress state (i.e. over-consolidation ratio, consolidation regime, and stress history), soil type (i.e. clay content), and soil physical state (i.e. moisture content).

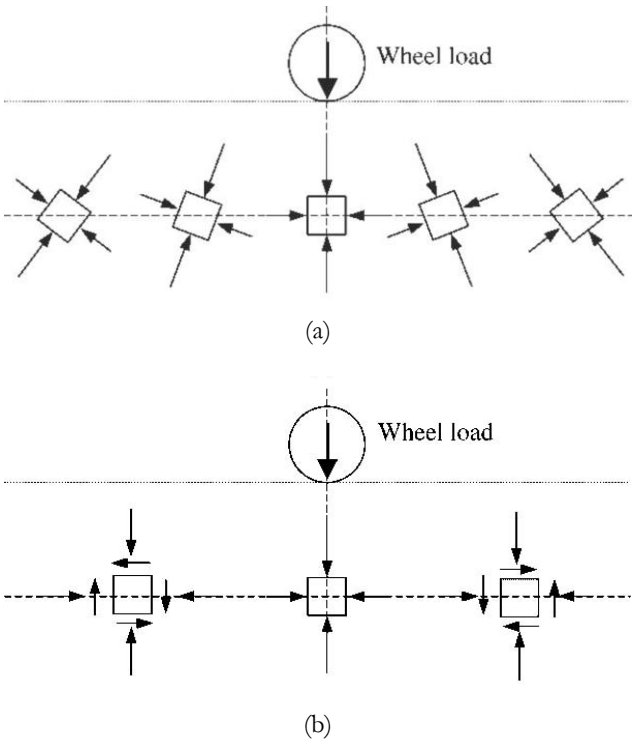

Figure 2.4: Stresses on pavement elements: (a) principal stresses and planes (b) shear and normal stresses on horizontal and vertical planes (after Brown, 1996)

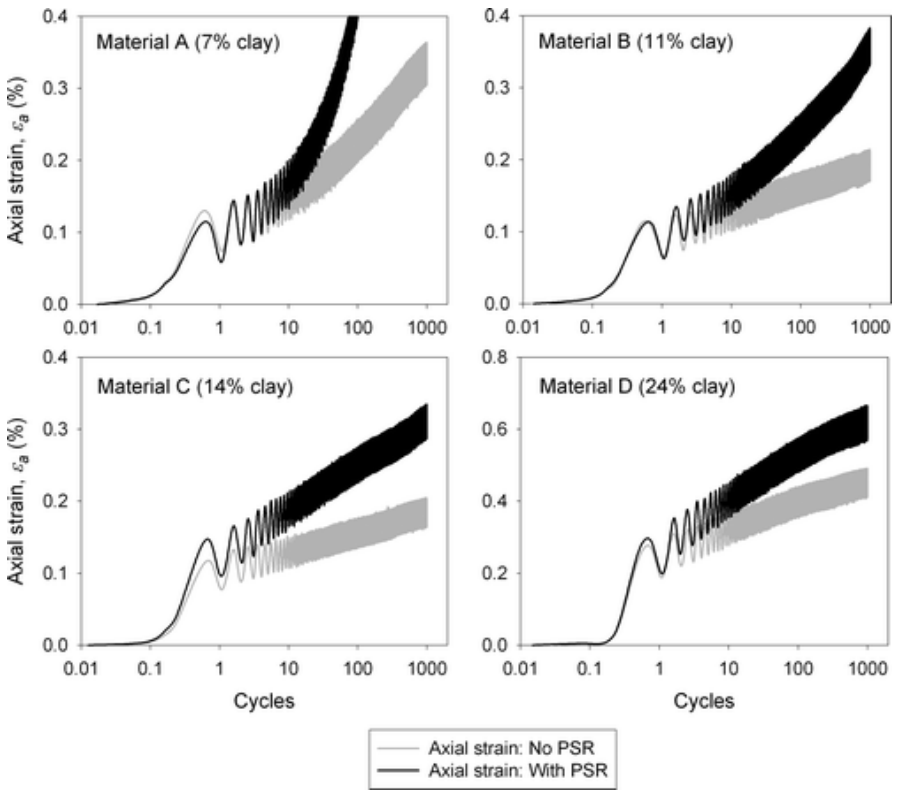

Figure 2.5: Permanent deformation of Materials A, B, C, and D as a result of cyclic loading with and without principal stress rotation (Gräbe and Clayton, 2009)

2.5 Use of Geosynthetics in Railway Ballast

Geosynthetics are predominantly used in geotechnical engineering to improve the mechanical properties of soils. There are two major classifications of Geosynthetics: geotextiles and geomembranes (Ingold, 1994). Closely related to geotextiles are geogrids, geomeshes, geonets and geomats which have been used extensively in geotechnical engineering, with geogrids and geotextiles used in rail track. The discussions in this section will be limited to geogrids as it is the reinforcement technique widely used to improve the mechanical properties of railway ballast.

The improvement offered by geogrids in railway ballast is believed to be the reduction in permanent vertical settlement and lateral spread. This is thought to be due to the restriction provided by geogrids to the lateral movement of ballast particles. McDowell et al. (2006) demonstrated using a three dimensional discrete element model (DEM) of geogrid reinforced ballast triaxial sample (Figure 2.6(a)) that the increase in stiffness of geogrid reinforced aggregates is also due to the aggregate-geogrid interlock. The aggregate-geogrid interlock argument was supported by showing the large concentration of particle contact forces within the vicinity of the geogrid (Figure 2.6(b)). In addition, they reported that when a single layer of geogrid at mid-height of the sample was used,

the axial and radial displacements were found to be approximately 50 % greater than those using the three layers of geogrid, thereby demonstrating the probable effectiveness of multiple layers of geogrid in certain applications.

Indraratna et al. (2010) in a field assessment of the performance of geogrid reinforced railway ballast, demonstrated that the lateral strains of fresh ballast are significantly reduced by the inclusion of a geocomposite (comprising of geogrid and non-woven geotextile) layer while a negligible effect was observed when the same geocomposite was used in recycled ballast (Figure 2.7). This behaviour was attributed to the increased global interface friction resistance developed with the angular particles and the geocomposite layer. Chen et al. (2012) used DEM to corroborate the significant influence of geogrids on the permanent settlement of ballast (Figure 2.8). The effect of a geogrid on the resilient modulus of the reinforced ballast specimen was also shown to be relatively small, but the modulus was relatively unaffected. By observing the contact force distribution, Chen et al. (2012) suggested that an increase in apparent confinement would reduce the settlement in geogrid reinforced ballast.

Brown et al. (2007) showed by means of full scale laboratory pull-out tests on geogrids having different aperture sizes, that the optimum aperture size for aggregates having an average particle size of about 40 mm was between 60 - 80 mm (Figure 2.9). In addition, they demonstrated that there is a non-linear relationship between resilient stiffness at low strain and tensile strength for the polymeric geogrids used. Brown et al. (2007) also suggested on the basis of their experiments that overburden pressure, which provides the normal force on the plane of the geogrid, has an important influence on the reinforcing effect of geogrids.

One of the drawbacks of the use of geogrids in ballast is the restriction it imposes on future maintenance activities. Geogrids would be destroyed during tamping. The addition of synthetic randomly oriented fibres in ballast thus provides a potentially new method of reinforcing ballast that is able to withstand typical tamping operations.

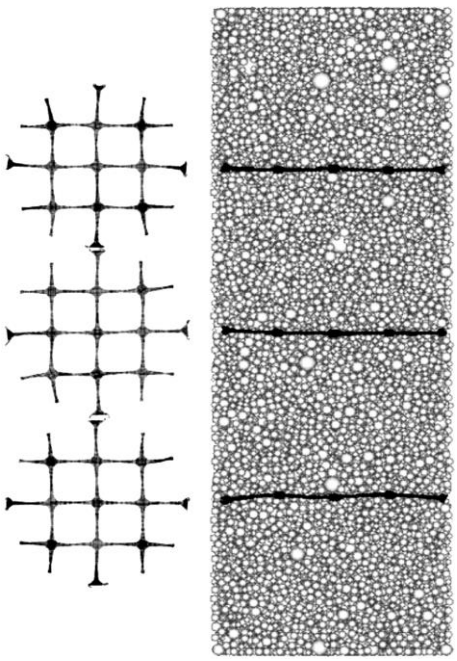

(a)

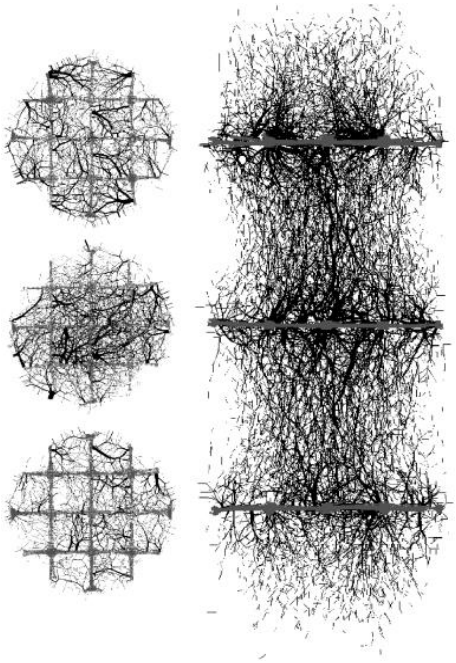

(b)

Figure 2.6: (a) Deformed triaxial sample with three geogrid layers, and (b) Contact force distribution and geogrid after partial horizontal and vertical loading (after McDowell et al., 2006)

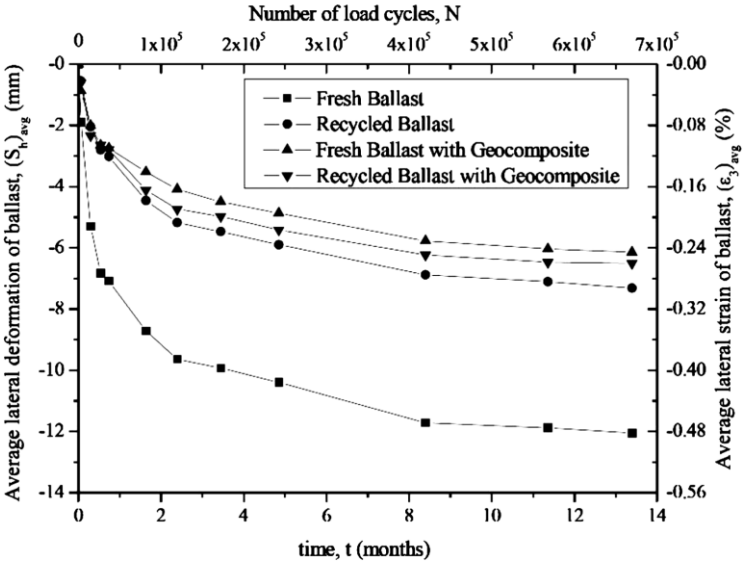

Figure 2.7: Field assessment of the effect of a geocomposite layer on the average lateral strain of ballast (after Indraratna et al., 2010)

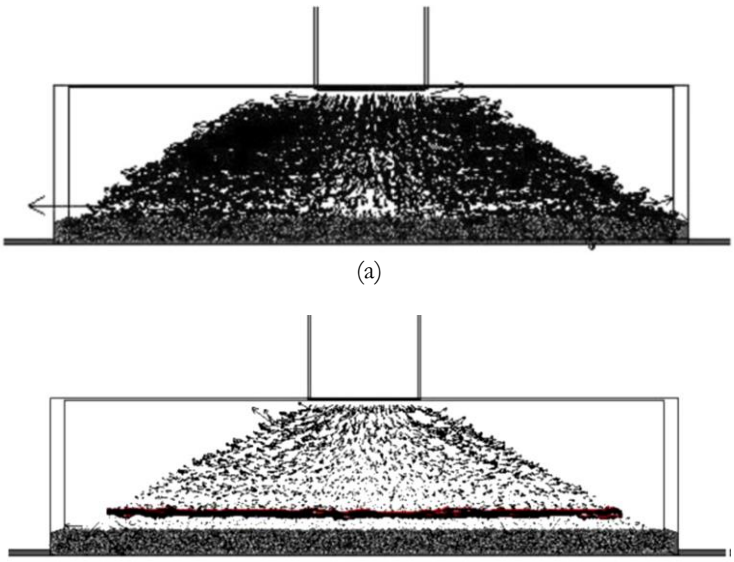

(a)

(b)

Figure 2.8: Displacement vectors of ballast particles at maximum load during the ninth load cycle, (a) Unreinforced sample (maximum magnitude of displacement vectors = 13mm); (b) reinforced sample (maximum magnitude of displacement vectors = 8.4mm)

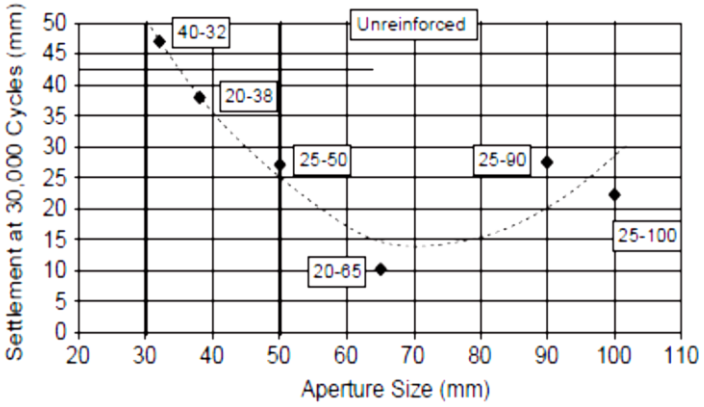

Figure 2.9: Influence of aperture size on settlement of geogrid reinforced ballast (after Brown et al., 2007)

2.6 Fibre Reinforcement of Sand

Soil reinforcement in general utilizes the tensile strength of the reinforcing element to improve the strength of the soil (Ingold, 1994). The use of randomly distributed and orientated fibres to reinforce soils leads to a more isotropic distribution of stress within the soil, while impeding the development of shear surfaces within the reinforced soil which exists with other forms of reinforcements such as geotextiles and geogrids (Yetimoglu and Salbas, 2003; Shukla et al., 2010).

A number of factors influencing the effectiveness of fibre reinforcements in sand can be considered:

1. *Fibre properties* – these are properties relating to each fibre within a mixture. These include; fibre content, geometry (e.g. length, diameter, thickness and aspect ratio), elastic modulus, and tensile strength.
2. *Soil characteristics* – particle size, shape and gradation.
3. *Reinforced soil characteristics* – these are characteristics of the sand-fibre mixture. These include stress level (confining or normal stress), relative density, fibre/particle relative dimensions and orientation of fibres.

2.6.1 Fibre Properties

Fibre content

Previous research has shown that a general increase in the shear strength of fibre reinforced sands occurs as the fibre content increases until it reaches an asymptotic upper limit (Gray and Alrefeai, 1986). Several investigators (Yetimoglu and Salbas, 2003; Sadek

et al., 2010; Tang et al., 2010) have also reported a reduced post-peak strength loss in reinforced soils when compared to unreinforced soils as fibre content increases.

The influence of fibre dimensions (length, diameter and aspect ratio) on the effect of increasing fibre contents has not been effectively addressed in the literature. For instance, for a given fibre content, different fibre lengths could be used with the difference only being the number of individual fibres. The micro-mechanics of this has not been considered by previous investigators.

Fibre dimensions

Most fibres used as soil reinforcements in the literature are either rectangular or round in cross-section. This is mainly because commercially available fibres are primarily concrete additives or an additive to the root zone of sports surfaces. Their dimensions can be characterized by their diameter (or thickness and width), length and aspect ratio (ratio of the length to diameter).

For a given fibre content, higher strengths in non-clay soils are produced as the aspect ratio increases (Maher and Gray, 1990; Zornberg, 2002; Michalowski and Cermak, 2003; Consoli et al., 2009). Its definition means that an increase in the aspect ratio could be due to an increase in fibre length or a reduction in fibre diameter each of which would have different implications for the mechanism of strength improvement. Figure 2.10 shows the increase in shear strength for sands plotted as a function of the fibre content for two different fibres.

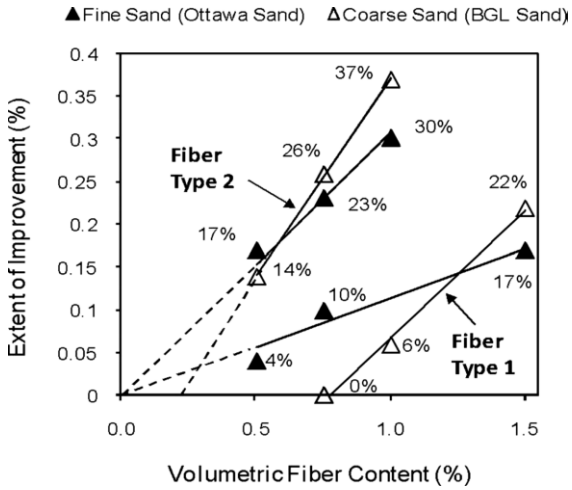

Fibre type	Length (mm)	Diameter (mm)
1	7	0.18
2	27	0.18

– Ottawa sand (D_{50} = 0.39 mm)

– BGL sand (D_{50} = 1.45 mm)

Figure 2.10: Improvement in shear strength of fibre-reinforced sand (after Sadek et al., 2010)

It has also been shown that when the fibre content (by weight) and aspect ratio are kept constant, an increase in the fibre length produces an increase in the shear strength of the reinforced soil (Ranjan et al., 1996; Zornberg, 2002; Michalowski and Cermak, 2003). Michalowski and Cermak (2003) and Sadek et al. (2010) have attributed this to a 'scale effect' which depends on the relative size of fibre and soil particles.

Mechanical properties of fibres

The mechanical properties of fibre reinforcement are typically characterised by the Young's modulus, E_f and tensile strength. The material used mostly for fibre reinforcement of sand is polypropylene with a typical value of Young's modulus ranging between 0.9 – 3 GPa (e.g. Consoli et al., 2009; Diambra et al., 2010; Dos Santos et al., 2010). Gray and Ohashi (1983) reported that an increase in E_f produced an increase in bulk shear strength but reduced stiffness at small strains of the composite. In contrast, Michalowski and Zhao (1996) showed that an increased E_f produced increase in both shear strength and initial stiffness of the composite. Gray and Ohashi (1983) explained that the loss in initial stiffness was an artefact of the direct shear test itself. They argued that the application of the normal stress produced a temporary compression of the fibres and the compression had to be overcome by sufficient shear distortion of the specimen before any shear strength increase developed. They further showed that this behaviour in addition to the fibre stiffness is pronounced when there is an increase in fibre content, verticality of fibre orientation, or looseness of the specimen.

2.6.2 Bulk Properties of Reinforced Soil

Relative particle/fibre dimensions

Previous research has investigated the importance of the effect of particle/fibre dimension. These include the work of Sadek et al. (2010), Michalowski and Cermak (2003), Michalowski and Zhao (1996), and Ranjan et al. (1996). Sadek et al. (2010) in testing two types of sand having an average particle size (D_{50}) of about 0.39 mm and 1.45 mm, showed that the reinforcing effect in the fine sand is more pronounced when the fibre content is small. However, the relative increase in strength of the coarse sand is less at low fibre content but greater for larger fibre content (Figure 2.10).

Michalowski and Cermak (2003) proposed two explanations for this behaviour: (1) Micromechanics of the sand-fibre interaction, and (2) Influence of fibres on the dilatancy of sand. Michalowski (1997), suggested two possible sand-fibre interaction mechanisms (Figure 2.11):

1. *Short fibre reinforced soil*: This is observed when the soil particles are small compared to the diameter of the fibre (Figure 2.11(a)). The fibre-matrix interface may be

considered as continuous and frictional as the extent of fibre-grain contact becomes large. This may also be expressed as,

$$D_N = \frac{D_f}{D_{50}} \tag{2.2}$$

Where D_N = Normalised diameter; D_f = diameter of fibre; D_{50} = average particle size of soil. This implies that $D_N > 1$.

2. *Continuous thin filament fibre*: This is observed when the diameter of the fibre is about an order of magnitude less than the average particle size. This may result in the slipping of the fibres into the pore space during deformation of the soil matrix. This implies that $D_N < 0.1$.

   The reinforcing effect of this configuration would only occur if the fibres behave as continuous and flexible filaments so that a force in the filament can be induced due to the "belt-friction effect" with the filament wrapped around the grains (Figure 2.11(b)).

$$L_f >> D_{50}$$

This implies that $L_N \geq 10$, where L_N is

$$L_N = \frac{L_f}{D_{50}} \tag{2.3}$$

where L_N = Normalised length; L_f = fibre length.

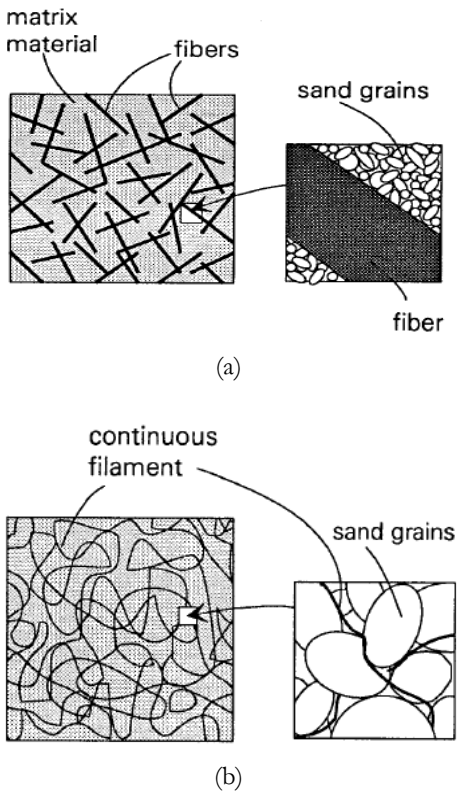

Figure 2.11: Possible sand-fibre interaction (a) Short random oriented fibre reinforced soil, and (b) Continuous thin filament reinforced soil (after Michalowski, 1997)

Fibre Orientation

Different forms of fibre orientation have been explored by previous investigators. Apart from random oriented fibres, vertical, horizontal and fibres inclined at specific angles have been used (Gray and Ohashi, 1983; Jewell and Wroth, 1987; Michalowski and Cermak, 2002).

Michalowski and Cermak (2002) while testing fibre reinforced sand in a triaxial apparatus, reported a greater increase in shear strength of the specimen when the orientation of the fibres was horizontal. Fibres orientated in the vertical direction showed no appreciable increase in soil strength (Figure 2.12). They concluded that the increase in strength was due to the horizontal fibres being aligned in the direction of the largest extension of the specimen (i.e. the horizontal direction). Randomly oriented fibres produced a lower improvement in strength than horizontal oriented fibres, as would be expected. Diambra et al. (2007) while performing triaxial extension tests on horizontally orientated fibre reinforced sand specimens also reported a smaller improvement in strength compared with triaxial compression tests.

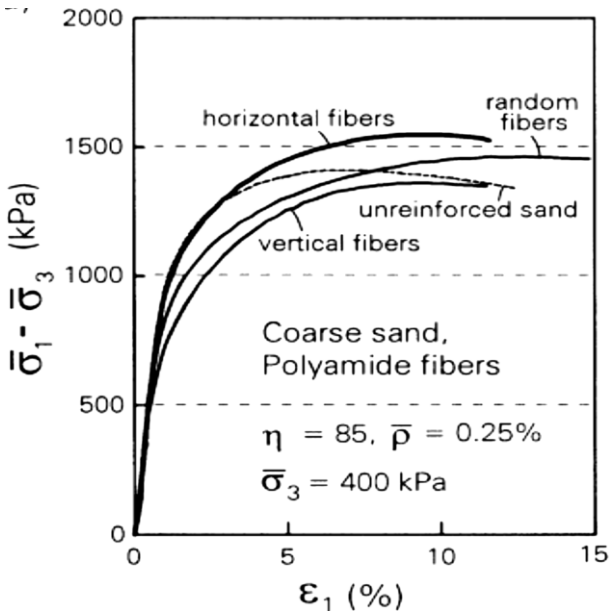

Figure 2.12: Coarse sand reinforced with polyamide fibres at different orientations (after Michalowski and Cermak, 2002)

It is evident that the effectiveness of fibre reinforcements depends on their orientation which in turn may depend on the compaction of the specimen and the technique used for its placement. It is generally agreed that the preferred plane of orientation of randomly placed fibres is the horizontal plane.

2.6.3 Mechanical Behaviour of Fibre-Reinforced Sands

Shear Strength

There is a general consensus amongst researchers that the peak shear strength envelope of fibre-reinforced soils is curvi-linear (Figure 2.13). Above a threshold confining stress, referred to as the critical confining stress, the failure envelope of reinforced sand is parallel to that of the corresponding unreinforced sand. When the confining stress is below the threshold magnitude, the sand-fibre interaction is conjectured to be dominated by a slip-yield mechanism (i.e. the fibres tend to slip or pull out when the soil is being sheared) and the reinforcing mechanism is considered to have not been fully mobilised even though an apparent improvement in the angle of shearing resistance is observed.

Most researchers have attributed the behaviour at high confining stresses (Figure 2.13) to the rupture of fibres during shearing. It was noted that the fibres stop contributing to the strength improvement of the composite once this occurs.

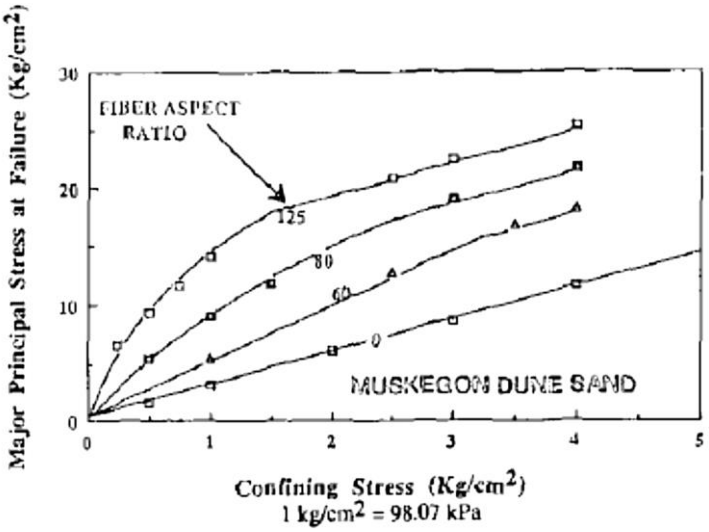

Figure 2.13: Principal Stress Envelopes from Triaxial Compression tests on reinforced sand (after Maher and Gray, 1990)

This explanation did not hold for the tests reported by Maher and Gray (1990) in which the glass fibres that were used remained intact at the end of the tests and yet a bilinear failure envelope was still observed. Michalowski (2008) suggested that the bilinear characteristics at relatively high confining stresses could be attributed to the arching of sands around fibres, which in turn prevents the transfer of stresses to the fibres.

Maher and Gray (1990) reported that the critical confining stress is relatively unaffected by fibre content and average particle size, but is quite sensitive to the aspect ratio of the fibre, particle shape and gradation of the soil. They also stated that the critical confining stress increases as the aspect ratio of the fibre decreases.

Stress-Strain Behaviour

No clear characteristic stress-strain behaviour of reinforced sands has been reported in the literature. While some investigators (e.g. Yetimoglu and Salbas, 2003) reported a peak and subsequent strain-softening of the composite (Figure 2.14), others (e.g. Heineck et al., 2005; Consoli et al., 2009; Diambra et al., 2010) reported strain-hardening behaviour (e.g. Figure 2.15). These differences have made it difficult to ascertain the effect of the addition of fibre reinforcements on the stress-strain behaviour of sand.

An explanation for these differences could be the wide range of test methods and sample preparation techniques adopted for these tests. Another reason could be the different types and definition of sample preparation parameters like density and void ratio in the literature. Changes in the stress-strain behaviour of reinforced sands may be due to the changed density or void ratio, rather than just the fibre reinforcements.

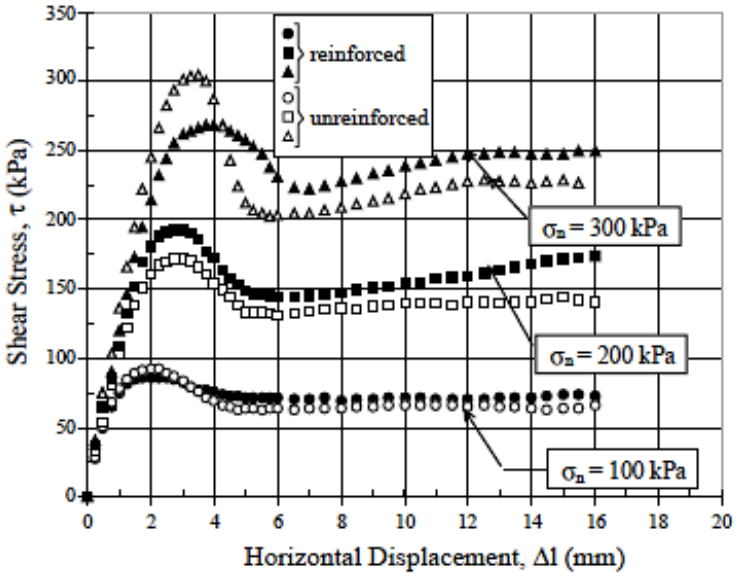

Figure 2.14: Shear stress-horizontal displacement response for unreinforced and reinforced sand with fibre content (by weight) = 0.50% (after Yetimoglu and Salbas, 2003)

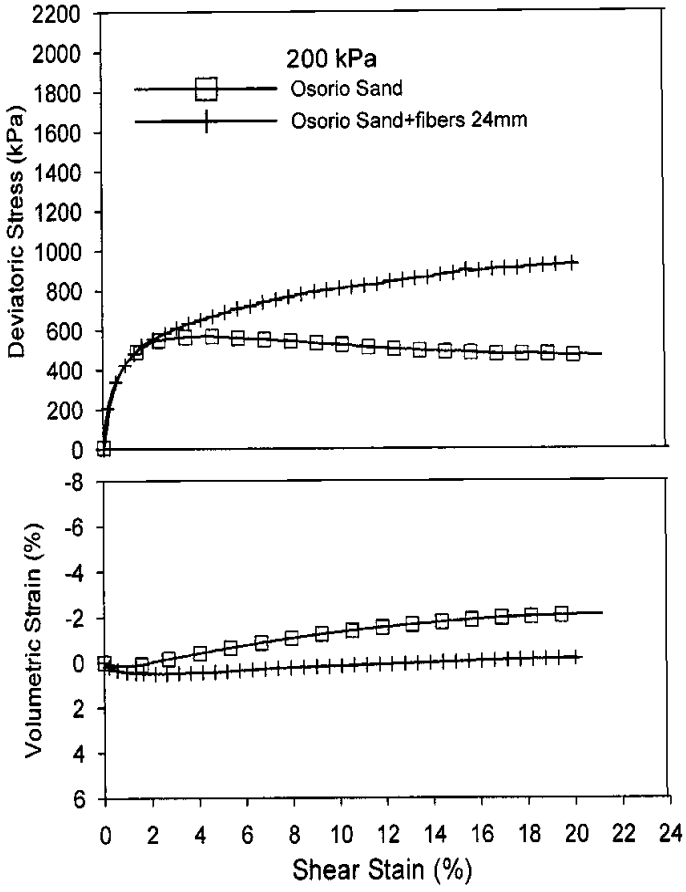

Figure 2.15: Stress-strain and volumetric response of fibre reinforced and unreinforced Osorio sand at a confining pressure of 200 kPa (after Heineck et al., 2005)

Initial Stiffness

The effect of reinforcement on the initial stiffness of fibre reinforced sand has been reported in a very limited form in the literature. This is partly because most of the laboratory tests performed were limited in terms of their ability to make small strain measurements. However, an indication of the small strain response of the composite can still be observed from the initial stiffness of the stress-strain plots.

Sadek et al. (2010) reported an increase in the slope of the stress-displacement curve at very small displacements when a fine sand (D_{50} = 0.39 mm) was reinforced with polypropylene fibres. Contrary behaviour was then seen when a coarse sand (D_{50} = 1.45 mm) was used. Diambra et al. (2010), Heineck et al. (2005) and Ibraim and Fourmont (2007) all reported that addition of fibres did not influence the initial stiffness of the composite and that the reinforcements only become effective at medium to large strains. Michalowski and Cermak (2003) while performing tests on triaxial specimens, reported that the drop in initial stiffness of a polyamide fibre reinforced sand increases as the fibre content increases. However, no appreciable decrease in stiffness was observed when steel fibres were used. Michalowski and Cermak also suggested, based on the results of their laboratory tests and those reported by Michalowski and Zhao (1996), that the initial stiffness was influenced by the stiffness and roughness characteristics of the fibres.

Michalowski and Cermak (2003) suggested that the loss in initial stiffness was probably due to changes in the fabric of the sand produced by the introduction of polyamide fibres. The presence of the fibres produces a non-homogeneous distribution of void ratio in the composite with larger voids occurring in the pockets of sand close to the fibres. The fibres are then subjected to compression and bending on the application of the confining pressure, but, once shearing starts, fibres in tension experience gradual stretching while those in compression kink. Thus the initial stiffness of the composite is less than unreinforced sand having the same theoretical average void ratio. They supported this argument by showing the pronounced reduction in initial stiffness observed when the fibre content of the polyamide fibres was increased.

Behaviour under Dynamic Loading

There is general agreement among investigators that fibre reinforcements improve the stiffness of soils in a way similar to static loads (e.g. Maher and Woods, 1990; Li and Ding, 2002). For example, Maher and Woods (1990) reported an increase in shear modulus of randomly distributed fibre reinforced sand as the magnitude of shear strain increased. They also showed that the contribution of fibres to the shear modulus is more

pronounced at lower confining stresses and drops sharply as the confining stress increases.

2.6.4 Stress Distribution in Fibres

The increase in strength in fibre reinforced soils has been attributed to the mobilisation of tensile force in individual fibres present in the composite. In the field of composites, fibre composites can be broadly grouped into (1) Bonded fibre composites, and (2) Continuous filament reinforcements. This grouping is entirely based on the manner in which the fibres are attached to the matrix material. The matrix material can be any of steel, wood, plastic or soil.

Bonded Fibre Composites

These are composites in which the fibres have a perfect (or glued) surface bond with the matrix material. As in fibre composites, the strength improvement in reinforced sands is derived from the transfer of stress from the sand to the fibres. The mechanism of the stress transfer has been investigated by Cox (1952) among others. All the studies were related to the variation of stresses along the length of the fibre and were conducted based on the following assumptions (Vinson and Chou, 1975):

1. The loading condition of fibres is limited to simple tension.
2. The effects of fatigue and creep are not included.
3. The fibres in the composite materials are assumed to be of uniform strength.

There is a general agreement in the field of fibre composites that the stress developed in a fibre undergoing stress is dependent on its length. Hence, fibres used in composites may be categorized as either Continuous or Discontinuous (short).

Continuous fibres

These are composite fibres with lengths extending from one end to the other end of the composite material as shown in Figure 2.16. It is assumed that the bonding between the fibres and the matrix is satisfactory and that the strain of the composite is identical to that in the fibre and in the matrix.

Discontinuous (short) fibres

These fibres have ends within the composite shown schematically in Figure 2.11(a). In short fibre composites, the assumption of identical strains does not hold as the strains within the fibres, matrix and the composites will not be equal. Owing to the difference in strains, shear stresses are induced around the ends of the fibres and the resulting shear force then causes the fibre to act in tension. Figure 2.17 shows the idealised variation of

tensile stress in a fibre along its length. The maximum stress attainable in the fibre is the ultimate strength (σ_{fu}) and the minimum length required for the tensile stress to build up is known as the critical length, (l_c).

Continuous Filament Reinforcements

These are composites in which there is no bond between the fibres and the matrix material. Michalowski (1997) while considering the effect of the relative size of fibre to grain, suggested that the matrix-filament (fibre) interaction can be considered to be of two kinds as explained in Section 2.6.2. Michalowski (1997) argued that the reinforcing effect of a continuous thin filament (i.e. when the diameter of the fibre is about an order of magnitude less than the particle size) would only become effective if the fibres behave like continuous and flexible filaments so that the force in the filament can be developed by a "belt friction effect" since the filament will be wrapped around the grains (Figure 2.18).

Upon the deformation of the matrix material, tensile force is induced in the filament can be theoretically expressed as

$$T_2 = T_1 e^{\mu\beta} \tag{2.4}$$

where μ = coefficient of friction between the grains and filament; and β = envelope angle, equal here to $\beta_1 + \beta_2$.

During shear deformation, only a portion of the filament is likely to be stretched. This portion more or less contributes significantly to the improvement in strength of the composite. The remaining part of the filament might experience compression and the portions of filament in transition between compression and extension might slip.

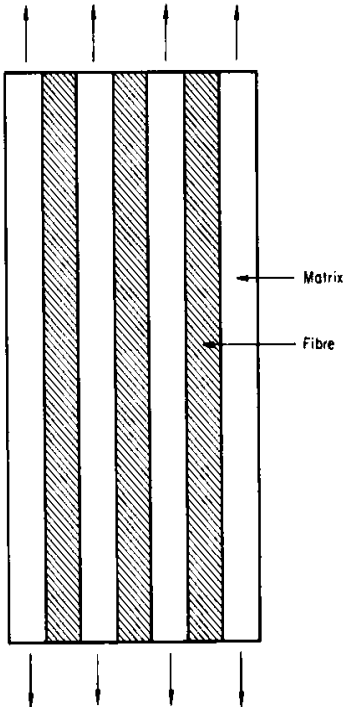

Figure 2.16: Fibre reinforced (continuous fibres) composite material (after Vinson and Chou, 1975)

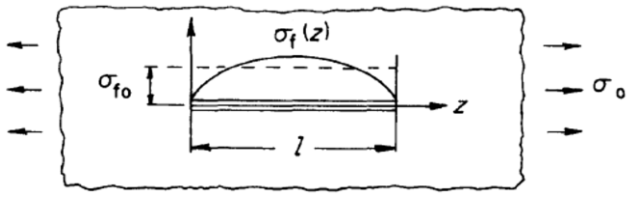

(a)

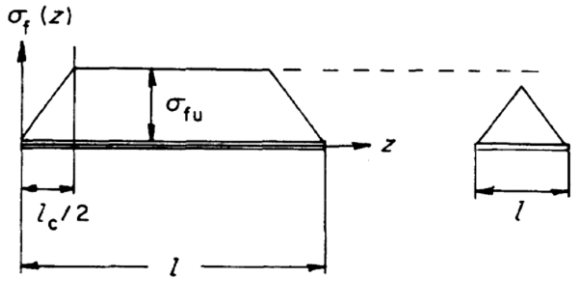

(b)

where,

- σ_o - applied tensile stress
- σ_{fo} - average fibre stress
- σ_{fu} - ultimate fibre strength
- l - fibre length
- l_c - fibre critical length

Figure 2.17: Stress distribution of a fibre parallel to the applied tensile stress (a) Actual stress distribution, and (b) simplified stress distributions for $l > l_c$ and $l < l_c$ (after Fukuda and Chou, 1982)

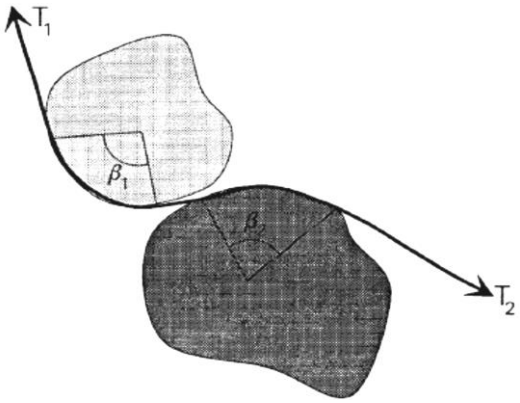

Figure 2.18: Filament wrapped around clusters of grains (after Michalowski, 1997)

2.6.5 Micromechanics of Fibre Reinforced Sands

The interaction mechanism of fibre reinforced granular material and the factors influencing it have been identified to be a key component in the scientific understanding of fibre reinforced materials. Previous research has relied on macro-mechanical behaviour of the composite to infer its micro-mechanical response. Discrete element method (DEM) is a tool that can be used to link understanding between the particle-scale interactions and the overall material response of granular materials (O'Sullivan, 2011) but has not been widely used in investigating fibre reinforced soils.

Maeda and Ibraim (2008) performed two dimensional DEM biaxial compression simulation of specimens containing a mixture of sands and fibres. The sand particles were modelled by rigid disks having a D_{50} of 7.1 mm connected by contact bonds with tension and shear strengths, and without rotational constraints. The fibres were modelled by connecting small circular particles with a bond contact algorithm in which the strength of the bond is fairly high. By calculating the average tensile stresses in the fibres, Maeda and Ibraim (2008) showed that under isotropic compression, the magnitude of the average tensile stresses in the fibres depends on the particle rearrangement which in turn depends on the applied stress (Figure 2.19).

During shear deformation, Maeda and Ibraim (2008) reported that the average tensile stress in the fibres remained unchanged from the initial isotropic compression stage until the axial strains exceeded 0.2 %. This was attributed to the dominating behaviour of the matrix material at small strains. Also, higher fibre contents produced higher average fibre tensile stresses (Figure 2.20).

The distribution of the tensile stresses was also shown to be non-homogenous and the highest tensile stress was mobilised in the fibres oriented in the horizontal direction.

However, this observation was not consistent within a given specimen suggesting that local micro fabric and local structural rearrangement might play a significant role in the interaction mechanism. Maeda and Ibraim (2008) introduced two fabric indices (N_cF_1 and N_cF_2) quantifying fabric intensity over the principal stress directions. N_c represents the coordination number, while F_1 and F_2 represent the principal values of the fabric tensor corresponding to the major and minor principal stress directions respectively. Based on the DEM simulations, they suggested that the presence of fibres in granular materials can prevent the loss of fabric in the minor principal stress direction. The unreinforced specimen exhibited a decrease in N_cF_2 (Figure 2.21(b)) with increasing global deformation, indicating a loss in inter-particle contacts in the lateral direction, while N_cF_1 (Figure 2.21(a)) remained unchanged.

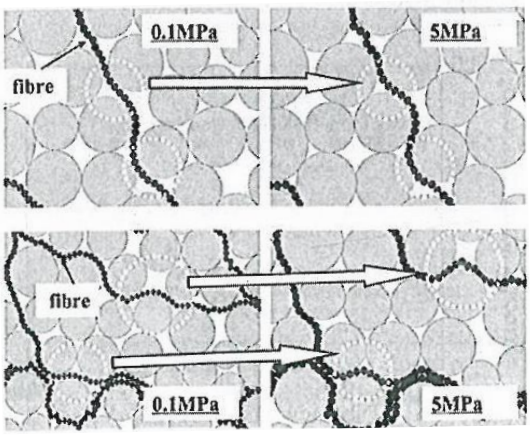

(a)

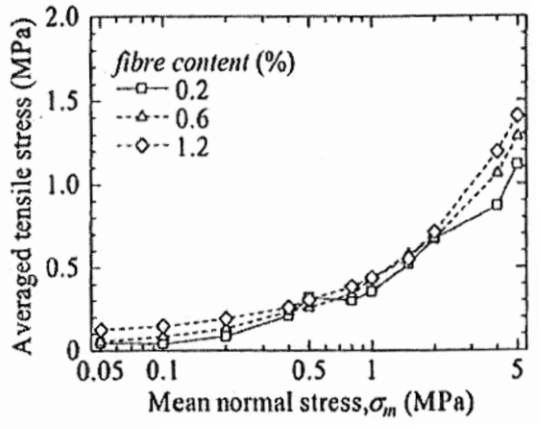

(b)

Figure 2.19: (a) Change in the configuration of fibre during isotropic compression, and (b) averaged tensile stress in fibres developed with macro deformation under isotropic compression (after Maeda and Ibraim, 2008)

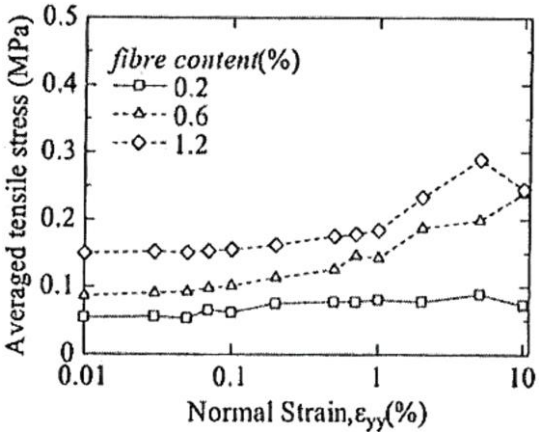

Figure 2.20: Averaged tensile stress in fibres developed with macro deformation under shearing (after Maeda and Ibraim, 2008)

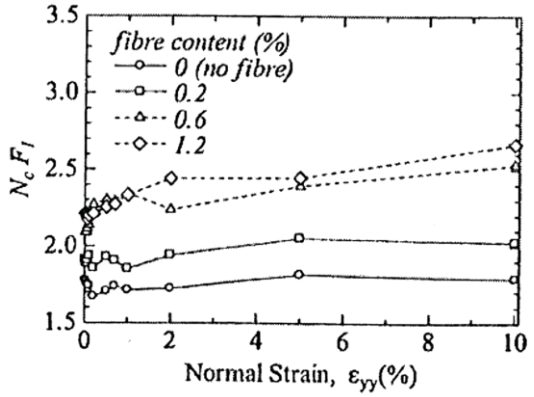

(a)

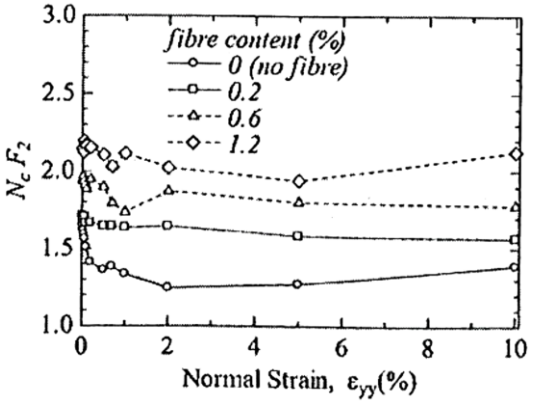

(b)

Figure 2.21: Contact fabric for granular matrix phase; (a) and (b) shows fabric in the direction of major and minor principal stress respectively (after Maeda and Ibraim, 2008)

2.7 Conclusions

Modern rail track comprises the super-structure and the sub-structure. Ballast being one of the key components of the sub-structure, has many functions including retaining the track position, reducing the sleeper bearing pressure on the underlying materials, and providing drainage for water falling onto the track. The mechanical response of ballast is generally governed by the characteristics of the particles, the bulk properties of the granular assembly, loading, and particle degradation.

The use of geogrids is beneficial for the improvement of some mechanical properties of ballast. This is seen particularly in the reduction of the lateral spread of ballast particles, hence, reducing the permanent vertical settlement. In considering the micro-mechanics of geogrid reinforced ballast, it was shown that the location of the geogrid plays a vital role in the response of the ballast layer to permanent vertical settlement. However, one of the drawbacks in the use of geogrids in ballast is the restriction it imposes on future maintenance activities that can be carried out. The addition of synthetic randomly orientated fibres provides a potentially new method of reinforcing ballast able to withstand typical tamping operations.

Fibre reinforcements have been shown to improve the mechanical properties of granular materials such as sand. The effectiveness of fibre reinforcements in sand can be considered to be influenced by: (1) *Fibre properties* – these include fibre content, fibre geometrical properties (e.g. length, diameter and aspect ratio), elastic modulus, and tensile strength; (2) *Soil characteristics* – these include particle size, shape and gradation; and (3) *Reinforced soil characteristics* – these include stress level (confining or normal stress), density, fibre/particle relative dimensions and orientation of fibres.

The relative dimensions of the fibres and soil grains have also been found to be important in the effectiveness of fibre reinforcements and thus suggested to be relevant to the micro-mechanics of the fibre-sand interaction. In particular, it has been shown that the rearrangement of particles within a fibre reinforced soil specimen is important in the development of interactions to mobilise tensile forces in the fibres. In addition, it is considered that the presence of fibres in granular materials can prevent the loss of fabric in the minor principal stress direction.

Chapter 3

Structure of Fibre Reinforced Granular Materials

3.1 Introduction

It is well established that the degree of particle packing significantly influences the strength and deformation behaviour of soils and crushed rocks. A granular material prepared at a higher initial density is known to exhibit a higher peak friction angle and to be stiffer than the same material prepared at a lower initial density. The effective density of granular materials is strongly related to the interparticle coordination number. When the initial density of granular materials is low, the interparticle coordination number is low, and shear deformation causes particle rotation and buckling of internal force chains. At high density, the coordination number is high. This in turn hinders particle rotation, hence converting the applied shear stress to either dilation (leading to a reduction in coordination number) or frictional slippage at contacts (Cho et al., 2006). In terms of railway track stability, there is similarly a consensus that the strength and stability of ballast is enhanced by increased ballast density (e.g. Selig and Waters, 1994; Indraratna et al., 1998). The most critical stage of ballast life has been identified as the time immediately after track construction or maintenance i.e. when the ballast is at its loosest state (Indraratna et al., 1998). This further highlights the importance of the density/packing of ballast for the overall performance of the track.

Evidence of how the addition of randomly oriented fibres affects the packing of a granular medium was reported by Diambra et al., (2010). By carrying out standard laboratory compaction tests on sand-fibre mixtures having different fibre contents, Diambra et al., (2010) showed that the addition of fibres to sand produces a gradual reduction in the maximum dry density of the mixture. In addition, they showed that the optimum moisture content of sand-fibre mixtures is unaffected by the addition of fibres due to their low moisture absorption (< 0.1% by mass). However, the effect of fibres on the packing structure has not been systematically examined while considering among

other factors the definition of void ratio, dry density and fibre content of the mixture. Also, the effect of the addition of fibres in specimens composed of larger sized particles (e.g. scaled ballast) is unknown. It is expected that understanding the effects of fibres on packing in a granular medium will lead to a more rigorous scientific understanding of the fibre-particle interaction in fibre reinforced granular materials.

This chapter examines the effect of random fibre inclusions on the packing structure of coarse sand and scaled ballast. Laboratory tests were carried out to assess the effects of the variation of fibre content on the minimum and maximum void ratios of fibre reinforced granular materials. To provide further understanding, a mathematical framework was derived and interpreted to describe the effects of fibre reinforcement on granular materials (i.e. Leighton Buzzard sand and scaled ballast).

3.2 Materials

3.2.1 Leighton Buzzard Sand (Fraction A)

Tests on Leighton Buzzard (LB) sand (Fraction A) were carried out to provide a baseline for the transfer of laboratory testing of random fibre reinforcements in sand, which are widely reported in the literature, to scaled ballast sized particles. Leighton Buzzard (A) is light brown coloured, uniformly graded quartz sand with rounded to sub-rounded particles. Its particle size distribution is shown in Figure 3.1.

3.2.2 Scaled Ballast

The testing of scaled ballast (SB) offers an attractive means of developing an understanding of the mechanics of full size ballast. This is mainly due to the challenges encountered when testing full size ballast particles in laboratory triaxial tests. As a result of the relatively large maximum ballast particle size (typically 62.5 mm), a large sample size with a diameter of about 300 - 400 mm is required. Large scale triaxial tests have been reported in the literature (e.g. Indraratna et al., 1998; Anderson and Fair, 2008; Aursudkij et al., 2009), but the associated challenges persist. The use of aggregates from the same parent rock having a similar but scaled particle size distribution curve is an alternative that has been investigated in previous research, mostly in the context of rockfill materials. Sevi et al. (2009), Ishikawa et al. (2011) and Le Pen et al. (2014) have reported tests on scaled ballast to demonstrate plastic deformation under cyclic loading, deformation under a moving wheel load and investigate how ballast shoulder width and height contribute to a railway sleeper's resistance to lateral movement respectively. In this research, two levels of scaled ballasts were used. The scaled ballast materials used has a parallel gradation of 1/5 and 1/3 that of standard Network Rail ballast (Figure 3.1,

Table 3.1) and the Coefficient of uniformity, C_u of the test materials are shown in Table 3.2.

An illustration of the degree of similarity of the particles across the size range is given in plan view images of randomly selected ballast particles from scaled to full size (Figure 3.2). By scaling the images so that the particles appear to have the same size, the differences in shape associated with different particle sizes is not noticeable with the naked eye.

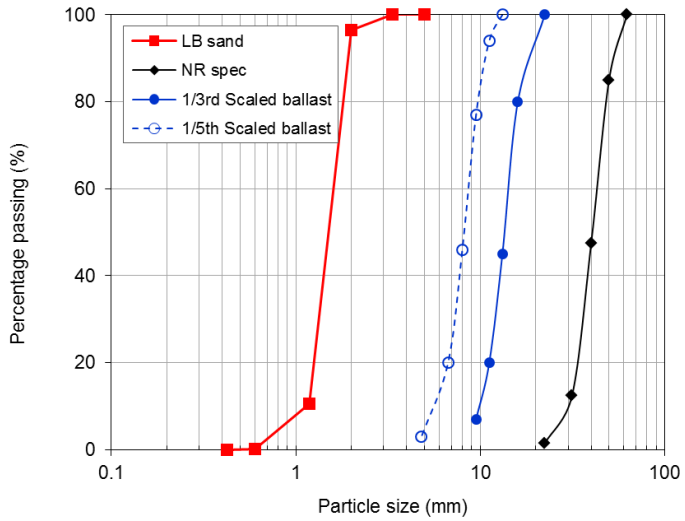

Figure 3.1: Particle size distribution of Leighton Buzzard sand (fraction A), 1/5 and 1/3 scaled, and Network Rail standard ballast

Table 3.1: Full size ballast specification, 1/3rd and 1/5th scale equivalent

% passing by weight (median of NR range)	**Sieve size (mm)**	**1/3rd scale (mm)**	**1/5th scale (mm)**
100	62.5	20.83	12.5
85	50	16.67	10.0
47.5	40	13.33	8
12.5	31.5	10.50	6.3
1.5	22.4	7.47	4.5

Table 3.2: Coefficient of uniformity, C_u for the test materials

Materials	Standard Network Rail ballast	1/3 SB	1/5 SB	LB sand
Coefficient of uniformity, C_u	1.4	1.5	1.5	1.4

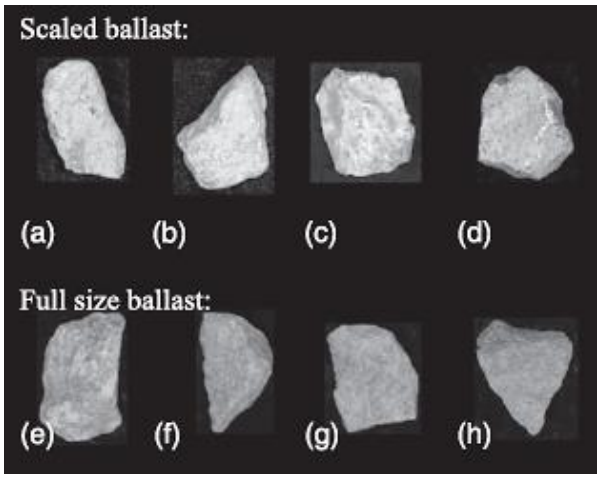

Figure 3.2: Example particles in sieve intervals in millimetres: (a) 9.5 - 11.2; (b) 11.2 - 13.2; (c) 13.2 - 16.0; (d) 16.0 - 22.4; (e) 22.4 - 31.5; (f) 31.5 - 40.0; (g) 40.0 - 50.0; (h) 50.0 - 62.5 (after, Le Pen et al., 2014)

3.2.3 Fibres

Polypropylene (PP) and polyethylene (PE) fibres were used in this research (Figure 3.3). PP fibres were used to reinforce the LB sand specimens and the PE fibres to reinforce the scaled ballast (both $1/5^{th}$ and $1/3^{rd}$) specimens. PP is a thermoplastic polymer like polyethylene (PE) that is used in a wide variety of applications. Typically, PP has a higher melting point than PE with higher rigidity and hardness. It also has good chemical resistance, heat resistance and very low water absorption. In this research, the fibres used were in the form of strips (tape) and their key properties are presented in Table 3.3.

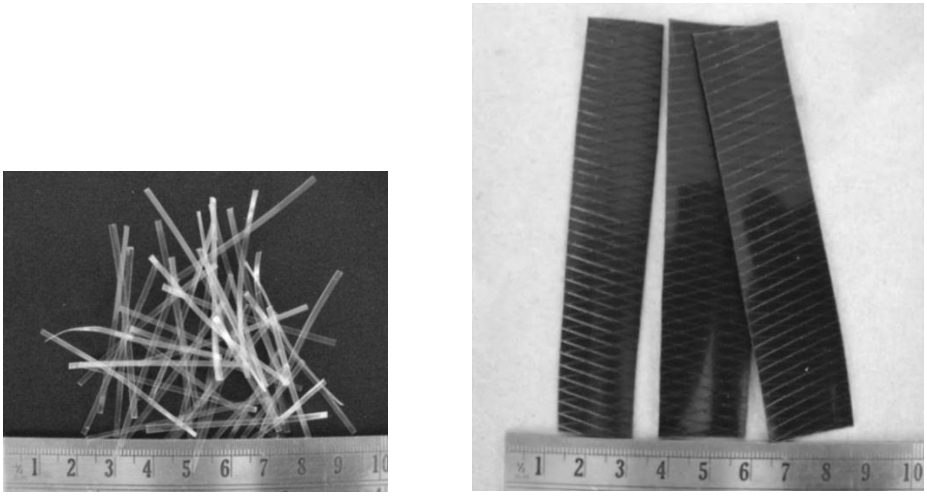

(a) (b)

Figure 3.3: Fibres used in the laboratory tests (a) polypropylene and, (b) polyethylene

Table 3.3: Typical values of the basic properties of polypropylene and polyethylene fibres

	Polypropylene	**Polyethylene**
Specific gravity	0.905	0.920
Tensile strength	~ 42 MPa	20.3 MPa[1], 11.2 MPa[2]
Softening temperature	135°C	85°C
Moisture absorption	< 0.1%	< 0.1%

[1] Longitudinal; [2] Transverse

3.3 Sample Preparation

The sand-fibre mixture was prepared by shaking known masses of fibre and sand in a tied transparent bag. This ensured that an adequate mix of the fibres and sand in the vertical and horizontal directions was achieved. Visual inspection of the mixture showed that the orientation and distribution of the fibres were reasonably random and homogenous respectively.

The scaled ballast-fibre mixture was prepared using a similar method to that of the sand-fibre mixture except that mixing was done in a plastic container. Plastic bags could not be used owing to the relatively large weight of the scaled ballast and the associated handling difficulty. The resulting mixture appeared to be reasonably random and homogeneous. The fibres used for each material are described in Table 3.4.

3.3.1 Maximum dry density tests

For the fibre reinforced LB sand, the maximum dry density was determined by tamping using a circular shaped tamper weighing 2 kg into a standard Proctor compaction mould. This method was used because of the fibre segregation that occurs while using standard methods (e.g. *pluviation*). Initial trials with pure sand showed that thirty (30) tamps in three layers produced reproducible dry densities within ± 0.7% of that determined using the standard pluviation method. Each test (i.e. each target fibre content) was repeated up to five times to establish the repeatability of the results.

For scaled ballast, a tamping method similar to that used for the sand was adopted, using a cylindrical mould 150 mm in diameter and 246 mm in height (Figure 3.4). Preliminary tests showed that twenty (20) blows from a standard Proctor rammer (weight of rammer = 2.5 kg) produced a density similar to that using the vibration method of compaction. The scaled ballast (and reinforced scaled ballast) was compacted in three layers. To prevent particle breakage due to the impact of the rammer, a circular shaped laminated piece of wood padded with rubber was placed on top of each layer during compaction.

3.3.2 Minimum dry density tests

The Tube Method, which gives acceptable and consistent results, was used to determine the minimum dry density of the reinforced LB sand. This involves placing a long narrow tube open at both ends upright in a mould of known volume. A quantity of dry or reinforced sand sufficient to fill the mould is placed in the tube and then the tube is slowly lifted allowing the sand to trickle into the mould until the mould overflows. The top of the mould is then levelled and the measured masses and volumes, the specific gravities of the sand and fibres are used to determine the void ratios as defined in Section 3.4. Owing to the size of the tube used, the fibre length investigated in the minimum dry density tests for sand was 23 mm.

As there are no widely established methods for determining the minimum density of large sized granular materials, a method of carefully placing scaled ballast in the cylindrical mould, such that the particles would not densify was adopted for the scaled ballast. The dimensions of the fibres and the corresponding granular matrix used for the maximum and minimum dry density tests are presented in Table 3.4.

Figure 3.4: Cylindrical compaction mould used for the determination of the dry density of scaled ballast

Table 3.4: Materials used with the corresponding fibre properties

Material	**Fibre type**	**Dimensions**		
		Fibre width (mm)	Fibre length (mm)	Fibre thickness (mm)
LB Sand	Polypropylene	2	23	0.1
1/3 SB	Polyethylene	20	100	0.5

3.4 Description of Parameters

There is no universally accepted definition of void ratio for fibre reinforced granular materials. The main area of disagreement is whether the volume of fibres is considered to be part of the volume of solids or voids. Each approach has implications for the calculated void ratio of the mixture.

Diambra et al. (2010) considered the fibres to be part of the solids component of the sand-fibre mixture and defined the void ratio as the volume of voids divided by the volume of grains plus fibres. This definition does not obviously account for the fact that, in a sand-fibre mixture, grain-fibre interaction may lead to an increase in the void and/or non-sand volume compared with pure sand, under the same compactive effort. In particular, the approach will perhaps misleadingly give a lower void ratio for reinforced sand than for the same sand without reinforcement, because the volume of solids

(defined in this case as fibres plus sand) increases. Michalowski and Cermak (2003) adopted the same approach of considering the volume of fibres to be part of the solid skeleton but did not present any experimental evidence of its effect on the packing of the mixture. Diambra et al. (2013), in developing a constitutive model for fibre reinforced sands, considered the total volume of voids to be divided into two parts 'attached' to either the sand matrix or to the fibres.

To overcome these limitations a three phase system consisting of voids (air), fibres and grains is considered (Figure 3.5), with relations between the phases defined as:

Void ratio (e): the ratio of the volume of voids (V_v) to the volume of the grains, hereafter termed "solids" (V_s).

$$e = \frac{V_v}{V_s} \tag{3.1}$$

Volumetric fibre ratio (V_{fr}): the ratio of the volume of fibres (V_f) to the volume of solids (V_s)

$$V_{fr} = \frac{V_f}{V_s} \tag{3.2}$$

Specific volume (v): the ratio of the total volume (fibres + solids + voids, $V_T = V_s + V_f + V_v$) to the associated volume of solids (V_s)

$$v = \frac{(V_s + V_f + V_v)}{V_s} \tag{3.3}$$

The proposed definitions have the advantage of considering fibres independently of the solids and the voids while taking V_s to be the common denominator for both parameters. The dry bulk density of the mixture is given as:

$$\rho_{bulk} = \frac{m_f + m_s}{V_f + V_s + V_v} \tag{3.4}$$

where m_f and m_s are the mass of fibre and solids in the mixture respectively.

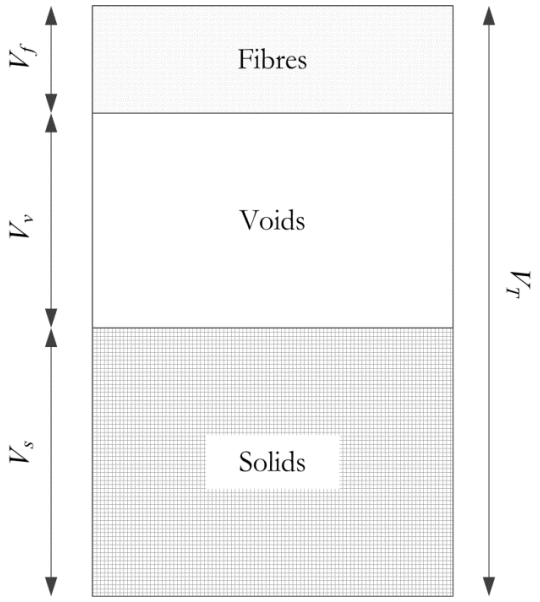

Figure 3.5: Volumes of phases in a fibre reinforced granular material

3.5 Dry Density Test Results

The standard deviation (maximum and minimum) of the void ratio obtained in both LB sand and scaled ballast at different fibre contents are presented in Table 3.5. The maximum and minimum void ratios (i.e. e_{max} and e_{min}) for both sand and scaled ballast increase gradually with increasing V_{fr} (Figure 3.6), indicating that the addition of fibres interferes with the packing of the particles. Ibraim and Fourmont (2007) reported a loss in dry density of the sand-fibre mixture which they attributed to the greater resistance to compaction provided by the fibres. However, the behaviour of the constituents (i.e. the volumes of fibres, solids and voids) in relation to the observed macro-mechanical behaviour is not fully understood.

Table 3.5: Maximum standard deviation of the void ratios obtained from each test

		Standard deviation	
		Min.	Max.
LB sand	e_{max}	0.0042	0.0066
	e_{min}	0.00141	0.0057
Scaled ballast	e_{max}	0.0057	0.0101
	e_{min}	0.0044	0.0121

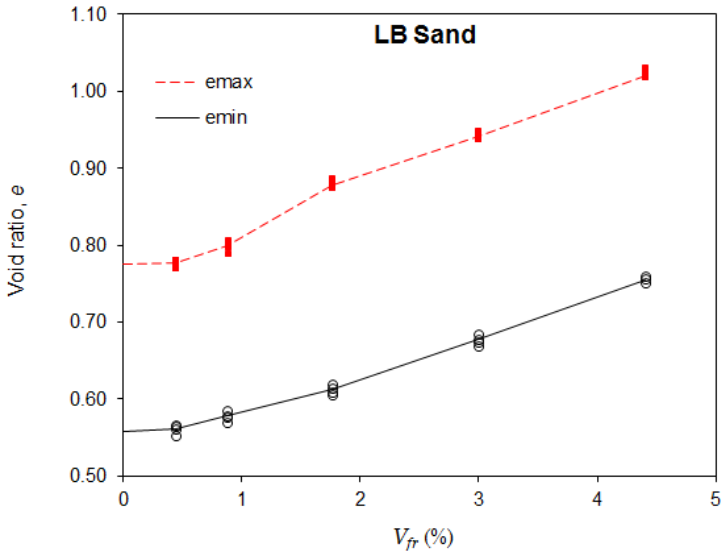

(a)

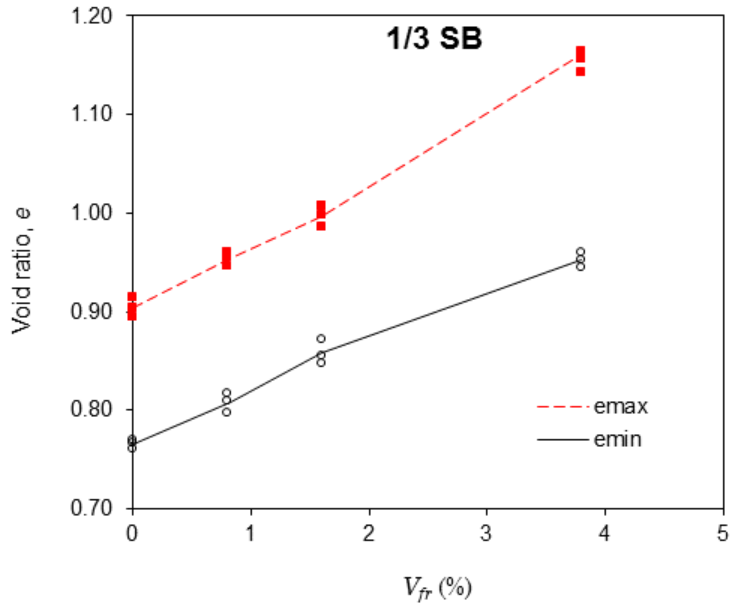

(b)

Figure 3.6: Effect of increasing V_{fr} on the void ratio of (a) fibre reinforced LB sand, and (b) fibre reinforced 1/3rd scaled ballast

3.6 Principles of fibre/particle interaction

The effect of the addition of fibres on the maximum and minimum void ratios of granular materials as shown in Figure 3.6 highlights the need to develop a better understanding of the interaction that takes place at the grain level. This is important as it will serve as a basis for understanding the proposed use of random fibre reinforcements in railway ballast.

Consider a volume of fibres V_f introduced into a particulate material of initial total volume V_{To}, initial voids volume V_{vo} and fixed volume of solids V_s. The initial void ratio is $e_o = V_{vo}/V_s$ and the addition of the volume of fibres ΔV_f may cause the volume of voids to change by an amount ΔV_v where,

$$\Delta V_v = \alpha . \Delta V_f \tag{3.5}$$

This gives a change in total volume ΔV_T of

$$\Delta V_T = (1 + \alpha) . \Delta V_f \tag{3.6}$$

and a change in void ratio Δe of

$$\Delta e = \frac{\Delta V_v}{V_s} = \frac{\alpha . \Delta V_f}{V_s} = \alpha . \Delta V_{fr} \tag{3.7}$$

A graph of void ratio, e against volumetric fibre ratio V_{fr} will have slope α. Increases in volume have been taken as positive.

Unless α = -1, the addition of fibres will cause an increase in the total volume associated with the volume of solids V_s, with the fibres displacing solids, voids or both from the initial total volume V_{To}. In principle, four categories/regions of substitution of solids or voids by fibres are possible.

1. If α = -1, the total volume occupied by the mixture does not change and the fibres are accommodated within the existing voids, whose volume decreases by an amount equal to the volume of fibres added. This may be viewed as fibres substituting for voids.

2. If -1 < α < 0, the void ratio falls but the decrease in void volume is less than the volume of fibres added. The total volume increases in accordance with Equation ((3.6) as the fibres substitute for both voids and solids.

3. If $\alpha = 0$, the void ratio does not change but the total volume associated with a given volume of solids V_s will increase in accordance with Equation (3.5). This may be viewed as fibres substituting for solids. Figure 3.6(a) shows that this occurs only for the LB sand at values of V_{fr} less than approximately 0.5%.

4. If $\alpha > 0$, the fibres not only substitute for solids but also disrupt their ability to pack. This causes the void ratio to increase and the total volume to increase by more than the volume of fibres added. This behaviour is exhibited by the LB sand for values of V_{fr} greater than approximately 0.5%, and by the scaled ballast for all values of V_{fr}.

Examples of the four categories/regions are compared with the data for e_{min} for the LB sand in Figure 3.7. Superficially, the plot suggests that Case 4 gives the closest fit to the e_{min}/V_{fr} data, with a value of $\alpha \approx 4$. The plot also suggests that Cases 1 and 2, in which the added volume of fibres is wholly or even partly accommodated within the existing voids, is in most cases unlikely.

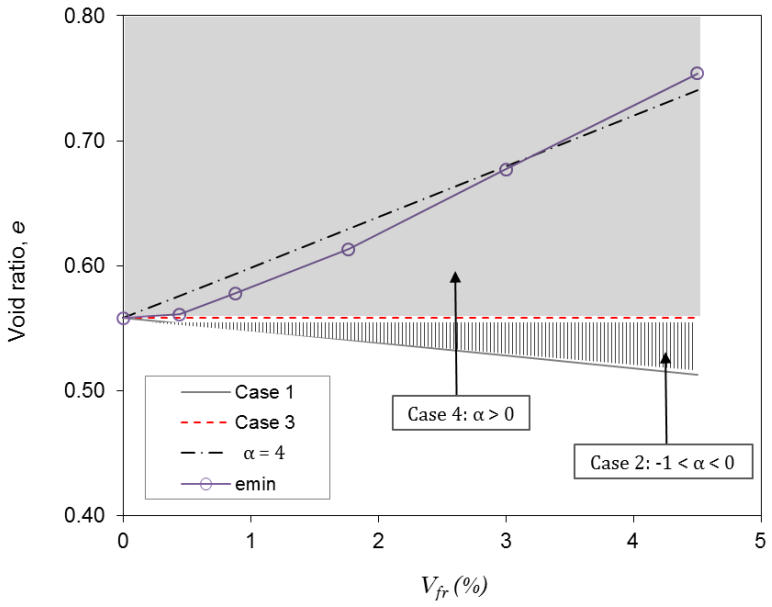

Figure 3.7: Void ratio e against volumetric fibre ratio V_{fr} plot for three scenarios of fibre-particle interaction compared with data for e_{min} for Leighton Buzzard sand

However, it is the local slope of the e/V_{fr} plot that is important, and simply fitting a straight line to the data masks important variations in behaviour as V_{fr} is increased. The slopes, α of the e_{min} and e_{max} data for the Leighton Buzzard sand and scaled ballast are plotted against V_{fr} in Figure 3.8. Figure 3.8(a) shows that at low fibre contents (V_{fr} < 0.5%), the fibres can be considered to substitute the solids in the sand-fibre mixture as α is close to zero. However, as V_{fr} approaches 1%, α becomes larger, indicating that the addition of further fibres both displaces solids and disrupts their ability to pack. The rise in α for the minimum void ratio curve is initially less pronounced and smoother, but the maximum value is similar reflecting the near-parallel nature of the e/V_{fr} plots shown in Figure 3.8(a).

Figure 3.8(b) shows a very different behaviour for the scaled ballast, with the addition of fibres displacing solids and disrupting packing right from the start. Also, the values of α are generally greater for e_{max} than for e_{min} and can thus be considered to be consistent with the widening of the range ($e_{max} - e_{min}$) as V_{fr} is increased. The slight reduction in α when $V_{fr} \approx 1.6\%$ is due to the local fluctuation in the e_{max} curve as seen in Figure 3.6.

In principle, when a volume of fibres V_f is added to a granular material (Figure 3.9(a)) it will bring about changes in the total volume V_T and the volume of voids V_v for a given volume of solids V_s (Figure 3.9(c)) or changes in the volume of solids and the volume of voids (as well as the volume of fibres) within a given constant total volume V_{T0} (Figure 3.9(b)).

For a given volume of solids V_s, Equations (3.5) and (3.6) may be combined to give expressions for the rate of change of volume of voids with the volume of fibres added,

$$\left.\frac{dV_v}{dV_f}\right|_{V_s} = \alpha \tag{3.8}$$

and the rate of change of total volume with volume of fibres added,

$$\left.\frac{dV_T}{dV_f}\right|_{V_s} = (1 + \alpha) \tag{3.9}$$

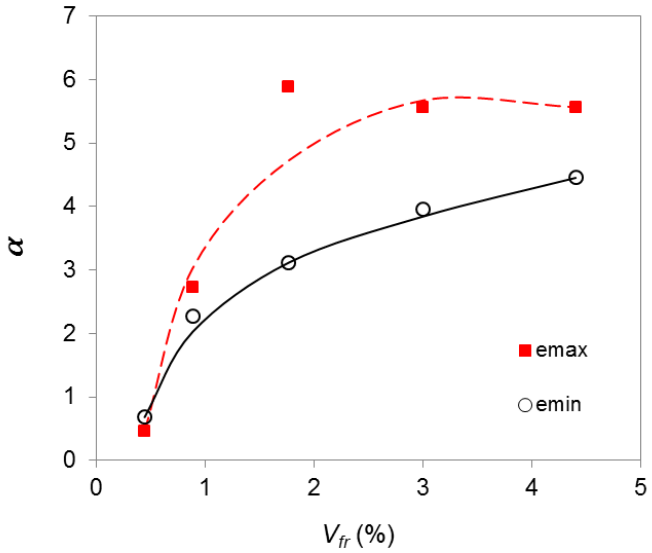

(a)

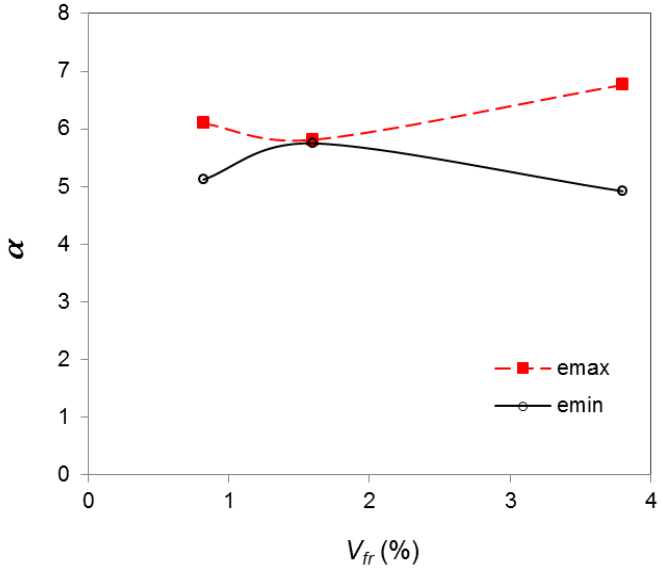

(b)

Figure 3.8: Variation of the local slope of the e/V_{fr}, α with V_{fr} for (a) LB sand and (b) Scaled ballast

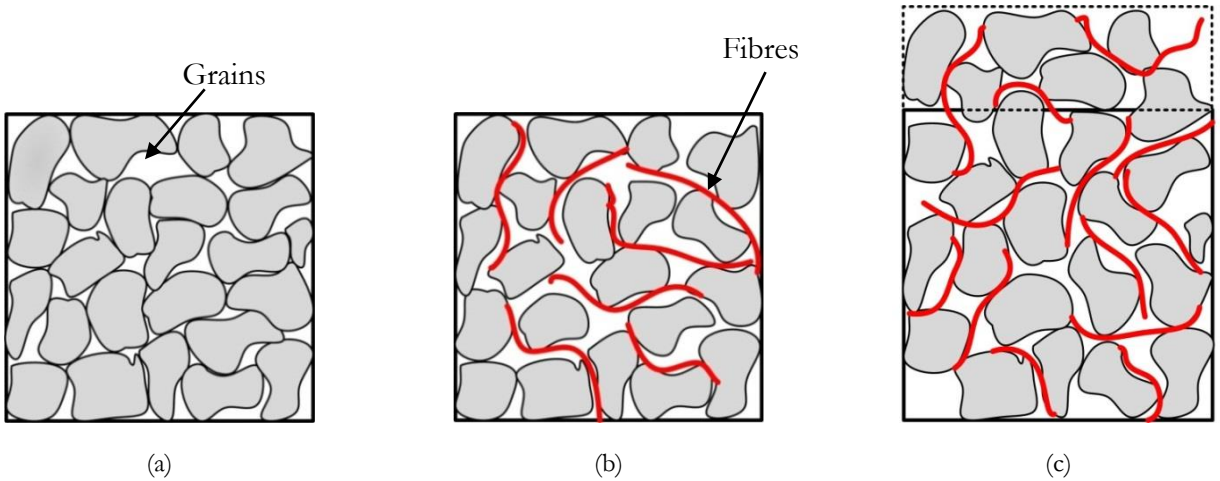

Figure 3.9: Illustration of the effect of adding volume of fibres, V_f (a) Unreinforced granular material i.e. V_{T0}, V_{V0} and V_S; (b) Fibre reinforced granular material at constant V_{T0}, (V_S + ΔV_S) and (V_{V0} + ΔV_V); (c) Fibre reinforced granular material at constant V_S, (V_{T0} + ΔV_T) and (V_{V0} + ΔV_V)

To derive a measure of how voids and solids are displaced for an initial total volume as fibres are added, corresponding equations for the changes in V_s and V_v within a given (constant) total volume V_{T0} may be developed as follows:

After the addition of a volume of fibres ΔV_f, the constant volume of solids V_s initially contained within the original total volume V_{T0} occupies the new total volume $V_{T0} + \Delta V_T$. Thus the volume of solids contained within the original volume V_{T0} becomes,

$$V_s \times \frac{V_{T0}}{V_{T0} + \Delta V_T} = \beta . V_s$$

where,

$$\beta = \left(1 + \frac{\Delta V_T}{V_{T0}}\right)^{-1} \approx \left(1 - \frac{\Delta V_T}{V_{T0}}\right)$$

Similarly, the volume of fibres contained within the original total volume V_{T0} is

$$\Delta V'_f = \Delta V_f \times \frac{V_{T0}}{V_{T0} + \Delta V_T} = \beta . \Delta V_f$$

The volume of voids contained within the original total volume V_{T0} is

$$(V_{v0} + \alpha . \Delta V_f) \times \frac{V_{T0}}{V_{T0} + \Delta V_T} = \beta . (V_{v0} + \alpha . \Delta V_f)$$

and the change in the volume of voids contained within the original total volume V_{T0} is

$$\Delta V'_v = \beta . (V_{v0} + \alpha . \Delta V_f) - V_{v0}$$

If $\Delta V_T << V_{T0}$ so that $\beta \approx 1$, $\Delta V'_v \approx \alpha . \Delta V_f$ and,

$$\left.\frac{dV_v}{dV_f}\right|_{V_T} = \frac{\Delta V'_v}{\Delta V'_f} = \alpha \qquad (3.10)$$

The change in the volume of solids contained within the original total volume V_{T0} is

$$\Delta V'_s = \left(\frac{V_{T0}}{V_{T0} + \Delta V_{T_0}} - 1\right) . V_s = \left(\frac{-\Delta V_T}{V_{T0}}\right) . \frac{V_{T0}}{1 + e_0} = \frac{-\Delta V_T}{1 + e_0}$$

Also,

$$\Delta V_T = 1 + \alpha \, . \Delta V_f = 1 + \alpha \, . \frac{\Delta V'_f}{\beta}$$

Hence if $\Delta V_T << V_{T0}$ so that $\beta \approx 1$, $\Delta V'_v \approx \alpha \cdot \Delta V_f$ and,

$$\left.\frac{dV_s}{dV_f}\right|_{V_T} = \frac{\Delta V_s}{\Delta V_f} = -\frac{1+\alpha}{1+e_0} \tag{3.11}$$

Also,

$$\left.\frac{dV_v}{dV_s}\right|_{V_T} = -\frac{\alpha.\ 1+e_0}{1+\alpha} \tag{3.12}$$

Equation (3.11) and (3.12) give an indication of the relative rates of substitution of voids and solids in a given total volume. Experimental results for $\left.\frac{dV_s}{dV_f}\right|_{V_T}$, and $\left.\frac{dV_v}{dV_f}\right|_{V_T}$ for LB sand and scaled ballast are plotted in Figure 3.10 and 3.10. Owing to the large variability of the data locally, it is the general trend of the results that is of more significance. The substitution rate of V_s relative to V_f for both LB sand and SB specimens is negative at all V_{fr}, indicating a reduction in V_s with increasing V_f. Furthermore, Figures 3.9(a) and 3.10(a) suggests that for a unit increase in V_f, V_s reduces three times as much at large fibre contents (e.g. V_{fr} > 3%). This is further illustrated by phase relation diagrams of unreinforced and fibre reinforced granular materials in Figure 3.12.

At low fibre contents (e.g. V_{fr} < 1%), negative values are observed owing to the initial reduction in V_v as the V_f occupies void spaces. The substitution rates of V_v relative to V_f for both LB sand and SB specimens (Figure 3.10(b) and 3.10(b)) at constant V_T suggests that V_v increases to almost twice the V_f at large fibre contents (e.g. V_{fr} > 3%). This confirms the explanation given earlier in Section 3.5 that the presence of fibres prevents particles from packing densely, thereby creating voids especially within the vicinity of the fibres.

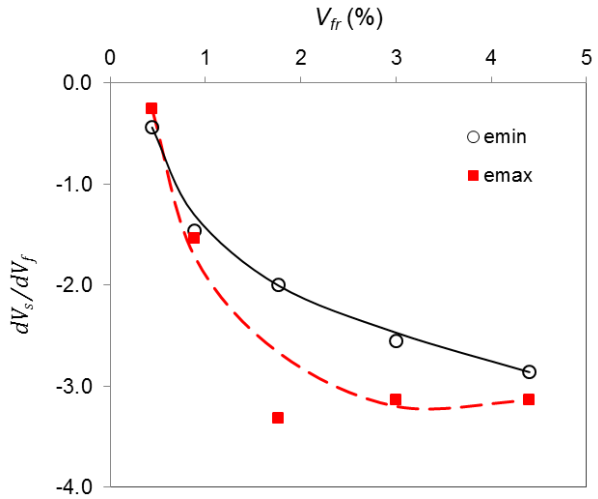

(a)

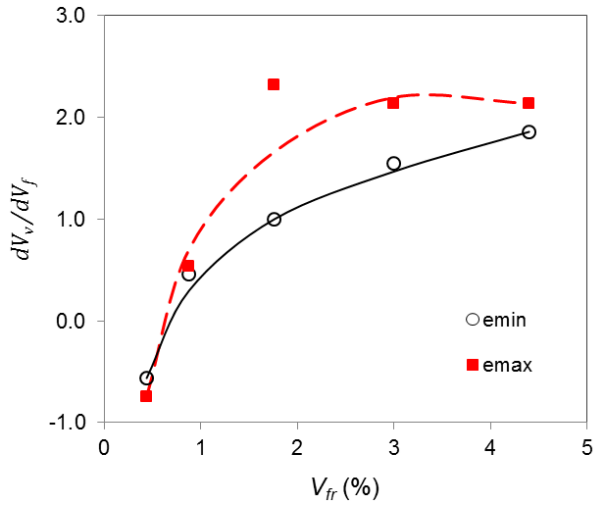

(b)

Figure 3.10: Experimental results showing the relative rates of substitution (a) dV_s/dV_f, and (b) dV_v/dV_f at constant V_T for LB sand

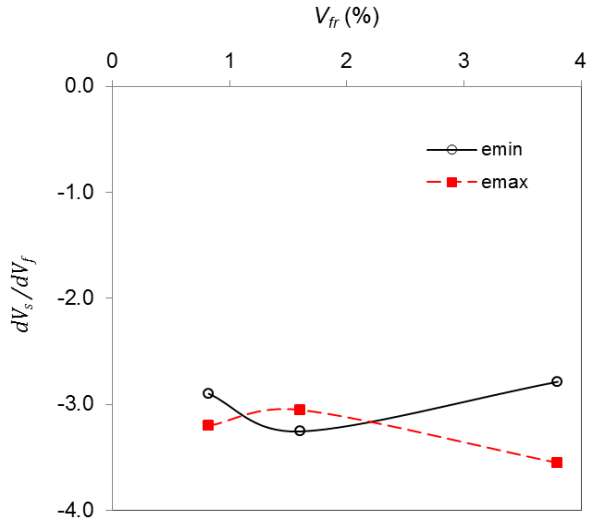

(a)

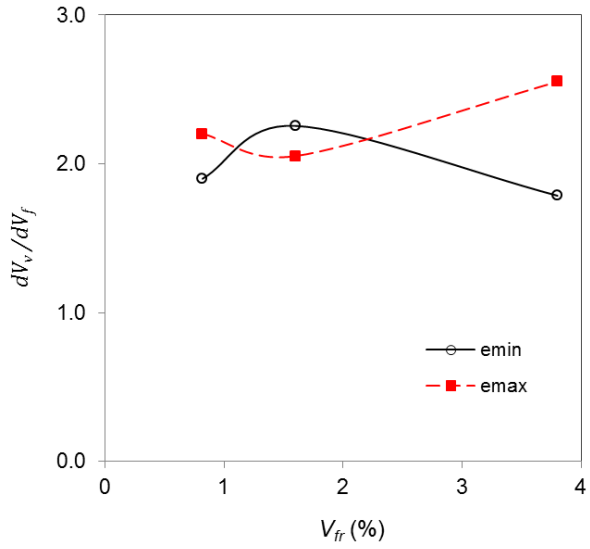

(b)

Figure 3.11: Experimental results showing the relative rates of substitution (a) dV_s/dV_f, and (b) dV_v/dV_f at constant V_T for 1/3 scaled ballast

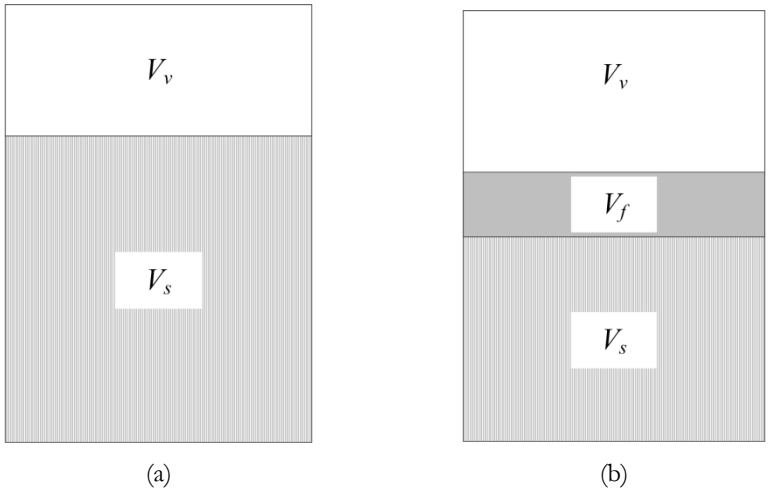

Figure 3.12: Phase relations diagram of (a) unreinforced (b) fibre reinforced granular material at constant V_T and compactive effort

3.7 Discussion

An important consequence of the data presented in Figure 3.6 is that changing the volume fraction of fibres V_{fr} at constant void ratio will affect the relative density of the specimen. For example, a specimen at a given void ratio could be relatively loose when V_{fr} is low but relatively dense when V_{fr} is high. Appreciation of the implication of this phenomenon on the mechanical behaviour of fibre reinforced granular materials is important as it provides the basis for a more robust understanding of fibre/particle interaction mechanisms. Also, fibre/particle interaction described in Section 3.6 further provides an insight into the effect of V_{fr} on the packing characteristics of the mixture. The addition of fibres to a granular material prevents the grains from packing and thus creates both macro voids (due to the packing of a smaller number of solids within a given total volume) and micro voids (arising from the inability of fibres to form perfect bonds with particles).

3.8 Conclusions

The effects of random fibre inclusions on the packing structure of coarse sand and scaled ballast have been investigated with reference to two proposed constituent parameter definitions: the *Void ratio* (e), defined as the ratio of the volume of voids (V_v) to the volume of the grains (V_s); *Volumetric fibre ratio* (V_{fr}), defined as the ratio of the volume of fibres (V_f) to the volume of solids (V_s). A parameter called α is also introduced and it is defined as the increase in the volume of voids ΔV_v caused by the addition of a volume of fibres ΔV_f.

Based on the experimental results and the discussion of fibre-particle interaction description presented in this chapter, the following conclusions can be drawn:

1. As shown by the e_{max} and e_{min} curves of the reinforced LB sand and scaled ballast samples, the maximum and minimum void ratios of reinforced samples increases gradually with increasing V_{fr}. This indicates that the addition of fibres interferes with the packing of the particles, generally displacing both voids and solids (particles).
2. The effect of adding fibres appears to be relatively insignificant at very low V_{fr}. This is consistent with a very low volume of added fibres being accommodated within the existing void space without disrupting particle packing.
3. Principally, the interaction between fibres and particles is such that the fibres added to a granular material displace both voids and solids in the ratio,

$$\left.\frac{dV_v}{dV_s}\right|_{V_T} = -\frac{\alpha \cdot \ 1+e_0}{1+\alpha}$$

4. The relative substitution rates of the V_s and V_v in a fibre reinforced granular mix are much higher than the amount of V_f added. Hence, indicating that fibres not only prevent grains from packing but also create voids likely in close proximity to the fibres.

Chapter 4

Monotonic Triaxial Tests on Granular Materials: Apparatus and Methods

4.1 Introduction

The study of the behaviour of fibre reinforced granular materials of large particle size has received relatively little attention. The available literature on the behaviour of fibre reinforced material is on a well-graded gravel material reported by Lirer et al. (2011). They reported triaxial tests carried out on specimens reinforced with fibres having diameters ranging between 0.076 mm – 0.1 mm and lengths between 50 mm – 100 mm. These tests were carried out at effective stresses of 50 and 400 kPa, which is greater than those in a typical railway ballast in the unloaded state (e.g. Indraratna et al., 2010; Sevi and Ge, 2012). In addition, the influence of the relative dimensions of the fibres and particles was not fully investigated.

The behaviour of reinforced sand has been widely reported in the literature. However, a poor understanding of the interaction mechanisms responsible for the effect of the addition of fibres persists. To bridge this gap in knowledge, triaxial compression tests were carried out on fibre reinforced Leighton Buzzard (LB) sand and scaled ballast (1/5 and 1/3 scale). This was to provide an understanding of the behaviour and mechanics of fibre reinforced granular material, with a view of up scaling the technique for potential use in railway ballast. The use of scaled ballast materials can lead to an understanding of the mechanics of full scale materials while avoiding the challenges associated with testing full scale ballast in the laboratory (e.g. Ishikawa et al., 2011; Sevi and Ge, 2012). The major challenge of testing full scale ballast materials is the need for a large specimen size, which is a direct consequence of its large particle size (maximum particle size ≈ 63.5 mm) and makes such apparatus expensive and difficult to operate.

Le Pen et al. (2013) quantified the form of an individual particle by measuring the longest (*L*), shortest (*S*) and intermediate (*I*) orthogonal dimensions (Figure 4.1) and combining two or all of them to derive a dimensionless index. Particle form quantification can be done by using the position of the particle on a plot of I/L against *S/I* to classify the particle as either flat, spherical, columnar or flat-columnar (Figure 4.2). Le Pen et al. (2013) showed that plotting the dimensional index – i.e. *I/L* and *S/I* of ballast particles of different sizes on a Zingg plot reveals a broad classification of the particles into four zones as shown in Figure 4.3(a) and (b). A plot of cumulative distributions of *S/L* also confirms the closeness of the particle forms (Figure 4.4). They noted that the nearness of the data from the different particle size to the crossover may tend to over emphasise differences that in reality are slight. Le Pen et al. (2013) concluded that although measurable variations in form and roundness occur with particle size over a range of sieve intervals, these differences are slight and do not rule out the use of scaled material in investigating the factors influencing macro-mechanical behaviour. This agreed with the findings of Sevi (2008).

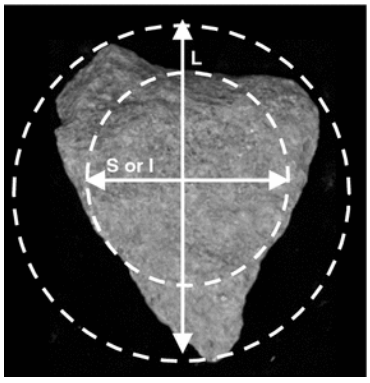

Figure 4.1: Form indicators

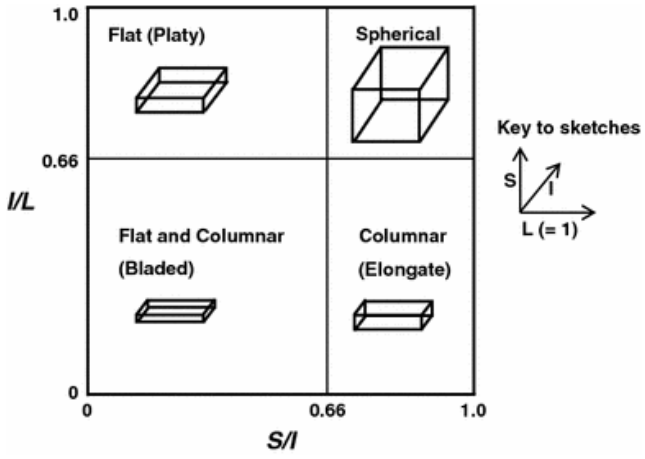

Figure 4.2: Zingg plot to characterize particle form (redrawn from Zingg (1935), alternative descriptors in brackets selected from Blott and Pye (2008)) (after Le Pen et al., 2013)

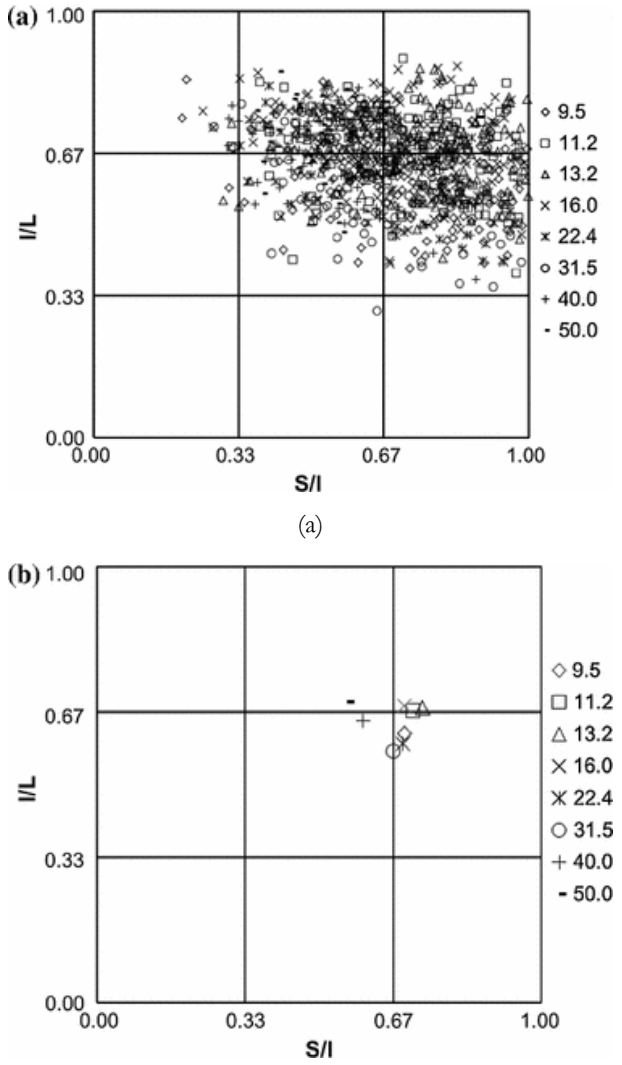

Figure 4.3: Zingg plots of all scalene ellipsoid equivalent sphericity (SEES) data for (a) individual particles (b) averages

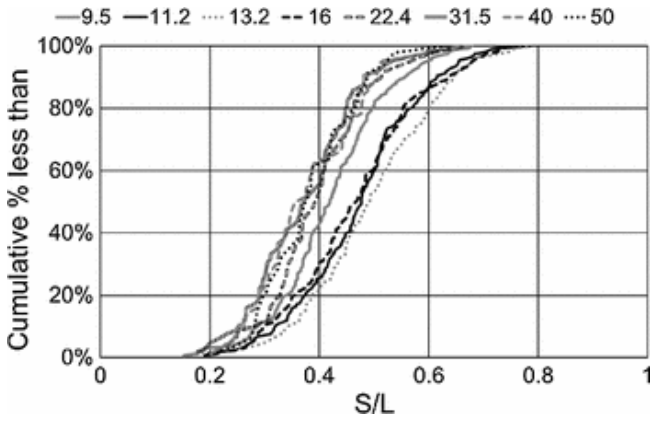

Figure 4.4: Cumulative distribution curves for S/L, the legend shows the catching sieves in mm

This chapter describes the methods used in carrying out monotonic triaxial tests on fibre reinforced granular materials (i.e. LB sand, 1/5 and 1/3 scaled ballast). It discusses the repeatability of triaxial tests on fibre reinforced specimens, and compares triaxial tests on dry and saturated 1/5 and 1/3 SB samples.

4.2 Monotonic Triaxial Test on reinforced LB sand

4.2.1 Test Apparatus

Triaxial tests were carried out on 100 mm diameter by 200 mm high specimens of dry reinforced sand in a Mini-dyn triaxial apparatus (GDS, 2014). The triaxial cell is screw-driven from an integral base unit housing the motor drive (Figure 4.5). Axial force and axial deformation are applied through the base of the cell and measured using a LVDT incorporated into the apparatus and an internal load cell. The triaxial tests were carried out on dry specimens open to the atmosphere and thus, with no application of back pressure.

(a) (b)

Figure 4.5: (a) Triaxial set up showing the Mini-dyn apparatus without sample (b) Deformed triaxial sample at the end of the test

4.2.2 Calibration and Data Logging

The load cell was calibrated using a dead-weight calibration system (*DH Budenberg* Ltd., 580-series hydraulic dead-weight tester). Data from the pressure controllers, load cell and axial displacement transducer were logged using commercially available software (GDS, 2014) every 10 seconds. Figure A1 in Appendix A shows the calibration results for the load cell used. The maximum error was ± 0.002 kN.

4.2.3 Test Procedure

The preparation of fibre reinforced specimens can be particularly challenging in terms of ensuring a random orientation and distribution of the fibres. The main challenge is avoiding segregation of the fibres. The specimen preparation process may be divided into two stages; mixing of fibres and sand in predetermined proportions to achieve an even and random distribution; and placing the mixture into the split mould at the desired density/void ratio.

The effect of adding fibres to sand has been discussed in Chapter 3. In the triaxial tests on sand, the fibre reinforced specimens were prepared at the same density index $I_D \approx 0.70$. This was achieved by taking into consideration the maximum and minimum void ratios at each volumetric fibre ratio (V_{fr}) as shown in Figure 3.6(a). The fibres used were polypropylene and the dimensions of each material and the test conditions are shown in the Table 4.1.

Known masses of fibres and sand were mixed by hand of the components in a tied transparent bag. This ensured that an adequate mix of the fibres and sand in the vertical and horizontal directions was achieved. The sand-fibre mixture was then carefully placed in the split mould in three layers so as to maintain the random orientation and even distribution of the fibres.

Table 4.1: Fibre properties used for triaxial test

	Fibre			**Density Index**	**Confining pressure (kPa)**	**Specimen dimensions dia. × ht. (mm)**
	Fibre length (mm)	Fibre width (mm)	Fibre thickness (mm)			
LB sand	23 – 47	1.5	~ 0.1	~ 0.70	20	100 × 200
1/3 Scaled ballast	50 - 150	10 - 20	~ 0.1	~ 1.00	30	150 × 300
1/5 Scaled ballast	10 - 100	10 - 50	~ 0.1	~ 1.00	30	150 × 300

The target void ratio of the specimen was achieved by gently tamping the mixture to a predetermined height corresponding to the required void ratio. The top cap was placed on the specimen and a vacuum of about 15 kPa applied to the specimen so that the spilt mould could be removed.

The triaxial cell was filled with de-aired water and the cell pressure was applied. During the application of cell pressure, the vacuum was slowly released to ensure that the total radial stress on the specimen did not exceed the required cell pressure. The relatively low radial stress used in the triaxial tests was to replicate the typical low confining stresses within ballast reported in the literature (e.g. Indraratna et al., 2010; Sevi and Ge, 2012). Specimens were sheared at a rate of 0.5 mm/min. This strain rate allowed adequate control of the cell pressure during shear deformation. Tests were stopped after an axial strain of about 18 % had been achieved.

4.2.4 Description of Parameters

Stress parameters

The axial stress is calculated (in kPa) as,

$$\sigma'_1 = \frac{Q}{A_{eff}} + \sigma_c \tag{4.1}$$

where Q is the ram load (in kN), A_{eff} (m^2) is the effective cross-sectional area of the specimen during shearing (m^2) and σ_c is the cell pressure (in *kPa*).

The A_{eff} of the specimen was calculated based on the assumption that the specimen remains a right circular cylinder during shearing and is given as,

$$A_{eff} = \frac{V_0 + \Delta V}{H_0 + \Delta H}$$

where V_0 and H_0 are the initial volume and height of the sample, and ΔV and ΔH are the measured changes in volume and height during shearing.

The radial stress is given by,

$$\sigma_3 = \sigma_c + \delta\sigma_r \tag{4.2}$$

where $\delta\sigma_r$ is the additional radial stress due to membrane deformation. The average additional radial stress due to the deformation of the membrane were calculated according to Fukushima (1984), method III:

$$\delta\sigma_r = \frac{2t_m\,\varepsilon_r\,E_m}{d} \tag{4.3}$$

- E_m is the membrane Young's modulus (1200 kPa). This value was calculated from extension tests carried out on strips of the rubber membrane used in the 150mm triaxial tests. The results of the extension tests are shown in Appendix A, Figure A3.
- t_m is the membrane thickness
- d is the current sample diameter calculated using A_{eff}
- ε_r is the sample radial strain

At the cell pressures (20 kPa for LB sand and 30 kPa for scaled ballast) used in this study, the additional radial stress on the samples at the end of shear deformation due to the membrane was typically found to be a maximum of 12 % of the applied confining pressure.

The mean effective stress, p', and deviator stress, q, are defined as follows:

$$p' = \frac{\sigma'_1 + 2\sigma'_3}{3} \tag{4.4}$$

$$q = \sigma'_1 - \sigma'_3 \tag{4.5}$$

Strain parameters

Axial strain (ε_a) was calculated as the change in height of the specimen in the axial direction divided by the initial height H_0 of the sample.

$$\varepsilon_a = \frac{\Delta H}{H_0}$$

Volumetric strain (ε_{vol}) is the change in volume of the specimen (measured by the cell pressure controller which measures the volume of the water going in and out of the cell while maintaining a constant pressure) divided by the initial specimen volume.

Radial strain (ε_r) is the change in specimen diameter calculated from the axial and volumetric strains.

$$\varepsilon_r = 0.5 \cdot \varepsilon_{vol} + \varepsilon_a \tag{4.6}$$

Other parameters

Secant Modulus (E_{secant}): the gradient of the line from the origin to any point on the deviator stress-axial strain curve.

Mobilised effective friction angle (φ'_{mob}): considering the Mohr-Coulomb criterion, the mobilised effective friction angle at any stage of shearing for a material with zero cohesion is given as,

$$Sin\phi'_{mob} = \frac{\sigma'_1 - \sigma'_3}{\sigma'_1 + \sigma'_3}$$

Rate of dilation (*d*):

$$d = -\left(\frac{\delta\varepsilon_{vol}}{\delta\varepsilon_s}\right)$$

where, $\delta\varepsilon_{vol}$ is the volumetric strain increment and $\delta\varepsilon_s$ is the triaxial shear strain increment defined as $\delta\varepsilon_s = 2/3\ \ \delta\varepsilon_a - \delta\varepsilon_r$.

4.2.5 Typical Test Results

Figure 4.6 shows the deviator stress and volumetric strain plotted against axial strain for one unreinforced and two reinforced sand specimens. The latter demonstrates the repeatability of the tests while the figure in general shows that the addition of fibres increases the peak deviator stress and reduces dilation compared with the unreinforced specimen.

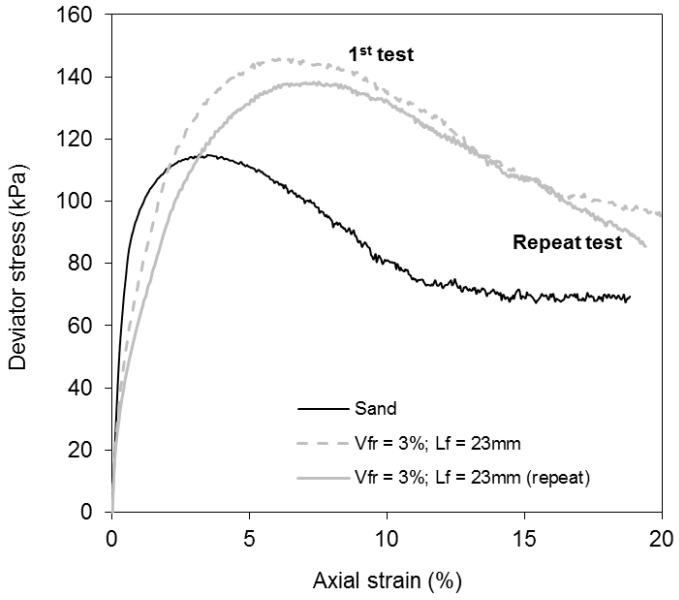

(a)

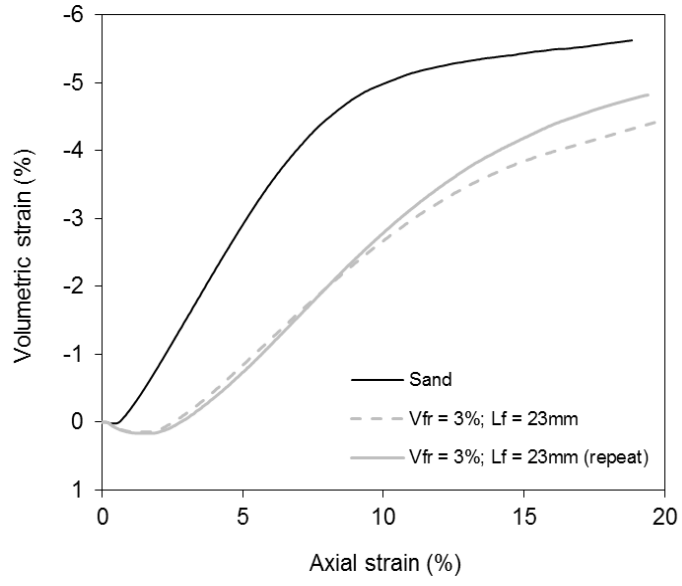

(b)

Figure 4.6: Typical plots of deviator stress and volumetric strain plotted against axial strain for unreinforced sand and reinforced sand specimens, tested dry at a cell pressure of 20 kPa

4.3 Monotonic Triaxial Tests on Scaled Ballast

4.3.1 Test Apparatus

Tests were carried out on a 150 mm diameter × 300 mm high specimen of scaled ballast using a strain-controlled triaxial apparatus (GDS, 2014). The set-up of the apparatus is similar to that described in Section 4.2.1: Global axial displacement was measured using a displacement transducer (LVDT) located on top of the triaxial cell while the axial force was measured by an internal load cell (Figure 4.7(a) and (b)). Local instrumentation was not attached to the specimens due to the erratic nature of measurements emanating from random movements of the relatively large particles and the fact that the strains for typical railway ballast tested to failure fall within the range that the global axial displacement transducer can reliably measure (Atkinson, 2000). A pressure transducer was attached to the cell pressure inlet to measure the cell pressure being applied to the specimen. Volume change was measured by the cell pressure controller.

To ensure that the applied axial load was transmitted vertically to the sample via the centre of the top platen, the top cap arrangement shown in Figure 4.8 was used. This arrangement also allows for sample misalignment during docking.

4.3.2 Calibration and Data Logging

The load cell and pressure transducer were calibrated using a dead-weight calibration system (*DH Budenberg* Ltd., 580-series hydraulic dead-weight tester). A micro-meter was used to calibrate the global axial LVDT. Data from the pressure controllers, load cell and axial displacement transducer were logged with a similar setup to that described in Section 4.2.2. The calibration results are shown in Appendix A (Figure A2). The maximum error for the axial displacement LVDT was ± 0.100 mm while the maximum errors of the cell pressure transducer and load cell were ± 0.70 kPa and ± 0.18 kN respectively. The resolution of the cell pressure controller was ± 0.1 kPa and the maximum variation in pressure recorded during shear deformation was ± 1.4 kPa.

4.3.3 Test procedure

Scaled ballast specimens (unreinforced and reinforced) were prepared at the densest state (approximately corresponding to e_{min}) for the volumetric fibre ratio (V_{fr}) being considered. For the sake of comparison, loose specimens of unreinforced 1/5 and 1/3 scaled ballast were also prepared. The variation in the maximum and minimum void ratios (e_{max} and e_{min}) of reinforced scaled ballast is shown in Figure 3.6(b). This implies that each test specimen will have different initial densities whose value will correspond to those given in Figure 3.6(b). Random fibre reinforced scaled ballast specimens were

prepared by hand-mixing a known mass of fibres in a plastic container (Figure 4.9(a)). This ensured that an adequate mix of the fibres and scaled ballast in the vertical and horizontal directions was achieved.

The scaled ballast-fibre mixture was then placed into a split cell mould lined with a rubber membrane in three layers. Each layer was compacted by gently tamping with a circular tamper and vibrating for two minutes under a surcharge of about 5 kg. The split mould containing the scaled ballast was then placed on the triaxial pedestal after which the top cap was placed on the specimen and a vacuum of about 15 kPa applied to the specimen so that the spilt mould could be removed (Figure 4.9(b) – (d)). This revised method for preparing scaled ballast triaxial specimens at maximum dry densities was necessitated by the requirement of preparing the specimen in a split mould. The use of standard Proctor hammer blows associated with the method described in Section 3.3.1 will damage the porous discs at the base of the split mould. However, this revised method produced comparable e_{min} values as shown in Table 5.3.

Before applying the cell pressure, the triaxial cell was filled with de-aired water. During the application of cell pressure, the vacuum was released gradually so as to ensure that the total radial stress on the specimen did not exceed the required cell pressure. The relatively low radial stress used in the triaxial tests was to replicate the typical low confining stresses within ballast reported in the literature (e.g. Indraratna et al., 2010; Sevi and Ge, 2012). Specimens were sheared at a rate of 0.05 mm/min and tests were stopped after an axial strain of about 15 % was achieved. This strain rate allowed close control of the cell pressure during shear deformation.

(a)

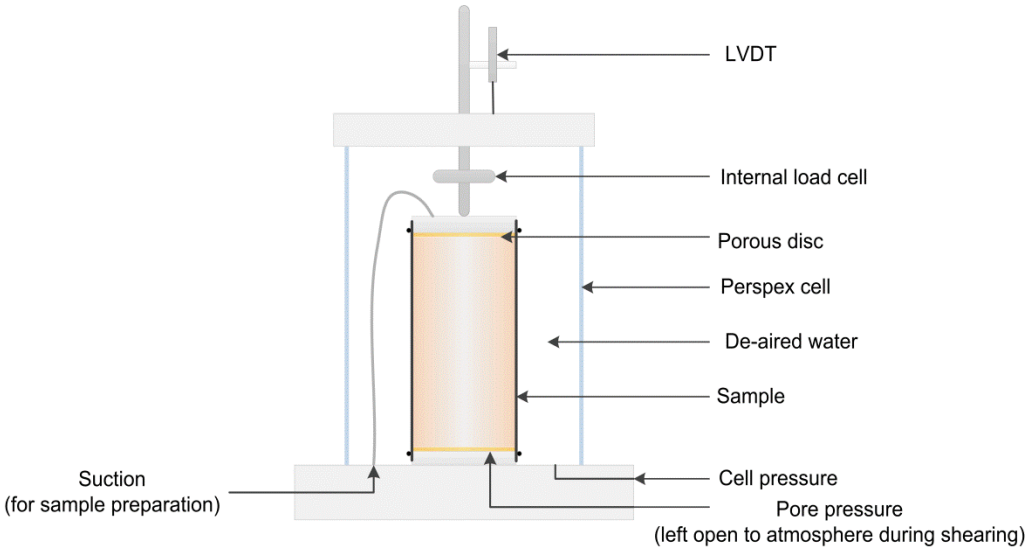

(b)

Figure 4.7: (a) Triaxial test setup before placement of cell showing scaled ballast sample under suction, computer and pressure controllers (b) schematic of triaxial test setup

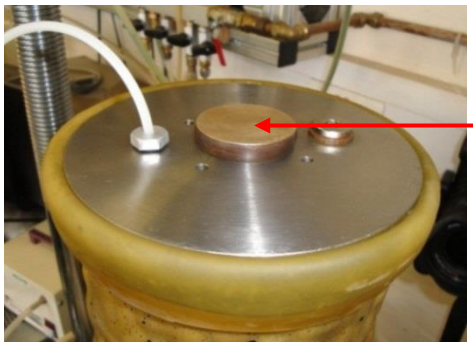

Figure 4.8: Specimen showing top cap arrangement

(a)

(b)

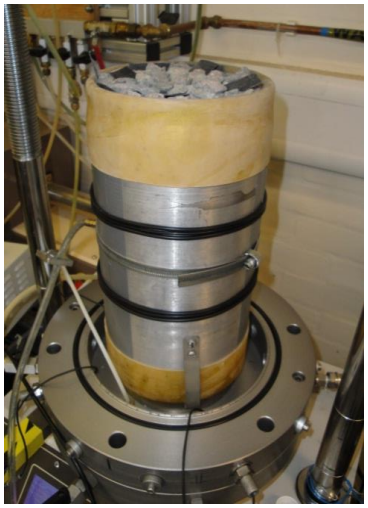

(c)

(d)

Figure 4.9: Fibre reinforced specimen preparation (a) Fibre and scaled ballast mixing (b) compaction (c) split mould containing fibre scaled ballast mixture placed on triaxial pedestal (d) scaled ballast triaxial specimen held under suction

4.3.4 Typical Test Results

Figure 4.10 shows that there is close agreement between the results of the triaxial tests on a dry and saturated 1/3 SB samples. Typical plots of the deviator stress and volumetric strain against axial strain for the unreinforced and reinforced 1/3 scaled ballast specimens are shown in Figure 4.11. The plots also show repeatability of the tests on reinforced specimens while the beneficial effect of the addition of fibres to scaled ballast can be observed in the higher peak strength exhibited by the reinforced specimen. The volumetric response of the unreinforced scaled ballast (1/3 SB) is typical of dense granular materials with the sample exhibiting initial compression and then dilation. The volumetric strain plot also shows that the addition of fibres appears to suppress dilation of the reinforced specimen compared with the unreinforced specimen. In neither specimen (i.e. reinforced and unreinforced), was there any indication of the test reaching the critical state. A plot of the stress ratio, q/p', and the volumetric strain against axial strain for both unreinforced 1/5 and 1/3 SB (Figure 4.12) shows close agreement in the mechanical behaviour at the two scales.

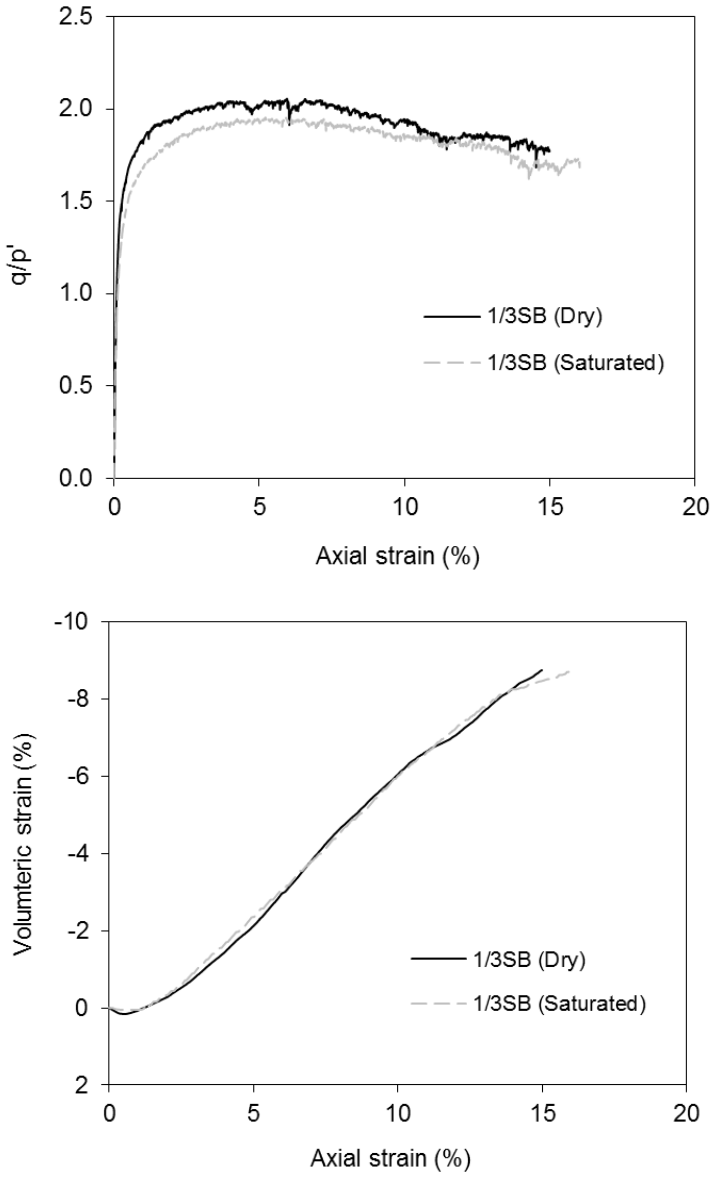

Figure 4.10: Comparison of triaxial test on dry and saturated 1/3 SB samples at an effective stress of 30 kPa

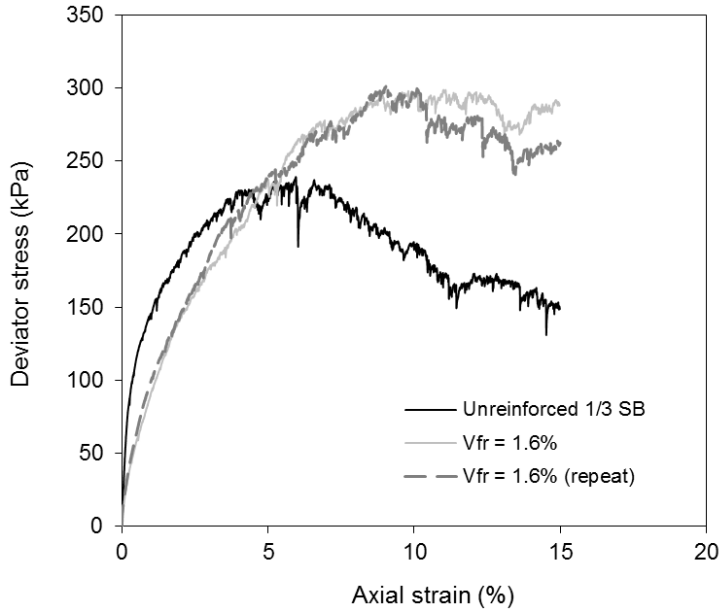

(a)

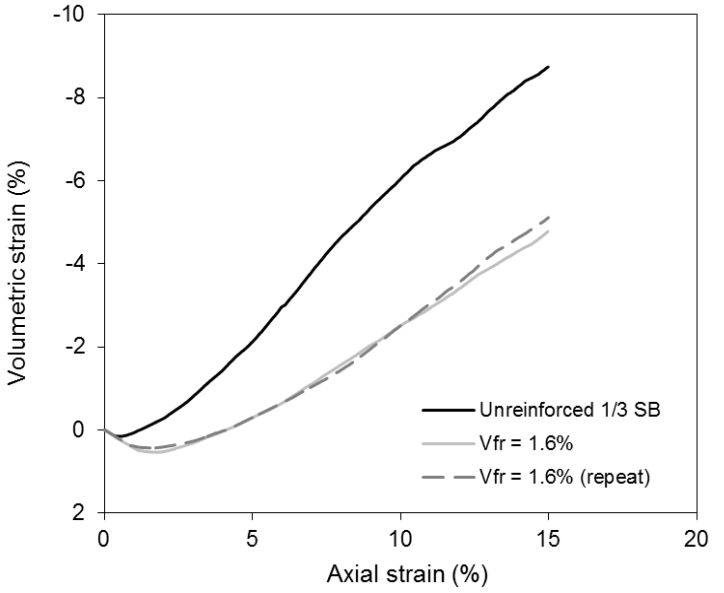

(b)

Figure 4.11: Typical plots of (a) deviator stress and (b) volumetric strain against axial strain for unreinforced and reinforced 1/3 scaled ballast specimens with V_{fr} = 1.6% showing the effects of the additional of fibres and repeatability of the triaxial tests on reinforced specimens. Cell pressure = 30 kPa

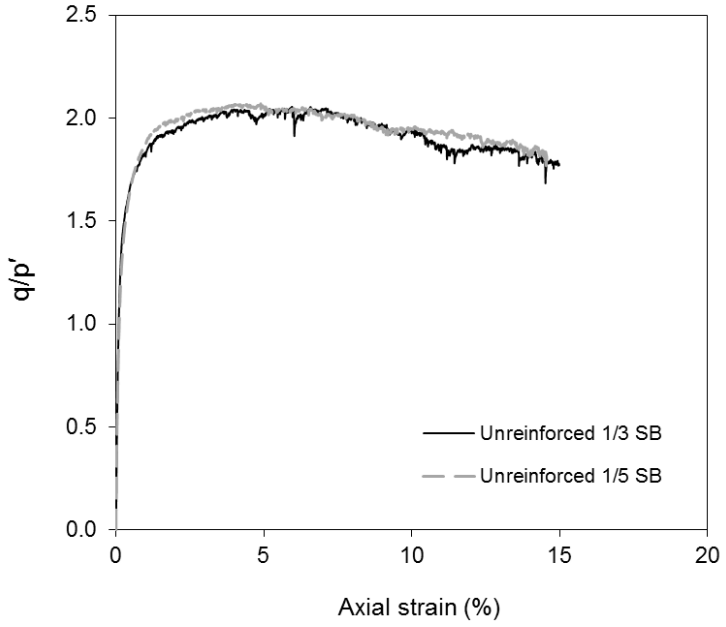

(a)

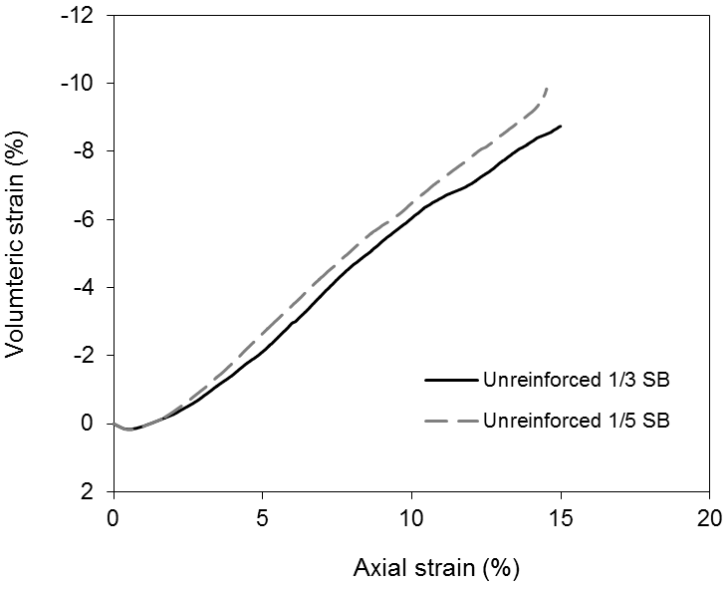

(b)

Figure 4.12: Comparison of triaxial tests on 1/5 and 1/3 SB samples (a) stress ratio, q/p' (b) volumetric strain. Cell pressure = 30 kPa

4.4 Conclusions

The apparatus and methods for performing monotonic triaxial tests on fibre reinforced LB sand, 1/5 and 1/3 scaled ballasts have been described in this chapter. The following conclusions can be drawn:

1. The addition of fibres in LB sand and scaled ballast specimens produced an increase in the peak deviator stress and suppresses dilation with good repeatability.
2. There is close agreement between the results of the triaxial tests on a dry and saturated 1/3 SB samples.
3. A plot of the stress ratio, q/p', and the volumetric strain against axial strain for both unreinforced 1/5 and 1/3 SB shows close agreement in the mechanical behaviour at the two scales.

Chapter 5

Monotonic Triaxial Tests on Granular Materials: Results and Analysis

5.1 Introduction

This chapter examines the mechanical behaviour of fibre reinforced granular materials (i.e. LB sand, 1/3 and 1/5 scaled ballast) in monotonic triaxial tests. Triaxial tests were carried out on LB sand to provide an initial comparison with previous research and to develop a fundamental understanding of the stress-strain behaviour of a fibre-reinforced soil under low confining stresses. For scaled ballast, triaxial tests were aimed at developing an understanding of the effect of relative fibre/particle dimensions on the mechanical behaviour of reinforced specimens and hence the mechanics of reinforcement in fibre reinforced granular materials.

The focus of the triaxial tests was generally limited to the study of the effects of fibre reinforcement on the initial stiffness, mobilised peak strength and volumetric response of fibre reinforced LB sand and scaled ballast. No measurable particle breakage was observed, thus the effect of reinforcements on particle breakage was not investigated.

5.2 Leighton Buzzard Sand

Peak Strength and Volumetric Behaviour

A summary of the triaxial tests performed is presented in Table 5.1. Figures 5.1 and 5.2 show that the reinforced LB sand specimens exhibited a significant improvement in peak mobilised strength as V_{fr} and L_f increased. In general, the addition of fibres delayed the mobilisation of peak strength until larger axial strains had occurred, and extended the range of axial strain over which the peak strength was maintained. The reinforced specimens also exhibited reduced post-peak loss of strength compared with the unreinforced specimens. The addition of fibres suppressed dilation, an effect that

appears to become more pronounced with increasing V_{fr}. Varying L_f did not seem to influence dilation (Figure 5.2). Initial compression was more pronounced in the reinforced specimens, probably due to the increase in the macro-voids in the reinforced specimen as a result of the effect of the fibres on packing.

Table 5.1: Fibre content and fibre lengths used in the triaxial tests on LB sand

V_{fr} (%)	0	0.2	0.2	1.8	1.8	3.0	3.0	4.5	4.5
L_f (mm)	-	23	47	23	47	23	47	23	47

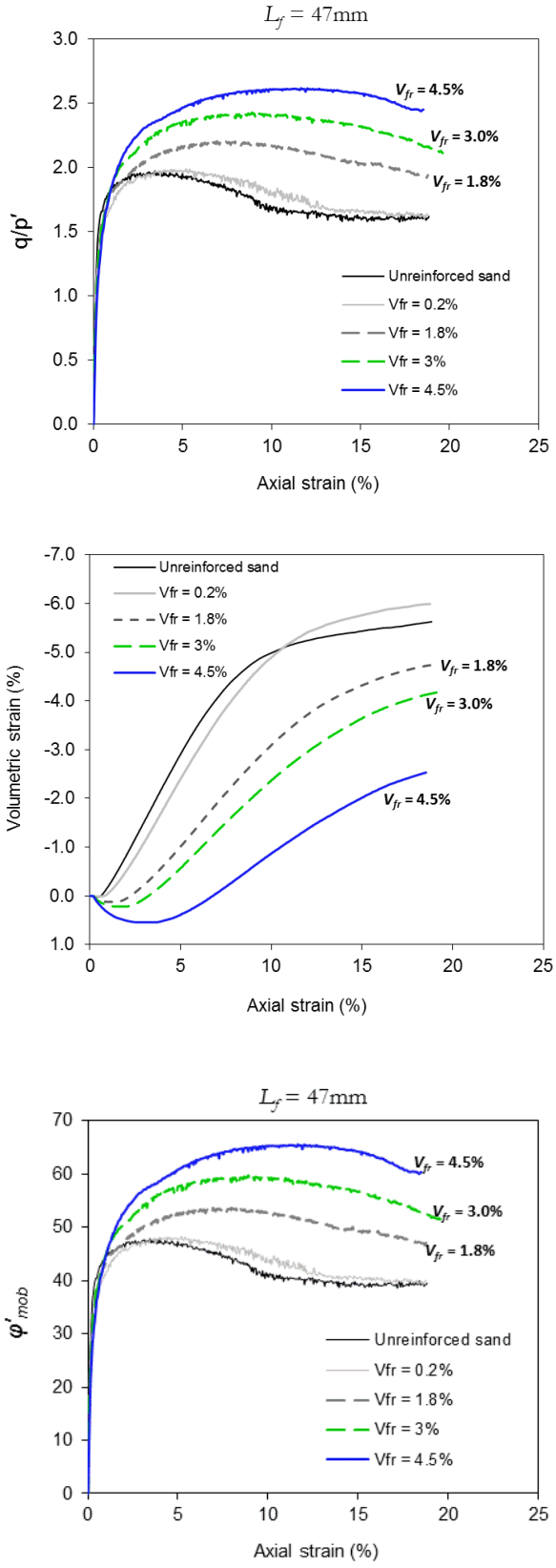

Figure 5.1: Effect of varying V_{fr} on the stress ratio, q/p', mobilised angle of friction, φ'_{mob} and volumetric strain of reinforced LB sand at cell pressure = 20 kPa

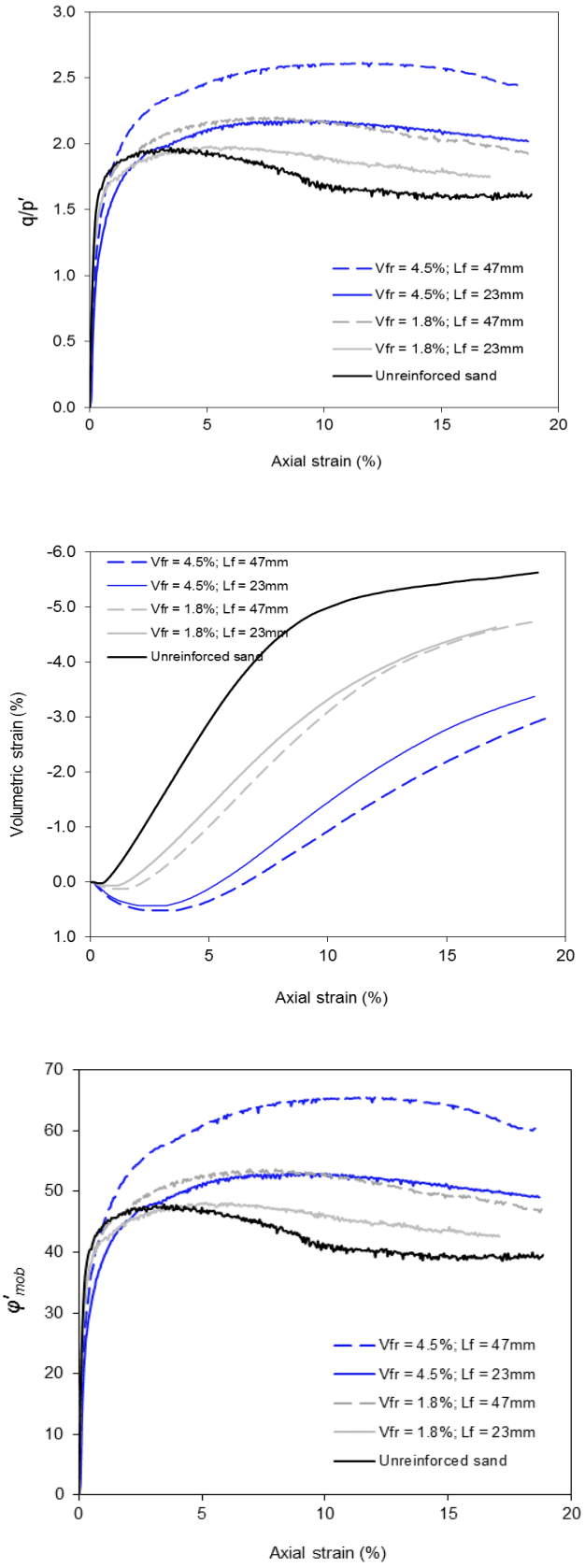

Figure 5.2: Effect of varying L_f on the stress ratio, q/p', mobilised angle of friction, φ'_{mob} and volumetric strain of reinforced LB sand at cell pressure = 20 kPa

Stress-dilatancy

Figures 5.3 and 5.4 confirm the inhibiting effect of fibre reinforcements on the dilation of the reinforced LB sand specimen. The maximum rate of dilation of all LB sand specimens tested coincided with the maximum stress ratio as expected in granular materials. The plots also show the effects of varying V_{fr} and L_f on the stress-dilatancy; the stress ratio when $d = 0$ (i.e. the onset of dilation) and the corresponding mobilised friction angle (i.e. φ'_{dil}) are shown in Table 5.2.

Radial strain

In the reinforced sand specimens, less radial strain (reduced radial expansion) was observed compared with the unreinforced specimens at axial strain greater than 1% (Figure 5.5). The smaller dilation and radial strain exhibited by the reinforced specimens might be due to the apparent confinement of the soil grains by the fibres. The addition of fibres tends to lock the sand grains and hence inhibit lateral movement of the particles. Diambra et al. (2007) reported that the preferred orientation of fibre reinforced specimens are typically within $\pm \pi/4$ of the horizontal plane. This might have contributed to the reduced radial strain of the reinforced specimens.

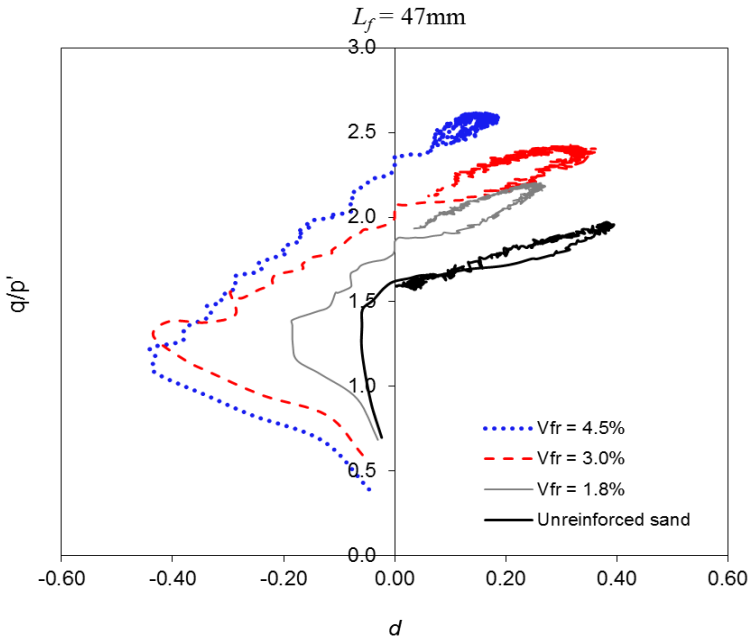

Figure 5.3: Effects of V_{fr} with constant L_f on the stress-dilation relationship of reinforced and unreinforced sand specimens

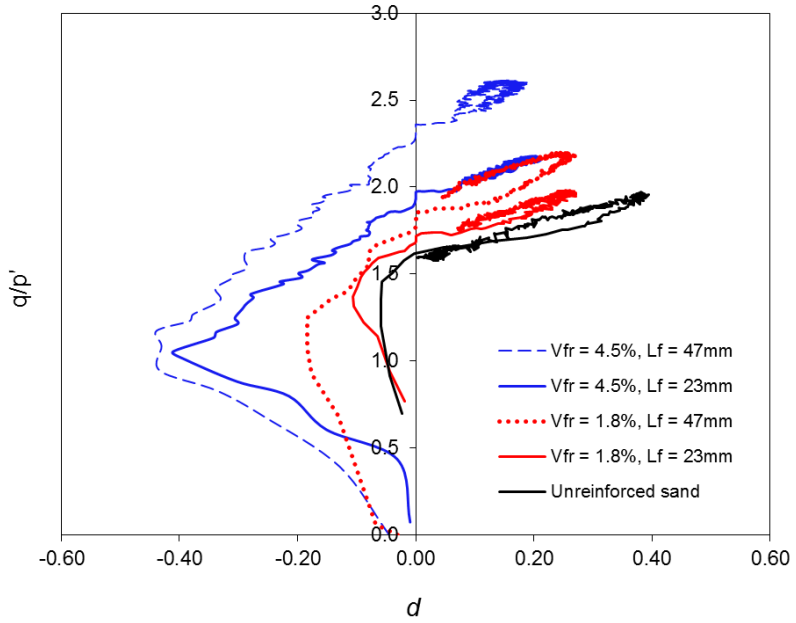

Figure 5.4: Effects of varying V_{fr} and L_f on the stress-dilation relationship of reinforced and unreinforced sand specimens

Table 5.2: Effect of varying V_{fr} and L_f on the stress ratio at $d = 0$, M and the mobilised friction angle at the onset of dilation, φ'_{dil}

Material	L_f(mm)	M	φ'_{dil}(°)	$\frac{\Delta\, q/p'}{\Delta d}$
Unreinforced LB sand	-	1.61	39.42	0.85
V_{fr} = 1.8%	23	1.71	41.65	0.96
V_{fr} = 1.8%	47	1.83	44.63	1.46
V_{fr} = 3.0%	47	2.08	44.76	1.02
V_{fr} = 4.5%	23	1.95	47.38	1.08
V_{fr} = 4.5%	47	2.33	57.05	1.66

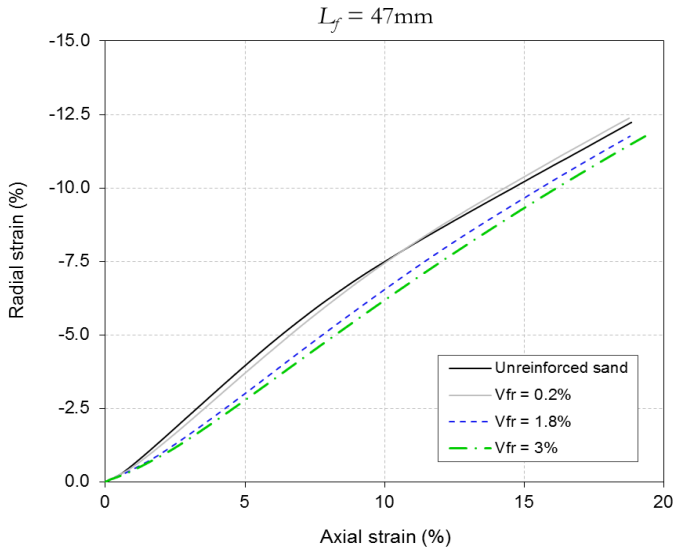

Figure 5.5: Effect of fibre reinforcement on the radial strain of reinforced and unreinforced sand specimens

5.3 Scaled Ballast

Mobilised Strength and Volumetric Behaviour

To investigate the effects of fibre reinforcement across two scales of ballast (i.e. 1/5 and 1/3 SB), the triaxial tests are reported hereafter in terms of relative fibre/particle dimensions. The relative dimensions are referred to as the normalized length, width and thickness (L_N and W_N respectively), given by,

$$L_N = \frac{L_f}{D_{50}} \qquad W_N = \frac{W_f}{D_{50}}$$

where L_f = fibre length, W_f = fibre width and D_{50} = median particle size of the granular medium (i.e. 1/5 and 1/3 SB). The normalized dimensions of the materials used in the triaxial tests are presented in Table 5.3.

In both 1/5 and 1/3 SB reinforced specimens, there is a general increase in peak mobilised friction angle as V_{fr} increases while the mixture also becomes more ductile as indicated by the reduction in the post-peak strength loss (Figure 5.6 and 5.7). Figure 5.8 and 5.9 show the beneficial effect of increasing L_N and W_N while V_{fr} is kept constant. Li and Zornberg (2013) suggested that the shear strength at large strains (rather than the peak shear strength) of the soil matrix defines the contribution of the soil matrix to the equivalent shear strength of fibre reinforced soils. To highlight the effects of L_N and W_N on the mobilised strength of the mixture, a parameter $T\varphi'_{mob}$ is adopted,

$$T\varphi'_{mob} = \frac{tan\varphi'_{reinforced_{\varepsilon_{shear}}}}{tan\varphi'_{unreinforced\varepsilon_{shear}}} - 1 \quad (5.1)$$

where is the normalised mobilised friction angle, $\varphi'_{\text{reinforced}}$ is the mobilised friction angle of the reinforced granular material at a given shear strain, $\varphi'_{\text{unreinforced}}$ is the mobilised friction angle of the unreinforced material at a given shear strain.

$T\varphi'_{mob}$ has the advantage of accounting for the mobilised effective friction angle with respect to the magnitude of the shear strain of the specimen in question. It also approximately isolates the effects of the mobilisation of the tensile force in the fibres on the macro-mechanical behaviour of the specimen from other possible influencing factors (e.g. initial packing of the reinforced specimens). For an unreinforced sample, $T\varphi'_{mob} = 0$ at any given shear strain while $T\varphi'_{mob} \neq 0$ for reinforced samples, hence indicating the magnitude of change in the mobilised friction angle. Figures 5.11 and 5.12 suggests that the magnitude of the mobilised tensile force in each individual fibres in a granular matrix at large shear strains depends on both L_N and W_N. Figure 5.11 also indicates that for significant improvement in the mobilised friction angle of reinforced specimens, $L_N \geq 7$.

Similar to the observation with fibre reinforced sand, fibre reinforced scaled ballast (FRSB) exhibited reduced volumetric strain compared with the unreinforced specimen. This corroborates the findings of Michalowski and Cermak (2003) and Dos Santos et al. (2010). Diambra et al. (2013) however reported an increase in the dilation of fibre reinforced sand. They argued that this was a consequence of an apparent densification of the granular matrix due to the presence of fibres in the voids. This fundamental difference is considered to be an an inevitable consequence of the specimen preparation method employed by Diambra et al. (2013). In preparing triaxial specimens, Diambra et al. (2013) considered a constant volume of specimen and mass of sand while the fibre content was increased. To make the sand-fibre mixture fit into the specimen volume, the compactive effort was increased as the fibre content increased so that the specimens were prepared approximately in different ways. This produced denser reinforced specimens as the void ratio decreases towards the minimum value for the unreinforced sand. The specimen preparation method adopted in this research produced fibre reinforced specimens with relatively higher void ratios when compared to the unreinforced specimen.

It can also be observed that the initial compression and the general volumetric response of a reinforced specimen is more dependent on increases in V_{fr} than in L_N and W_N (Figure 5.6 – 5.10). This is probably due to the impact of V_{fr} on the structural packing of the mixture as discussed in Chapter 3.

Table 5.3: Triaxial test conditions, normalised dimensions of the fibres and grains used and fibre/particle numbers for triaxial test on 1/5 and 1/3 SB specimens

Granular medium	D_{50} (mm)	Test name	V_{fr} (%)	e_o	L_f (mm)	W_f (mm)	L_N	W_N	Avg. N_p	N_f	N_{fp} (%)
		T5D	-	0.74	-	-	-	-			
		T5L	-	0.89	-	-	-	-			
1/5 SB	8	T51	1.6	0.82	58	12	7.1	1.4	10743	138	1.28
		T52	1.6	0.84	58	20	7.1	2.5	10838	82	0.76
		T53	3.2	0.89	58	20	7.1	2.5	10270	146	1.42
		T54	6.5	0.98	58	20	7.1	2.5	9660	281	2.91
		T3D	-	0.76	-	-	-	-			
		T3L	-	0.87	-	-	-	-			
		T31	1.6	0.79	50	35	3.6	2.5	2044	54	2.64
1/3 SB	14	T32	1.6	0.80	100	10	7.1	0.7	2024	96	4.74
		T33	1.6	0.80	100	20	7.1	1.4	2032	48	2.36
		T34	1.6	0.79	100	35	7.1	2.5	2026	27	1.33
		T35	3.2	0.91	100	35	7.1	2.5	1892	57	3.01

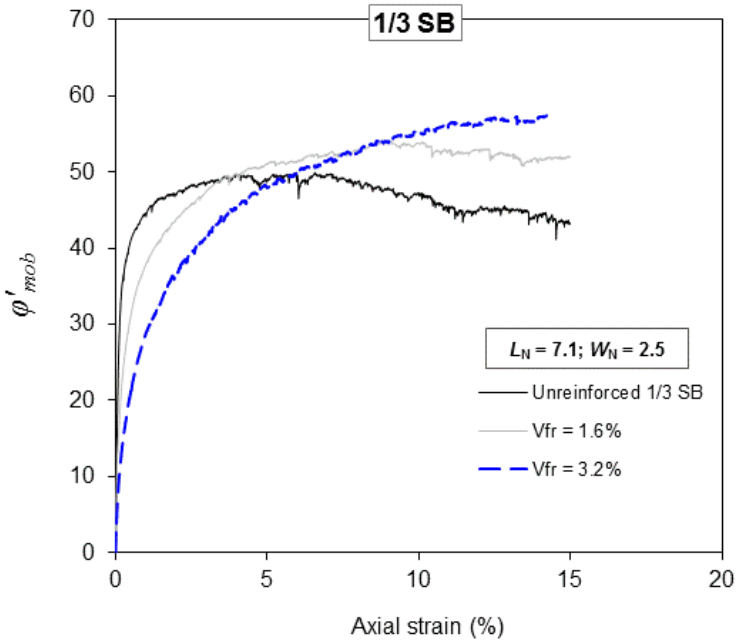

(a)

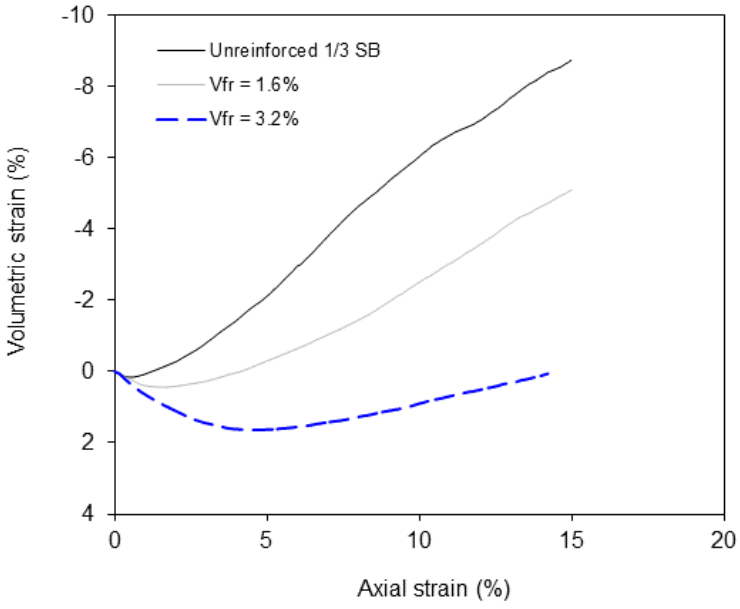

(b)

Figure 5.6: Effect of increasing V_{fr} when L_N = 7.1 and W_N = 2.5 on (a) the effective friction angle (b) volumetric strain for reinforced 1/3 SB at a cell pressure of 30 kPa

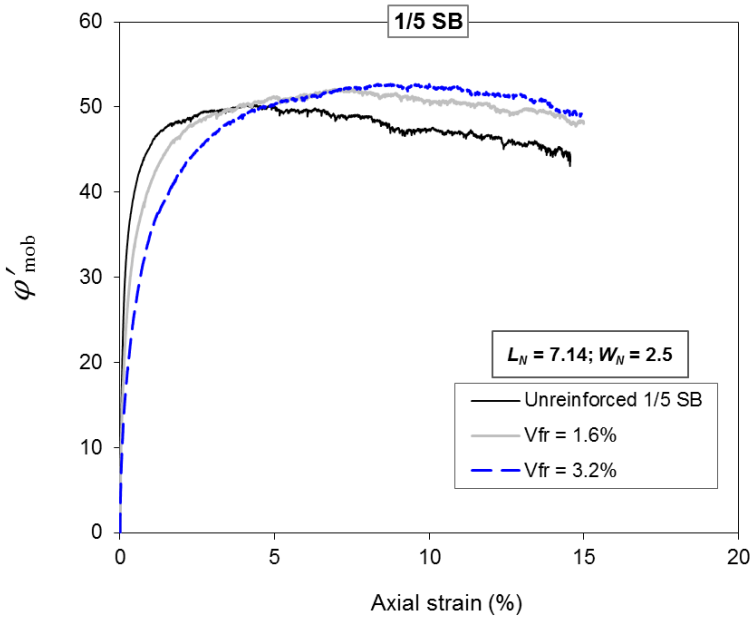

(a)

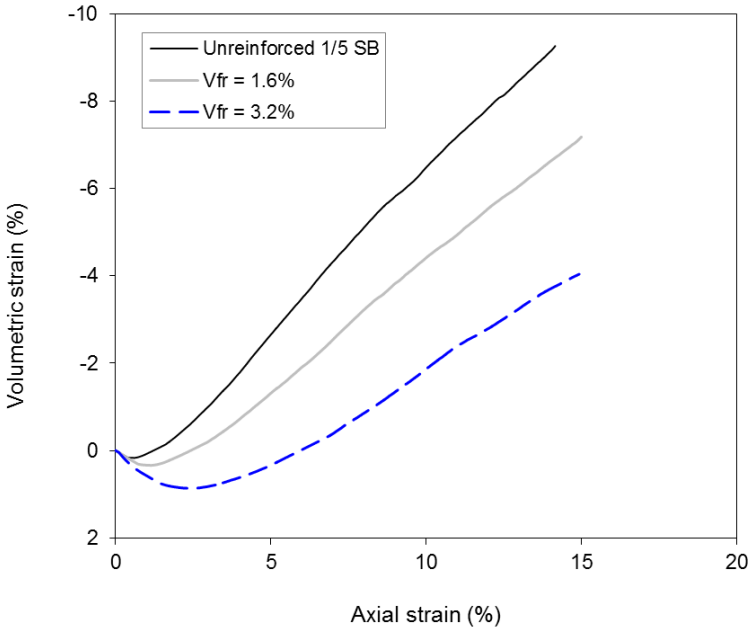

(b)

Figure 5.7: Effect of increasing V_{fr} when L_N = 7.1 and W_N = 2.5 on (a) the effective friction angle (b) volumetric strain for reinforced 1/5 SB at a cell pressure of 30 kPa

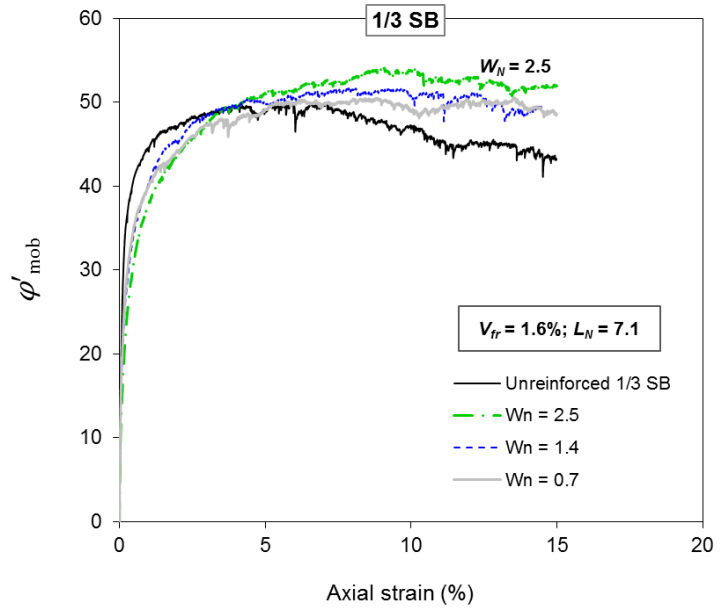

(a)

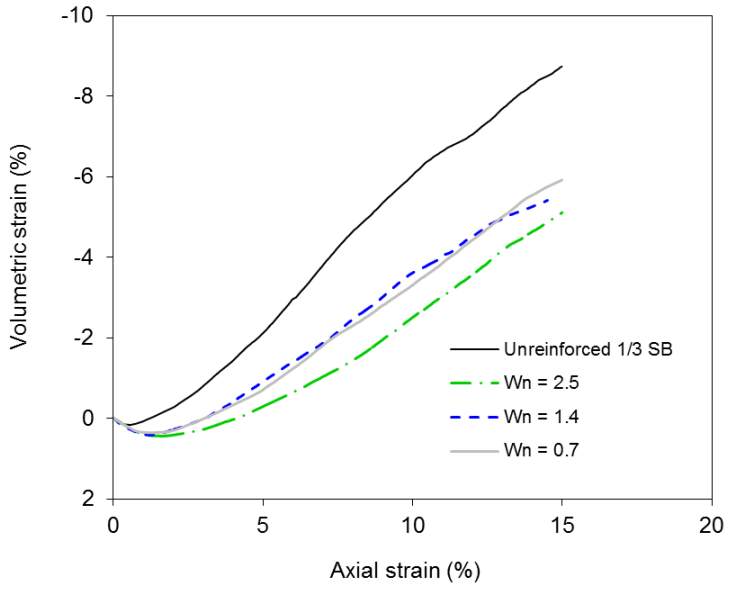

(b)

Figure 5.8: Effect of increasing W_N when V_{fr} = 1.6% and L_N = 7.1 on (a) the effective friction angle (b) volumetric strain for reinforced 1/3 SB at a cell pressure of 30 kPa

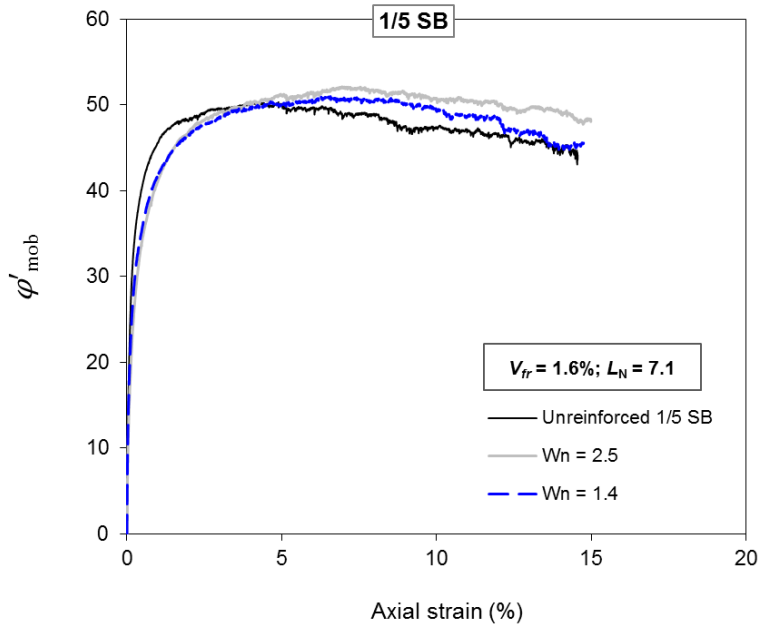

(a)

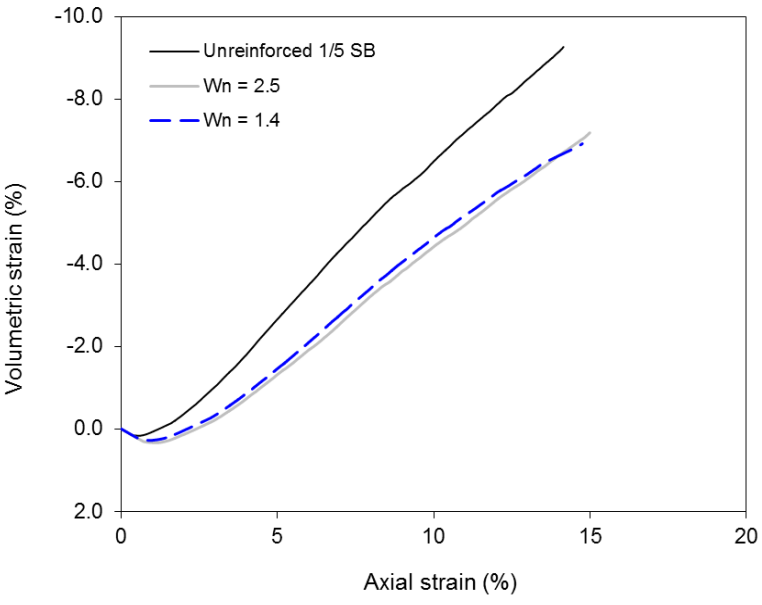

(b)

Figure 5.9: Effect of increasing W_N when V_{fr} = 1.6% and L_N = 7.1 on (a) the effective friction angle (b) volumetric strain for reinforced 1/5 SB at a cell pressure of 30 kPa

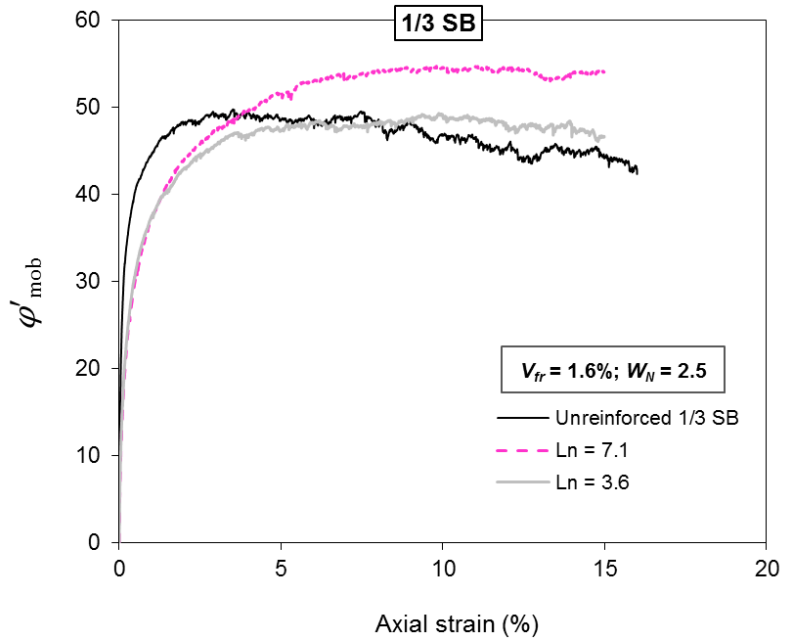

(a)

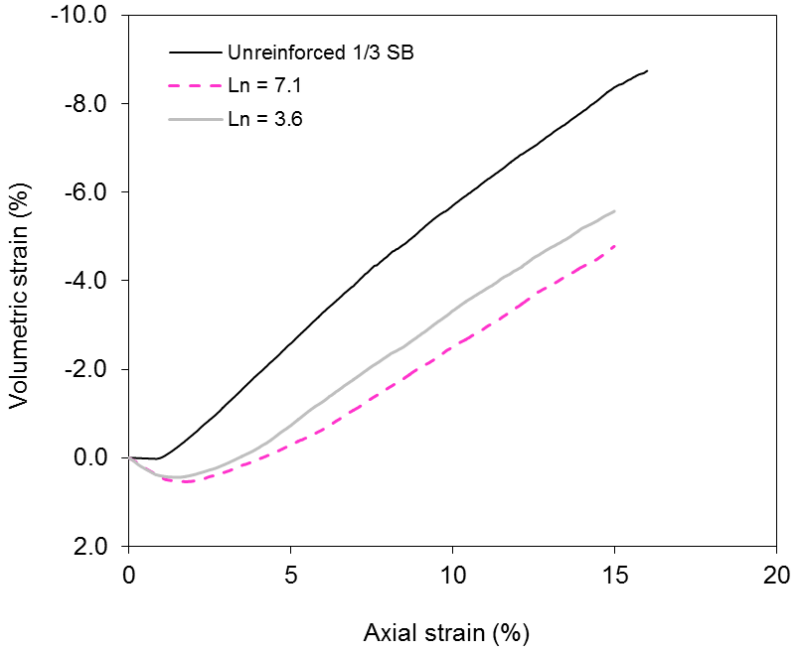

(b)

Figure 5.10: Effect of increasing L_N when V_{fr} = 1.6% and W_N = 2.5 on (a) the effective friction angle (b) volumetric strain for reinforced 1/3 SB at a cell pressure of 30 kPa

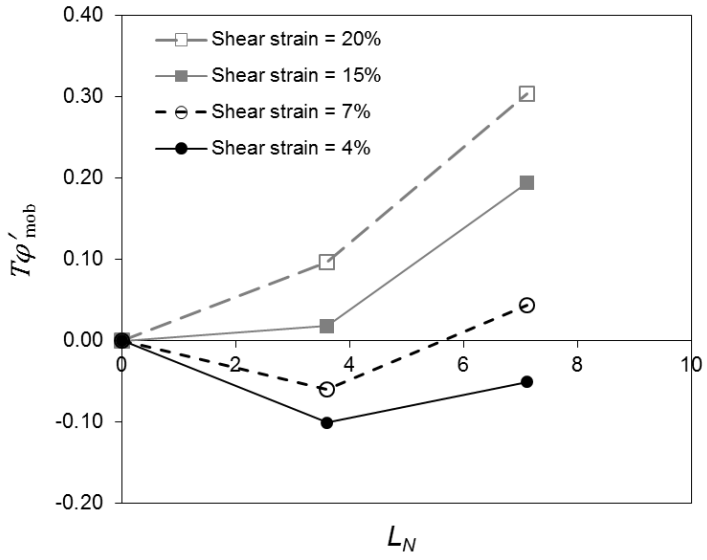

Figure 5.11: Effects of varying L_N on the $T\varphi'_{mob}$ of reinforced 1/3 SB specimens with W_N = 2.5 and V_{fr} = 1.6% at different shear strains

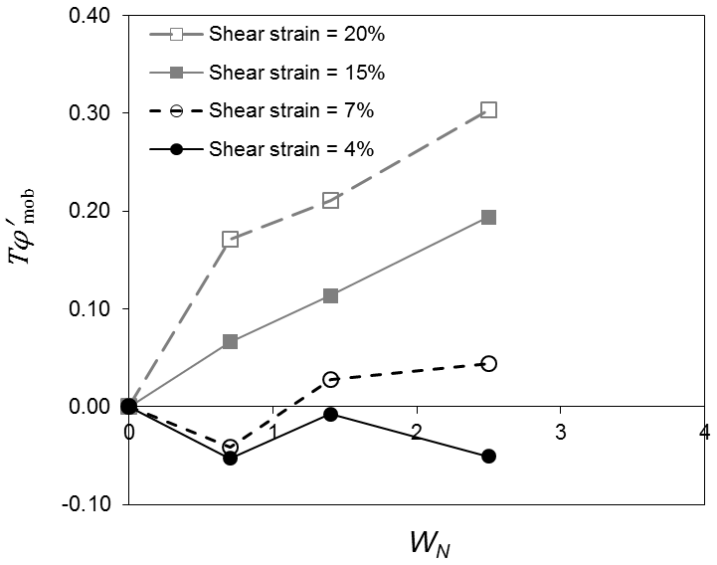

Figure 5.12: Effects of varying W_N on the $T\varphi'_{mob}$ of reinforced 1/3 SB specimens with L_N = 7.1 and V_{fr} = 1.6% at different shear strains

Stress-dilatancy

Owing to the slightly noisy nature of the stress-strain plots (e.g. Figure 4.11), the raw data were smoothed using the moving average filter technique implemented in MATLAB (Figure 5.13). The moving average filter smooths data by replacing each data point with the average of the neighbouring data points defined within the span. The response of the smoothing is given by

$$y_s\ i\ = \frac{1}{2N+1}\left(y\ i+N\ + y\ i+N-1\ +\ldots+y\ i-N\ \right) \tag{5.2}$$

where $y_s(i)$ is the smoothed value for the ith data point, N is the number of neighbouring data points on either side of $y_s(i)$, and $2N+1$ is the span.

Figures 5.14 – 5.16 shows the effect of V_{fr}, L_N and W_N on the stress ratio-dilatancy relationships of the reinforced specimens. For comparison, the rates of dilation of unreinforced Dense and Loose 1/3 SB specimens are also included. To emphasize the effect of fibre reinforcements on dilation, the compression areas (i.e. when $d < 0$) of the plots have been removed and a line of the form $q/p' = \beta d + M$ (where α is the rate of increase of stress ratio with rate of dilation, and M is the stress ratio when $d = 0$) fitted through the data points as shown in Figure 5.14(b) – 5.16(b) and Table 5.4 – 5.6. The plots show that at a given rate of dilation, the mobilised strength is generally greater in fibre reinforced specimens. In addition, Figure 5.15(b) and 5.16(b) suggests that the relative fibre/particle dimensions influence the rate of increase of mobilised strength with rate of dilation, β.

Table 5.4: Effect of V_{fr} on the rate of increase of mobilised strength with rate of dilation, β and stress ratio at $d = 0$, M when $L_N = 7.1$ and $W_N = 2.5$

Material	β	M	R^2	φ'_{dil}(°)
Unreinforced Dense 1/3 SB	0.94	1.68	0.90	41.01
Unreinforced Loose 1/3 SB	0.79	1.59	0.92	38.87
V_{fr} = 1.6%	1.70	1.74	0.90	42.49
V_{fr} = 3.2%	1.91	1.94	0.91	47.25

Table 5.5: Effect of L_N on the rate of increase of mobilised strength with rate of dilation, β and stress ratio at $d = 0$, M when $V_{fr} = 1.6\%$ and $W_N = 2.5$

Material	β	M	R^2	φ'_{dil}(°)
$L_N = 3.6$	1.13	1.64	0.93	40.21
$L_N = 7.1$	1.70	1.74	0.90	42.49

Table 5.6: Effect of W_N on the rate of increase of mobilised strength with rate of dilation, β and stress ratio at $d = 0$, M when $V_{fr} = 1.6\%$ and $L_N = 7.1$

Material	β	M	R^2	φ'_{dil}(°)
$W_N = 0.7$	1.16	1.70	0.97	41.61
$W_N = 2.5$	1.70	1.74	0.90	42.49

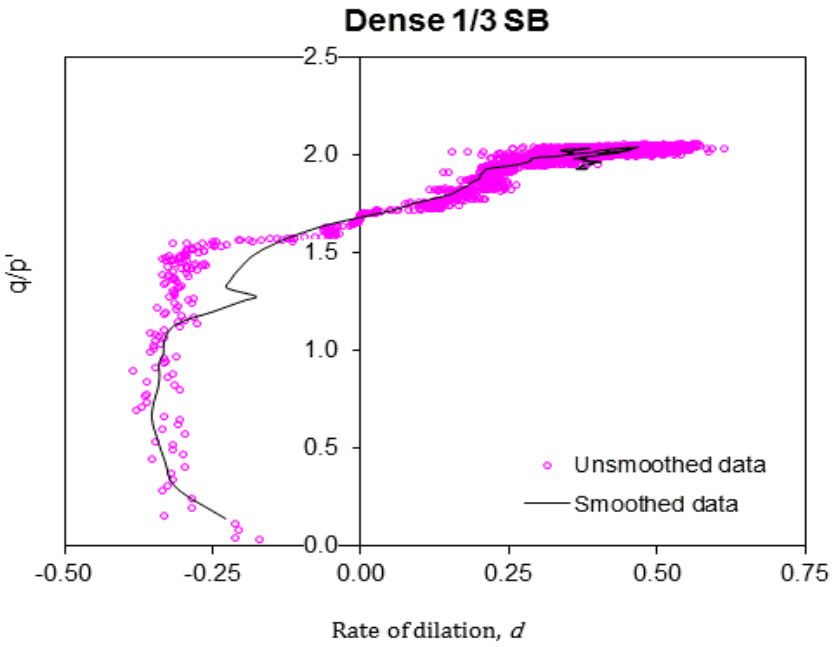

Figure 5.13: Data smoothening for Dense 1/3 SB sample

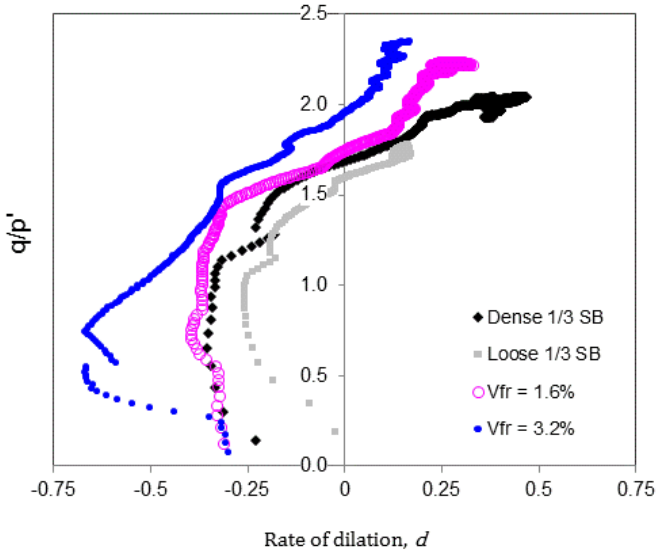

(a)

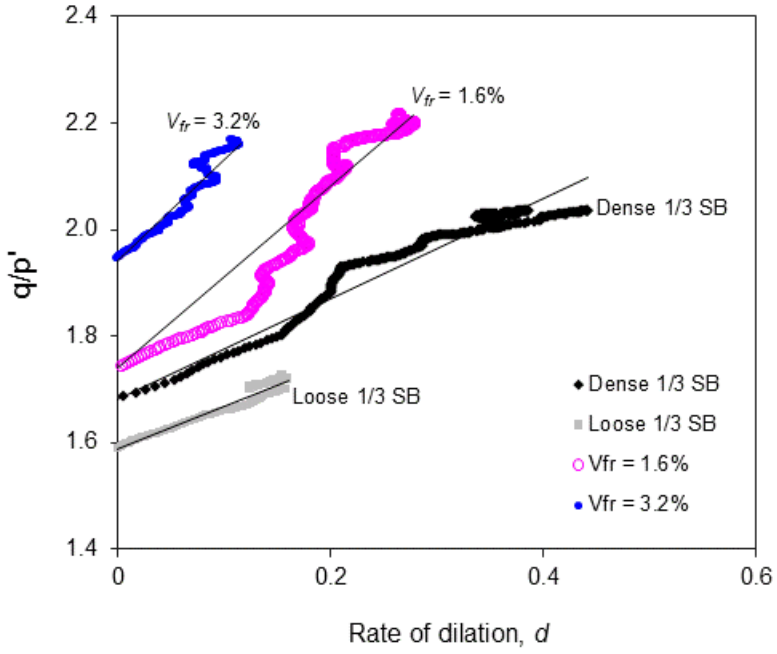

(b)

Figure 5.14: Effects of V_{fr} on the rate of dilation, d, of 1/3 SB specimens while L_N = 7.1 and W_N = 2.5 (a) whole test, (b) when $d \geq 0$

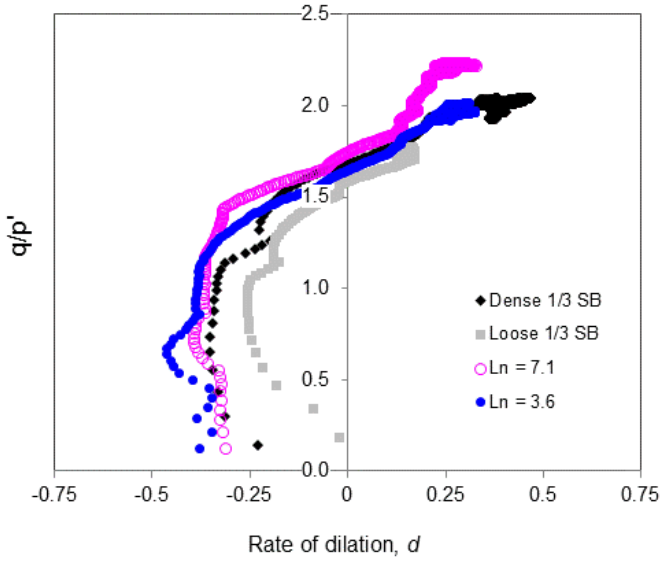

(a)

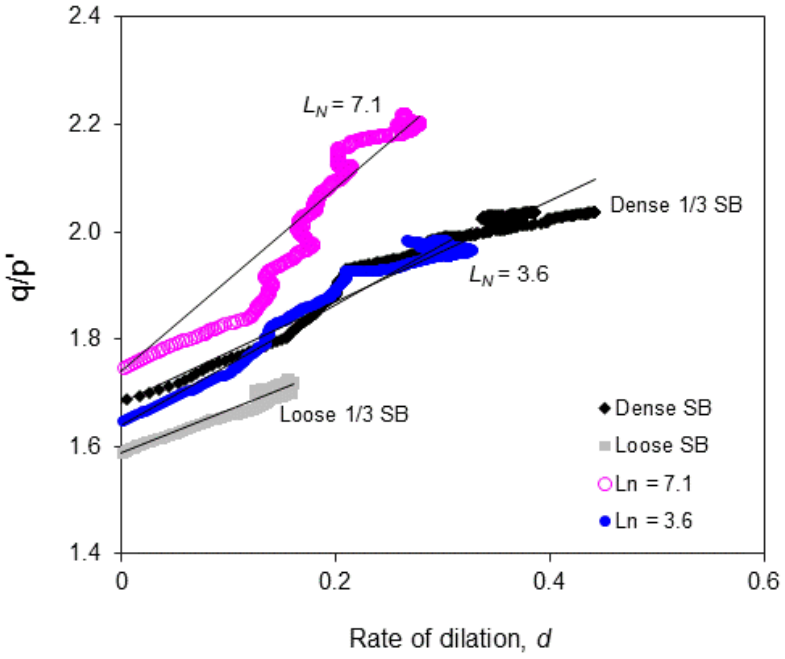

(b)

Figure 5.15: Effects of L_N on the rate of dilation, d of 1/3 SB specimens while V_{fr} = 1.6% and W_N = 2.5 (a) whole test, (b) when $d \geq 0$

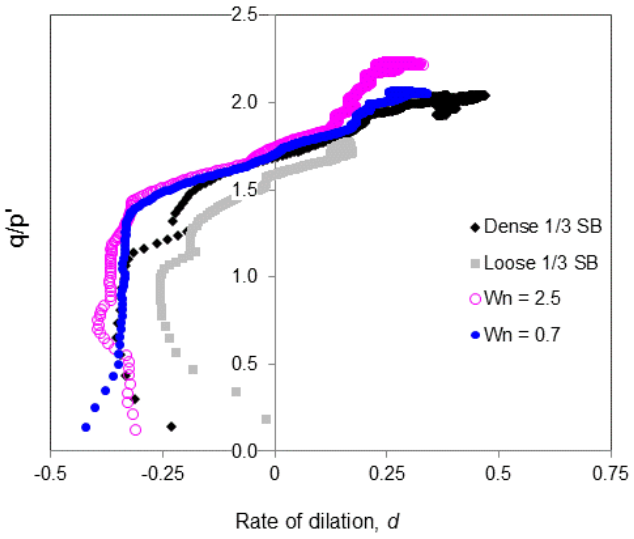

(a)

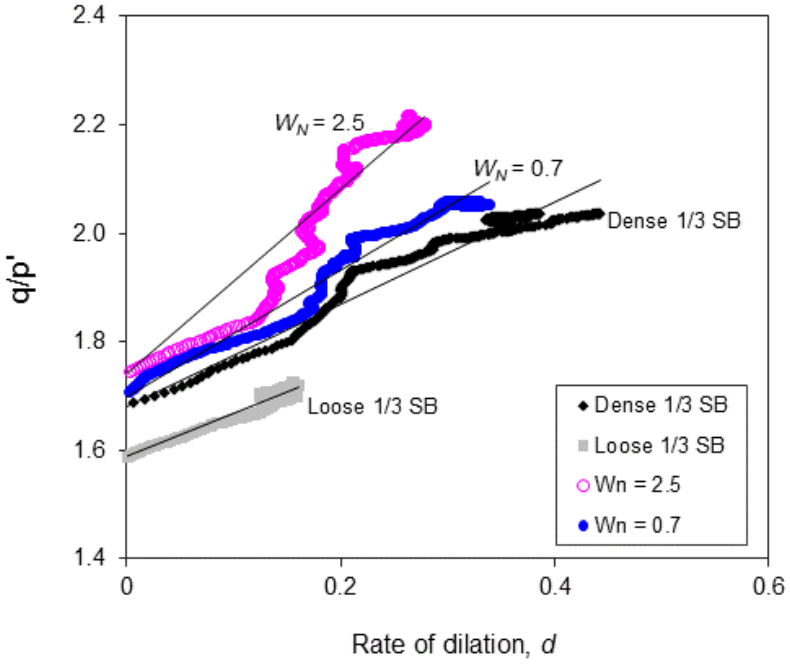

(b)

Figure 5.16: Effects of W_N on the rate of dilation, d of 1/3 SB specimens while L_N = 7.1 and V_{fr} = 1.6% (a) whole test, (b) when $d \geq 0$

Initial stiffness

The stiffness (described by the secant modulus, E_{secant}) degradation curves for the unreinforced 1/3 SB Dense and Loose specimens and reinforced specimens are shown in Figures 5.17 – 5.19. As would be expected, the stiffness of the Loose 1/3 SB specimen is lower than that of the Dense specimen. The stiffness of the reinforced specimens appears not to be significantly influenced by L_N, although it is less than the stiffness of both Loose and the Dense 1/3 SB specimens (Figure 5.17). The stiffness of the mixture is decreased by increasing V_{fr} (Figure 5.19). this could be due to the higher initial void ratios of fibre reinforced specimens (Figure 3.6(b)). Also, an increase in W_N reduces the stiffness of the reinforced specimens (Figure 5.18).

The adverse effect of increasing fibre content on the stiffness of a fibre reinforced granular material has been reported by previous researchers (e.g. Michalowski and Cermak, 2003; Heineck et al., 2005; Diambra et al., 2010). This behaviour has been attributed to the non-homogeneity of the void distribution within the specimen. However, the effect of the relative fibre/particle dimensions has never been investigated. The results presented in Figure 5.17 and 5.18 suggest that fibre content (V_{fr}) is not the only possible influence on the initial stiffness of fibre reinforced granular materials. The difference in behaviour can be explained by the micro-mechanics of the fibre/particle interaction. Mitchell and Soga (2005) suggested that between the pre-yield and full plastic yield zones, volume changes exhibited by granular materials depend on the interactions between fabric and stress state and the propensity for shear deformation without overall volume change. This highlights the importance of the fibre reinforcment mechanism which will be disscused further in Section 5.5.

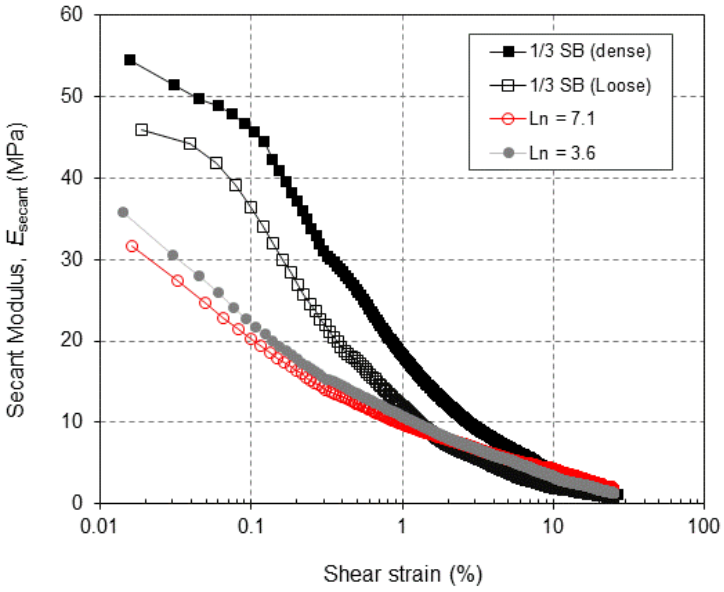

Figure 5.17: Effect of L_N on Secant Modulus, E_s of fibre reinforced 1/3 SB with V_{fr} = 1.6% and W_N = 2.5

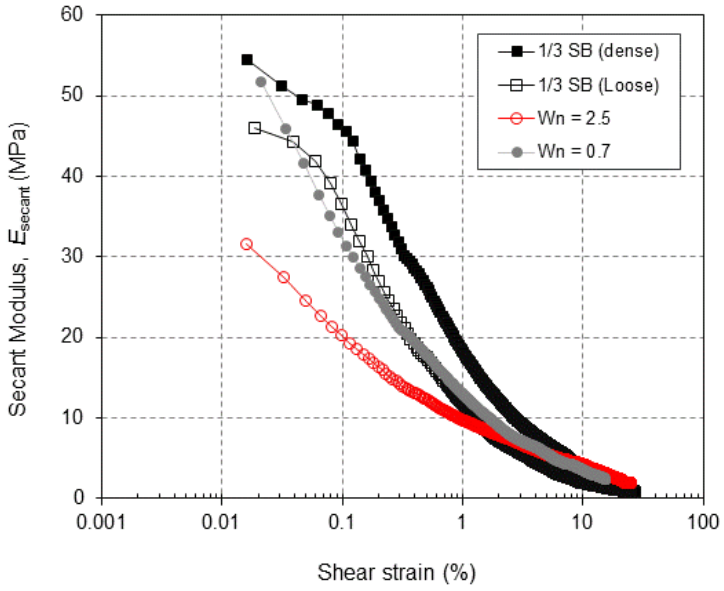

Figure 5.18: Effect of W_N on Secant Modulus, E_s of fibre reinforced 1/3 SB with V_{fr} = 1.6% and L_N = 7.1

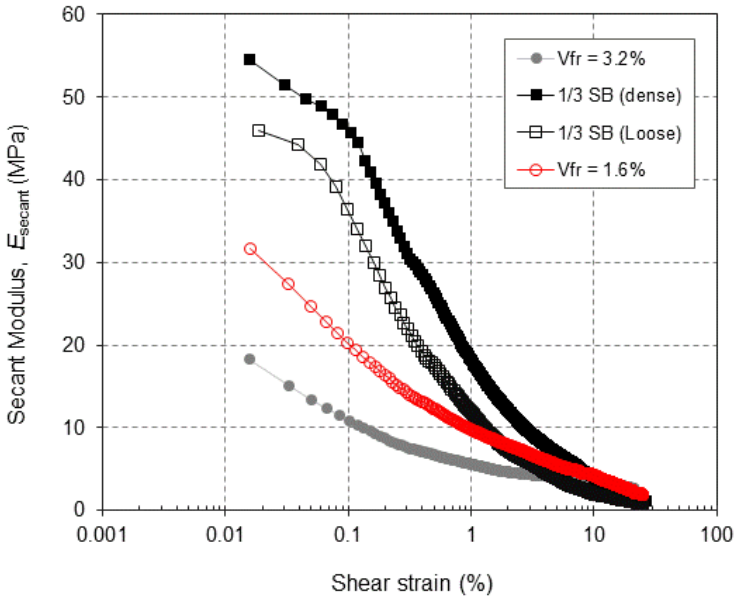

Figure 5.19: Effect of V_{fr} on Secant Modulus, E_s of fibre reinforced 1/3 SB with W_N = 2.5 and L_N = 7.1

5.4 Behaviour of fibre reinforced granular materials at different scales

The behaviour of granular materials is fundamentally governed by the interactions at the grain scale. The effect of fibre/particle scale has been shown to be important in understanding the mechanical behaviour of the composite material (Michalowski and Zhao, 1996; Lirer et al., 2011). Diambra et al. (2013) stated that the lack of understanding of the interaction mechanism between soil and fibres is one the limitations of the use of fibre reinforcements at an industrial scale. In addition, since the use of fibre reinforcements in railway ballast is novel, there is a need to assess the reinforcing mechanisms of fibre reinforced specimens across scales (i.e. 1/5 and 1/3 SB).

The triaxial test results for the reinforced specimens (i.e. LB sand, 1/5 and 1/3 SB) consistently showed that increasing L_f, W_f and V_{fr} increases the peak mobilised strength and inhibits the dilation of the mixture. At low axial strains (i.e. $\varepsilon_a \leq 2$ %), the reinforced specimens all exhibited a loss of stiffness which became more pronounced as V_{fr} increased and was relatively unaffected by the fibre dimensions. The observed loss of stiffness at low strains corroborates the findings of previous researchers (e.g. Heineck et al., 2005; Ibraim and Fourmont, 2007; Diambra et al., 2010). The loss in stiffness can be attributed to the increase in both macro voids (voids due to packing of a smaller number of solids within a given total volume) and micro voids (arising from the inability of fibres to form perfect bonds with particles). This is similar to the explanation of Michalowski

and Cermak (2003), in which they attributed the loss in initial stiffness to the non-homogeneity of the void distribution within the specimen and suggested that not all fibres would respond immediately to deformation by stretching. The interaction mechanism between the fibres and grains can then be considered to be dominated by the granular matrix material at low strains.

The mobilised strength of the reinforced specimens improved despite the inevitable looser packing of the granular matrix owing to the presence of fibres. The results presented in Section 5.3 also shows that the volumetric behaviour of the fibre reinforced granular materials is principally influenced by V_{fr}. It could then be conjectured that the fibre content in fibre reinforced granular materials (which leads to the creation of macro and micro voids) mostly influence the micro-mechanical interactions governing volume change of the specimen (e.g. sliding, rolling, coordination number and local voids). The improvement in terms of mobilised strength in fibre reinforced granular materials depends largely on the potential for the tensile forces in the fibres to be mobilised.

In Section 4.3.5 (Figure 4.12), the unreinforced 1/3 and 1/5 SB were shown to behave similarly in terms of the relationships between stress ratio, q/p' and volumetric strain with axial strain. However, plots of the mobilised friction angle and volumetric strain against axial strain for the reinforced 1/5 SB and 1/3 SB specimens having similar V_{fr}, L_N and W_N are different (Figure 5.20 and 5.21).

The difference in the observed mobilised strength can also be expressed by normalising the mobilised friction angle of any test by the friction angle (Equation (5.3)) at the onset of dilation for the unreinforced dense specimen as shown in Figure 5.22.

$$N\varphi'_{mob} = \frac{tan\varphi'_{mob}}{tan\varphi'_{dil}} \tag{5.3}$$

These results also suggest that in addition to the proposition made by Michalowski and Cermak (2003) about the relative dimensions of fibres and grains, the number of individual fibres potentially available to develop interaction mechanisms with particles is also important when considering the mechanical behaviour of fibre reinforced granular materials across different particle size ranges.

By assuming that 1/5 and 1/3 SB are approximately spherical with a diameter equal to the average particle size, D_{50}, an approximation of the number of particles (N_p) in a fibre reinforced specimen can be determined. Likewise, the number of individual fibres (N_f) can be determined by manual counting. The ratio of the number of fibres to the number

of particles is then referred to as the fibre/particle number, N_{fp}. The values obtained for each of the materials tested in this research are shown in Table 5.7.

$$N_{fp} = \frac{N_f}{N_p} \tag{5.4}$$

A better agreement in the stress-strain and volumetric strain behaviour at the two scales (i.e. 1/5 and 1/3) is apparent between triaxial tests performed on specimens having similar N_{fp}, L_N and W_N (Figure 5.23). A better agreement in terms of the normalised friction angle, $N\varphi'_{mob}$ for specimens with similar N_{fp}, L_N and W_N, is also observed as shown in Figure 5.24. This indicates that as the scaling of a granular material increases, the number of individual fibres required to develop similar macro-mechanical behaviour across the scales in question decreases provided that the fibre thickness is constant so as to make the bending stiffness of the fibres insignificant. This is a result of the corresponding decrease in N_p when the scaling of a granular material increases while V_T is constant.

Table 5.7: Relative fibre/particle numbers for triaxial test on 1/5 and 1/3 SB specimens

	V_{fr} (%)	Avg. N_p	N_f	N_{fp} (%)
1/3 SB	1.6	2026	27	1.33
	3.2	1892	57	3.01
1/5 SB	1.6	10838	82	0.76
	3.2	10270	146	1.42
	6.5	9660	281	2.91

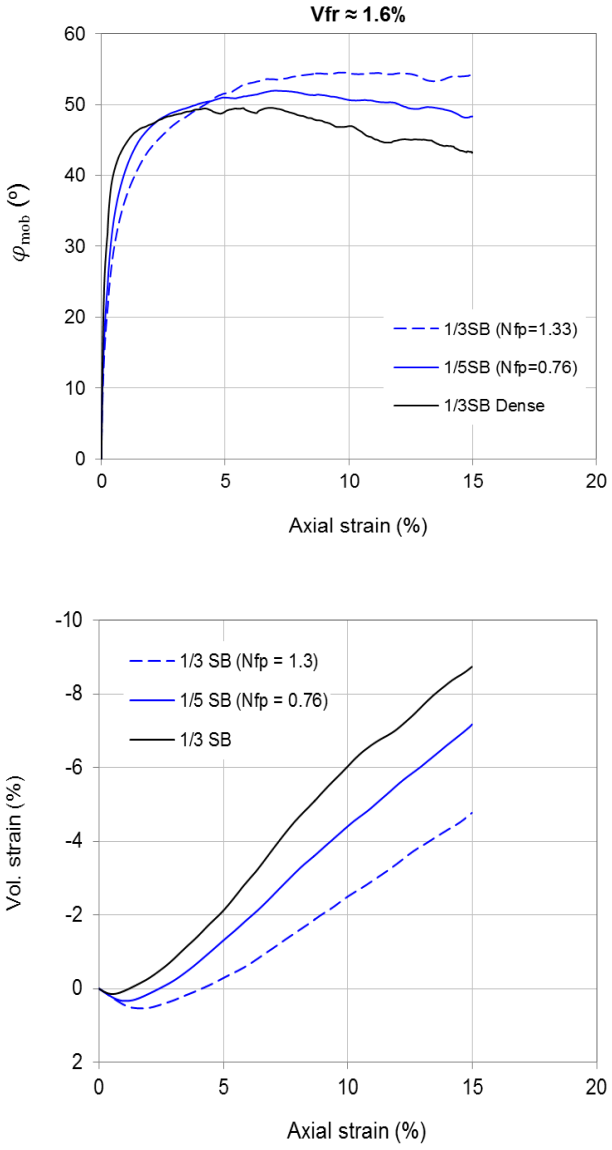

Figure 5.20: Fibre/particle number effects on mobilised friction angle and volumetric strain of reinforced 1/5 and 1/3 SB when L_N = 7.1 and W_N = 2.5 for V_{fr} = 1.6%

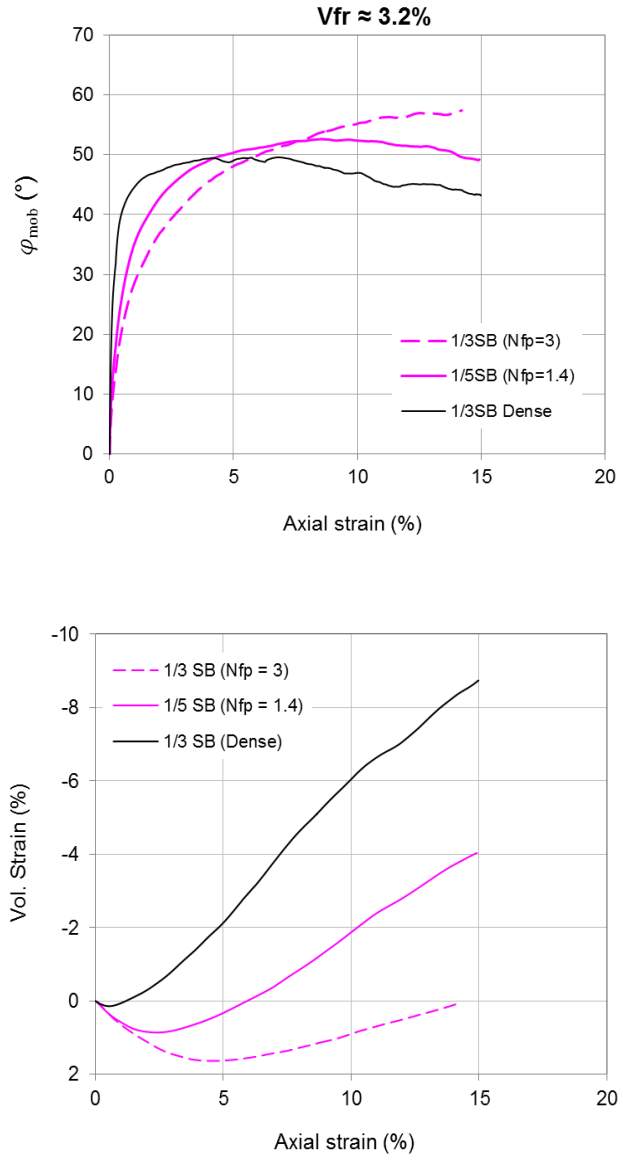

Figure 5.21: Fibre/particle number effects on mobilised friction angle and volumetric strain of reinforced 1/5 and 1/3 SB when L_N = 7.1 and W_N = 2.5 for V_{fr} = 3.2%

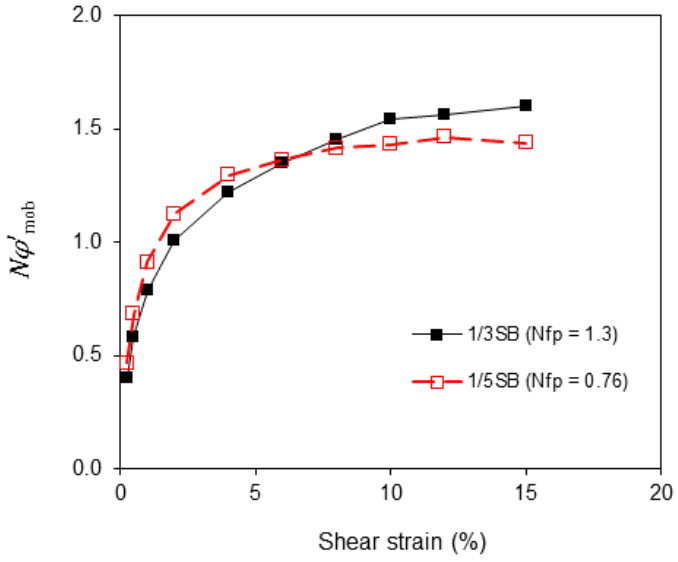

(a)

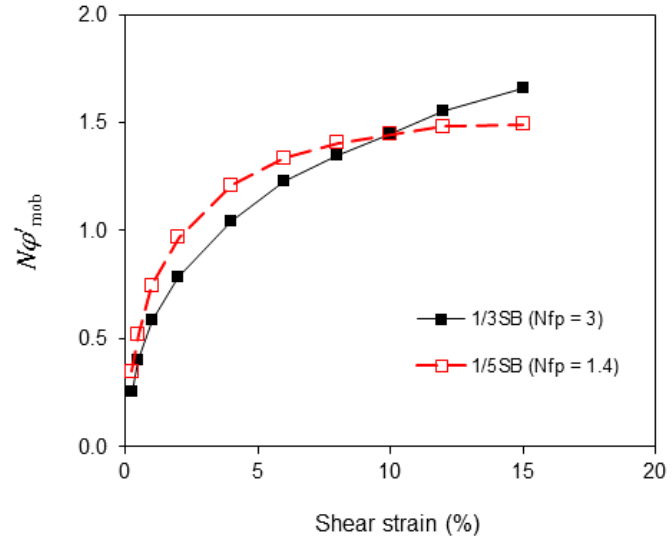

(b)

Figure 5.22: Effects of fibre/particle number, N_{fp} on $N\varphi'_{mob}$ for 1/5 and 1/3 SB specimens having similar L_N and W_N when, (a) V_{fr} = 1.6%, and; (b) V_{fr} = 3.2%

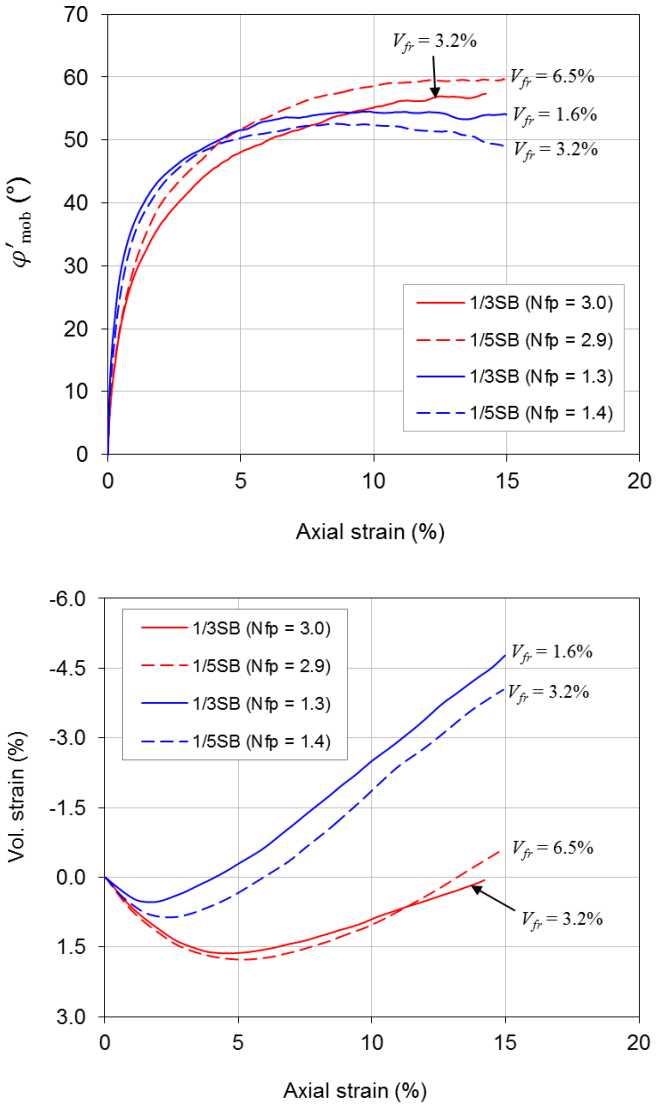

Figure 5.23: Mobilised friction angle and volumetric strain of reinforced 1/5 and 1/3 SB specimens at constant N_{fp}, L_N = 7.1 and W_N = 2.5

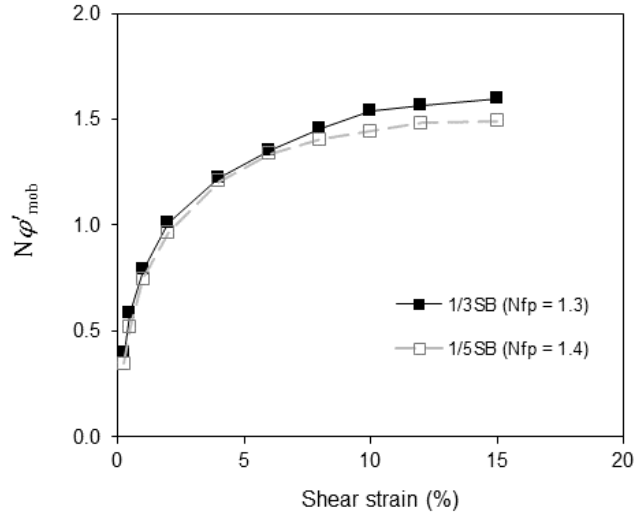

(a)

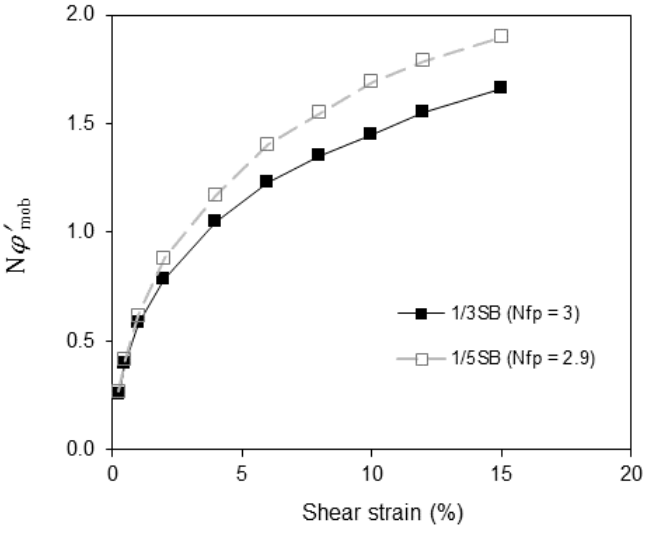

(b)

Figure 5.24: Normalised friction angle of reinforced 1/5 and 1/3 SB specimens at constant L_N = 7.1 and W_N = 2.5 (a) N_{fp} ≈1.3, and; (b) N_{fp} ≈ 3

5.5 Fibre Reinforcement Mechanism in Granular Materials

The triaxial test results and observations of the reinforced scaled ballast specimens have revealed that the reinforcement mechanism of granular materials is influenced by the number of fibres available for interaction with the granular matrix material and the relative dimensions of fibres and grains in the matrix. This implies that the micro-mechanical interaction between the fibres and particles (both LB sand and scaled ballast) is probably a combination of surface contact between fibres and particles, and mobilisation of tensile forces in fibres due to stretching between particles. It is generally agreed that mobilisation of the tensile forces in the fibres is the primary cause of improvement in geosynthetic reinforced soils. However, the fibre-particle interaction that precedes the mobilisation of tensile forces in the fibre reinforced granular materials remains unclear.

Based on the experimental and analytical evidence presented in this study, a hypothetical explanation of the reinforcement mechanism is proposed. The reinforcement mechanism can be broadly considered in two stages:

1. Development of significant fibre/particle contact points.
2. Tensile force mobilisation in the fibres.

The reinforcement mechanism stages are described as follows:

5.5.1 Fibre/particle Interaction Mechanism Development

This stage starts with the development of significant fibre/particle contacts. The occurrence of this depends on the fibre/particle number, N_{fp}, and the normalised width of fibres (W_N).

Fibre/particle number (N_{fp})

This ensures that there is a sufficient quantity of individual fibres to produce enough fibre/particle interactions to generate noticeable improvement in the macro-mechanical behaviour of the mixture. N_{fp} is of greater importance when considering fibre/particle interactions across scales than fibre content expressed in terms of V_{fr} or by weight when the thickness of the fibre is not scaled. This is because V_{fr} does not account for the changes in the relative number of particles associated with changes in particle size ranges and changing scales when the fibre thickness is not scaled.

Normalised width (W_N)

This is required for the development of adequate surface contact between the fibres and particles. It ensures that there is a sufficient grip on the fibres by the particles. Based on

the experimental evidence presented in this study, the minimum value for W_N in the scaled ballast specimen required for a noticeable improvement in its macro-mechanical behaviour was found to be about 2.5. This implies that on the average two particles of the granular matrix must have contact with an individual fibre across its width to provide a sufficient grip. In reality, the number of particle contacts on an individual fibre might be more or less than this and contacts might evolve during shear deformation. The principal consideration is the ability of the particles to develop sufficient contact points with the fibres.

Thickness of fibres

An important aspect of the development of interaction mechanism is that the fibres remain flexible within the mixture. Fibres that are too thick could become potentially weak planes within the granular matrix, as the interface friction between geomaterials and polymers is known to be less than inter-particle friction. On the other hand if the fibres are too thin, they may become entangled with other fibres in the granular mixture without developing contact with the granular matrix. Thinner fibres may also be prone to tearing and wear or attrition by the sharp edges of angular particles. In the current test programme, there were no visible signs of plastic straining of the fibres although small perforations were noticed on some fibres.

5.5.2 Tensile Force Mobilisation

It has been argued in the preceding sections that the improvement of the mobilised shear strength in fibre reinforced granular materials depends on the potential for the tensile forces in the fibres to be mobilised. In fibre reinforced granular material specimens, the fibres typically undergo stretching during shear deformation. The magnitude of the mobilised tensile force in each fibre is therefore due to the number of fibre-pinching points on an individual fibre (Figure 5.25). Previous research into short fibre composites has shown that the maximum stress attainable in the fibre is the ultimate strength (σ_{fu}), and the minimum length required for the tensile stress to build up is the critical length, l_c (as explained in Section 2.6.4). Hence, above the critical fibre length, there is a potential for the development of tensile forces provided there are adequate interactions between the fibres and the granular matrix. In principle, the normalised length (L_N) should be large enough for an adequate number of fibre-stretch points to develop on an individual fibre. The experimental evidence presented in this study shows that the value of L_N for scaled ballast should be greater than 7. This implies that on average about 7 fibre-pinch contact points will be developed on an individual fibre. The overall magnitude of the improvement in mobilised strength will then be due

to the number of individual fibres held by such fibre-pinch contact points. This will be governed by the ratio of the number of fibres to the number of particles, N_{fp}.

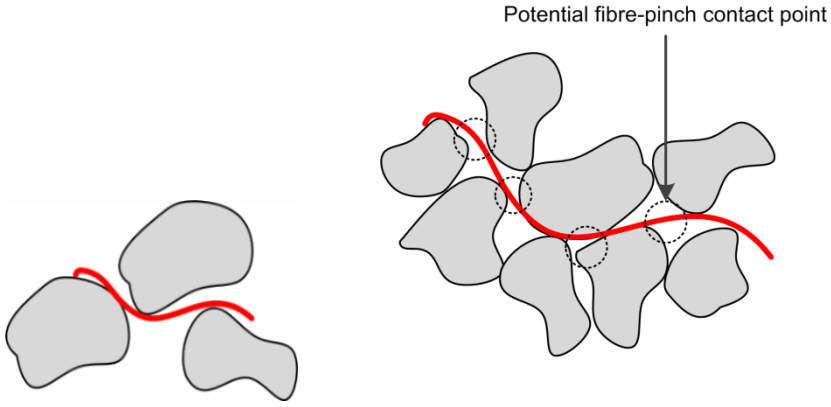

Figure 5.25: Potential fibre-pinch contact points in a fibre reinforced granular matrix with relatively (a) short fibre and (b) long fibre

5.6 Potential Applications in Railway Ballast

As shown in the preceding sections in this Chapter, the addition of fibres seems to have a slight adverse effect on the initial stiffness of both reinforced LB sand and scaled ballast specimens. Previous research investigating the behaviour of railway ballast subjected to cyclic loading has however shown that cyclic densification of ballast plays a significant role in the increase of its resilient modulus (Sevi and Ge, 2012). With regard to the increase in mobilised shear strength, the initial stabilisation that ballast undergoes during the first several cycles of load might produce enough shear strain for the mobilisation of the tensile forces in the fibres. Hence, the influence of the higher void ratios of reinforced scaled ballast samples might become suppressed as the initial density of cyclic triaxial test samples is considered to be relatively unimportant in its stiffness response because of the initial stabilisation (conditioning). In addition, the average cumulative shear strain of fresh ballast in the field has been shown to be about 3.5% after about 650,000 load cycles (Indraratna et al., 2010) thus suggesting that adequate shear strain would be developed in the fibre reinforced ballast to mobilise fibre tensile force.

Experience of the use of geogrids in ballast has shown that the improvement offered is predominantly due to the reduction in permanent vertical and lateral strains. The resilient modulus has been found to be relatively unaffected by the presence of geogrids.

Evidence from the triaxial tests reveals that fibre reinforcements in scaled ballast suppress volume change and can enable it to mobilise significantly higher strength with less volume change. This suggests that fibre reinforcements can potentially reduce lateral spread (minor principal strain) of railway ballast and hence vertical plastic settlement. Two dimensional DEM of fibre reinforced sands as presented by Maeda and Ibraim (2008) has shown that fibre inclusions reduce the loss of fabric in the minor principal strain direction (lateral direction). Also, the micromechanical explanation of the geogrid-ballast interaction as revealed by DEM simulations suggests that the apparent increase in confinement in the ballast is probably responsible for the reduced permanent vertical settlement and lateral spread (Lu and McDowell, 2010; Chen et al., 2012). This is similar to the micromechanical explanations made for fibre reinforced sands in this thesis.

5.7 Conclusions

The following conclusions can be drawn from the experimental results and discussions presented in this chapter:

1. The addition of fibres in both reinforced LB sand and scaled ballast specimens produced higher mobilised strength and a reduction in post-peak loss of strength. The magnitude of the increased mobilised strenght in both reinforced LB sand and scaled ballast specimens depend on V_{fr}. In reinforced scaled ballast specimens, the magnitude of mobilised strength increase is also dependent on the relative dimensions of the fibre and particles expressed as L_N (ratio of the fibre length to D_{50}) and W_N (ratio of the fibre width to D_{50}) which influence the stress-strain behaviour of reinforced specimens at a given V_{fr}.
2. The reinforced LB sand and scaled ballast specimens exhibited reduced dilation during shear deformation and the suppression of dilation became more apparent with increasing V_{fr}. The intial compression of the reinforced specimens was predominantly influenced by V_{fr}.
3. At a given rate of dilation, reinforced specimens demonstrated greater mobilised strength than the unreinforced specimens. The results also indicate that the relative fibre/particle dimensions (L_N and W_N) influence the rate of increase of mobilised strength with rate of dilation, α.
4. The intial stiffness (described by the secant modulus, E_{secant}) of the reinforced SB specimens is influenced by V_{fr} and W_N while the effect of L_N is relatively unnoticeable. The loss in stiffness may be attributed primarily to the non-homogeneity of the void distribution within the specimen and the nature of the fibre reinforcement mechanism at the fibre/particle level.

5. Across different scales of the same parent material, N_{fp} (defined as the ratio of the number of fibres, N_f to the number of particles, N_p) has been shown to be of more importance than fibre content expressed as V_{fr} or by weight. This is due to the inability of V_{fr} to scale the number of fibres relative to the number of particles if the thickness of the fibres remains the same. The lack of scaling of the thickness of the fibres ensures that they are thin and thus remain flexible within the granular matrix.
6. A fibre reinforcement hypothesis describing qualitatively the macro-mechanical behaviour of granular materials as observed from the experimental results is proposed, comprising the development of significant fibre/particle gripping and tensile force mobilisation in the fibres.

Chapter 6

Image-Based Deformation Study of Reinforced Scaled Ballast Triaxial Specimens

6.1 Introduction

The use of digital cameras to monitor deformation of soils has been employed in recent times mainly due to its ability to provide effective continuous information at both the full field and local micro-scale. Its use has been particularly prominent in monitoring deformation of soils in centrifuge models where plane strain conditions are imposed on the model (e.g. White et al., 2003). Image-based deformation measurements has also been employed on laboratory element tests (e.g. Liang et al., 1997; Macari et al., 1997; Alshibli and Al-Hamdan, 2001; Rechenmacher and Finno, 2004; Gachet et al., 2007; Sevi et al., 2009; Bhandari and Powrie, 2013b). These were mainly to study strain localisation and to measure local strain on specimens. Bhandari (2009) demonstrated that significant deformation characteristics of triaxial samples can be effectively studied using an image-based deformation measurement technique (Triax-DIC) that would not have been noticed by the naked eye or through local instrumentation attached to the samples.

As shown in Chapter 5, the fibre reinforcement of granular materials significantly influences the mechanical behaviour (in terms of volumetric response and mobilised strength) of the mixture. There is a general consensus among researchers that the micromechanics of the fibre/particle interaction significantly influence the mechanical properties (e.g. Michalowski and Zhao, 1996; Diambra et al., 2013; Ajayi et al., 2014). Parameters governing the fibre/particle interaction mechanisms include the relative fibre/particle dimensions, fibre content etc. However, no attempt has been made to study the deformation of fibre reinforced granular materials at both the full field and local micro-scale level.

In this chapter, an image-based deformation measurement method developed by Bhandari et al. (2012) is utilised to study the local deformation of fibre reinforced triaxial

specimens. In a departure from similar techniques developed for laboratory element tests, the technique developed by Bhandari et al. (2012) considers the effects of specimen image distortion due to various refraction indices of the water in the cell and the cell wall. In addition, the technique has the advantage of being able to measure the volume change of the specimen (via volume/pressure controller) and the flexibility of conveniently carrying out tests under different radial stresses while images of the deforming sample is being captured.

6.2 Experimental Set-Up

Two digital cameras (SONY DSC-R1 Cyber shot 10 mega pixels) were placed along the radii of the transparent triaxial cell at an angular interval of about 120° when viewed in plan. Images of the deforming specimens were captured at regular axial strain intervals. The triaxial set up showing the transparent cell, two digital cameras, a light source and reflector are shown in Figure 6.1.

The cameras were attached to a cantilever arm fixed to the base of the triaxial apparatus so that the camera would remain in the same position relative to the base of the specimen during the shearing process (Figure 6.1). The optical axes of the cameras were set to coincide with the mid-height of the specimen. The aspect ratio of the image area analysed was 3V:2H and the images were captured in manual focus mode and saved in a JPEG format. A lighting arrangement as shown in Figure 6.1 was used to provide constant illumination of the specimen. A curtain of reflective aluminium foil was placed around the triaxial cell to ensure uniform illumination of the specimen. Due to the changes in colour of the latex membrane when immersed in water for a long period of time, an artificial texture for image correlation was produced by spraying quick drying enamel paint onto the membrane. The movements of discrete points on the membrane are then tracked by the measuring system rather than those of the actual scaled ballast particles. This will in most circumstances be reasonable: similarity of deformations between the specimen and the membrane is routinely assumed and enables local linear variable differential transformers (LVDTs) to be attached to the membrane rather than having to be pinned through into the specimen itself.

6.3 Brief description of technique

The image-based technique used in this study involves the following main steps (Figure 6.4): (1) pre-processing, i.e. the establishment of measurement points on the specimen surface and the determination of their positions in the captured image; (2) processing, i.e. the determination of the movements of the measurement points between

pairs of successive images using a digital image correlation algorithm; and (3) post-processing, i.e. the calculation of strain contours and vectors.

6.3.1 Pre-processing

The process of establishing measurement points on the specimen surface involves the representation of the points in the image plane (assumed to be in front of the outer cell wall) using the adopted coordinate system (Figure 6.2) and ray tracing the measurement points on the image plane to determine its location. Ray tracing involves tracing the path of each ray of light backward from the camera focus and through to the image point (in the image plane) to the specimen surface (Figure 6.3). Measurement points were established on the surface of the specimen at equal intervals on the circumferential axis and on the vertical axis.

To obtain the camera parameters (i.e., focal lengths), calibration of the two cameras was performed using the Camera Calibration Toolbox for MATLAB (Bouguet, 2008) with a planar checkerboard as a calibration pattern at different orientations about the image plane position and keeping the camera stationary. The principal point was assumed to be at the image centre, and the lens distortion was assumed to be insignificant. Further details of the pre-processing stage are described in Bhandari et al. (2012).

6.3.2 Processing

At this stage, digital image correlation of the reference and deformed image of the specimen is performed. The images are analysed using a numerical matching technique to identify the most similar patterns in the subsequent images (Figure 6.5). This is based on the assumption that the pattern between successive images is approximately constant and the local textural information is unique. The image subsets in the reference image are compared to that of the current (deformed) image by the matching algorithm. The normalized cross-correlation coefficient matching algorithm (Equation 6.1) was utilised to identify the most similar patterns in the subsequent images. The normalised similarity measure is generally accepted to be optimal for DIC, as it can account for variations in lighting and image contrast that might otherwise lead to erroneous correlations (Viggiani, 2012).

$$C_n\ u,v\ = \frac{\sum_{x=1}^{N}\sum_{y=1}^{N} t\ x,y\ - t\ \cdot (s\ u+x,v+y\ - \overline{s_{u,v}}\ )}{\sqrt{\sum_{x=1}^{N}\sum_{y=1}^{N} t\ x,y\ - t\ ^2}\ \sqrt{\sum_{x=1}^{N}\sum_{y=1}^{N}(s\ u+x,v+y\ - \overline{s_{u,v}})^2}} \tag{6.1}$$

where x and y are the (2D) spatial coordinates, u and v the displacements of a pixel from the reference image subset $\boldsymbol{t}$ to a new position in the current image subset $\boldsymbol{s}$ (Figure 6.5). The arithmetic mean of the reference subset is represented by $\bar{t}$, and $\overline{s_{u,v}}$ represents the

arithmetic mean of the current image subset underneath the reference subset, the left corner of which lies on pixel (*u*, *v*).

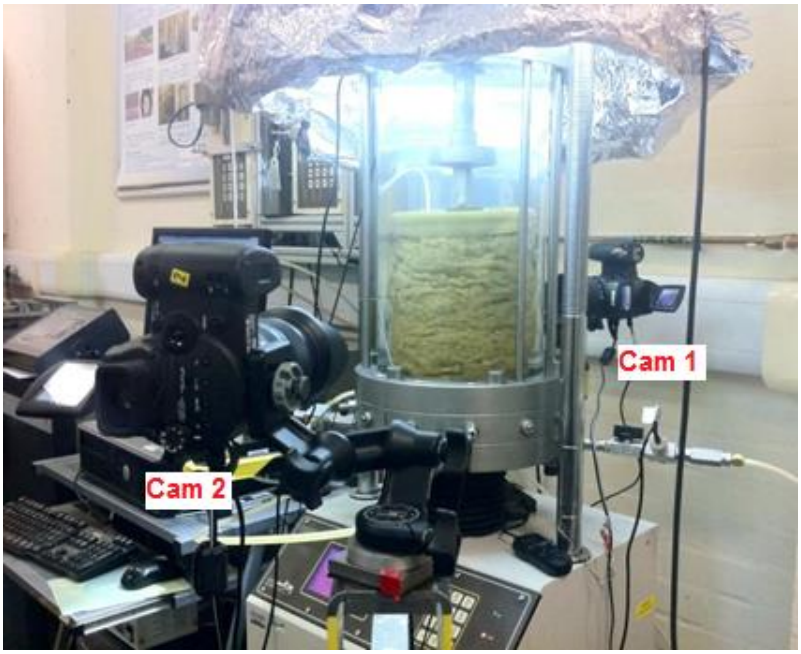

Figure 6.1: The triaxial setup for image-based deformation study showing the transparent cell, cameras, uniform light source and light reflecting curtain

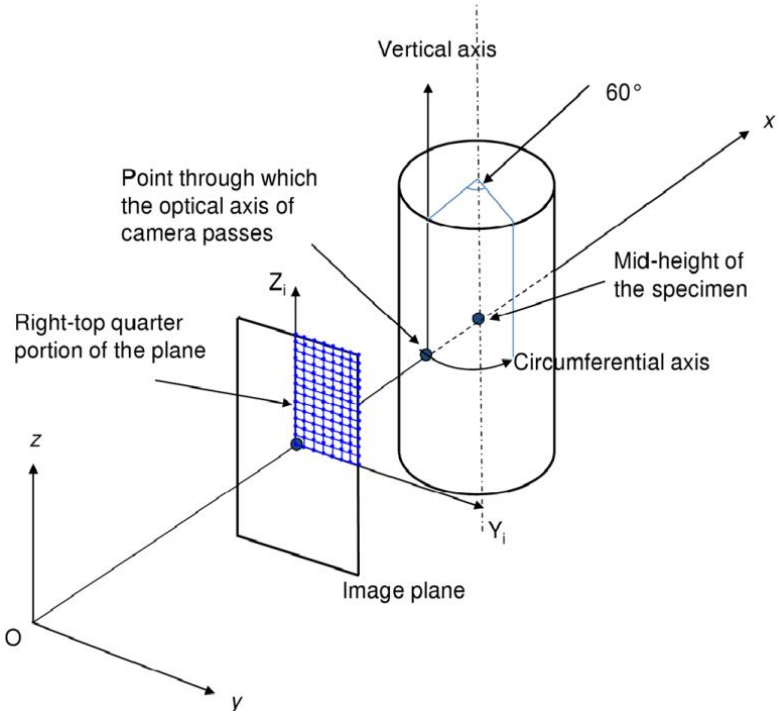

Figure 6.2: Coordinate axes, specimen, and the image plane in front of the triaxial cell, after Bhandari et al. (2012)

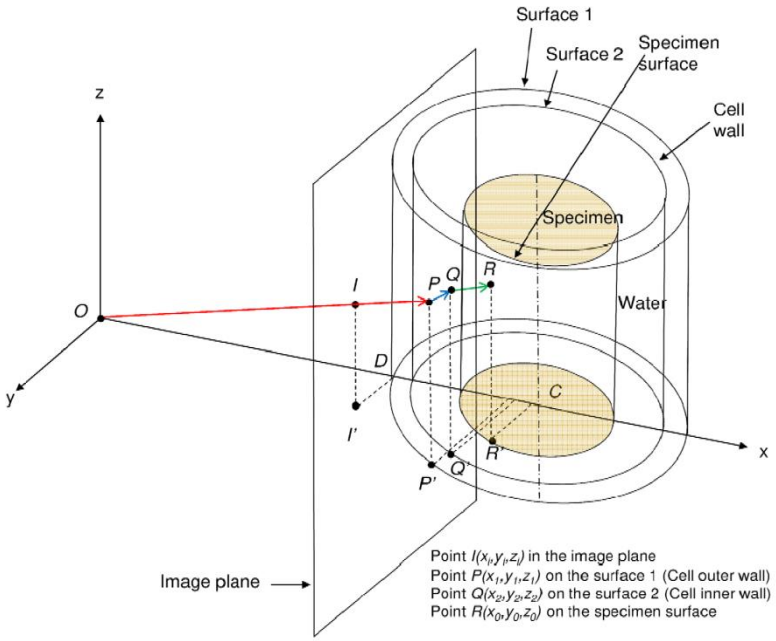

(a)

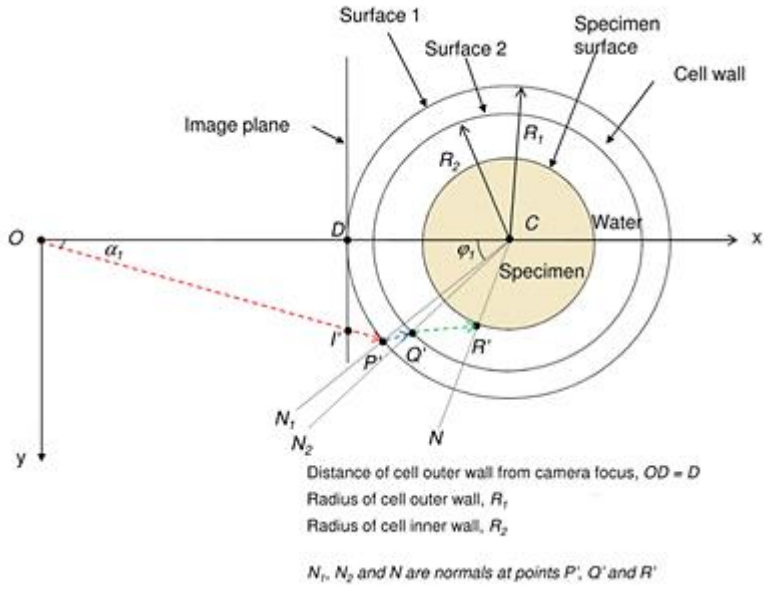

(b)

Figure 6.3: Schematic representation of the ray tracing technique for an individual ray: (a) 3D view and (b) plan view, after Bhandari et al. (2012)

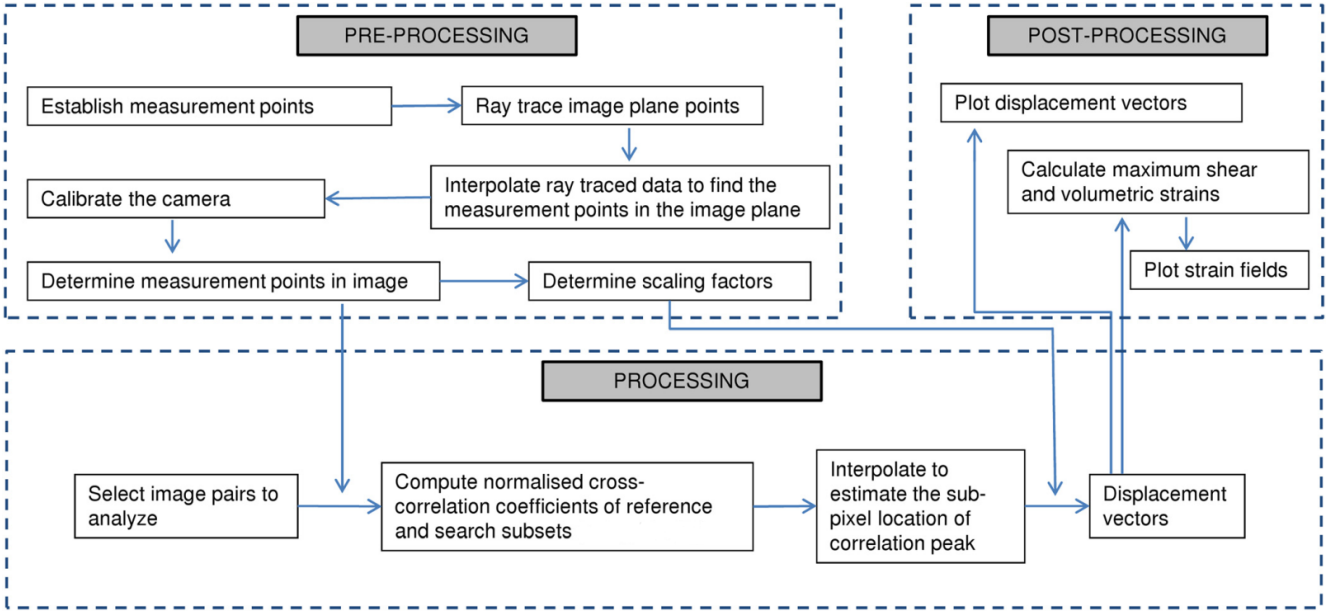

Figure 6.4: Flow chart and structure of the image-based measurement technique (Bhandari et al., 2012)

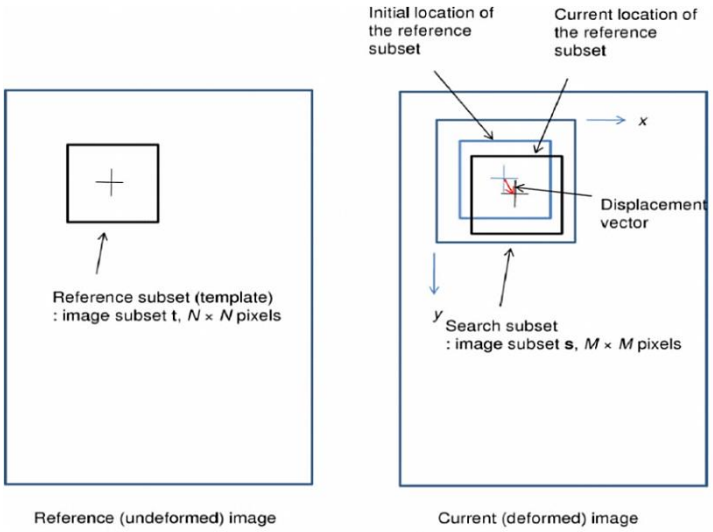

Figure 6.5: Principle of digital image correlation (DIC) (after, Bhandari, 2009)

6.3.3 Post-processing

The images of the specimen were captured at regular intervals corresponding to 0.25% axial strain. The measurement points were on a 15 mm grid spacing covering an area of 135 mm × 195 mm (Figure 6.6), and the displacement components obtained were smaller than the grid spacing. Having determined the displacement components in both the *x* (circumferential) and *y* (vertical) directions at each measurement point, the region was divided into quadrilateral (four noded) elements and the finite element approach was used to determine the principal strains. A detailed procedure for determining the maximum shear and volumetric strains for each element are described in Bhandari et al. (2012).

6.3.4 Resolution, Precision and Accuracy

In the analysis, a resolution of 0.01 pixel was chosen for the sub-pixel interpolation. The precision of digital image correlation (DIC) applications in geotechnical engineering is known to depend on the image quality, subset size and the distance of movement (White et al., 2003). Based on the empirical equation given by White et al. (2003), the precision of the DIC technique used in this research is expected to be better than 0.0033 pixel for the 181 × 181 pixel subset used to analyse the images.

According to White et al. (2005), the accuracy of DIC is dependent on the optics of the image formation, the image processing algorithm, and the transformation by which image-space coordinates (pixels) are converted into object-space coordinates. The accuracy of the current technique was found to be better than 0.10 pixels or 0.004 mm in the object-space at a nominal image scale of 0.04 mm/pixel at the centre of image (Bhandari et al., 2012).

6.4 Typical results

Typical displacement vectors, horizontal and vertical displacement contours, and strain fields (maximum shear strain and volumetric strain) for an unreinforced 1/5 SB specimen obtained by analysing images from one of the cameras are shown in Figure 6.8. The corresponding deformation stage is shown in Figure 6.7. Due to space constraints within the triaxial cell, the entire height of the specimen could not be captured in the images analysed. However, the height of the specimen captured in the analysed images is more than half with the images centred at the mid-height of the specimen.

In Figure 6.8, the horizontal axis of each plot represents the circumferential distance of the specimen in millimetres and the vertical axis represents the specimen height in millimetres. A reference vector is shown below the displacement vector field (Figure 6.8(a)) and the colour bar displayed to the right of the strain fields (i.e. Figure 6.8(d) and (e)) represents the corresponding strain in percentage. Negative strain in the volumetric strain plot indicates dilation.

Figure 6.8(a) and (b) shows that the vertical displacement of the specimen decreases from the top to the bottom. This is consistent with a uniform vertical strain because the top platen of the triaxial apparatus is moving down while the bottom platen remains fixed in relation to the camera. Hence, strain fields are more appropriate in describing the deformational behaviour of the specimen as they are dimensionless and independent of the displacement reference or datum point.

Figure 6.6: Typical captured image of a triaxial specimen during shear deformation showing measurement grids used for image-based deformation measurement

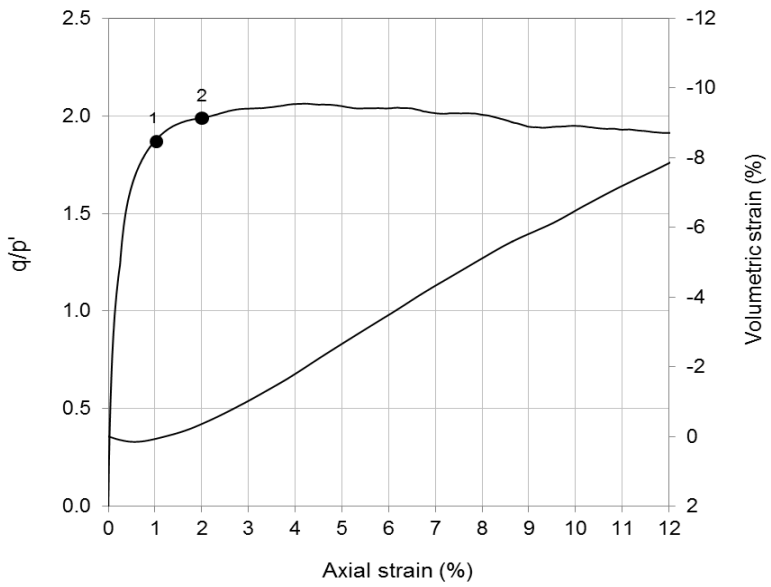

Figure 6.7: Stress ratio, q/p' and volumetric strain plotted against axial strain for unreinforced Dense 1/5 SB at cell pressure = 30 kPa showing deformation steps

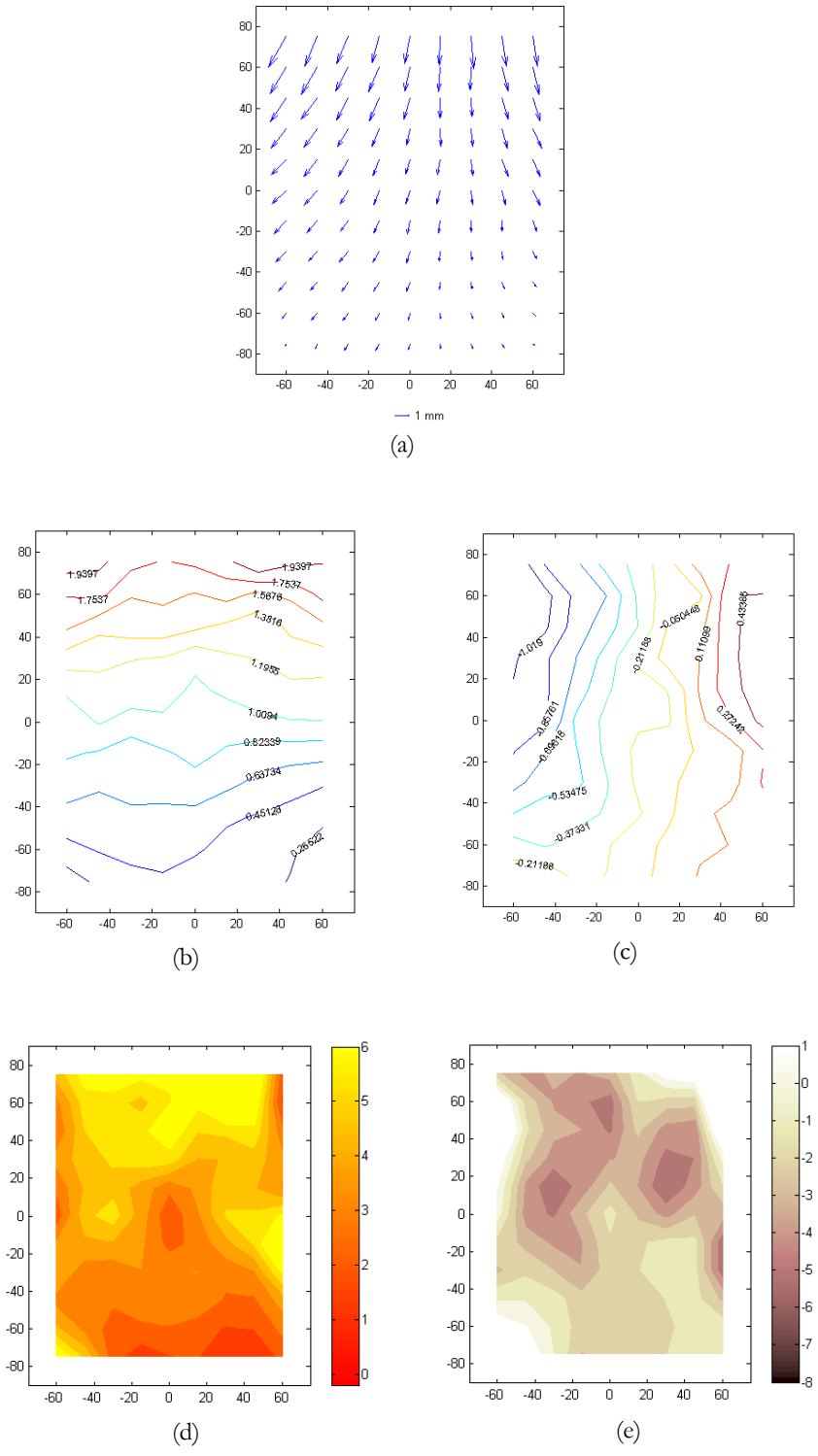

Figure 6.8: Unreinforced 1/5 SB specimen typical fields for deformation stages 1-2% axial strain: (a) displacement vectors, (b) vertical displacement contours, (c) horizontal displacement contours, (d) maximum shear strain, and (e) volumetric strain

6.5 Deformation characteristics of 1/5 SB triaxial specimens

The imaged-based deformation technique was used to investigate the deformation of unreinforced and reinforced 1/5 SB specimens. L_N and W_N for the reinforced specimens were kept constant while N_{fp} was varied. The specimen preparation technique used in these series of triaxial tests was the same as described in Section 4.3. Images of the triaxial specimens analysed are shown in Figure 6.9. For the ease of comparison and understanding, the analysed images from one of the cameras are presented. The triaxial tests have also been divided into two stages: (1) Pre-peak deformation (i.e. ε_a = 0.25 – 4.25 %), and (2) Post-peak deformation (i.e. ε_a = 5 – 13 %).

6.5.1 Pre-peak Deformation

Figures 6.10 and 6.11 show the stress ratio, q/p', and volumetric strain relationships with axial strain for unreinforced Dense and Loose 1/5 SB samples and fibre reinforced (N_{fp} = 0.76 and N_{fp} = 2.9) 1/5 SB specimens respectively. The points marked on the plot (Figure 6.10 and 6.11) indicate the instant at which the images of the deforming specimen were captured and each step corresponds to about 1% (i.e. 0.25 - 1.25; 1.25 - 2.25; …. 4.25) axial strain.

Figure 6.12 shows that the Loose sample exhibits a more near-vertical deformation than in the Dense sample. Similarly, a more nearly vertical deformation is also seen in the reinforced specimen with a higher V_{fr} (represented here by N_{fp} = 2.9) than in low V_{fr} (i.e. N_{fp} = 0.76) (Figure 6.15).

The corresponding maximum shear and volumetric strain fields for the initial deformation steps of the unreinforced specimens are presented in Figures 6.13 and 6.14. In the strain field plots, the limits (i.e. minimum and maximum) of the colourbar are kept constant, thus each pair (e.g. Dense SB and Loose SB) of plots can be compared and should then be considered by observing the overall behaviour with regard to the development of strains (shear and volumetric) in the specimen. The unreinforced Dense and Loose 1/5 SB specimens exhibited a gradual development of shear and volumetric strains over the pre-peak deformation stage and thus indicates yielding of the specimen. However, the occurrence of yield in the reinforced specimens appear to be inhibited as N_{fp} increases (Figure 6.16(b) and 6.17(b)).

Start End

(a) Unreinforced Dense 1/5 SB

Start End

(b) Unreinforced Loose 1/5 SB

Start End

(c) N_{fp} = 0.76, reinforced 1/5 SB

Start End

(d) N_{fp} = 2.9, reinforced 1/5 SB

Figure 6.9: Photographs of triaxial specimens at the start and end of shear deformation carried out at 30 kPa cell pressure

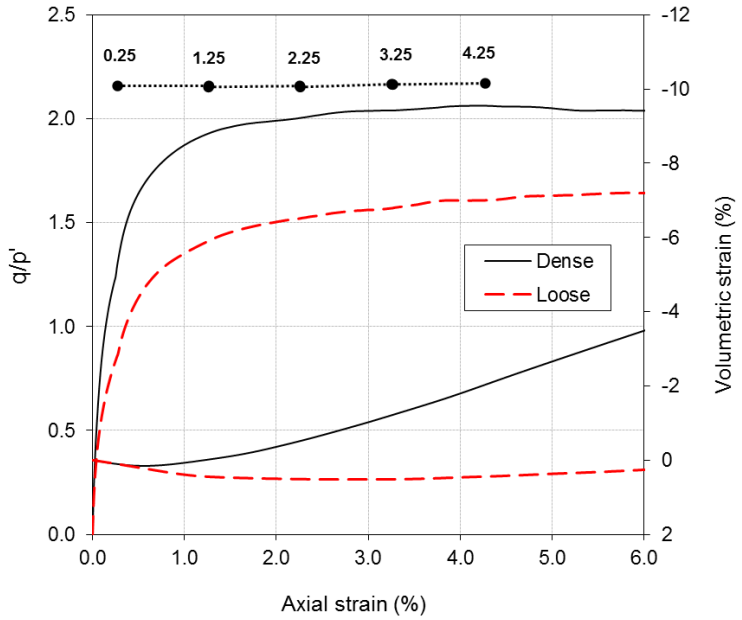

Figure 6.10: Stress ratio, q/p', and volumetric strain plotted against axial strain for Dense and Loose unreinforced 1/5 SB specimens during pre-peak deformation

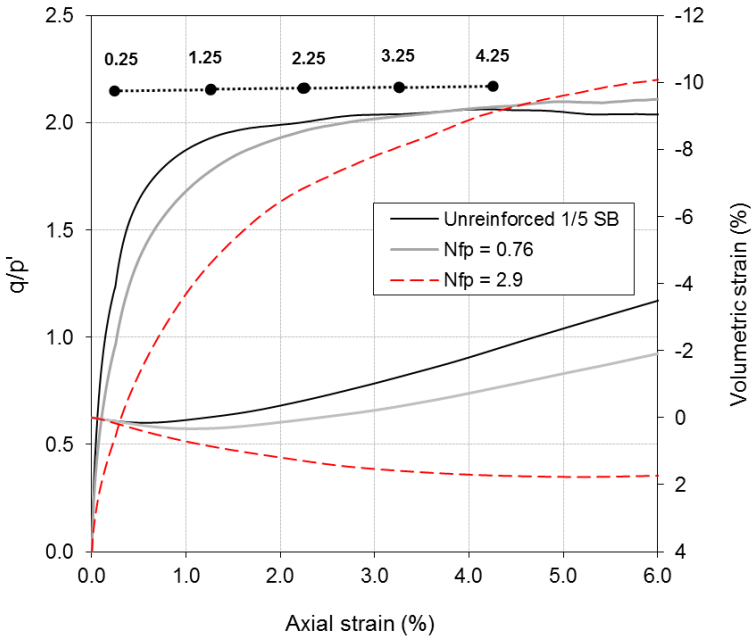

Figure 6.11: Stress ratio, q/p', and volumetric strain plotted against axial strain for reinforced 1/5 SB specimens during pre-peak deformation

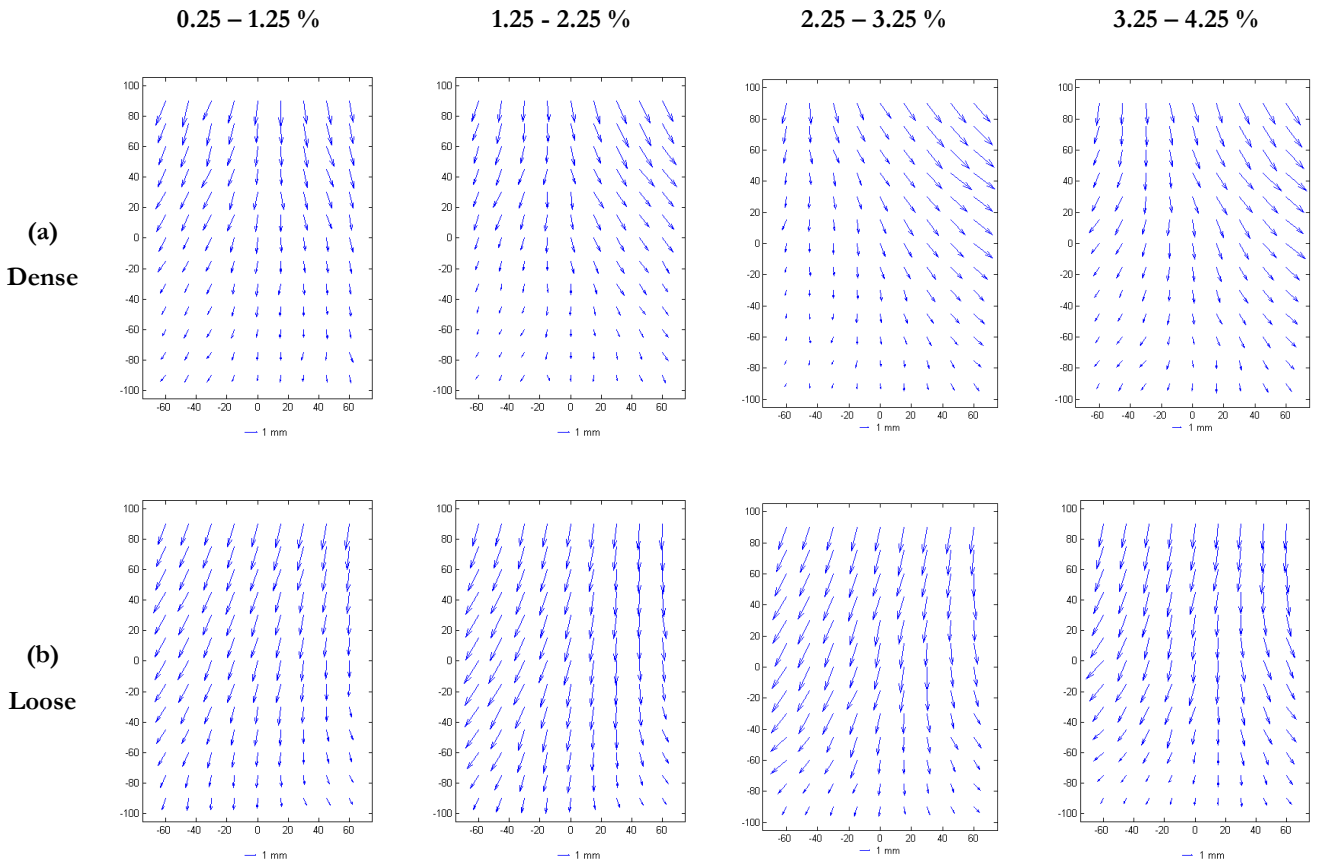

Figure 6.12: Pre-peak displacement vectors for unreinforced 1/5 SB specimens (a) Dense (b) Loose

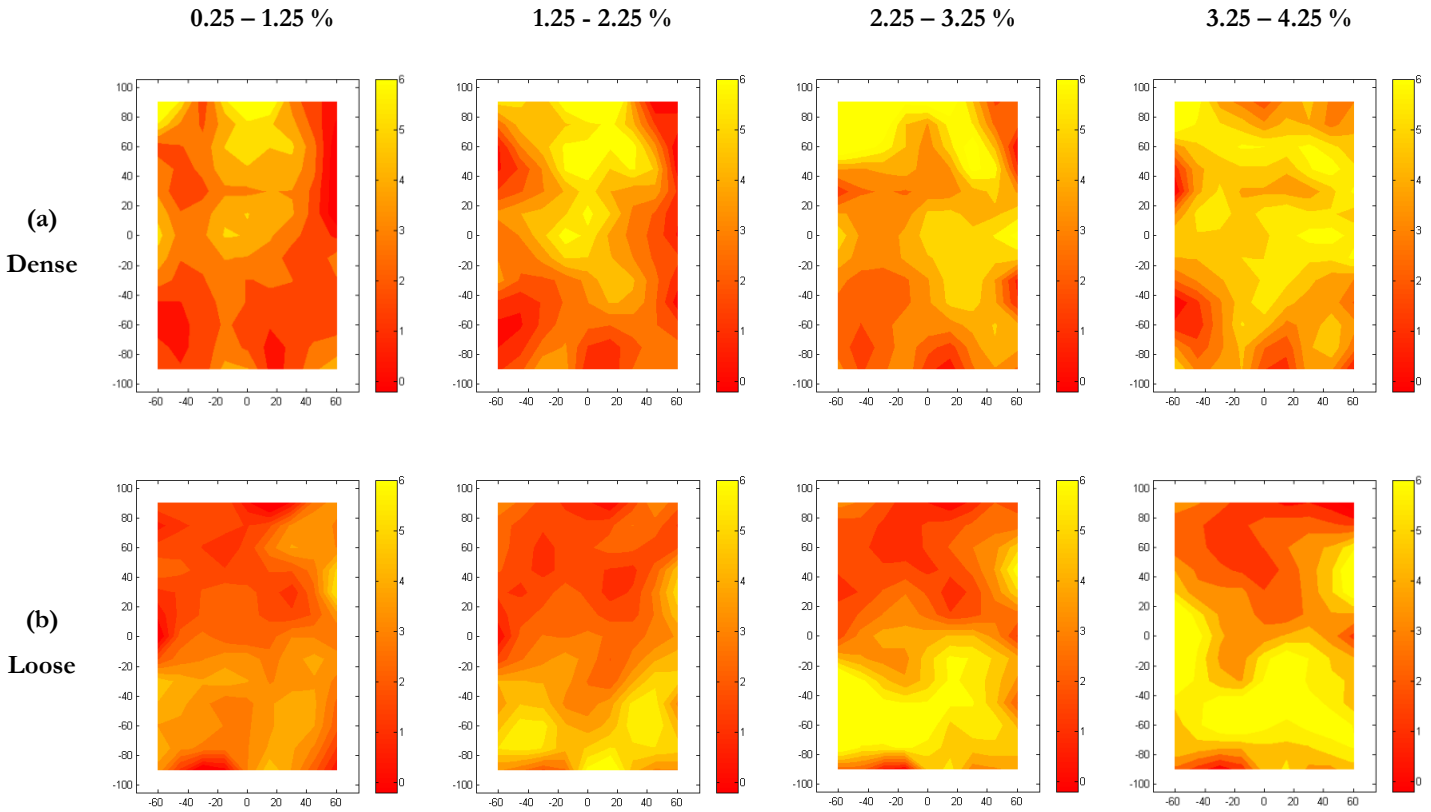

Figure 6.13: Pre-peak shear strain fields for unreinforced specimens (a) Dense 1/5 SB (b) Loose 1/5 SB

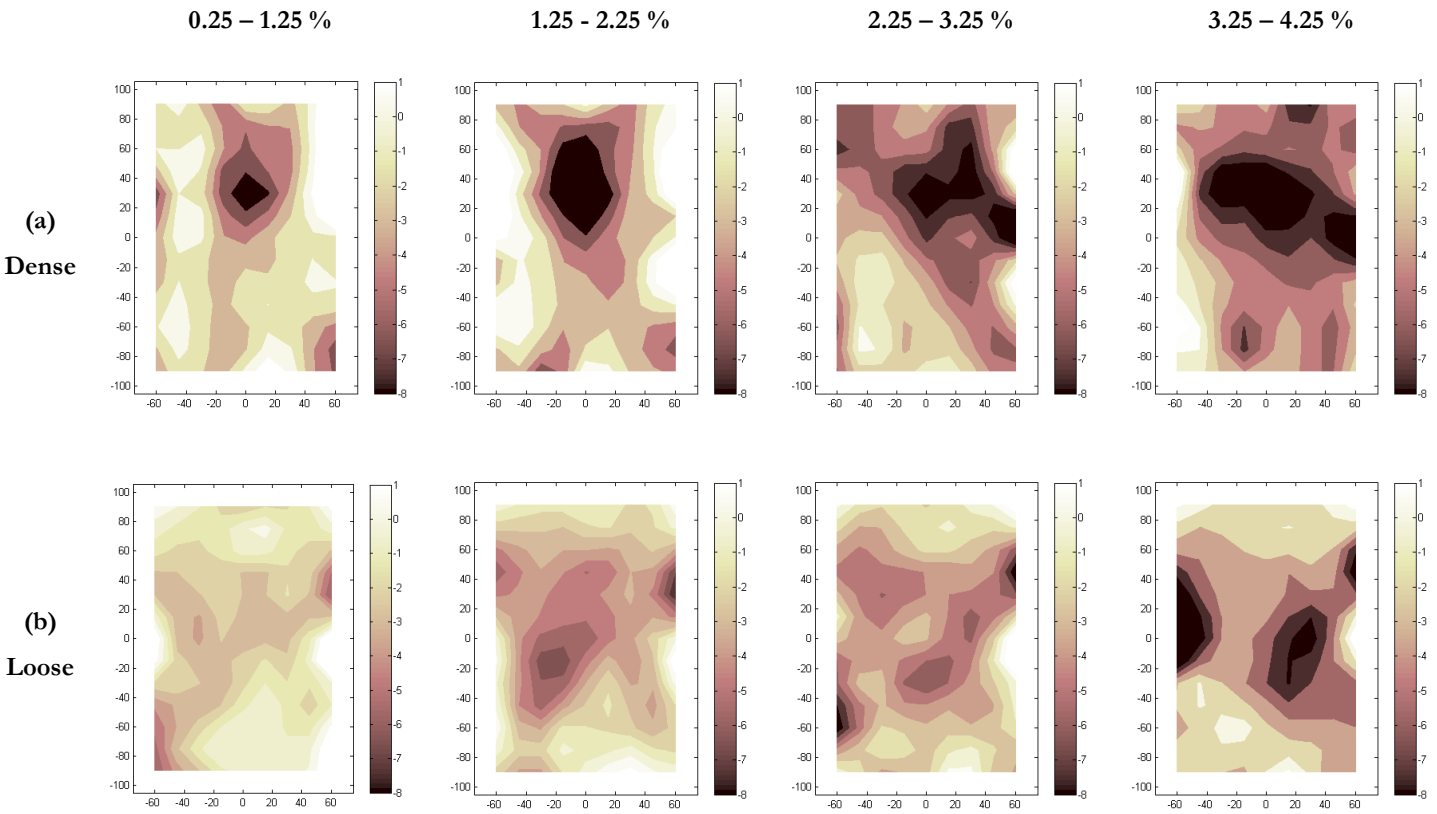

Figure 6.14: Pre-peak volumetric strain fields for unreinforced specimens (a) Dense 1/5 SB (b) Loose 1/5 SB

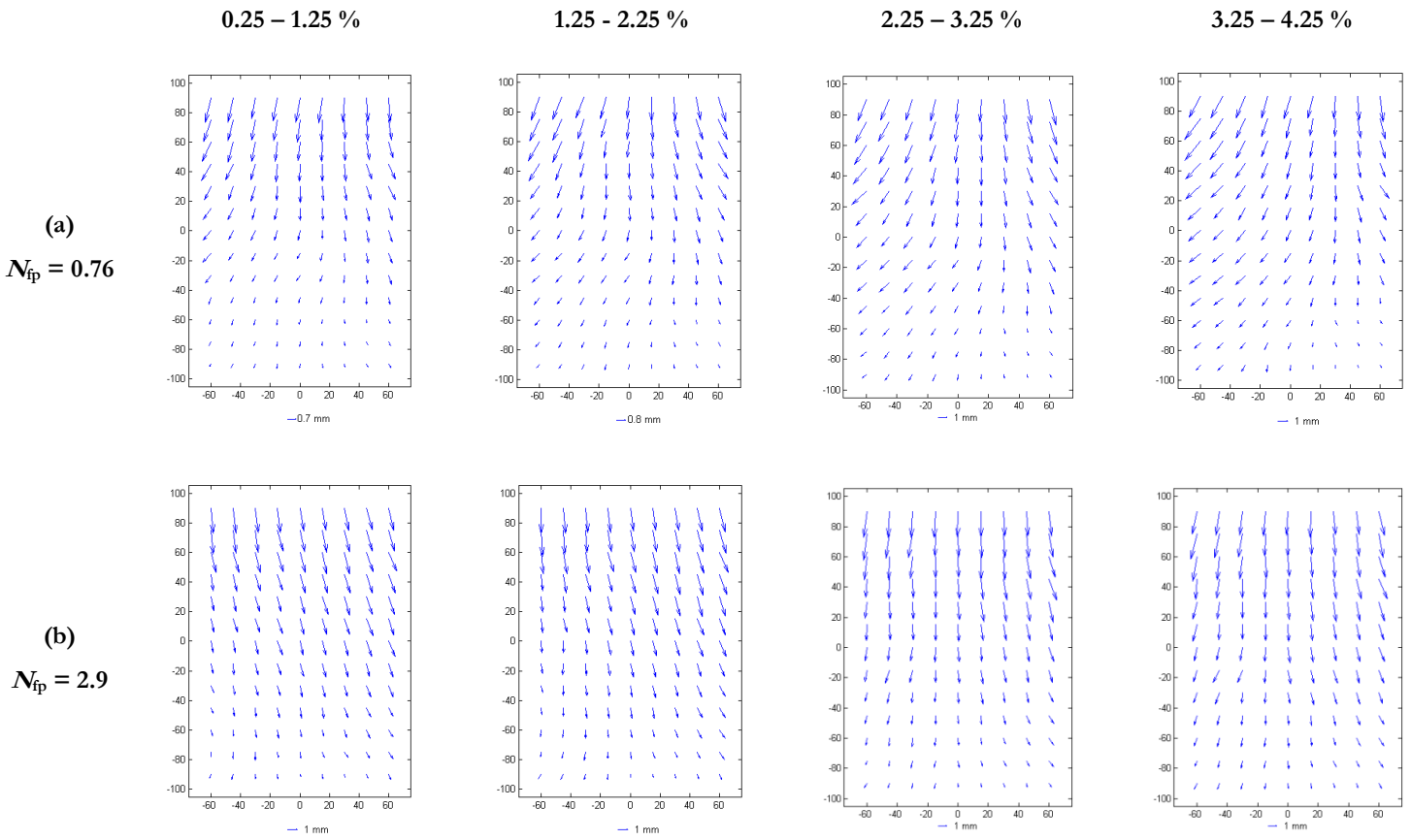

Figure 6.15: Pre-peak displacement vectors for fibre reinforced 1/5 SB specimens (a) N_{fp} = 0.76 (b) N_{fp} = 2.9

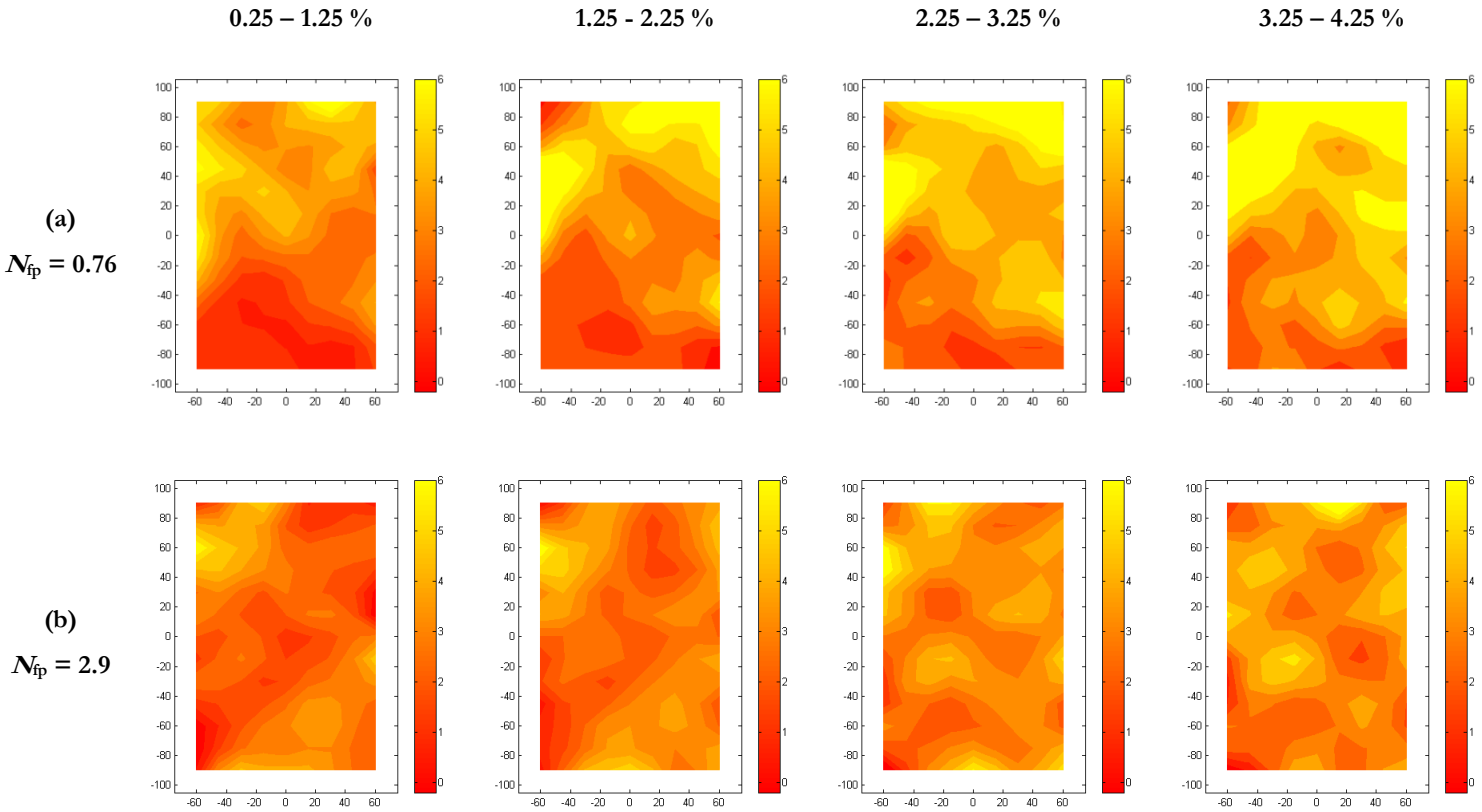

Figure 6.16: Pre-peak shear strain fields for fibre reinforced 1/5 SB specimens (a) N_{fp} = 0.76 (b) N_{fp} = 2.9

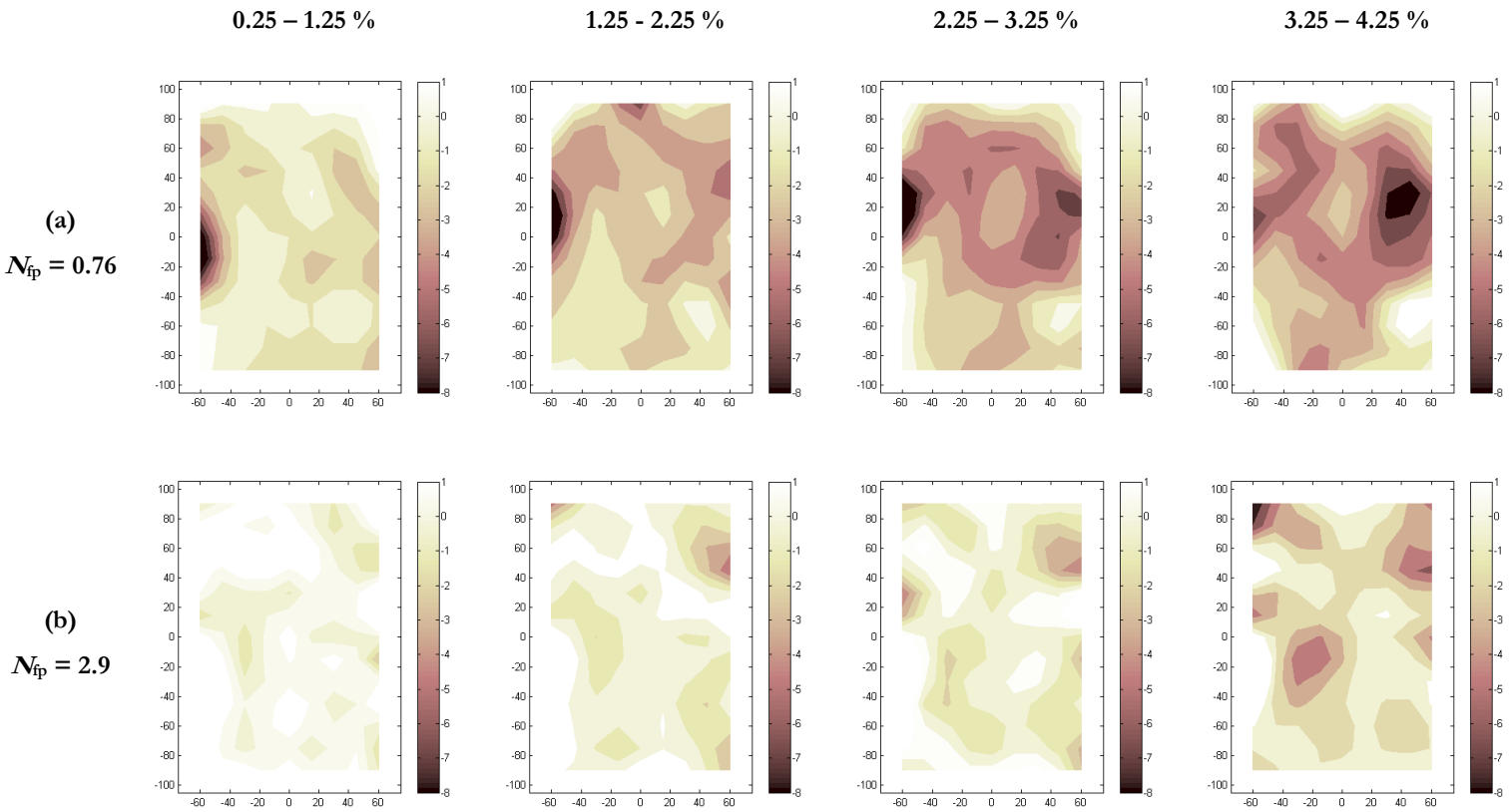

Figure 6.17: Pre-peak volumetric strain fields for fibre reinforced 1/5 SB specimens (a) N_{fp} = 0.76 (b) N_{fp} = 2.9

6.5.2 Post-peak Deformation

The stress ratio, q/p' and volumetric strain plots for the unreinforced and reinforced specimens are shown in Figure 6.18 and Figure 6.19. During post-peak deformation, the non-axisymmetric behaviour of the specimens (both unreinforced and reinforced 1/5 SB) is evident in the vector displacement plots (Figure 6.20 and Figure 6.23). Similar to the pre-peak deformation stage, the N_{fp} = 2.9 specimen exhibited more nearly vertical deformation than the Dense, Loose and N_{fp} = 0.76 specimens.

The evolution of the shear and volumetric strain in the Dense and Loose specimens continued in the same manner as observed at the end of the pre-peak deformation stage (Figure 6.21 and Figure 6.22). However, the specimen with N_{fp} = 2.9 exhibited a more-homogenous distribution of shear and volumetric strains (Figure 6.24(b) and 6.25(b)).

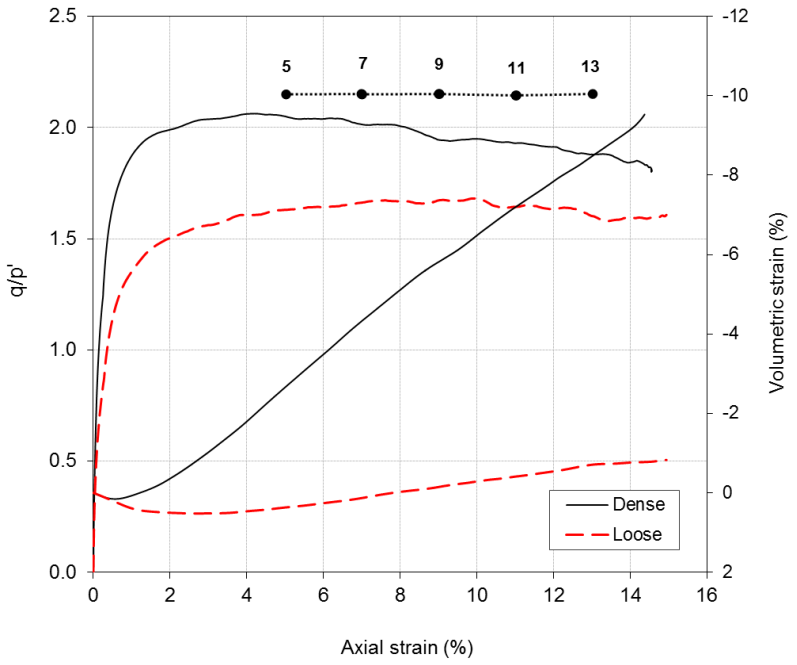

Figure 6.18: Stress ratio, q/p', and volumetric strain plotted against axial strain for unreinforced 1/5 SB specimens (post-peak deformation)

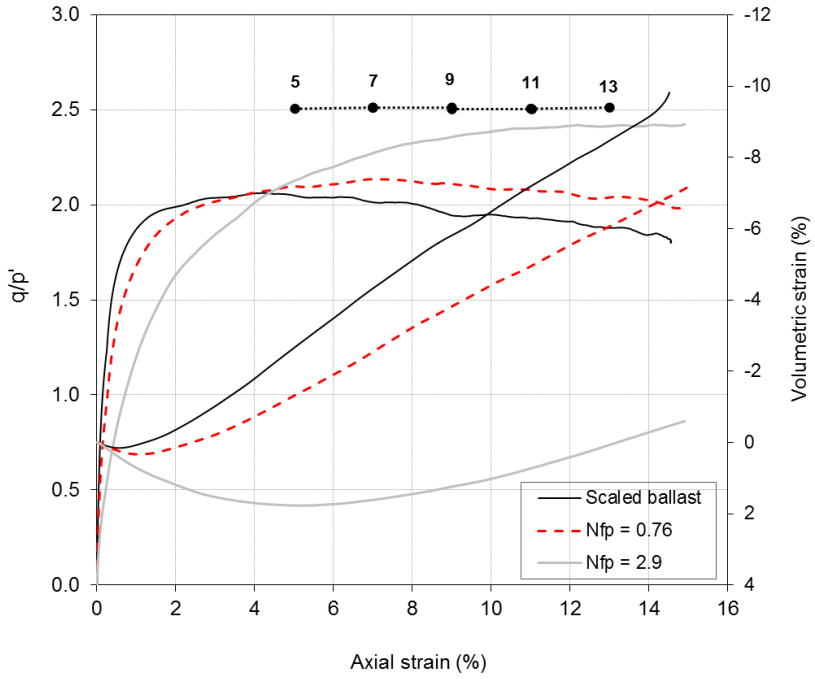

Figure 6.19: Stress ratio, q/p', and volumetric strain plotted against axial strain for fibre reinforced 1/5 SB specimens (post-peak deformation)

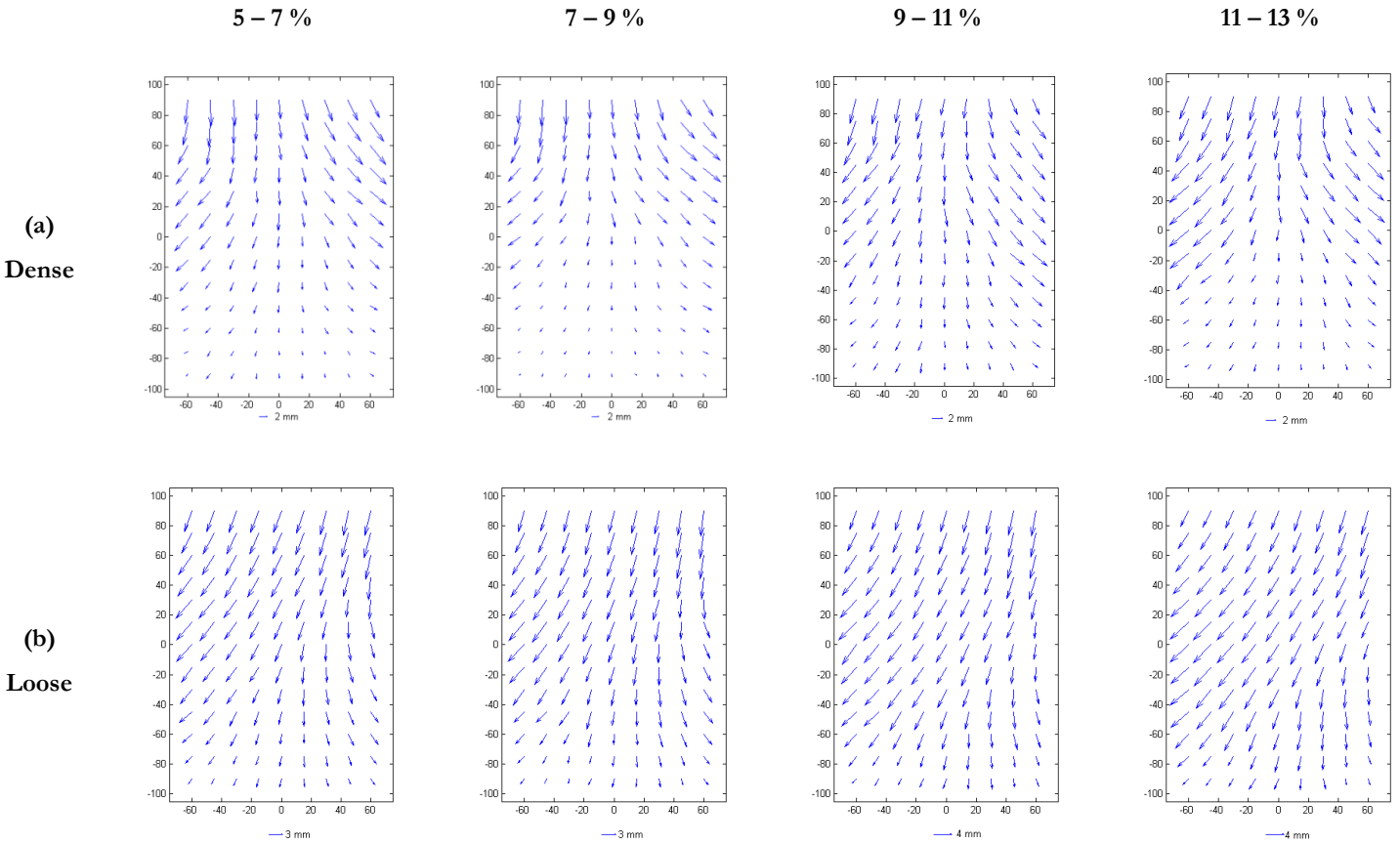

Figure 6.20: Post-peak displacement vectors for unreinforced 1/5 SB specimens (a) Dense (b) Loose

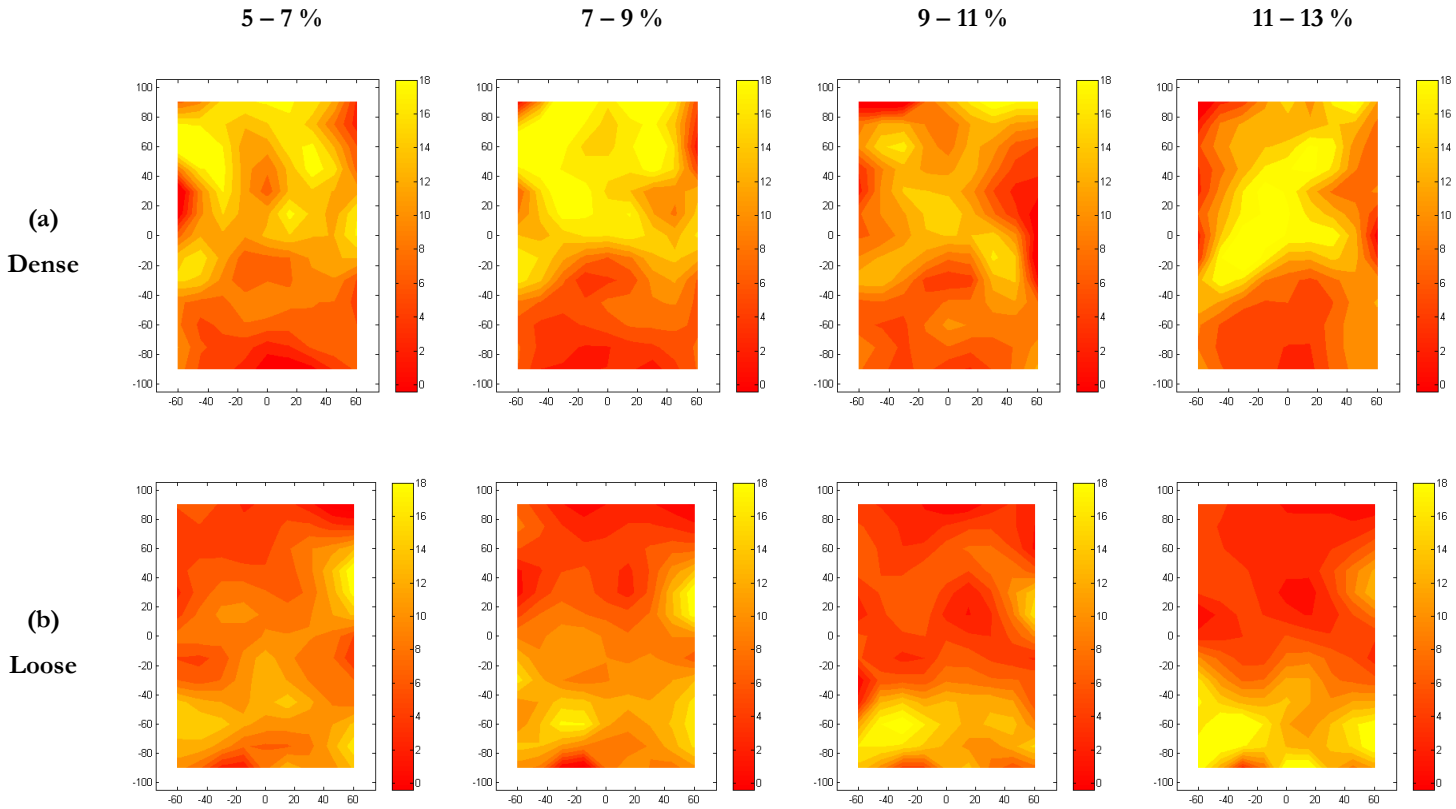

Figure 6.21: Post-peak shear strain fields for unreinforced 1/5 SB specimens (a) Dense (b) Loose

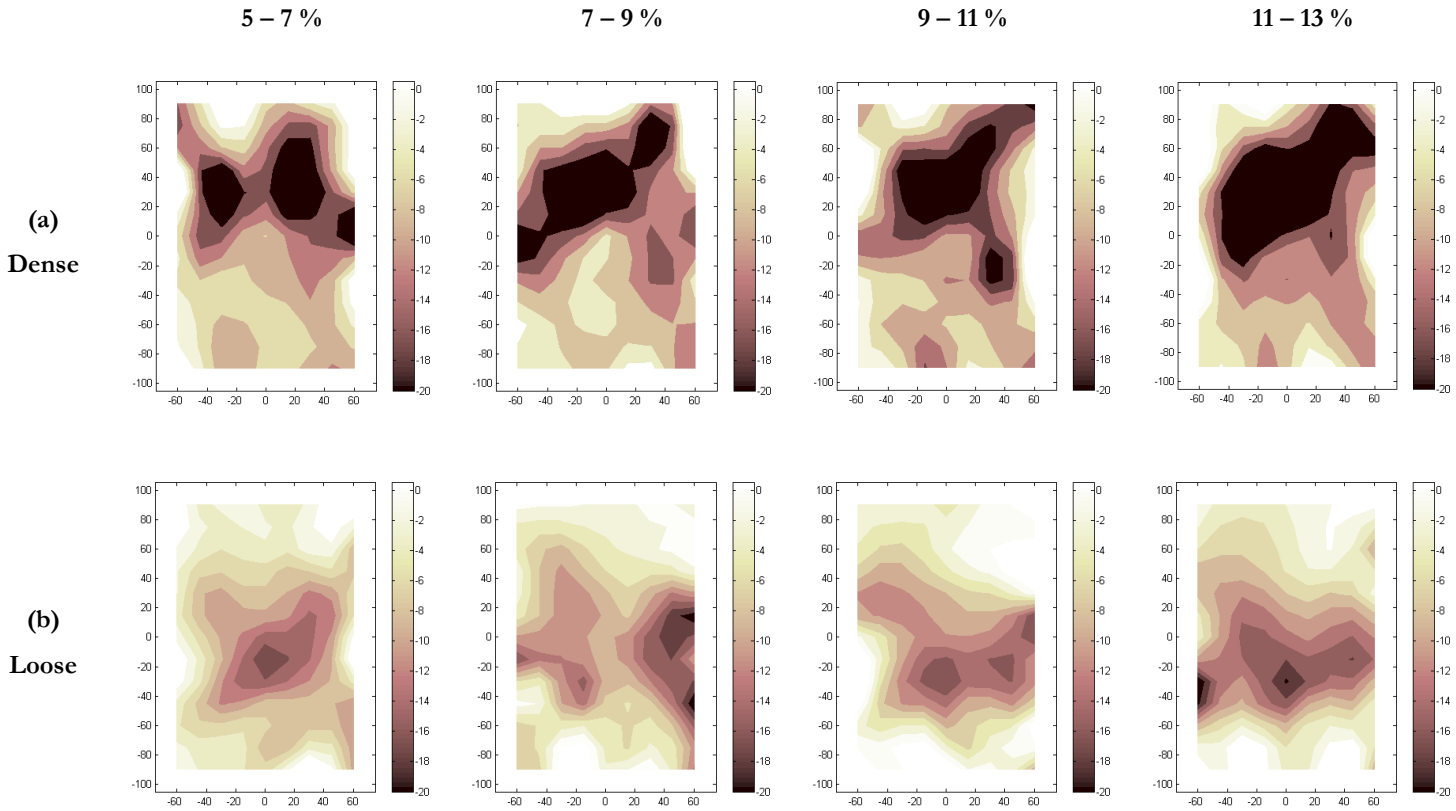

Figure 6.22: Post-peak volumetric strain fields for unreinforced 1/5 SB specimens (a) Dense (b) Loose

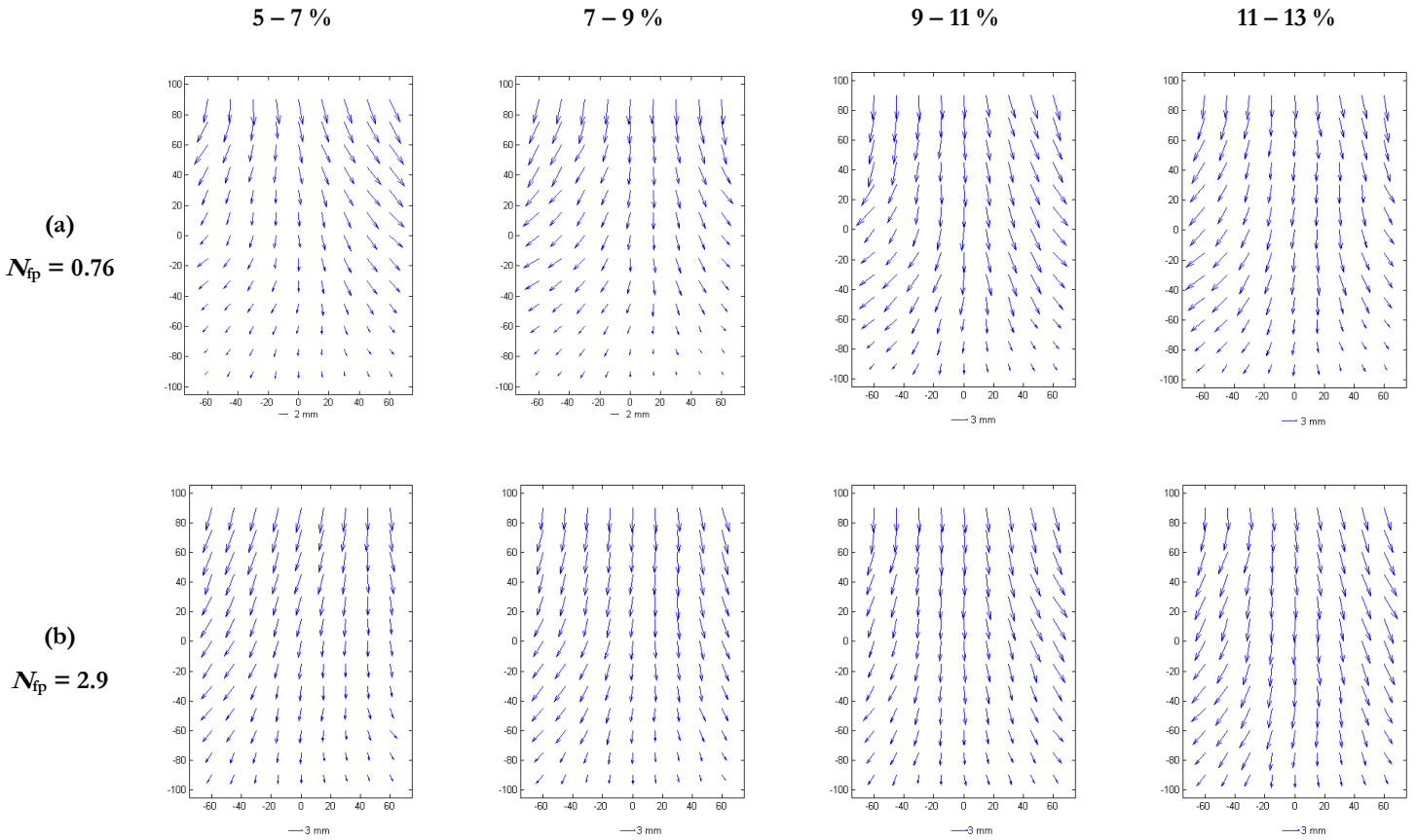

Figure 6.23: Post-peak displacement vectors for fibre reinforced 1/5 SB specimens (a) N_{fp} = 0.76 (b) N_{fp} = 2.9

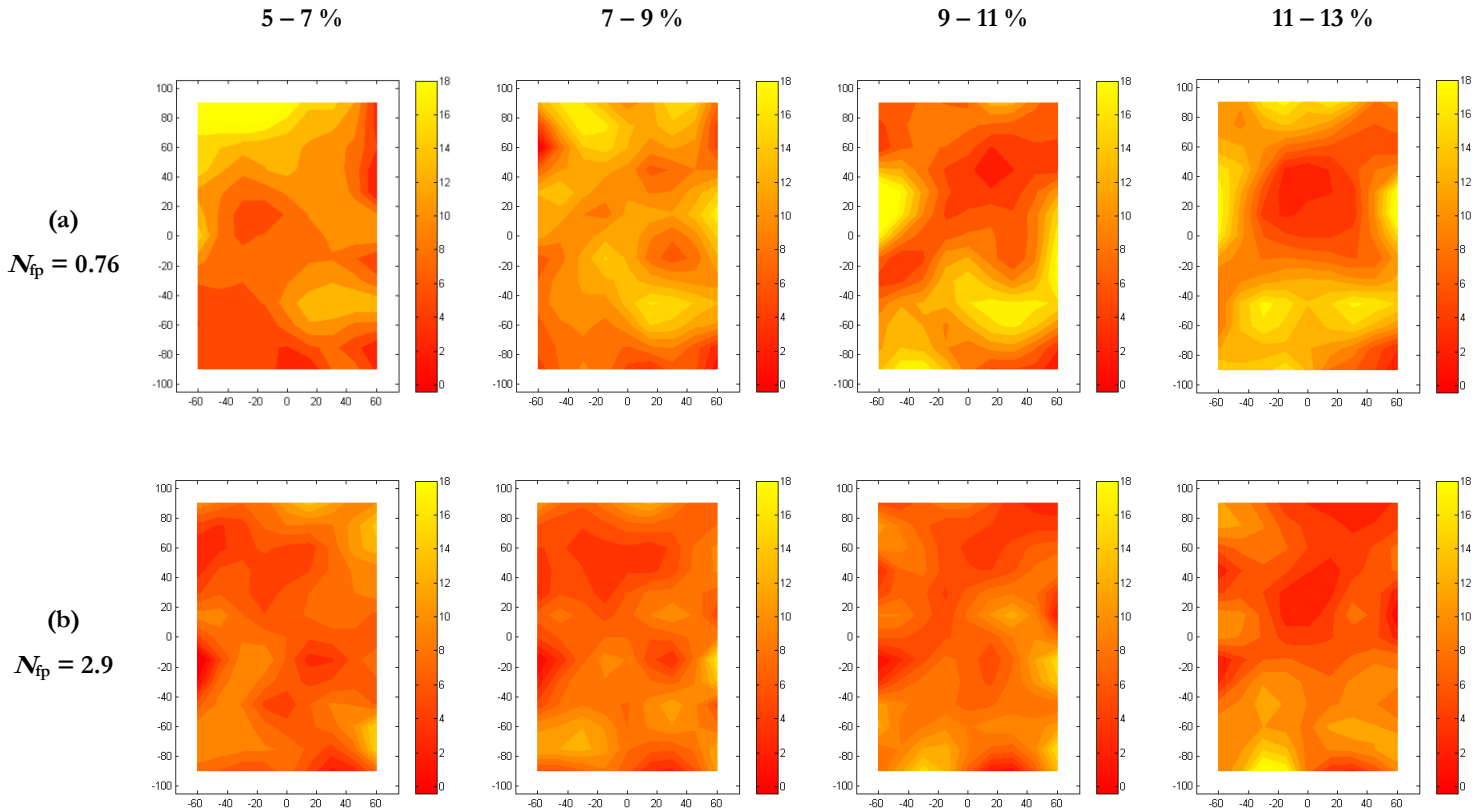

Figure 6.24: Post-peak shear strain fields for fibre reinforced 1/5 SB specimens (a) N_{fp} = 0.76 (b) N_{fp} = 2.9

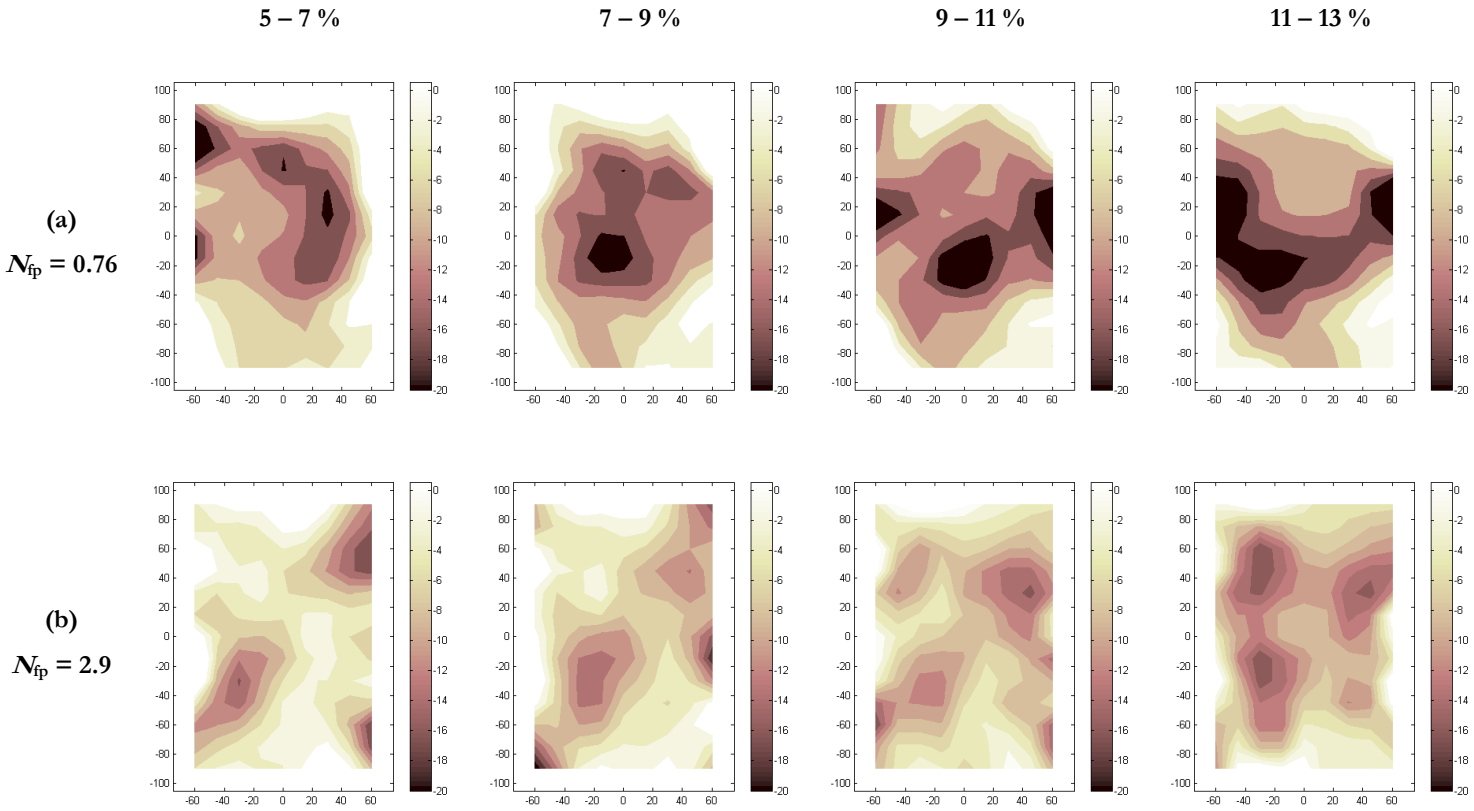

Figure 6.25: Post-peak volumetric strain fields for fibre reinforced 1/5 SB specimens (a) N_{fp} = 0.76 (b) N_{fp} = 2.9

6.6 Discussion

The pre-peak and post-peak deformation characteristics of unreinforced and fibre reinforced 1/5 SB specimens at constant confining pressure have been investigated using a digital image-based deformation measurement technique. During the pre-peak deformation stage, the deformation of the Dense, Loose and N_{fp} = 0.76 specimens was characterised by the initiation of non-distinct localised strains. The onset of the strain localisation coincided with the yielding of the specimen as seen in the stress ratio, q/p' plots (Figure 6.10 and 6.11). However, the N_{fp} = 2.9 specimen did not exhibit localised strains in the same manner as the Dense, Loose and N_{fp} = 0.76 specimens in all the deformation steps analysed. During the pre-peak deformation stage, the lack of substantial shearing of the N_{fp} = 2.9 specimen could be due to the looser packing of the granular matrix.

While the literature on the subject shows some disagreement, there is a growing consensus that the development of strain localisations in granular materials during shear starts at the onset of dilation (Desrues et al., 1996; Bhandari and Powrie, 2013a). Although strain localisation is not readily discernible by the naked eye until a clear shear band develops (Alshibli et al., 2003; Rechenmacher, 2006), it is evidenced in the current tests by the bulging deformation of the unreinforced dense sample (**Error! Reference source not ound.**(a)) and inverted 'V' shaped deformation contour pattern in **Error! Reference source not found.**(a). Strain localisation is associated with the development of micro voids (e.g. Desrues et al., 1996; Hall et al., 2010), as individual particles rotate and displace leading to the disruption of the fabric and the destructurisation of the material (Cresswell and Powrie, 2004). It is conjectured that the addition of fibres to scaled ballast inhibits the disruptive processes of particle rotation and displacement that lead to localised deformation during the early stages of a shear test. At larger displacements, tension in the fibres increases the effective confining stress to the grains and also suppresses dilation.

The post-peak deformation stage was also characterised by a more homogenous distribution of strains (shear and volumetric) in the reinforced specimens than the unreinforced specimens. The degree of uniformity in strains appears to be influenced by increasing N_{fp} (or fibre content). This indicates that strain distribution in the reinforced specimens is predominantly influenced by the reinforcing effect of the fibres. At large strains, fibres in granular materials are believed to be undergoing significant stretching thereby mobilising their tensile forces. This in turn creates an apparent confinement of the granular matrix (Diambra et al., 2013) and thus a diffused non-distinct strain localisation in the specimen. This suggests that fibre reinforcements in railway ballast can potentially reduce shear deformation (evident through reduced lateral spread) while increasing the mobilised strength of the composite. In addition, the more uniform distribution of strains

as observed in the reinforced scaled ballast specimen can potentially lead to a re-distribution of stresses (vertical and horizontal) within the reinforced ballast layer.

6.7 Conclusions

The image-based deformation measurement technique was used to investigate the deformation characteristics of unreinforced and reinforced 1/5 SB specimens and the following conclusions can be drawn:

1. During the pre-peak deformation stage, the occurrence of non-distinct localisation of strains is significantly influenced by the packing structure of the specimens. During this stage, the N_{fp} = 2.9 specimen exhibited a more nearly vertical deformation pattern (i.e. less lateral strain) than the Dense, Loose and N_{fp} = 0.76 specimens.
2. The reinforced specimens exhibited a more homogenous distribution of strains than the unreinforced specimens at larger axial strains (i.e. post-peak deformation). This behaviour can be attributed to the mobilisation of tensile forces in the reinforced specimens which in turn imposes a more uniform shear deformation of reinforced specimens especially at high fibre contents (i.e. N_{fp} = 2.9).
3. Initially, it is hypothesised that the smaller and more uniform strains in the reinforced specimens are a result of the presence of the fibres inhibiting the rotation and movement of individual grains that would otherwise lead to dilation and strain localisation.
4. The effects of fibre reinforcements on the deformation of reinforced 1/5 SB specimens as presented in this chapter suggests that shear deformation in reinforced railway ballast may be inhibited by the apparent confinement of the granular matrix provided by the fibres.

Chapter 7

Full-Scale Laboratory Tests on Fibre Reinforced Railway Ballast

7.1 Introduction

Model laboratory tests are a common feature of geotechnical engineering research owing to their cost-effectiveness and relative simplicity. In railway research, field testing of railway ballast under operating conditions is desirable. However, the high cost of such tests, the difficulty of access to the track and the inability to control adequately the many factors that might influence track behaviour make this unrealistic. This makes the use of full scale laboratory tests a viable alternative. Full scale laboratory tests on a rail track section have been reported by Le Pen (2008) and Aursudkij et al. (2009), and on a 1/5 scale model track by Ishikawa et al. (2011). These researchers have demonstrated that significant understanding of the mechanics of railway ballast and other factors including the type of sleeper, sleeper/ballast interface, loading conditions, ballast gradation and the effect of moving wheel loads on principal stress rotation can be developed.

In the preceding chapters, fibre reinforcements in LB sand, 1/5 and 1/3 scaled ballast have been shown to influence the mechanical properties (e.g. mobilised strength, volumetric behaviour) of the mixture. Across different particle size ranges, these mechanical properties were shown to be influenced by the N_{fp} (as defined in Section 5.4) and the relative dimensions of the fibre and matrix material (i.e. L_N and W_N). These results were obtained from monotonic triaxial tests which do not represent typical field loading conditions in a rail track (Brown, 1996).

In this chapter, the mechanical behaviour (i.e. plastic settlement, stiffness, stress distribution) of a fibre reinforced ballast (FRB) layer compared with an unreinforced ballast layer is investigated using the Southampton Railway Test Facility (SRTF). The test on FRB reported in this thesis is not exhaustive but rather an exploratory test. A detailed parametric investigation of FRB using the SRTF is outside the scope of this PhD

research. The aim of this chapter is therefore to demonstrate the feasibility of the application of FRB at full scale when subject to representative field loading conditions.

7.2 Southampton Railway Test Facility

The test rig used is essentially a single sleeper track recreated in the laboratory (Figure 7.1). It comprises two vertical sides 5 m long and 0.65 m high (Figure 7.2) held apart at a fixed distance of 650 mm, which is equal to a typical sleeper spacing. To impose plane strain conditions on the setup, heavy stiffened steel sections were used in the construction so that significant flexure of the rig will not occur during testing. Plastic sheets were attached to each side of the wall of the rig to minimize friction between the wall and the ballast particles. At the base of the rig, three layers of 12 mm thick rubber sheet were place on the hard laboratory floor to represent a slightly compressible subgrade and prevent ballast crushing.

The deflection of the sleeper during the application of cyclic loads was monitored by attaching six LVDTs at different locations along the sleeper (Figure 7.3). Vertical load (cyclic and static) was applied via a steel loading beam (Figure 7.4) by an INSTRON hydraulic load cell with a maximum capacity of 250 kN and a stroke length of ± 125 mm. To prevent sideways movement of the loading ram during the application of cyclic loads, a knife-edge loading point was attached to the vertical loading ram and a "Vee" socket attached to the loading beam (Figure 7.4(a)and(b)). The loading system was controlled and data logged by a type 8400 INSTRON controller at a rate of 33 data points per load cycle. The accuracy of the hydraulic loading cell was found to be 1% of stroke length and 1% of actual load (Le Pen, 2008).

To allow the measurement of confining stresses in the longitudinal direction within the ballast layer, four plates were attached to the wall of the test rig as shown in Figure 7.5. Four load cells are attached to the corners of each plate. Each was 300 mm high (corresponding to the thickness of the ballast layer below the sleeper), 250 mm wide and 12 mm thick (Figure 7.5(b) and (c)).

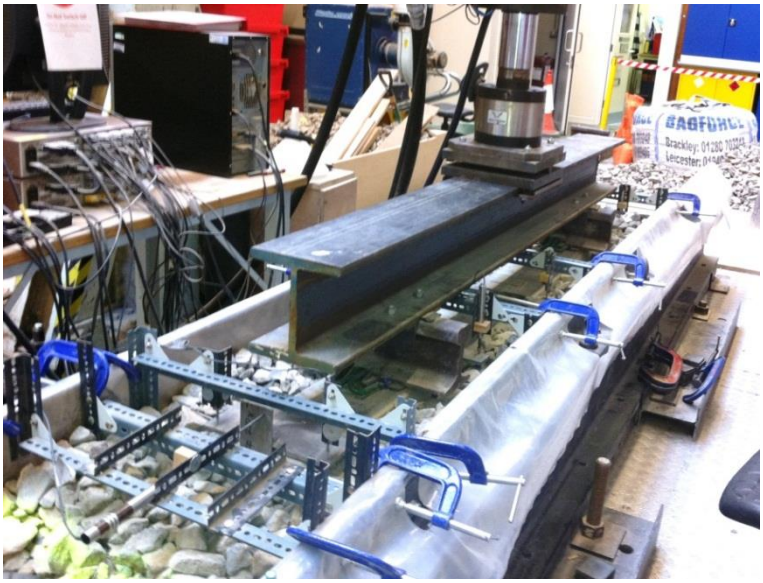

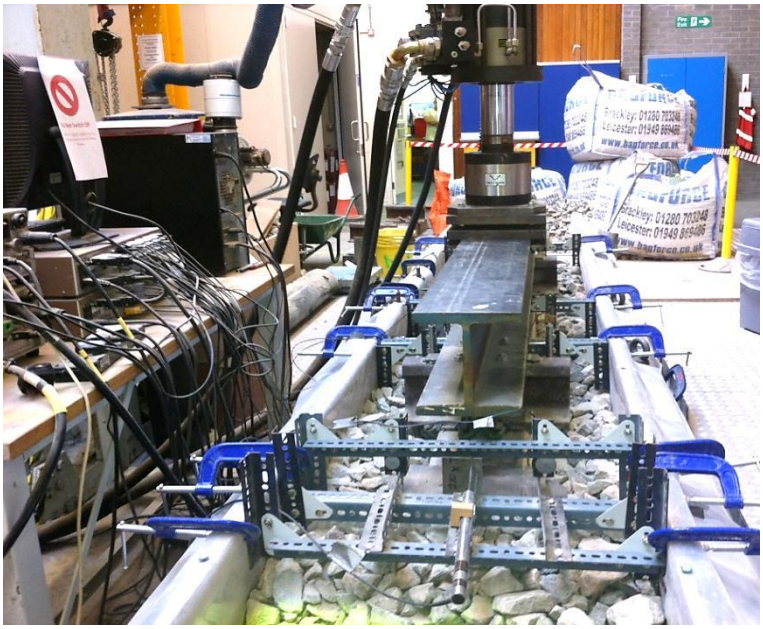

Figure 7.1: Different views of SRTF during testing

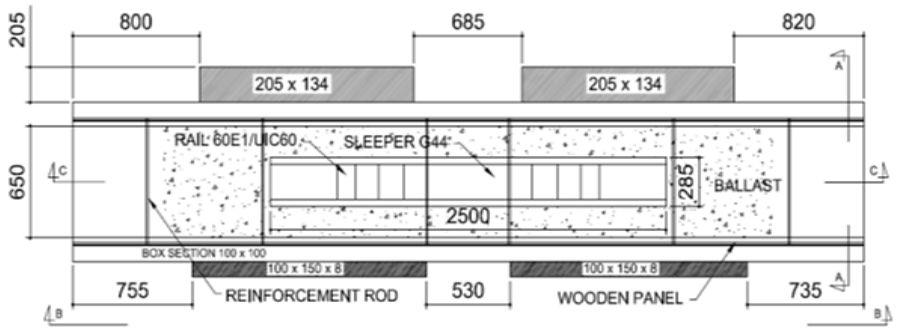

(a)

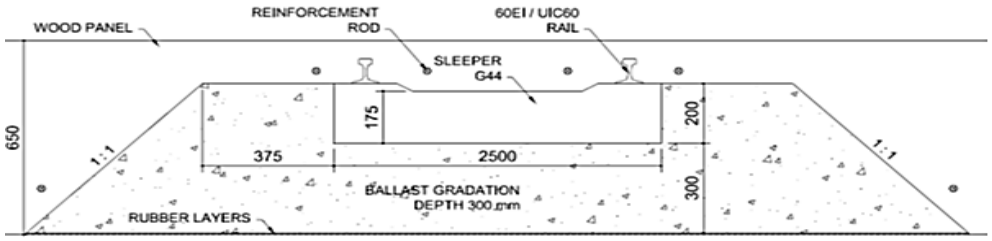

(b)

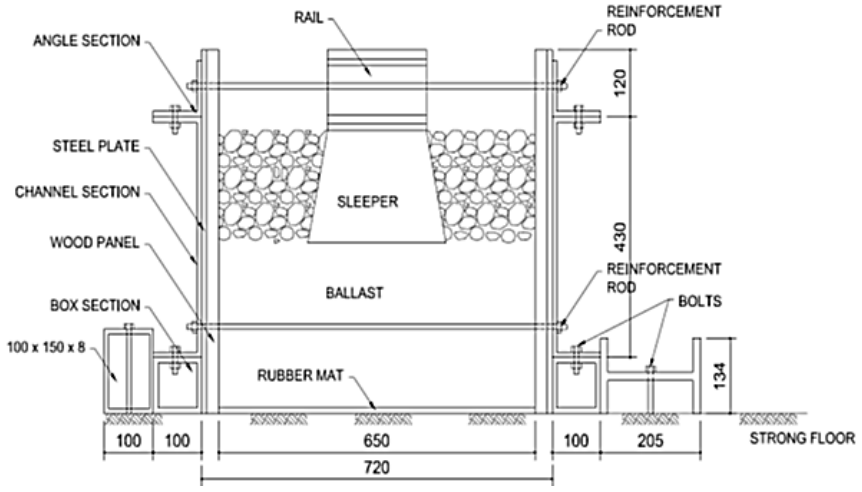

(c)

Figure 7.2: Southampton Railway Test Facility (a) plan view (b) cross-section view (C-C) (c) Side view (A-A) (after Le Pen, 2008)

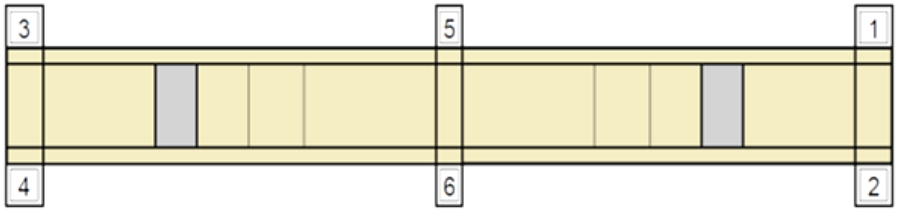

(a)

(b)

(c)

Figure 7.3: LVDT locations in the test rig (a) schematic of sleeper showing six LVDT locations (b) LVDT arrangement on sleeper during test setup (c) typical LVDT attachment showing connecting bracket (courtesy of Taufan Abadi)

(a)

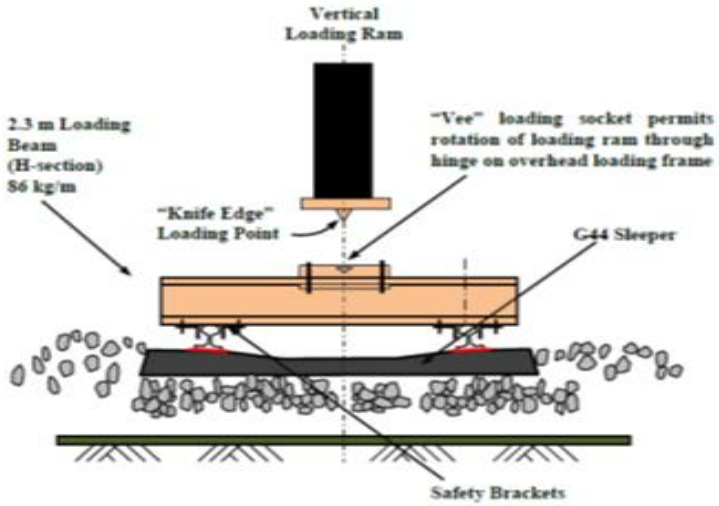

(b)

(c)

Figure 7.4: Vertical load arrangement system (a) loading beam in contact with the 'Vee' loading socket (b) schematic diagram of the loading beam and loading socket (c) overhead reaction frame of the loading system (courtesy of Taufan Abadi)

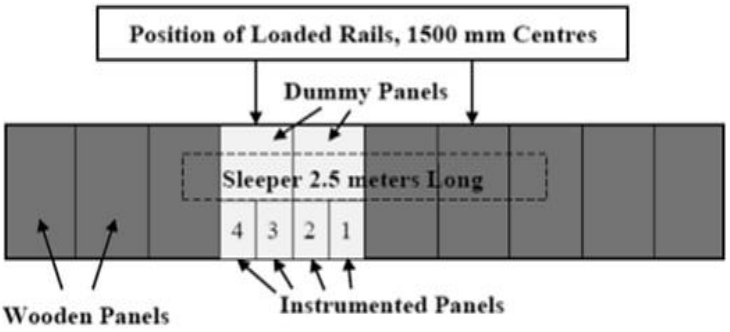

(a)

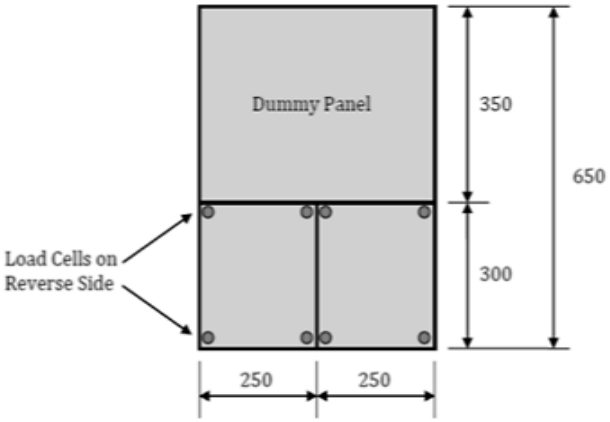

(b)

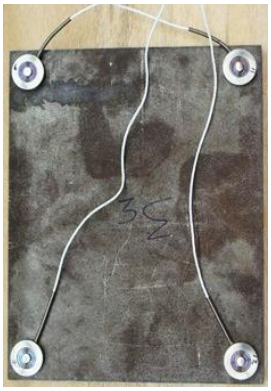

(c)

Figure 7.5: Pressure plate instrumentation (a) instrumented wall panels showing the location of pressure plates (b) schematic diagram of a typical pressure plate attached to the wall of the rig showing its dimensions relative to the wall (c) image of a typical pressure plate showing four load cells glued to its corners (courtesy of Taufan Abadi)

7.3 Test Procedure

7.3.1 Test materials

The ballast material used for these series of tests was crushed granite sourced from Cliffe Hill quarry. Its particle size distribution curve (standard Network Rail gradation) is shown in Figure 3.1. Polyethylene fibres like those reported in the preceding chapters were used and its dimensions and the fibre content (expressed here as N_{fp}) are shown in Table 7.1.

The dimensions of the fibres were chosen so that the normalised length, L_N = 7.5 and normalised width, W_N = 2.5. These values corresponds to the minimum L_N required for an adequate number of fibre-stretch points to develop on an individual fibre and the minimum W_N required for the occurrence of a significant number of fibre/particle contacts so as to produce noticeable macro-mechanical improvement in the ballast/fibre composite (Section 5.5). The fibre/particle number, N_{fp} = 1.33 (V_{fr} ≈ 0.6 %; fibre content by weight ≈ 0.2 %) was used to determine the fibre content of the composite (as described in Section 5.4 and 5.5).

7.3.2 Test setup

Unreinforced ballast

For the test on unreinforced ballast, the sample was placed uniformly into the test rig to achieve a depth of 300 mm. Freshly laid ballast in the field is typically compacted by a specified number of passing of a triple vibrating plate over the ballast. In the full-scale tests, the ballast layer was compacted by an electric plate vibrator with ten passes to create a level and even surface, especially within the vicinity of the sleeper. The density of the ballast layer was 1.64 Mg/m^3 (Table 7.2) which is similar to the typical ballast field density of 1.50 – 1.63 Mg/ m^3 (e.g. Aursudkij et al., 2009; Indraratna et al., 2011). The sleeper was then carefully placed on the ballast layer whilst ensuring it was positioned in the centre of the two vertical walls of the rig (Figure 7.6). The filling of the crib and shoulder continued until they were all level with the surface of the sleeper, creating the desired cross-section as shown in Figure 7.2. The LVDTs were then connected, the loading beam lowered and the "knife edge" ram connection placed across the "Vee" loading beam connection (Figure 7.4). The whole test setup was then left for a minimum of 24 hours to allow the ballast layer to become stable and settle under its own weight.

Table 7.1: Fibres used for the full scale test

	Polyethylene
Fibre length	300 mm
Fibre width	100 mm
Fibre thickness	0.5 mm
Fibre/particle number, N_{fp}	1.33

Table 7.2: Density of the test materials

Material	V_{fr} (%)	Density (Mg/m^3)
Unreinforced ballast	-	1.64
Reinforced ballast	0.6	1.63

Fibre reinforced ballast

The setup for the test on fibre reinforced ballast (FRB) was the same as for the unreinforced ballast test, with the exception of the mixing and placing of FRB in the test rig. The mixing of a known mass of fibre and ballast was carried out in small batches. This involved placing ballast and fibres into plastic containers in consecutive layers and then carefully pouring the mixture in to the test rig. The placing of the fibre/ballast mixture into the rig was approached with great care so as to prevent fibre segregation and thus produce an even distribution of fibres within the ballast layer. It was found by inspection that the mixture had a reasonably even distribution of fibres after it was placed in the test rig (Figure 7.7). The density of the fibre reinforced ballast layer is shown in Table 7.2.

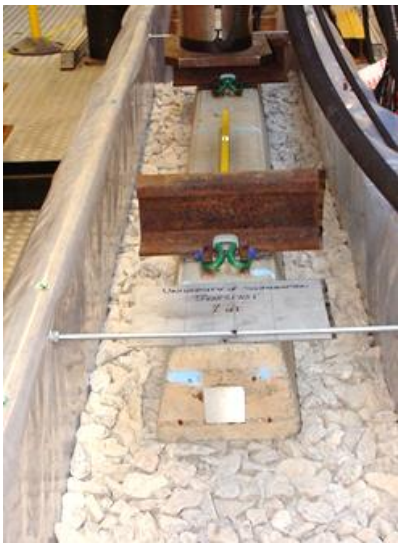

Figure 7.6: Sleeper placed on top of compacted unreinforced ballast layer (courtesy of Taufan Abadi)

Figure 7.7: Fibre reinforced ballast layer in the test rig before compaction

Cyclic loading

A cyclic load in the form of a sine wave was applied on the sleeper via the loading beam. The minimum and maximum values of load applied were 5 kN and 98.1 kN respectively at a frequency of 3 Hz. The first load cycle of each test was static, as the vertical load was ramped up to the maximum (i.e. 98.1 kN), reduced to the minimum (i.e. 5 kN) and then increased back to the datum (49 kN). Before applying the vertical load, the hydraulic loading cell was warmed up by setting the load ram to perform several up-down movements without coming in contact with the loading beam. This was to ensure that there was enough oil pressure in the system to attain the designated load.

7.4 Results[1]

7.4.1 Typical ballast layer settlement

Figure 7.8 shows the typical minimum and maximum irrecoverable settlement of the ballast layer during each load cycle as measured from the top of the sleeper ends by the LVDTS. By comparing LVDT 1 and 3, and LVDT 2 and 4 in Figure 7.8(a) and (b), the general trend and magnitude of the settlement are observed to be similar. To eliminate the effects of lack of adequate contact between the underside of the sleeper and ballast particles, and any density variation of the ballast layer, the first 10 cycles were not considered in the analysis. After the first 10 cycles, the sleeper and ballast layer can be considered to have stabilised.

Typical plots showing the development of the irrecoverable settlement of the ballast layer with the number of load cycles are shown in Figure 7.9. The trend of the linear and semi-logarithmic scale plots agrees well with the results of previous researchers (e.g. Anderson and Fair, 2008; Le Pen, 2008; Aursudkij et al., 2009; Indraratna et al., 2010; Sevi and Ge, 2012). The plots show a rapid increase in the plastic settlement with the rate of increase reducing with increasing number of load cycles.

Figure 7.10 shows the static load application with vertical strain (calculated using Eq.(7.1)) for the first load cycle. The plot shows no significant change in the initial stiffness when fibre reinforcement is added to the ballast layer. This could be due to the relatively low fibre content in the fibre reinforced layer, which supports the observations on the effect of fibre content on the initial stiffness of granular materials made in Section 5.3.

$$Vertical\ strain = \frac{\Delta H}{H_0} \tag{7.1}$$

where ΔH and H_0 are the change in height and initial height of the ballast layer respectively.

[1] Full scale tests on unreinforced ballast and analysis of raw data were performed by Taufan Abadi.

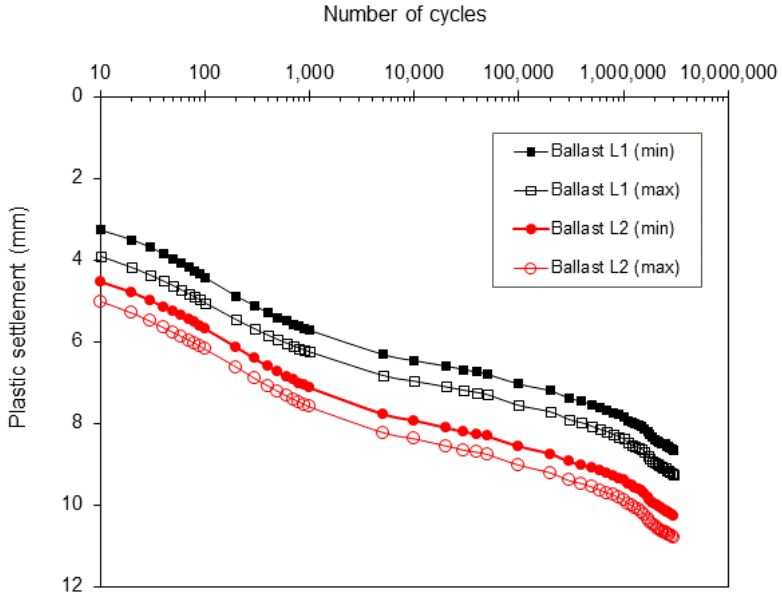

(a)

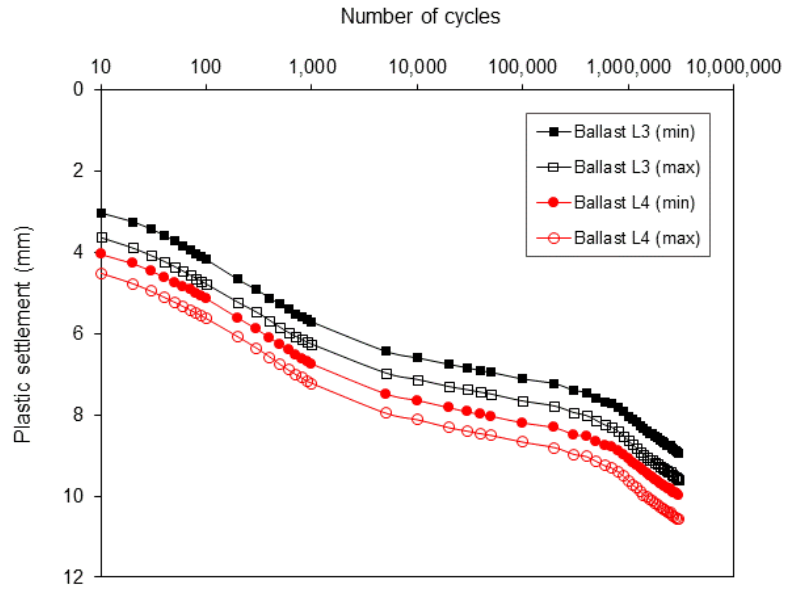

(b)

Figure 7.8: Typical vertical deformation of the LVDTs during cyclic loading of unreinforced ballast (a) LVDT 1 and 2 (RHS of sleeper in Figure 7.3(a)), (b) LVDT 3 and 4(LHS of sleeper in Figure 7.3(a))

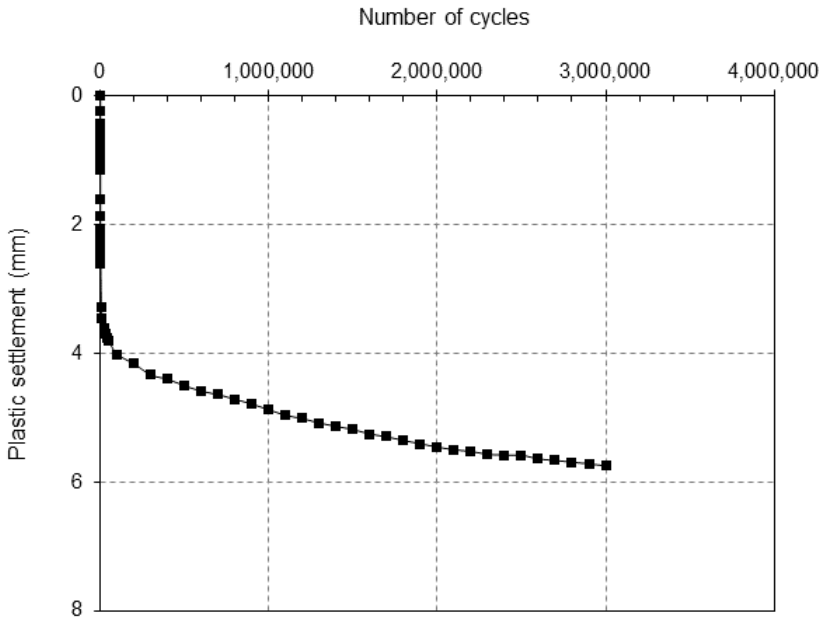

(a)

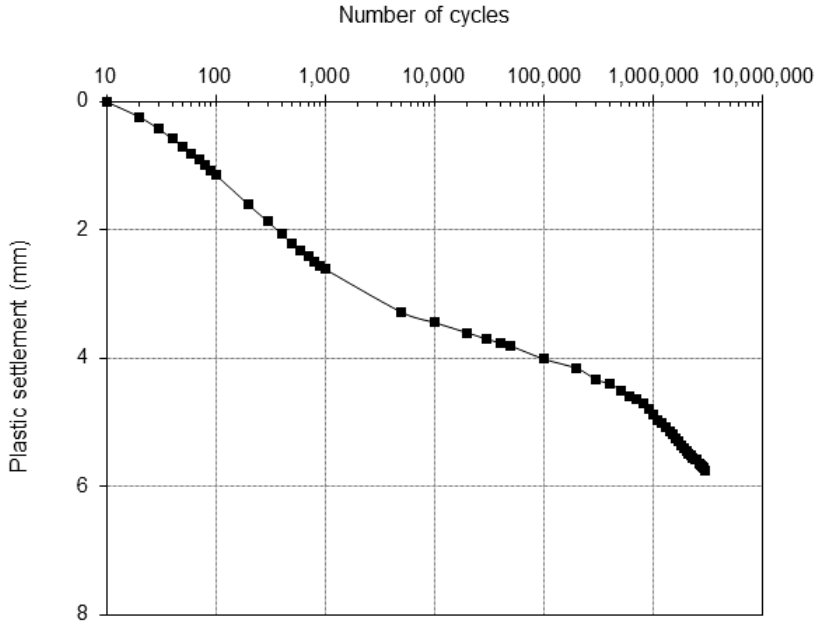

(b)

Figure 7.9: Typical plastic vertical settlement of unreinforced ballast during cyclic loading after re-zeroing plastic deformation at 10 cycles (a) linear scale, (b) semi-log scale

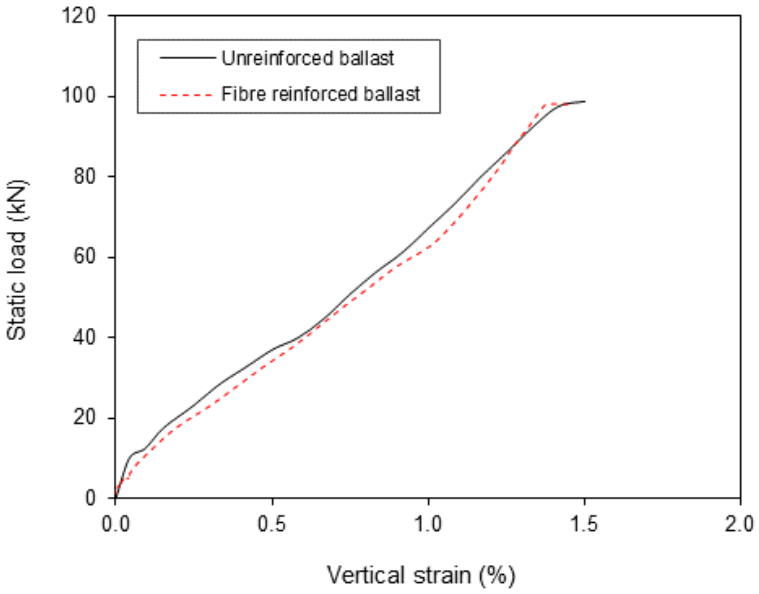

Figure 7.10: Static load application to maximum cyclic load (98.1 kN) on unreinforced and fibre reinforced ballast layer

7.4.2 Plastic Settlement

Figure 7.11 shows that there is a good improvement in the rate of settlement when fibre reinforcement is introduced into the ballast layer. Even though the improvement appears to be slight, the decreased rate at which plastic settlement develops is of significant importance. For example, it takes about 1.3 million load cycles for unreinforced ballast to develop a vertical strain of 1.6 % whereas an additional 1.6 million load cycles are needed for reinforced ballast to attain the same strain (Figure 7.12). This suggests that the use of fibre reinforcement in ballast can potentially increase its lifecycle by 20 %.

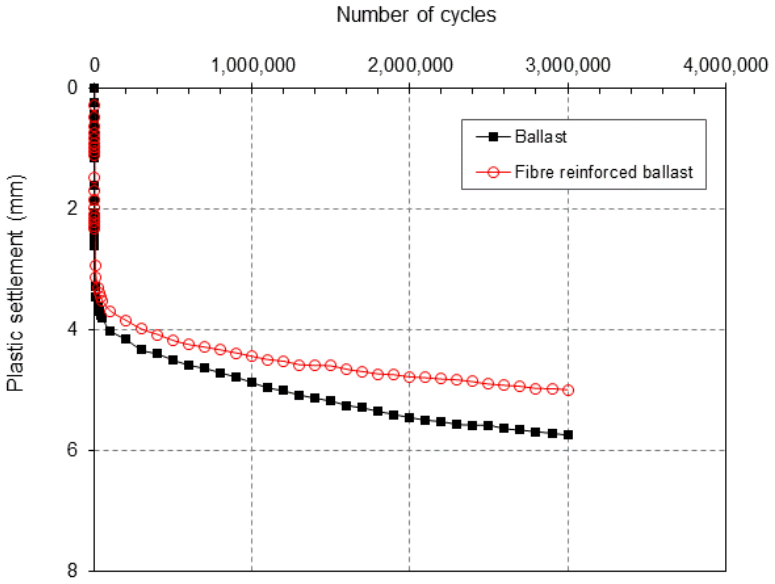

(a)

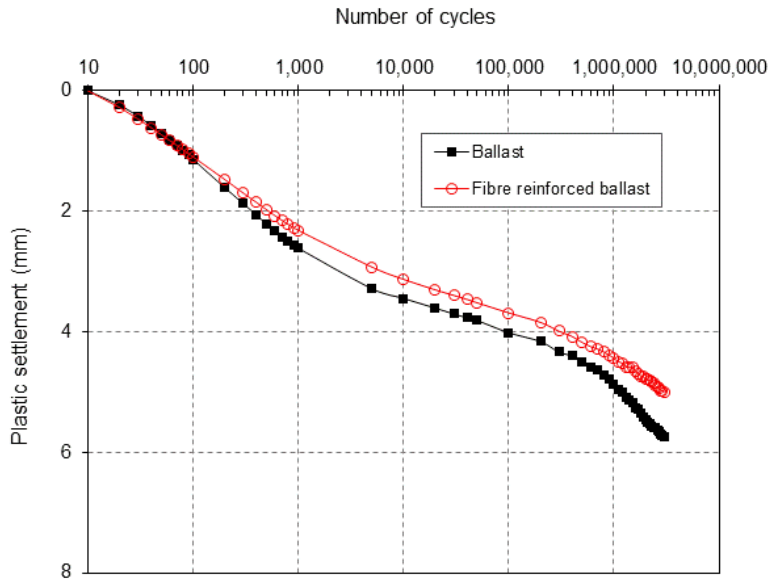

(b)

Figure 7.11: Average plastic deformation of reinforced and unreinforced ballast layer with increasing number of load cycles plotted (a) linear scale (b) semi-log scale

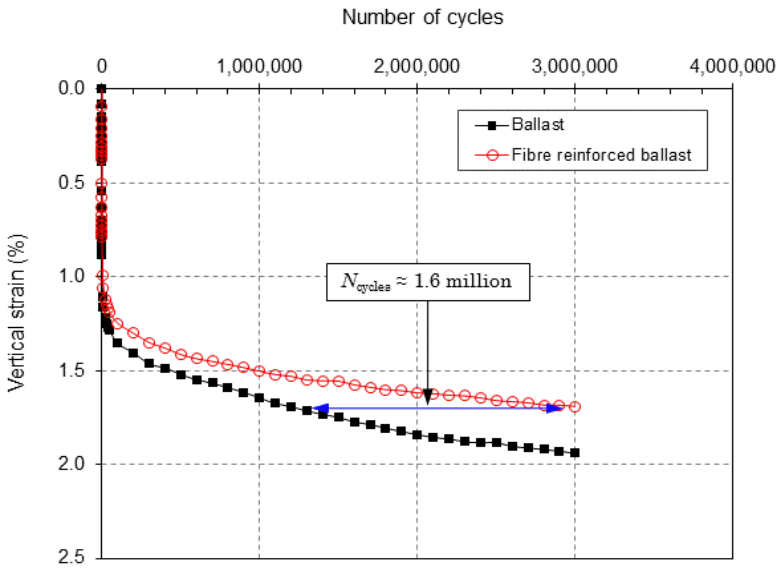

Figure 7.12: Plastic vertical strain plotted against the number of load cycles of reinforced and unreinforced ballast layer highlighting the potential benefit of fibre reinforcements

7.4.3 Stiffness

Track stiffness is calculated here using the Dynamic sleeper support stiffness (DSSS) method. The DSSS method can be defined as "*the peak load divided by the peak deflection of the underside of a rail seat area of an unclipped sleeper subjected to an approximately sinusoidal pulse load at each rail seat; the pulse load being representative in magnitude and duration of the passage of a heavy axle load at high speed*" (NetworkRail, 2005). DSSS is given by,

$$K_i = \frac{F}{2\delta_i} \tag{7.2}$$

where K_i is the track stiffness value (kN/mm), F is the applied load (kN) and δ_i is the deflection read by the i-th LVDT (LVDTi).

Equation (7.2) can be written as Equation (7.3) to account for the range of applied load and measured deflections.

$$K_i = \frac{F_{Max} - F_{Min}}{2\ \delta_{iMax} - \delta_{iMin}} \tag{7.3}$$

where F_{Max}, F_{Min} are the maximum and minimum applied cyclic load, and δ_{iMax}, δ_{iMin} are the corresponding maximum and minimum deflection measured by LVDTi.

Figure 7.13 shows the variation of the average sleeper support stiffness, K, calculated from six LVDTs (as shown in Figure 7.3(a)) with the number of load cycles for reinforced and unreinforced ballast. The plot shows that there is a reduction (about 17%

reduction at 3 million cycles) in the overall sleeper support stiffness for fibre reinforced ballast when compared with the unreinforced ballast.

Figure 7.14 shows the variation of sleeper support stiffness when it is calculated from the mid-sleeper deflections and from the corner of the sleepers. The unreinforced ballast layer showed a gradual increase in stiffness at the middle of the sleeper while the stiffness at the sleeper corners decreased (Figure 7.14(a)). The reinforced ballast layer did not exhibit a significant reduction in stiffness at the corners of the sleeper compared with the unreinforced ballast layer (Figure 7.14(b)). However, an increase in the mid-sleeper stiffness was also observed in the reinforced ballast. To highlight the variation of stiffness across the length of the sleeper, a sleeper-span stiffness ratio, K_{TS} is introduced (Equation 7.4).

$$K_{TS} = \frac{K_m}{K_{sc}} \tag{7.4}$$

where K_m and K_{sc} are the average track stiffness determined at the middle of the sleeper (i.e. from LVDT 5 and 6 as shown in Figure 7.3(a)) and the corners of the sleeper (i.e. from LVDT 1, 2, 3 and 4 as shown Figure 7.3(a)) respectively.

Figure 7.15(a) shows that there is a diverging trend in K_{TS} of the reinforced and unreinforced ballast layers when the number of load cycles exceeds 1 million. At the beginning of the test, the unreinforced ballast layer exhibited a more uniform track stiffness across the sleeper when compared to the reinforced ballast layer (Figure 7.15(b)). The rate of increase in the variation of sleeper support stiffness is greater in the unreinforced ballast layer.

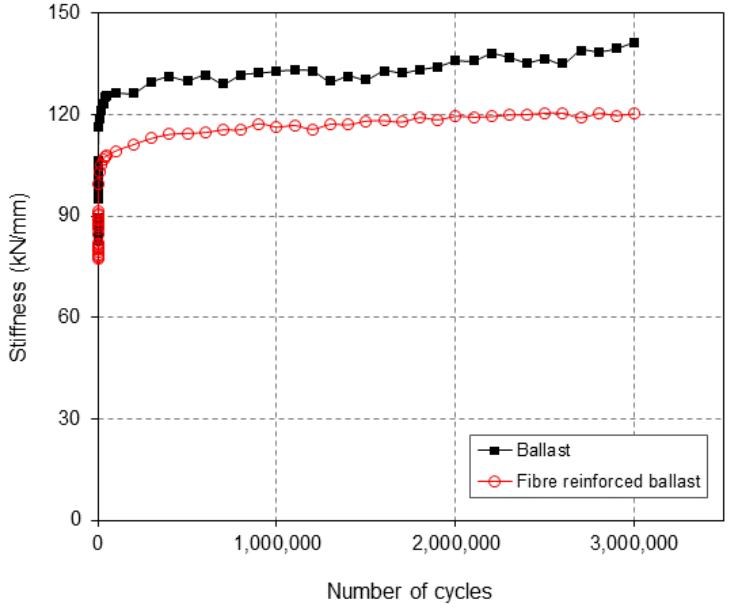

(a)

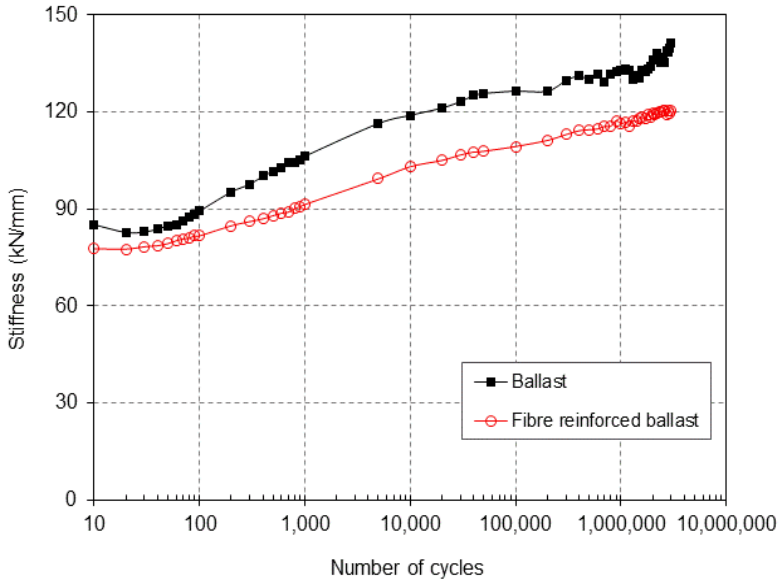

(b)

Figure 7.13: Sleeper support stiffness variation with increasing number of load cycles for unreinforced and reinforced ballast plotted in (a) linear scale (b) semi-log scale

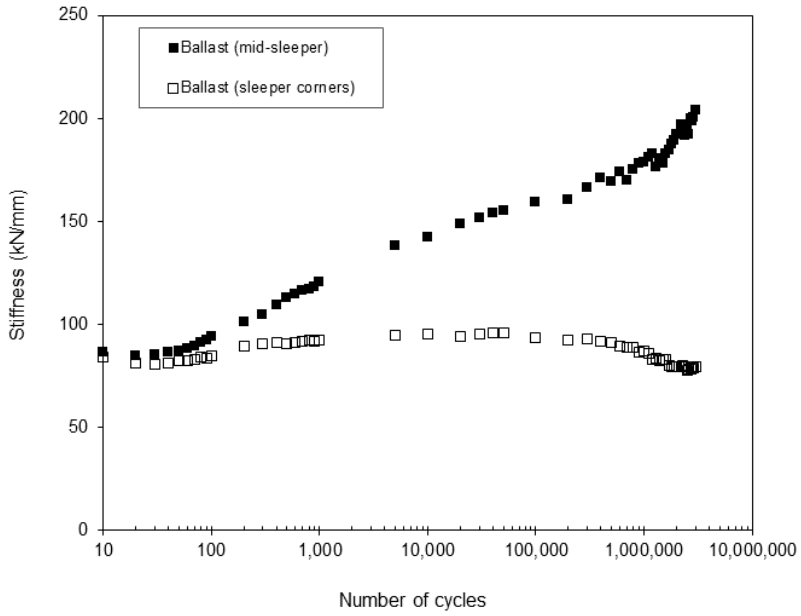

(a)

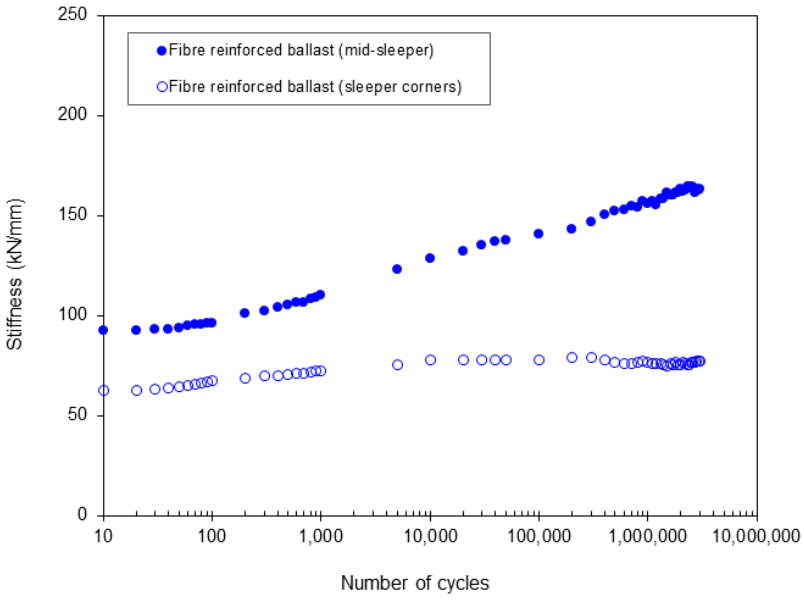

(b)

Figure 7.14: Track stiffness of reinforced and unreinforced ballast calculated using deflections at the middle and corners of the sleeper plotted in (a) linear scale (b) semi-log scale

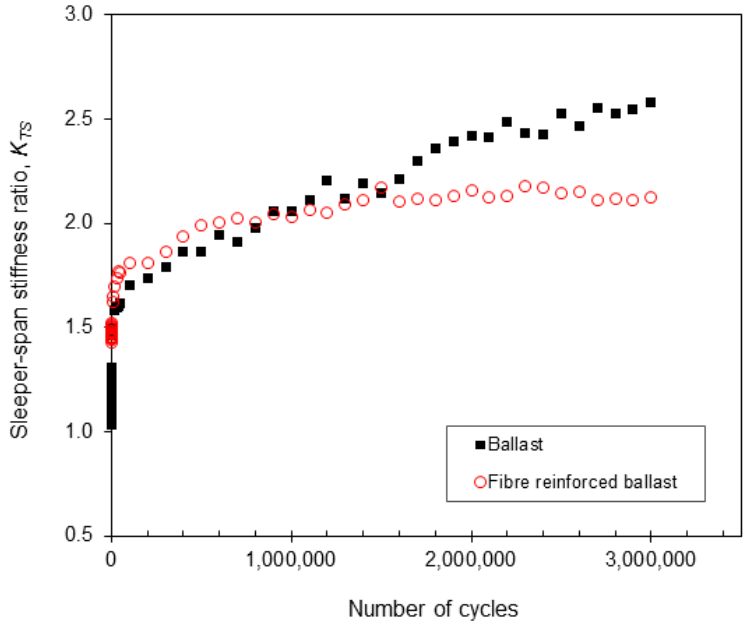

(a)

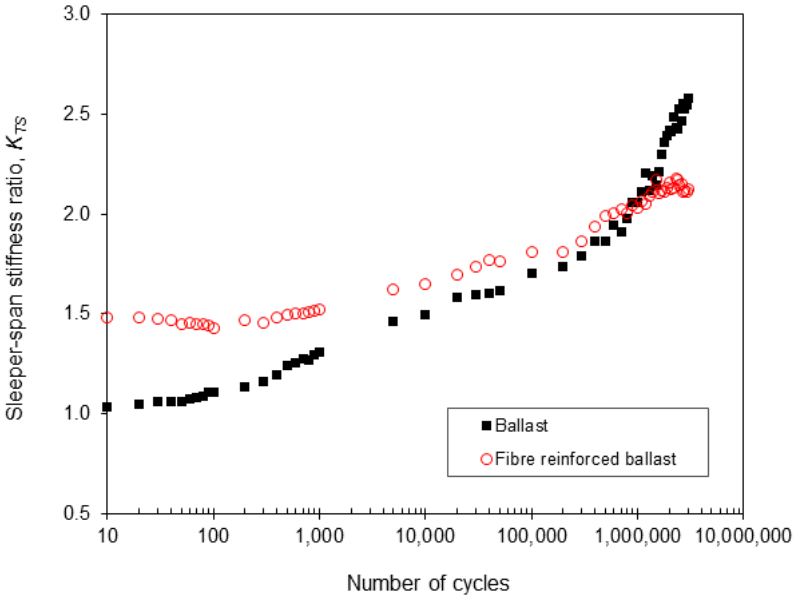

(b)

Figure 7.15: Track/sleeper stiffness ratio, K_{TS} for reinforced and unreinforced ballast plotted in (a) linear scale (b) semi-log scale

7.4.4 Longitudinal pressure

For comparison, data from the pressure plates located near the middle of the sleeper and near the outward side of the rail seat are presented (Figure 7.16). Typical minimum and maximum pressure readings for the unreinforced and fibre reinforced ballast layers as recorded by Plates 1 and 4 are shown in Figure 7.17 and 7.18. The values of the longitudinal pressure were less than 30 kPa and are well within the range of typical values measured in the field by Indraratna et al. (2010). In the unreinforced ballast layer, there is a trend of increasing longitudinal stress towards the middle of the sleeper and a reduction towards the edge of the sleeper as the number of cycles increases (Figure 7.17(a) and 7.18(a)). This indicates the densification of ballast particles towards the middle of the sleeper. However, fibre reinforcements appear to inhibit the continual growth of longitudinal stress towards the middle of the sleeper suggesting that they are also preventing mid-sleeper densification (Figure 7.17(b) and 7.18(b)).

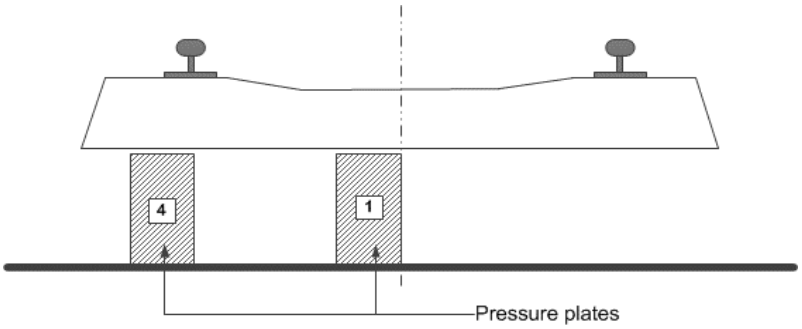

Figure 7.16: Schematic diagram of the cross-section of the test rig showing the locations of the pressure plates relative to the sleeper

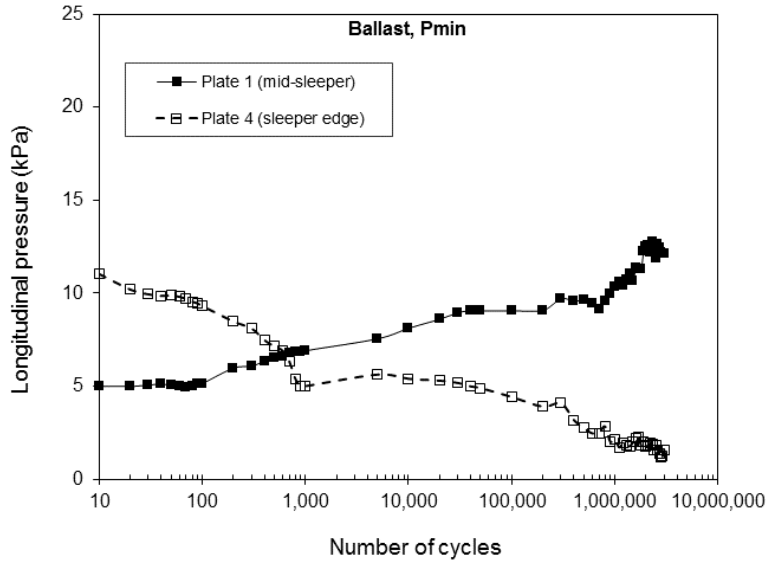

(a)

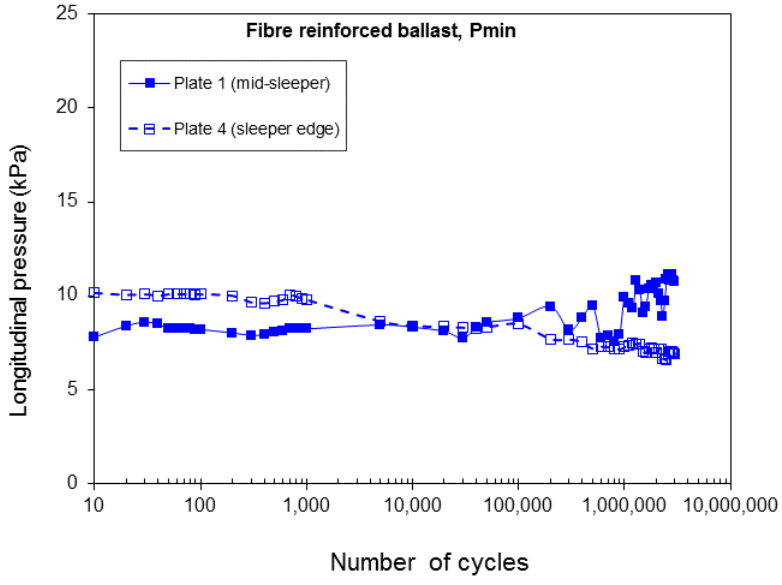

(b)

Figure 7.17: Variation of minimum longitudinal pressure, P_{min} with the number of cycles for (a) unreinforced ballast (b) fibre reinforced ballast

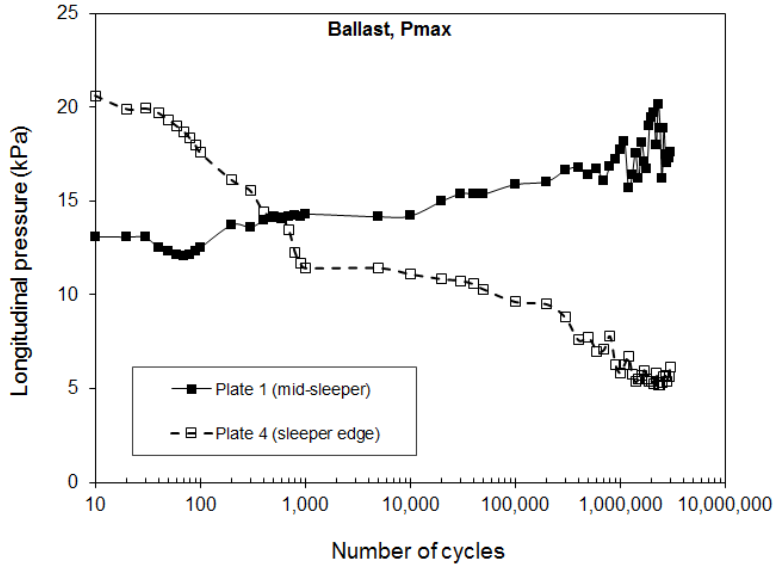

(a)

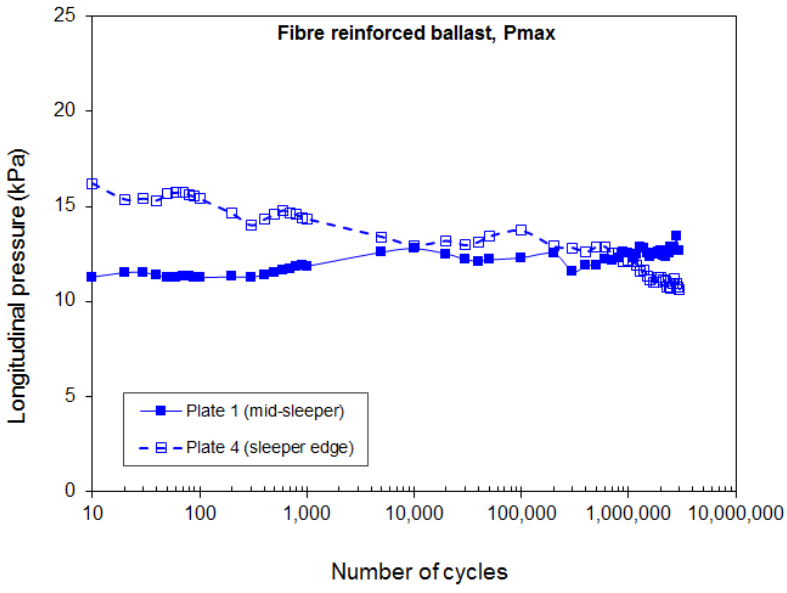

(b)

Figure 7.18: Variation of maximum longitudinal pressure, P_{max} with the number of cycles for (a) unreinforced ballast (b) fibre reinforced ballast

7.5 Discussion

The decreased rate of plastic settlement with increasing number of load cycles in the fibre reinforced ballast layer can be attributed to the mobilisation of tensile force in the fibres. The test results presented in this chapter suggests that the propensity for the mobilisation of tensile force in the fibres is greater than those experienced in the monotonic triaxial tests. This could be due to a combination of factors: (1) the typical rapid initial stabilisation experienced by the reinforced ballast layer at the beginning of the test, (2) relatively low fibre content of the reinforced ballast layer, and; (3) the additional confinement provided by the rigid walls of the apparatus.

During the first few cycles, the initial stabilisation that ballast undergoes is influenced by several factors including ballast density and sleeper/ballast contact interface. In addition to the initial stabilisation of the ballast particles, the first few cycles also allow the development of fibre/particle contacts. These contact points later evolve to become fibre-pinch contact points (Figure 5.25) upon the accumulation of irrecoverable shear strain within the reinforced ballast layer. The mobilised tensile force induced in the fibres reduces irrecoverable vertical strain by inhibiting the lateral spread of the ballast particles. This is similar to the reduction in the loss of fabric in the minor principal strain direction (lateral direction) of two dimensional DEM of fibre reinforced sands (Maeda and Ibraim, 2008) and the apparent increase in confinement of DEM geogrid reinforced ballast (Lu and McDowell, 2010; Chen et al., 2012).

The sleeper support stiffness provided by the fibre reinforced ballast layer was more uniform across the sleeper length than that provided by the unreinforced ballast layer (Figure 7.14). This behaviour is also evident in the more uniform longitudinal stresses measured at the middle and at the ends of the sleeper (Figure 7.17 and 7.18). The reduction in confining stress at the edge of the sleeper is indicative of a loss of support to the sleeper by the ballast particles. The presence of fibres in ballast can thus potentially provide a more homogenous stress and strain distribution within the mixture. This is similar to the observations made in Section 6.6 for triaxial tests.

7.6 Conclusions

Full scale exploratory tests to study the mechanical behaviour of fibre reinforced ballast layer have been carried out using the Southampton Railway Test Facility (SRTF). Based on the experimental results, the following conclusions can be drawn:

1. There was a measurable improvement in terms of reduced plastic settlement when fibre reinforcements were added to the ballast layer.
2. Fibre reinforced ballast exhibited a decreased rate of increase in plastic settlement especially at large number of load cycles (e.g. > 1 million cycles) when compared to unreinforced ballast. Even though the magnitude of the reduced plastic settlement in the reinforced ballast layer was relatively small, there is a potential benefit of about 20% increase in the maintenance cycle of reinforced ballast.
3. The sleeper support stiffness, *K*, of fibre reinforced ballast was slightly lower than the unreinforced ballast layer. The reinforced ballast layer however produced a more uniform stiffness across the length of the sleeper than the unreinforced ballast layer.
4. Fibre reinforced ballast inhibits the accumulation of confining pressure towards the middle of sleeper measured in unreinforced ballast. The addition of fibres in ballast inhibits lateral spreading of the ballast, creating a more uniform distribution of longitudinal stresses within the track section and thus preventing the loss of support at the sleeper corners and may increase the longevity of sleepers.

Chapter 8

Conclusions and Further research

8.1 Conclusions

The aim of this research was to assess the potential effectiveness of improving the mechanical properties of ballast by the addition of random fibres. This aim was achieved by investigating the effects of fibre reinforcements on:

1. The packing structure of granular materials (i.e. LB sand, 1/5 and 1/3 scaled ballast).
2. The mechanical properties of fibre reinforced granular materials through monotonic triaxial tests on granular materials having different ranges of particle sizes.
3. The local deformation of fibre reinforced specimens using an image-based deformation measurement technique for triaxial specimens.
4. The mechanical properties of full size ballast by performing full scale exploratory laboratory tests using the Southampton Railway Test Facility.

The main conclusions drawn from this research are summarised in the following sections.

8.1.1 Packing structure of fibre reinforced granular materials

The addition of fibres to LB sand and scaled ballast was shown to increase the e_{min} and e_{max} of the mixture as the fibre content increases when the compactive effort used remains the same. The presence of fibres in granular material was shown to prevent the close packing of the particles with the added fibres displacing both voids and solids.

8.1.2 Mechanical properties of fibre reinforced LB sand, 1/5 and 1/3 scaled ballast

Triaxial tests

The addition of fibre reinforcements to the LB sand and scaled ballast specimens produced higher peak strengths with a reduced post-peak strength loss while suppressing the dilation of the specimens. In addition to fibre content (V_{fr}), the initial stiffness, mobilised strength and volumetric behaviour of fibre reinforced scaled ballast specimens were found to depend on the normalised dimensions of the fibres (i.e. L_N and W_N). The minimum values of L_N and W_N required to produce a noticeable improvement in the macroscopic behaviour of the mixture were then deduced from the triaxial test results. Across different particle size ranges, the macro mechanical behaviour of the reinforced specimens was found to be more dependent on the fibre/particle number, N_{fp}, rather than fibre content defined in terms of volume (e.g. V_{fr}) or by weight, when the thickness of the fibres is kept constant to ensure they remain flexible.

The experimental results support the hypothesis that the fibre/particle reinforcement mechanism for relatively large sized particles consists of two stages:

1. The development of significant fibre/particle contact (grip) points – this is characterised by the gripping of individual fibres by particles. This stage depends on the fibre/particle number, N_{fp} and the normalised width of fibres (W_N).
2. The mobilisation of tensile force in the fibres – this stage typically occurs during shear deformation that causes the fibres to stretch. The magnitude of the mobilised tensile force in each fibre therefore depends on the number of fibre-stretch contact points on an individual fibre. This in turn will primarily depend on the normalised length of the fibres (L_N) and the fibre/particle number (N_{fp}).

Image-based deformation measurements revealed that the effect of fibres in the reinforced scaled ballast was evident through the more homogenous distribution of shear and volumetric strains at large strains when compared to the unreinforced specimens. This behaviour was attributed to the mobilisation of tensile forces in the reinforced specimens which in turn impose a more uniform shear deformation of reinforced specimens especially at high fibre contents.

Fibre reinforced ballast in full scale laboratory tests

Fibre reinforced ballast (FRB) provided an improvement in terms of reduced plastic settlement when compared to unreinforced ballast. At large number of load cycles (e.g. > 1 million), FRB exhibited a greater resistance to irrecoverable settlement than the

unreinforced ballast layer. In terms of sleeper support stiffness, the FRB layer provided a more uniform stiffness across the length of the sleeper even though the overall stiffness was slightly lower (about 17%) than the unreinforced ballast layer. The FRB layer also provided a more uniform stress distribution by constraining the development of confining stresses toward the middle of the sleeper and reduction of confining stresses at the sleeper edge. This implies that FRB can prevent the loss of support at the sleeper corners.

8.2 Implications of this research for future applications in railway ballast

It is generally agreed that the density of ballast significantly influences its strength and deformation characteristics. Hence, an understanding of the varying densities (both minimum and maximum) that will occur upon the addition of fibres to railway ballast is important both for interpreting its mechanical behaviour through laboratory tests and in the field. An important consequence of the presence of fibres in railway ballast is that changing the volume fraction of fibres V_{fr} at constant void ratio will affect the relative density of the specimen. For example, a specimen at a given void ratio could be relatively loose when V_{fr} is low but relatively dense when V_{fr} is high. During the shearing stage of a triaxial test, it can be argued that the voids (macro and micro) influence the micro-mechanical interactions governing volume change of the specimen (e.g. sliding, rolling, coordination number and local voids), while the shear strength mobilisation is enhanced by the tensile capacity of the fibres in the mixture. This suggests that even though the resulting ballast/fibre mixture might have a higher void ratio (i.e. looser when compared to unreinforced ballast), there are potential benefits in terms of its suppressed deformation and the corresponding shear strength enhancement.

Prior to this research, most (if not all) previous work related to random fibre reinforcement of granular materials has been limited to fine to medium sands thereby creating a knowledge gap in applying this reinforcement technique to large sized aggregates such as railway ballast. By developing a scaling relationship defining the length and width of fibres (i.e. L_N and W_N), and fibre content (N_{fp}), the behaviour of fibre reinforcement across two scales of railway ballast has been shown to have identifiable similarities. These scaling relationships have further enhanced the understanding of fibre reinforcement mechanisms in large-sized aggregates and thus provided a baseline for the use of fibres in railway ballast (as used in the full scale laboratory tests).

Lateral support of railway ballast has been identified as one of the key factors affecting its vertical and lateral deformation and its stiffness (Indraratna et al., 2011). In fibre reinforced soils, the mobilisation of tensile forces in the fibres is believed to produce an

apparent confinement of the matrix materials thereby increasing the peak strength of the mixture (e.g. Diambra et al., 2013). Experimental evidence from the image-based deformation measurements and the full scale laboratory tests carried out in this research suggests that there is an increase in the confinement of the matrix materials (i.e. scaled and full scale ballast). This is evident through the more homogenous shear and volumetric strain distribution of the reinforced scaled ballast specimen and the more uniform sleeper support stiffness and stress distribution in the fibre reinforced ballast layer.

8.3 Further research

The following recommendations are made for further research:

1. The principles of fibre/particle interactions presented here were based on macro observations at the specimen boundaries. To develop better understanding of these interactions at the grain scale, a more robust method of using micro-CT scanning can be adopted. This will substantiate the proposed fibre reinforcement mechanisms for large sized aggregates and analytical interpretative tools.
2. The orientation of the fibres in a typical fibre reinforced scaled ballast or ballast can be investigated using micro-CT scanning and performing extension tests on triaxial samples. In addition, a model apparatus capable of simulating typical rolling load conditions can be built to reproduce principal stress rotation and thus investigate the anisotropy of fibre reinforced materials.
3. The monotonic triaxial tests performed in this research were to provide baseline for further tests and are not representative of the typical cyclic loading experienced by railway ballast in the field. Hence, cyclic triaxial tests will provide an understanding of the effect of fibre reinforcement under cyclic loading.
4. The full scale laboratory tests carried out in this research were not exhaustive but rather exploratory and thus laid a foundation for future tests on fibre reinforced ballast. A comprehensive parametric study of fibre reinforcement in ballast using the full scale apparatus is necessary before any future field trials and subsequent large scale industrial applications of the proposed reinforcement technique in railway ballast can take place.
5. Field trials of fibre reinforced ballast to follow up on the understanding (e.g. potential strain re-distribution, plastic settlement, stiffness etc.) gained from laboratory tests. The field tests will be geared towards developing fibre/ballast field mixing and placement methods, implementation of proposed methods at a field location and monitoring and evaluation of track behaviour.

Appendices

Appendix A

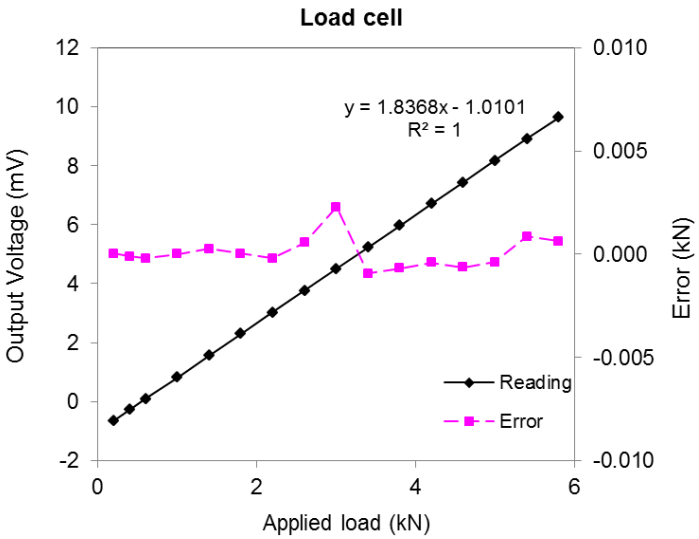

Figure A 1: Calibration result for load cell used in the Mini-Dyn triaxial apparatus

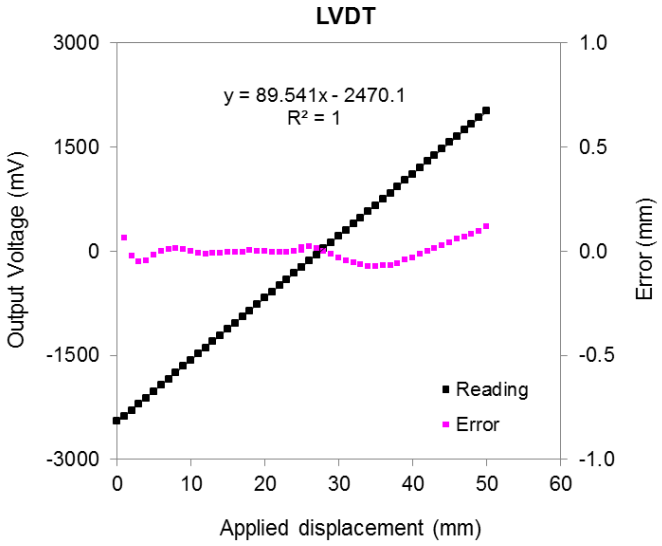

(a)

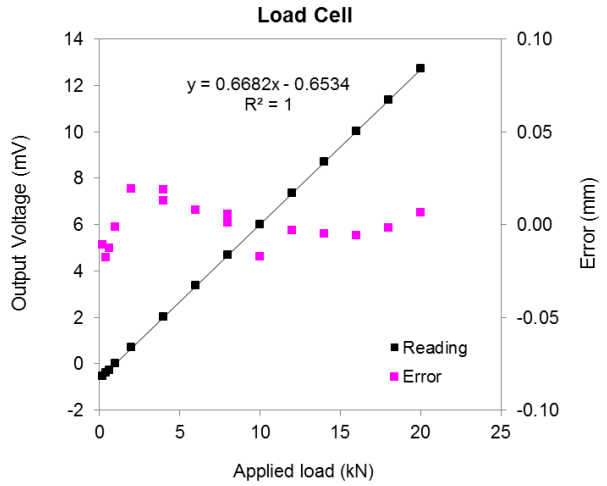

(b)

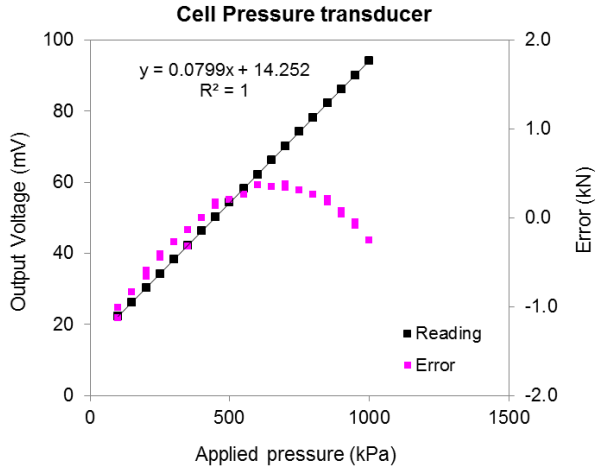

(c)

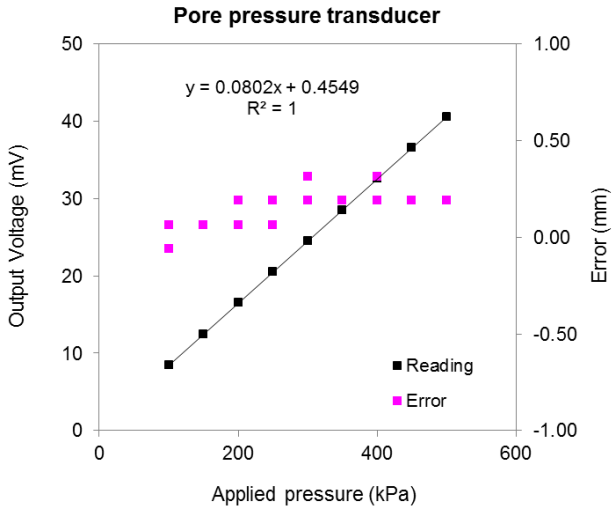

(d)

Figure A 2: Calibration results of instruments used for the 150 mm triaxial apparatus (a) Global axial LVDT (b) Load cell transducer (c) cell pressure transducer (d) Pore pressure transducer

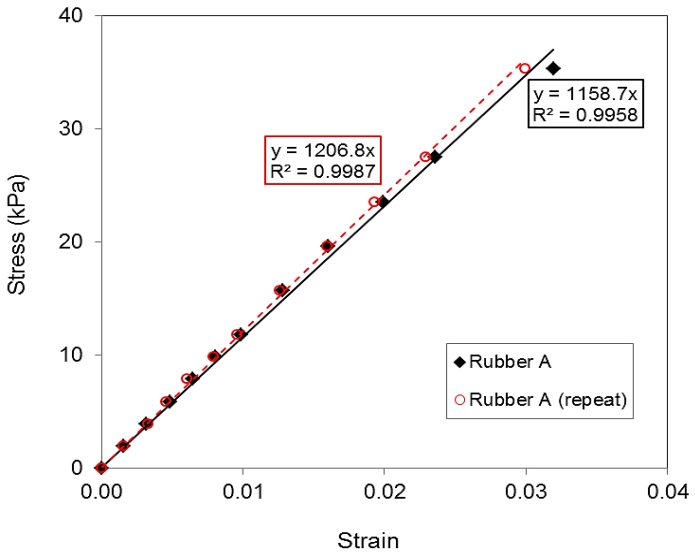

Figure A 3: Young Modulus determination from extension tests

Appendix B

Calibration of Cameras

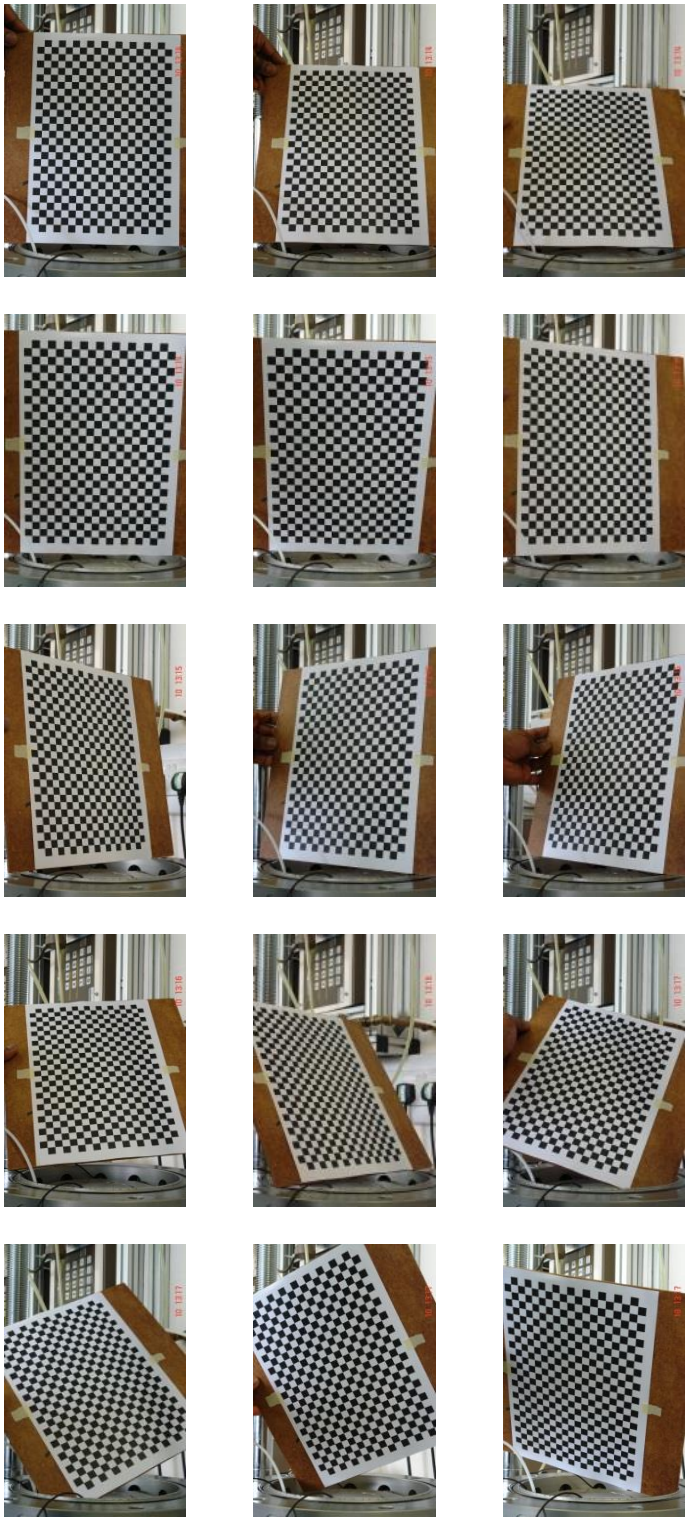

Figure B 1: Photographs of the calibration checkerboard used as a calibration pattern at different orientations while the camera was kept stationary. The size of each square is 10 mm × 10 mm.

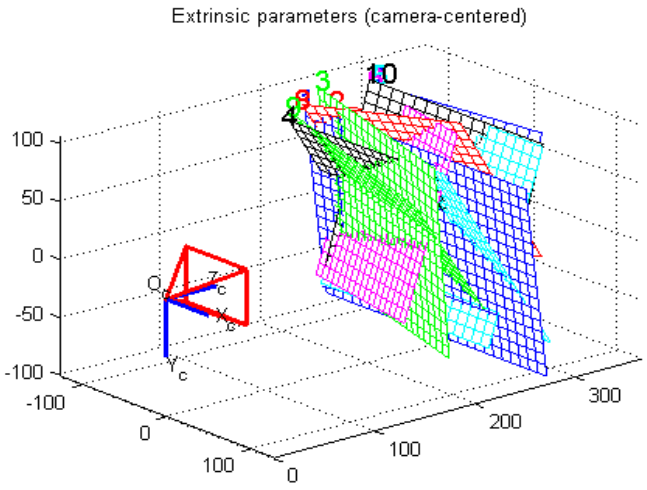

(a)

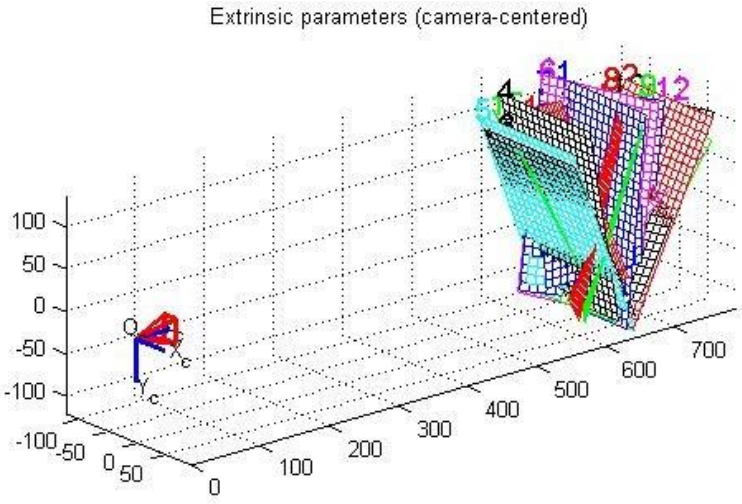

(b)

Figure B 2: Extrinsic parameters (camera-centred) determined for (a) Camera 1 and, (b) Camera 2

Intrinsic parameters for the cameras used

Table B 1: Intrinsic parameters for the camera

Parameter	**Camera 1**	**Camera 2**
Focal Lengths		
$fc(1) = f \times s_y$	2691.62680 ± 1.94603	6702.32790 ± 17.75403
$fc(2) = f \times s_z$	2717.10875 ± 2.00699	6652.26775 ± 18.76034
$cc(1) = o_y$	1938.36541 ± 2.01885	1338.42632 ± 20.22944
$cc(2) = o_z$	1298.92530 ± 1.82751	1965.30021 ± 28.46655
Skew alpha	0.00000 ± 0.00000	0.00000 ± 0.00000
Distortion		
k_1	-0.11135 ± 0.00187	0.07782 ± 0.02930
k_2	0.08044 ± 0.00531	-0.95380 ± 0.54316
k_3	0.00133 ± 0.00016	-0.00215 ± 0.00165
k_4	-0.00033 ± 0.00020	0.00017 ± 0.00119
k_5	0.00000 ± 0.00000	0.00000 ± 0.00000
Pixel error		
err (1)	0.53799	1.60429
err (2)	0.61106	2.06752

References

Ajayi, O., Le Pen, L., Priest, J., Zervos, A. & Powrie, W. (2014). Effects of Fibre Reinforcement on the Structure of Granular Materials. *Transportation Geotechnics, ASCE Geotechnical Special Publication,* In press (In press).

Alshibli, K., Batiste, S. & Sture, S. (2003). Strain Localization in Sand: Plane Strain Versus Triaxial Compression. *Journal of Geotechnical and Geoenvironmental Engineering,* 129 (6) 483-494.

Alshibli, K.A. & Al-Hamdan, M.Z. (2001). Estimating Volume Change of Triaxial Soil Specimens from Planar Images. *Computer-Aided Civil and Infrastructure Engineering,* 16 (6) 415-421.

Anderson, W.F. & Fair, P. (2008). Behavior of Railroad Ballast under Monotonic and Cyclic Loading. *Journal of Geotechnical and Geoenvironmental Engineering,* 134 (3) 316-327.

Atkinson, J.H. (2000). Non-Linear Soil Stiffness in Routine Design. *Géotechnique,* 50 (5) 487-508.

Aursudkij, B., Mcdowell, G.R. & Collop, A.C. (2009). Cyclic Loading of Railway Ballast under Triaxial Conditions and in a Railway Test Facility. *Granular Matter,* 11 (6) 391-401.

Bhandari, A. & Powrie, W. (2013a). Strength and Deformation Characteristics of a Locked Sand at Low Effective Stresses. *Granular Matter,* 15 (5) 543-556.

Bhandari, A.R. (2009). *The Mechanics of an Unbonded Locked Sand at Low Effective Stresses.* PhD Thesis, University of Southampton.

Bhandari, A.R. & Powrie, W. (2013b). Behavior of an Mbt Waste in Monotonic Triaxial Shear Tests. *Waste Management,* 33 (4) 881-891.

Bhandari, A.R., Powrie, W. & Harkness, R.M. (2012). A Digital Image-Based Deformation Measurement System for Triaxial Tests. *Geotechnical Testing Journal,* 35 (2) 209-226.

Blott, S.J. & Pye, K. (2008). Particle Shape: A Review and New Methods of Characterization and Classification. *Sedimentology,* 55 (1) 31-63.

Bouguet, J.-Y. (2008). *Camera Calibration Toolbox for Matlab* [Online]. Available: http://www.vision.caltech.edu/bouguetj/calib_doc/index.html [Accessed 12/02/2014].

Brown, S.F. (1996). Soil Mechanics in Pavement Engineering. *Geotechnique,* 46 (3) 383-425.

Brown, S.F., Kwan, J. & Thoma, N.H. (2007). Identifying the Key Parameters That Influence Geogrid Reinforcement of Railway Ballast. *Geotextiles and Geomembranes,* 25 (6) 326-335.

Cavarretta, I., Rocchi, I. & Coop, M.R. (2011). A New Interparticle Friction Apparatus for Granular Materials. *Canadian Geotechnical Journal,* 48 (12) 1829-1840.

Charles, J.A. & Watts, K.S. (1980). The Influence of Confining Pressure on the Shear-Strength of Compacted Rockfill. *Geotechnique,* 30 (4) 353-367.

Chen, C., Mcdowell, G.R. & Thom, N.H. (2012). Discrete Element Modelling of Cyclic Loads of Geogrid-Reinforced Ballast under Confined and Unconfined Conditions. *Geotextiles and Geomembranes,* 35 (0) 76-86.

Cho, G., Dodds, J. & Santamarina, J. (2006). Particle Shape Effects on Packing Density, Stiffness, and Strength: Natural and Crushed Sands. *Journal of Geotechnical and Geoenvironmental Engineering,* 132 (5) 591-602.

Consoli, N.C., Festugato, L. & Heineck, K.S. (2009). Strain-Hardening Behaviour of Fibre-Reinforced Sand in View of Filament Geometry. *Geosynthetics International,* 16 (2) 109-115.

Cox, H.L. (1952). The Elasticity and Strength of Paper and Other Fibrous Materials. *British Journal of Applied Physics,* 3 72 - 79.

Cresswell, A. & Powrie, W. (2004). Triaxial Tests on an Unbonded Locked Sand. *Geotechnique,* 54 (2) 107-115.

Desrues, J., Chambon, R., Mokni, M. & Mazerolle, F. (1996). Void Ratio Evolution inside Shear Bands in Triaxial Sand Specimens Studied by Computed Tomography. *Geotechnique,* 46 (3) 529-546.

Diambra, A., Ibraim, E., Russell, A.R. & Wood, D.M. (2013). Fibre Reinforced Sands: From Experiments to Modelling and Beyond. *International Journal for Numerical and Analytical Methods in Geomechanics,* 37 (15) 2427-2455.

Diambra, A., Ibraim, E., Wood, D.M. & Russell, A.R. (2010). Fibre Reinforced Sands: Experiments and Modelling. *Geotextiles and Geomembranes,* 28 (3) 238-250.

Diambra, A., Russell, A.R., Ibraim, E. & Wood, D.M. (2007). Determination of Fibre Orientation Distribution in Reinforced Sands. *Geotechnique,* 57 (7) 623-628.

Dos Santos, A.P.S., Consoli, N.C. & Baudet, B.A. (2010). The Mechanics of Fibre-Reinforced Sand. *Geotechnique,* 60 (10) 791-799.

Esveld, C. (2001). *Modern Railway Track*, MRT-Productions.

Fukuda, H. & Chou, T.-W. (1982). A Probabilistic Theory of the Strength of Short-Fibre Composites with Variable Fibre Length and Orientation. *Journal of Materials Science,* 17 (4) 1003-1011.

Fukushima, S., Tatsuoka, F., (1984). Strenght and Deformation Characteristics of Saturated Sand at Extremely Low Pressures. *Soils and Foundations,* 24 (4) 30-48.

Gachet, P., Geiser, F., Laloui, L. & Vulliet, L. (2007). Automated Digital Image Processing for Volume Change Measurement in Triaxial Cells. *Geotechnical Testing Journal,* 30 (2) 98-103.

Gds. (2014). *Geotechnical Digital Systems* [Online]. Available: http://www.gdsinstruments.com/ [Accessed 06/05/2014 2014].

Gräbe, P. & Clayton, C. (2009). Effects of Principal Stress Rotation on Permanent Deformation in Rail Track Foundations. *Journal of Geotechnical and Geoenvironmental Engineering,* 135 (4) 555-565.

Gräbe, P. & Clayton, C. (2014). Effects of Principal Stress Rotation on Resilient Behavior in Rail Track Foundations. *Journal of Geotechnical and Geoenvironmental Engineering,* 140 (2) 04013010.

Gray, D.H. & Alrefeai, T. (1986). Behavior of Fabric-Reinforced Versus Fiber-Reinforced Sand. *Journal of Geotechnical Engineering-Asce,* 112 (8) 804-820.

Gray, D.H. & Ohashi, H. (1983). Mechanics of Fiber Reinforcement in Sand. *Journal of Geotechnical Engineering-Asce,* 109 (3) 335-353.

Hall, S.A., Bornert, M., Desrues, J., Pannier, Y., Lenoir, N., Viggiani, G. & Besuelle, P. (2010). Discrete and Continuum Analysis of Localised Deformation in Sand Using X-Ray Mu Ct and Volumetric Digital Image Correlation. *Geotechnique,* 60 (5) 315-322.

Heineck, K.S., Coop, M.R. & Consoli, N.C. (2005). Effect of Microreinforcement of Soils from Very Small to Large Shear Strains. *Journal of Geotechnical and Geoenvironmental Engineering,* 131 (8) 1024-1033.

Ibraim, E. & Fourmont, S. (2007). Behaviour of Sand Reinforced with Fibres. *In:* LING, H. I., CALLISTO, L., LESHCHINSKY, D. & KOSEKI, J. (eds.) *Soil Stress-Stain Behavior: Measurement, Modeling and Analysis.*

Indraratna, B., Ionescu, D. & Christie, H.D. (1998). Shear Behavior of Railway Ballast Based on Large-Scale Triaxial Tests. *Journal of Geotechnical and Geoenvironmental Engineering,* 124 (5) 439-449.

Indraratna, B., Nimbalkar, S., Christie, D., Rujikiatkamjorn, C. & Vinod, J. (2010). Field Assessment of the Performance of a Ballasted Rail Track with and without Geosynthetics. *Journal of Geotechnical and Geoenvironmental Engineering,* 136 (7) 907-917.

Indraratna, B., Salim, W. & Rujikiatkamjorn, C. (2011). *Advanced Rail Geotechnology: Ballasted Track*, Taylor & Francis.

Indraratna, B., Wijewardena, L.S.S., Balasubramaniam, A.S. & Mostyn, G. (1994). Large-Scale Triaxial Testing of Greywacke Rockfill. *Geotechnique,* 44 (3) 539-544.

Ingold, T.S. (1994). *The Geotextiles and Geomembranes Manual*, Elsevier Advanced Technology.

Ishikawa, T., Sekine, E. & Miura, S. (2011). Cyclic Deformation of Granular Material Subjected to Moving-Wheel Loads. *Canadian Geotechnical Journal,* 48 (5) 691-703.

Janardhanam, R. & Desai, C.S. (1983). 3-Dimensional Testing and Modeling of Ballast. *Journal of Geotechnical Engineering-Asce,* 109 (6) 783-796.

Jewell, R.A. & Wroth, C.P. (1987). Direct Shear Tests on Reinforced Sand. *Geotechnique,* 37 (1) 53-68.

Le Pen, L. (2008). *Track Behaviour: The Importance of the Sleeper to Ballast Interface.* PhD, University of Southampton.

Le Pen, L., Bhandari, A. & Powrie, W. (2014). Sleeper End Resistance of Ballasted Railway Tracks. *Journal of Geotechnical and Geoenvironmental Engineering.*

Le Pen, L., Powrie, W., Zervos, A., Ahmed, S. & Aingaran, S. (2013). Dependence of Shape on Particle Size for a Crushed Rock Railway Ballast. *Granular Matter,* 15 (6) 849-861.

Li, C. & Zornberg, J. (2013). Mobilization of Reinforcement Forces in Fiber-Reinforced Soil. *Journal of Geotechnical and Geoenvironmental Engineering,* 139 (1) 107-115.

Li, J. & Ding, D.W. (2002). Nonlinear Elastic Behavior of Fiber-Reinforced Soil under Cyclic Loading. *Soil Dynamics and Earthquake Engineering,* 22 (9-12) 977-983.

Liang, L.Q., Saada, A., Figueroa, J.L. & Cope, C.T. (1997). The Use of Digital Image Processing in Monitoring Shear Band Development. *Geotechnical Testing Journal,* 20 (3) 324-339.

Lirer, S., Flora, A. & Consoli, N.C. (2011). On the Strength of Fibre-Reinforced Soils. *Soils and Foundations,* 51 (4) 601-609.

Lu, M. & Mcdowell, G.R. (2010). Discrete Element Modelling of Railway Ballast under Monotonic and Cyclic Triaxial Loading. *Geotechnique,* 60 (6) 459-467.

Macari, E.J., Parker, J.K. & Costes, N.C. (1997). Measurement of Volume Changes in Triaxial Tests Using Digital Imaging Techniques. *Geotechnical Testing Journal,* 20 (1) 103-109.

Maeda, K. & Ibraim, E. (2008). *Dem Analysis of 2d Fibre-Reinforced Granular Soils,* Amsterdam, I O S Press.

Maher, M.H. & Gray, D.H. (1990). Static Response of Sands Reinforced with Randomly Distributed Fibers. *Journal of Geotechnical Engineering-Asce,* 116 (11) 1661-1677.

Maher, M.H. & Woods, R.D. (1990). Dynamic-Response of Sand Reinforced with Randomly Distributed Fibers. *Journal of Geotechnical Engineering-Asce,* 116 (7) 1116-1131.

Mcdowell, G.R., Harireche, O., Konietzky, H., Brown, S.F. & Thom, N.H. (2006). Discrete Element Modelling of Geogrid-Reinforced Aggregates. *Proceedings of the Institution of Civil Engineers-Geotechnical Engineering,* 159 (1) 35-48.

Michalowski, R.L. (1997). Limit Stress for Granular Composites Reinforced with Continuous Filaments. *Journal of Engineering Mechanics-Asce,* 123 (8) 852-859.

Michalowski, R.L. (2008). Limit Analysis with Anisotropic Fibre-Reinforced Soil. *Geotechnique,* 58 (6) 489-501.

Michalowski, R.L. & Cermak, J. (2002). Strength Anisotropy of Fiber-Reinforced Sand. *Computers and Geotechnics,* 29 (4) 279-299.

Michalowski, R.L. & Cermak, J. (2003). Triaxial Compression of Sand Reinforced with Fibers. *Journal of Geotechnical and Geoenvironmental Engineering,* 129 (2) 125-136.

Michalowski, R.L. & Zhao, A.G. (1996). Failure of Fiber-Reinforced Granular Soils. *Journal of Geotechnical Engineering-Asce,* 122 (3) 226-234.

Mitchell, J.K. & Soga, K. (2005). *Fundamentals of Soil Behavior,* New Jersey, USA, John Wiley & Sons.

Networkrail (2005). Formation Treatments.

Networkrail. (2013). *Regulatory Financial Statements* [Online]. Available: http://www.networkrail.co.uk/browse%20documents/regulatory%20documents/regulatory%20compliance%20and%20reporting/regulatory%20accounts/nril%20regulatory%20financial%20statements%20for%20the%20year%20ended%2031%20march%202013.pdf [Accessed 18th March, 2014].

O'sullivan, C. (2011). Particle-Based Discrete Element Modeling: Geomechanics Perspective. *International Journal of Geomechanics,* 11 (6) 449-464.

Ranjan, G., Vasan, R.M. & Charan, H.D. (1996). Probabilistic Analysis of Randomly Distributed Fiber-Reinforced Soil. *Journal of Geotechnical Engineering-Asce,* 122 (6) 419-426.

Raymond, G. & Ismail, I. (2003). The Effect of Geogrid Reinforcement on Unbound Aggregates. *Geotextiles and Geomembranes,* 21 (6) 355-380.

Raymond, G.P. & Davies, J.R. (1978). Triaxial Tests on Dolomite Railroad Ballast. *Journal of the Geotechnical Engineering Division-Asce,* 104 (6) 737-751.

Raymond, G.P. & Diyaljee, V.A. (1979). Railroad Ballast Sizing and Grading. *Journal of the Geotechnical Engineering Division-Asce,* 105 (5) 676-681.

Rechenmacher, A.L. (2006). Grain-Scale Processes Governing Shear Band Initiation and Evolution in Sands. *Journal of the Mechanics and Physics of Solids,* 54 (1) 22-45.

Rechenmacher, A.L. & Finno, R.J. (2004). Digital Image Correlation to Evaluate Shear Banding in Dilative Sands. *Geotechnical Testing Journal,* 27 (1) 13-22.

Sadek, S., Najjar, S.S. & Freiha, F. (2010). Shear Strength of Fiber-Reinforced Sands. *Journal of Geotechnical and Geoenvironmental Engineering,* 136 (3) 490-499.

Selig, E.T. & Waters, J.M. (1994). *Track Geotechnology and Substructure Management*, T. Telford.

Sevi, A. & Ge, L. (2012). Cyclic Behaviors of Railroad Ballast within the Parallel Gradation Scaling Framework. *Journal of Materials in Civil Engineering,* 24 (7) 797-804.

Sevi, A.F. (2008). *Physical Modeling of Railroad Ballast Using the Parallel Gradation Scaling Technique within the Cyclical Triaxial Framework*. PhD Thesis, Missouri Univ. of Science and Technology, Rolla, MO.

Sevi, A.F., Ge, L. & Take, W.A. (2009). A Large-Scale Triaxial Apparatus for Prototype Railroad Ballast Testing. *Geotechnical Testing Journal,* 32 (4) 297-304.

Shukla, S.K., Sivakugan, N. & Singh, A.K. (2010). Analytical Model for Fiber-Reinforced Granular Soils under High Confining Stresses. *Journal of Materials in Civil Engineering,* 22 (9) 935-942.

Suiker, A.S.J., Selig, E.T. & Frenkel, R. (2005). Static and Cyclic Triaxial Testing of Ballast and Subballast. *Journal of Geotechnical and Geoenvironmental Engineering,* 131 (6) 771-782.

Tang, C.S., Shi, B. & Zhao, L.Z. (2010). Interfacial Shear Strength of Fiber Reinforced Soil. *Geotextiles and Geomembranes,* 28 (1) 54-62.

Thom, N.H. & Brown, S.F. 1989. The Mechanical Properties of Unbound Aggregates from Various Sources. *In:* JONES & DAWSON (eds.) *Unbound Aggregates in Roads*. London: Butterworth.

Viggiani, G. (2012). *Alert Doctoral School 2012: Advanced Experimental Techniques in Geomechanics*, ALERT Geomaterials.

Vinson, J.R. & Chou, T.W. (1975). *Composite Materials and Their Use in Structures*, Applied Science Publishers Ltd.

White, D., Take, W. & Bolton, M. (2005). Discussion of "Accuracy of Digital Image Correlation for Measuring Deformations in Transparent Media" by Samer Sadek, Magued G. Iskander, and Jinyuan Liu. *Journal of Computing in Civil Engineering,* 19 (2) 217-219.

White, D.J., Take, W.A. & Bolton, M.D. (2003). Soil Deformation Measurement Using Particle Image Velocimetry (Piv) and Photogrammetry. *Geotechnique,* 53 (7) 619-631.

Yetimoglu, T. & Salbas, O. (2003). A Study on Shear Strength of Sands Reinforced with Randomly Distributed Discrete Fibers. *Geotextiles and Geomembranes,* 21 (2) 103-110.

Zingg, T. (1935). Beitrag Zur Schotteranalyse. *Schweiz. Mineral. Petrogr. Mitt.,* 15 39 - 140.

Zornberg, J.G. (2002). Discrete Framework for Limit Equilibrium Analysis of Fibre-Reinforced Soil. *Geotechnique,* 52 (8) 593-604.